POLITECNICO

MILANO 1863

SCUOLA DI INGEGNERIA INDUSTRIALE
E DELL'INFORMAZIONE

Hingeless arm for space robotics actuated through shape memory alloys: thermal analysis and mechanical optimization

Master of Science in Aeronautical Engineering

Author: **Emanuele Casciaro**

Student ID: 952939
Advisor: Paolo Bettini
Co-advisor: Daniela Rigamonti
Co-advisor: Tiziana Biasutti
Academic Year: 2021-22

Abstract

The hostile space environment has forced Man to make instruments that can withstand extreme conditions, controlled remotely. The realization of light and flexible robotic arms to carry out risky, extremely long or impossible operations is an area of research in continuous growth.

This thesis aims to use NiTiNOL wires as actuators for a flexible and lightweight composite construction. In addition, the designed structure is continuous: this allows to make prototypes of the desired length without joints. The uses of the final component are different, and the most relevant are: the inspection of otherwise inaccessible areas and the refuelling of spatial structures. This work continues the one already dealt with in the thesis of Dr. Biasutti Tiziana: HINGELESS ARM FOR SPACE ROBOTICS ACTUATED THROUGH SHAPE MEMORY ALLOYS. The goal is to increase the TRL (technology readiness level) of already existing prototypes.

Thermal analysis and mechanical optimization of the structure are the areas on which we focus. The work is divided into four large analyses. The first concerns the thermal behaviour of the structure by simulating the spatial environment. The limits of direct exposure of the model to radiations are highlighted and the mechanisms to mitigate these problems are devised. The second analysis starts from these considerations and addresses the problem of thermal control of the structure and the cooling of NiTiNOL wires. The third aims to the mechanical optimization of the structure, varying fundamental geometric parameters such as pitch, diameter and width of the composite part. The purpose is to identify more flexible configurations which can be sufficiently rigid as well. The last analysis concerns the real activation of the created prototypes and the measurement of the displacement that the NiTiNOL wires can generate. The choice of the model that satisfies these four analyses is fundamental for the resolution of the problems that the component will face in its operating life.

Key-words: Shape memory alloys, NiTINOL, temperature, cooling, mechanical optimization, analysis, finite elements analysis

Abstract in italiano

L'ambiente spaziale ostile ha costretto l'uomo a realizzare strumenti, controllati a distanza, in grado di resistere a condizioni estreme. La realizzazione di bracci robotici leggeri e flessibili per effettuare operazioni rischiose, estremamente lunghe o impossibili è un'area di ricerca in continua crescita.

Questa tesi si propone di utilizzare fili di NiTiNOL come attuatori per una struttura leggera e flessibile in materiale composito. Inoltre, il componente progettato è continuo: ciò consente di realizzare prototipi della lunghezza desiderata senza giunzioni. Gli usi dello strumento finale sono diversi e i più rilevanti sono: l'ispezione di aree altrimenti inaccessibili e il rifornimento delle strutture spaziali. Questo lavoro prosegue quello già trattato nella tesi della Dott.ssa Biasutti Tiziana: HINGELESS ARM FOR SPACE ROBOTICS ACTUATED THROUGH SHAPE MEMORY ALLOYS. L'obiettivo è quello di aumentare il TRL (livello di preparazione tecnologica) dei prototipi già esistenti.

L'analisi termica e l'ottimizzazione meccanica della struttura sono le aree su cui ci siamo concentrati. Il lavoro è suddiviso in quattro grandi analisi. La prima riguarda il comportamento termico della struttura simulando l'ambiente spaziale. Vengono evidenziati i limiti dell'esposizione diretta del modello alle radiazioni e vengono ideati i meccanismi per mitigare questi problemi. La seconda analisi parte da queste considerazioni e affronta il problema del controllo termico della struttura e del raffreddamento dei fili di NiTiNOL. La terza mira all'ottimizzazione meccanica della struttura, variando i parametri geometrici fondamentali come il passo, il diametro e la larghezza della parte composita. Lo scopo è quello di identificare configurazioni più flessibili che possano essere anche sufficientemente rigide. L'ultima analisi riguarda l'attivazione reale dei prototipi creati e la misurazione dello spostamento che i fili di NiTiNOL possono generare. La scelta del modello che soddisfa queste quattro analisi è fondamentale per la risoluzione dei problemi che il componente dovrà affrontare nella sua vita operativa.

Parole chiave: leghe a memoria di forma, NiTiNOL, temperatura, raffreddamento, ottimizzazione meccanica, analisi, analisi agli elementi finiti

Contents

Introduction

In the field of space engineering, research and development of new and more efficient materials is a key aspect for achieving increasingly ambitious goals. In this perspective, the study of smart materials has a great importance. Smart materials are components with one or more properties that can be changed and controlled by external stimuli. They can be classified according to the working principle:

- Property change: they change a material property according to external stimulus, for example: color, properties of the optical signal, viscosity et alia.
- Energy transformation: they transform the incoming energy in the material into another form of energy, for example: change of temperature in light emission, change of temperature or stress in deformation, deformation in electrical signal et alia.

They can be composed of a single material or several materials embedded in a host structure and are chosen according to the function they must perform, the morphology of the host, the compatibility between different materials and invasiveness. The most used are:

- Piezoelectric materials: they can convert mechanical energy into electrical energy and vice versa.
- Shape memory materials: they have the ability to change the shape, even returning to their original form, when exposed to a heat source.
- Chromoactive materials: they change color when subjected to a certain variation in temperature, light, pressure, etc.
- Magnetorheological materials: they change their properties when exposed to a magnetic field.
- Photoactive materials: they come in several types. Electroluminescents emit light when they are fed with electrical impulses, fluorescents reflect light with greater intensity and phosphorescents are able to emit light after the initial source has ceased.

It is possible to further divide smart materials according to usage:

- Sensors: convert a physical action into electrical signals (optical fiber, piezoelectric, …)

- Actuators: convert the electrical signal into mechanical work (shape memory alloys, piezoelectric, …)

Some materials such as quartz (a piezoelectric material) can be used both as sensors and as actuators. We speak respectively of direct or reverse effect.

This thesis aims to continue the research undertaken by Dr. Biasutti Tiziana in her paper: *HINGELESS ARM FOR SPACE ROBOTICS ACTUATED THROUGH SHAPE MEMORY ALLOYS*. In the work mentioned, the aim was to create a borescope in composite material actuated through wires of NiTiNOL heated by Joule effect, so that it was possible to control the direction of movement of the structure. Firstly, it was indispensable to analyze the state of the art, the existing robotic structures and the use of SMA in the medical field as a starting point for the initial design phase of the prototype. Studies with finite element methods, using the Abaqus software, and simulations with configurations, using NiTiNOL wire models, were carried out in order to define the geometric properties of the design and predict its behavior. The following steps were the creation of the prototypes, the determination of how they could be manufactured and the establishment of a system in order to acquire experimental data. Eventually, it was necessary to run some tests on the prototypes to compare them with the numerical results.

The possible applications of this robotic arm are multiple. Since we are in a preliminary phase of the project, we can imagine its use not only as a borescope or to inspect inaccessible places but also as a system for the handling of objects (maybe directly exposed to the space environment) or as a remotely piloted refueling system.

The optimization of the structure and its analysis in the environment in which it will work constitute the next step after the conceptual design phase. In order to do this, it was necessary to carry out a thermal study as the temperature is a fundamental engine for the operation of the model. Moreover, it is worth noting other important aspects such as the implementation of a more accurate data acquisition system and the improvement of the instrumentation for the experiments.

Two software were used: Matlab, for data analysis, and Abaqus, for optimization and mechanical/thermal simulations regarding the structure. Finally, for the experimental part, Python was employed, with the working environment Visual Studio Code, to implement a procedure that would overcome the difficulties encountered experimentally. During the design of 3D models of the pieces created, the software Solidworks was used, whereas for the study of the data acquisition system and for the theoretical studies present in the appendices, Arduino was used with its programming environment and hardware.

This thesis does not follow a sequential course in the exposition of the arguments because more problems are analyzed, each with its own theoretical base and its own solutions. For this reason, it was decided to divide it into 2 macro sections: thermal

analysis and mechanical optimization. The thermal analysis part is divided into analysis of the activation of the structure in a spatial environment (Chapter 2) and analysis of the cooling of shape memory alloys (Chapter 3). The mechanical optimization part is divided into physical and geometric parameter variation (Chapter 4) and experimental test (Chapter 5). Chapter 1 deals with the theory of the memory alloys and the problem faced by this thesis.

The last part, Chapter 6, is one in which the optimal structure derived from the analyses is chosen and the next steps to follow in the creation of the prototype and the problems to be studied are explained. In the appendices there are all the graphs and data that, because of the space, could not be put in the thesis. There are also theoretical models of components that can be useful in subsequent works.

1 State of the Art

1.1. Shape memory alloys

Shape memory alloys or smart metals are expressions used to refer to a series of metal compounds that, when mechanically deformed, are able to return to their original shape if heated above a certain temperature. They are particularly efficient materials and are employed in aerospace applications also because of their low weight and the possibility of embedding them directly into structures in the form of wires. One of the most widely used is NiTiNOL (Ni-Ti Naval Ordinance Laboratory), an equi-atomic alloy composed of Nickel and Titanium. It is a corrosion-resistant and biocompatible material that can undergo large deformations, between 5-8%. The transition temperatures, which allow it to recover its original shape, can vary from -30 ℃ to 170℃. Therefore, the more Ti-rich the material the higher the transition temperature will be. The purpose of this thesis is to use NiTiNOL wires as actuators, preventing the recovery of the initial shape with constraints in order to generate recovery stresses which will be employed to actuate the host structure.

1.1.1. Structure of shape memory alloys

The reason for the peculiar behavior of NiTiNOL is to be found in its crystalline structure. NiTiNOL has two crystalline structures. The transition from one to the other constitutes a phase transition in the solid state. The transition between two states of matter is induced by the change in temperature, by the applied force, or by a combination of them. The two crystalline structures of NiTiNOL are:

- Austenite (parent phase, γ): is the stable phase at high temperature. It is characterized by a symmetry lattice body-centered cubic symmetry (BCC) which allows it to have a high elastic modulus. The material at this stage is hard and difficult to deform.
- Martensite (product phase, α'): is the stable phase at low temperature. It has a monoclinic crystal structure distorted, much less symmetrical than the BCC type, so it has a low elastic modulus and it is characterized by great flexibility. In the martensitic phase, therefore, the material subjected to mechanical stress is able to withstand a high degree of deformation without, however, breaking the chemical bonds.

In the product phase, if there are no stresses in the material, there can be up to 24 different orientations of the crystal lattice simultaneously, known as variants. In this case it is call twinned martensite. If, on the other hand, there are some strains, only the orientations that satisfy the stresses can be present and, in this case, we speak of detwinned martensite. There is also an intermediate phase during the transformation from cubic austenite to monoclinic martensite, called rhombohedral R-phase. The advantages of this phase are the extremely low temperature hysteresis and the high durability. The main disadvantage, instead, is the small SMA effect [1].

1.1.2. Martensitic transformation

The transformation that allows the transition from one phase to another is called martensitic transformation. The driving force of the transformation is Gibbs' free energy, through temperature and stress state. There is an equilibrium temperature T_{eq} where the ΔG of the two phases are equal: at lower temperatures the transformation is driven by α', while at higher temperatures it is stable γ. According to the state of departure and the state of arrival one can distinguish between forward and reverse transformation:

- Forward: from austenite to martensite. This transformation can be induced either by temperature, by cooling the material, or by a state of stress, and we will speak of thermally-induced martensite and mechanically-induced martensite (or Stress-Induced Martensite, SIM), respectively.
- Reverse: from martensite to austenite. This transformation can be induced by temperature heating the material above a certain temperature.
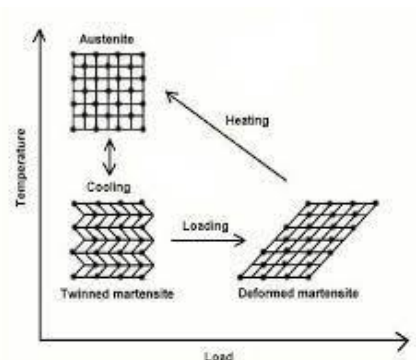
Figure 1: Mechanisms of transition from one phase to another

Considering the two driving parameters (stress state and temperature) we can distinguish four characteristic temperatures that mark the beginning and end of the transformation: austenitic start and finish temperature (A_S and A_F), which drive forward transformation, and martensitic start and finish temperature (M_S and M_F), which drive backward transformation. The stress state linearly affects the temperature like in the equations below (1.1):

$$\begin{cases} A_S(\sigma) = A_{S0} + \dfrac{\sigma}{c_A} \\[2mm] A_F(\sigma) = A_{F0} + \dfrac{\sigma}{c_A} \\[2mm] M_S(\sigma) = M_{S0} + \dfrac{\sigma}{c_M} \\[2mm] M_F(\sigma) = M_{F0} + \dfrac{\sigma}{c_M} \end{cases} \tag{1.1}$$

There are two types of solid-state transformations: diffusive and dysplastic. In diffusive transformations, the new phase is formed through the movement of atoms, over relatively long distances. The progress of the transformation depends on time and temperature. Dysplastic transformations do not require such movements; the atoms rearrange cooperatively into a new crystal structure, without changing the chemical composition of the starting phase. Since no atomic migrations are needed, dysplastic transformations advance independently of time. Martensitic transformations belong to the dysplastic type, obtained by cooling the parent or austenitic phase and the transformations are first order, meaning that heat is released when martensite is formed. There is a temperature range in which austenite and martensite coexist. In fact, during forward transformation, the martensitic fraction, i.e., the ratio between the volume of martensite present in the material and the total volume, increases, while during reverse transformation, it decreases. From the crystallographic point of view, the transformation of the austenitic phase into the martensitic phase can be considered as the sum of two contributions: the so-called Bain strain and the consequent accommodation (latex-invariant shear). Bain strain consists of a series of atomic motions smaller than the interatomic distances, in order not to generate the breakage of the chemical bonds. These motions lead to the formation of a new phase. The martensite formed by this transformation has a shape, and sometimes a volume, different from those of the austenitic parent phase. Therefore, an accommodation of the new structure within the material is required. The mechanisms through which this accommodation can be achieved are two: atomic slip and gemination. In both cases the material, while retaining the newly formed martensitic structure, assumes the same macroscopic shape as the parent phase. But, while atomic slip is a permanent process, typical of steels, since it irreversibly modifies the microstructure of the material, through the breaking and slipping of bonds, gemination is a reversible process.

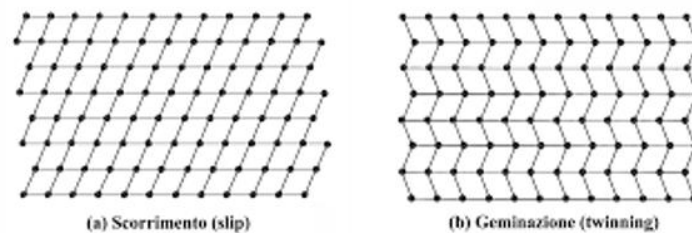(a) Scorrimento (slip) (b) Geminazione (twinning)

Figure 2: Difference between atomic slip and gemination

As it is, therefore, intuitive, in shape memory alloys the main mechanism of accommodation is that of gemination. Gemination occurs through a motion of the atoms facing a characteristic plane called twin boundary. Such a plane is a plane of perfectly specular symmetry, since each atom sees, on both sides of the plane, the same number of atoms, with the same symmetry as the bonds. The characteristics of the twin boundary mean that, due to an applied load and in isothermal conditions, the microstructure of the material is arranged according to a preferential variant, the orientation of which is more favorable to the applied stress. The phenomenon is called detwinning. While by unloading the specimen at a constant temperature, a permanent deformation remains. This is what happens when stress is applied. However, the recovery of the original shape without deformation occurs through temperature, in particular the high temperature causes a shift of the atoms which, from the different forms of the martensitic state, settle in a grid as regular and compact as possible: the result is a rigid cubic arrangement with centered body (austenitic phase). Martensitic transformation encompasses all these phenomena [2]. Another important peculiarity related to the thermal cycle, that the transformation follows to change its solid state, is hysteresis, i.e., different behavior in the heating and cooling phases, which causes the dissipation of a part of the energy supplied to the material. Microscopically, the phenomenon can be interpreted as the friction associated with the movement of the twinned edges.

1.1.3. Characteristic temperatures

A typical way to characterize phase transformations is to define the characteristic temperatures, which are obtained by heating and cooling the material, subjected to a constant load. It is thus possible to identify a hysteresis cycle in which, you can estimate some characteristic temperatures that determine the beginning and the end of the martensitic (M_s, M_f) and austenitic (A_s, A_f) phases.
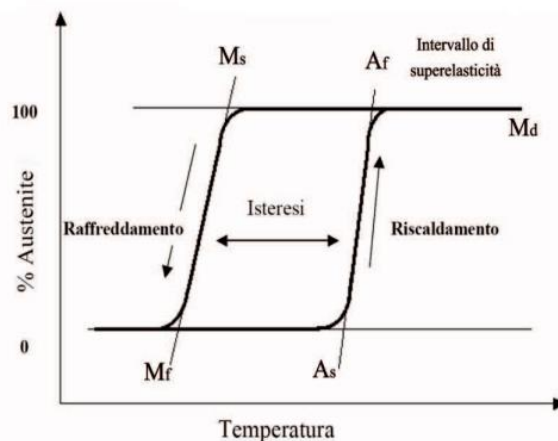
Figure 3: Curve relating the temperature and the volumetric fraction of austenite

- A_s, or Austenite Start: temperature at which the transformation from martensite to austenite begins while the material is heated.

- A_f, or Austenite Finish: temperature at which the transformation from martensite to austenite ends while the material is heated.
- M_s, or Martensite Start: temperature at which the transformation from austenite to martensite begins while the material is cooled.
- M_f, or Martensite Finish: temperature at which the transformation from austenite to martensite ends while the material is cooled.

Since the temperatures vary with the applied load, for each stress state you can recalculate the characteristic temperatures and see how they change. What you get is a graph that ties these two competitors into the martensitic transformation.
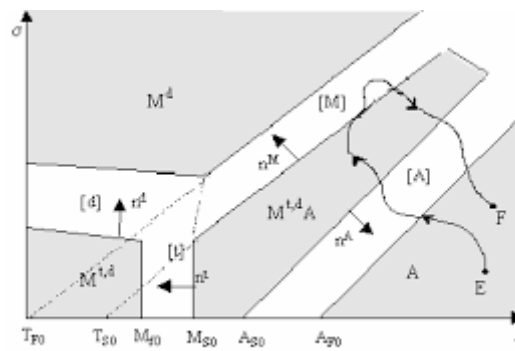
Figure 4: Variation of characteristic temperatures with stress state

It is possible to recognize 4 regions: austenite, twinned martensite, detwinned martensite and the last one in which martensite and austenite coexist. There are also two transition zones in which there is a transition from one phase to another, where the volumetric fraction of martensite and austenite changes [3].

1.1.4. Properties of shape memory alloys

The thermos-mechanical properties of shape memory alloys depend on: chemical composition, manufacturing process, thermal treatments and thermo-mechanical cycles (both during training and operative life). Two shape memory effects can be distinguished:

- Shape memory effect
- Pseudo-elastic effect

Both of these properties affect the material's response to external stimuli, i.e., temperature and stress state.

1.1.5. Shape memory effect

The shape memory phenomenon translates into the ability to return spontaneously to a preset shape, imposed by a previous treatment: in fact, when the piece, after having been plastically deformed at a low temperature by a stress lower than the martensite

yield stress, is heated until it exceeds the austenitic start temperature, regains the shape it had before being deformed. This capability is called one-way shape memory effect.
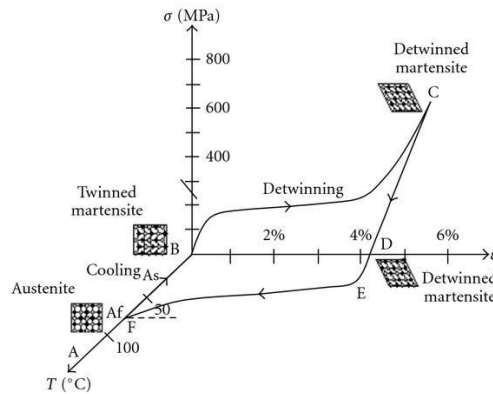
Figure 5: Cycle of the OWME
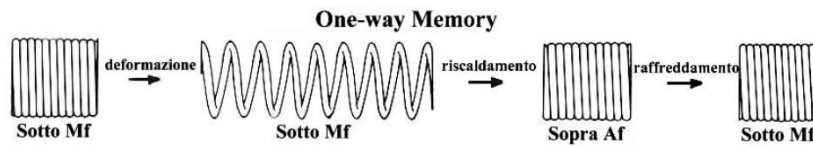
Figure 6: Example OWME

This behavior is perfectly summed up by the graph above. The material, in austenitic form, is loaded to yield stress. When the load is released what remains is a permanent deformation that can be recovered by bringing the material back into the austenitic phase. For this reason, it is necessary to carry out the reverse martensitic transformation, heating up to A_f. There is also the phenomenon of two-way shape memory, which can be simply described as the spontaneous change in shape of a specimen when heated or cooled. The material remembers both high-temperature and low-temperature shapes. No external force is required to activate the phenomenon. To manifest the effect, the material must undergo special thermo-mechanical preparation treatments. The stress that can develop a component produced in this way, however, is quite small.
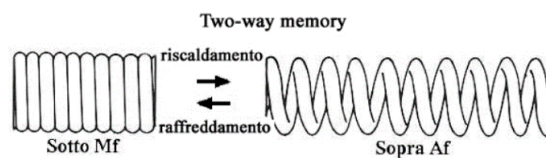
Figure 7: Example TWME

In order to achieve the two-way shape memory effect, it is necessary to start with an initial state of partially oriented martensite whose shape has previously been imposed on the material by training. The material is loaded until the elastic domain of the detwinned martensite is reached. At this point the load is removed and a residual strain is obtained which disappears when the part is heated above A_f temperature as

the part has recovered the shape of the austenitic phase, i.e., the second shape which the material stored during training. The next transformation is the cooling of the material under the M_s which, in this way, regains the initial form of partially oriented martensite [4].
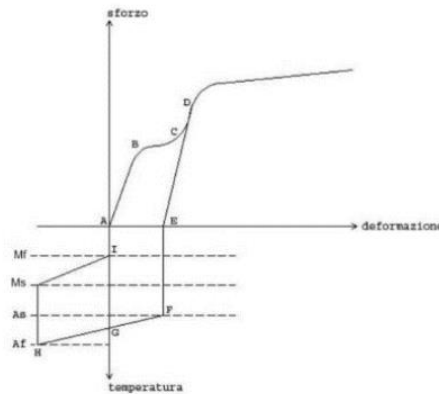
Figure 8: Cycle of the TWME

The most exploited effect is OWME, which is also used as an actuation system. In fact, after the material has been deformed at low temperature and subsequently heated, if it is prevented from returning to its initial shape by a load, it can generate a considerable force that can be used in engineering applications to move actuators and thus produce work. When the material is cooled again, the load will deform it again, making it return it to its original martensitic condition and resetting the mechanism.

1.1.6. Pseudo-elastic effect

Generally, martensite starts to form at M_s, in the absence of stress. In the same material, the phase change can also be generated at higher temperatures, if stress is applied. If you start from NiTiNOL in Austenite phase at constant temperature and above A_f (temperature at which all domains are austenitic) and a mechanical stress is applied it is possible to induce a phase transformation obtaining Martensite detwinned with the consequent achievement of considerable elongations (up to 10%). Upon subsequent release of the load, the new phase becomes unstable and the material recovers its original shape. Unlike the shape memory phenomenon, no increase in temperature is required for this to occur. In other words, the material seems elastic: this is why we speak of a pseudo-elastic effect or, improperly, of super-elasticity. This behavior can only be obtained if the temperature is in a range between the A_f temperature and the M_d temperature (M_d is the transition temperature between the pseudo-elastic phase and the austenitic phase only, which, for NiTiNOL alloys, is usually 50 K above the A_f temperature), i.e., the highest temperature at which it is possible to have martensite.
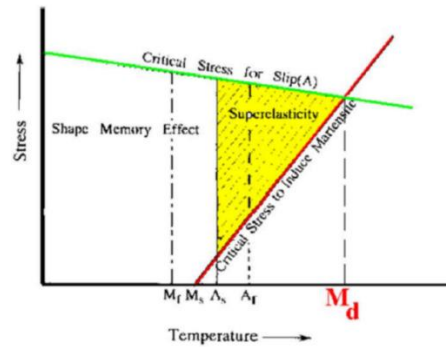
Figure 9: Range of existence of pseudo-elastic effect

As can be seen from the graph below, at temperatures above both A_f and M_d, the behavior of the material is dictated by the presence of the austenitic phase, presenting a typical behavior of traditional steels. At low temperatures, being in the presence of the martensitic phase, the behavior is typical of a one-way shape memory alloy, where the complete recovery of the residual deformation is achieved by an increase in temperature (carried out by heating or by means of a current passage). At intermediate temperatures the pseudoplastic behavior is observed, where the total recovery of the deformation occurs simply by removing the applied load.
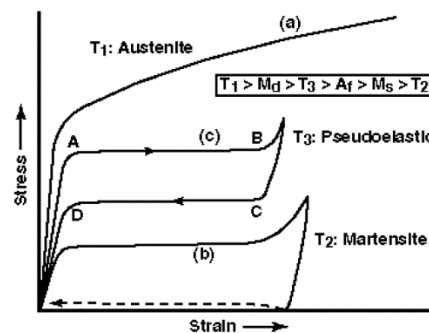
Figure 10: Behavior based on 3 different temperatures

1.1.7. Manufacturing of shape memory alloys

Smart metals, like NiTiNOL, can not only remember their original shape, but they can also be trained to "store" a new one. To understand how this happens, remember that the Nickel and Titanium atoms within one of the many crystalline regions, called "grains", are almost perfectly aligned in the austenitic phase. As in any crystal, there are inevitably some defects, called dislocations. Dislocations consist of a displacement of a crystalline plane produced by an intense mechanical stress that induces deformation. The formation of a dislocation implies that certain chemical bonds are broken. These defects are energetically stable and remain unchanged between the austenitic and martensitic phases because this transformation takes place without breaking and rearranging the chemical bonds. Therefore, the metal in the martensitic phase undergoing heating returns to its original form, characterized by the specific defect configuration in the austenitic phase. For this reason, to allow the storage of a

particular shape are the defects of the parent phase and changing these defects can also change to the stored form. To have both OWME and TWME, NiTiNOL needs to be trained:

- In order to achieve the one-way shape memory effect and provide the desired shape for the austenitic phase, a new set of defects must be created. This can be achieved by heating the material to approximately 500°C for 10 to 60 minutes. During the subsequent cooling, the atoms settle into positions, creating the new set of defects compatible with the shape imposed on the material. The shape can be redefined several times by simply repeating the heating process.

- To obtain the two-way shape memory effect, it is necessary to heat the material so as to obtain only the austenitic phase and then apply a deformation (maximum 6%) to obtain SIM. Therefore, it is necessary to cool the material under M_f constraining it in the deformed shape and then heat it to regain the original undeformed shape. The cycle must be repeated at least 10 times to obtain the effect.

1.1.8.   Test to characterize shape memory alloys

1.1.8.1. Differential scanning calorimetry

To estimate the transition temperatures of NiTiNOL, i.e., the temperatures at which the transition from martensite to austenite takes place, and vice versa, DSC (Differential Scanning Calorimetry) is used. Differential scanning calorimetry is an instrumental technique that is used to study thermal stability, temperature and heat associated with state transformations and chemical reactions. This technique is based on the detection and quantification of exothermic and endothermic phenomena affecting a given sample as a function of its temperature and the atmosphere, inert or reactive, in which the analysis is carried out. The instrument used consists of two heating resistors and two crucibles: in one, the sample of material to be analyzed is inserted and, in the other, an inert sample is inserted as a reference. Differential scanning calorimetry measures, as a function of sample temperature, the difference between the heat fluxes in the sample and the reference, while both are subjected to the same controlled temperature program. During heating, any state transformation or chemical reaction affecting the sample causes the resistor under the sample to transfer a different amount of heat compared to the heat transferred by the resistor under the inert reference. The measurement of the difference in heat flow as a function of the sample temperature is shown on a diagram with the temperature on the x-axes and the difference in heat flow on the y-axes. With reference to a generic shape memory alloy, during heating the relative thermogram shows an endothermic peak at the phase transition from martensite to austenite and, during cooling, an exothermic peak at the phase transition from austenite to martensite. The Onset points of

transformations can be identified, corresponding to the intersection between the tangent to the base line and the tangent to the inflection point before the peak, and the Endset points, corresponding to the intersection between the tangent to the base line and the tangent to the inflection point after the peak. These Onset and Endset points correspond to the start and end temperatures of the phase transformation.
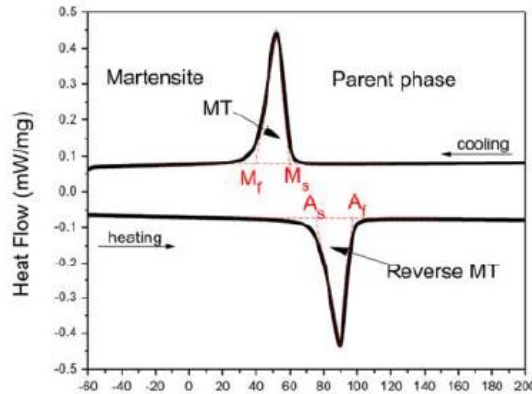
Figure 11: DSC to estimate the four characteristic temperatures of a shape memory alloy

1.1.8.2. Isothermal test

For the isothermal test (ASTM E111-97 [5]), the equipment that is used consists of an electromechanical machine and an oven, that keeps the temperature constant. The specimen is held in place by grips that fix the specimen and allow to apply a load along its longitudinal axis. The pressure applied by the grips must prevent the specimen from slipping. From the results, it is possible to evaluate the elastic moduli of the material at constant temperature.
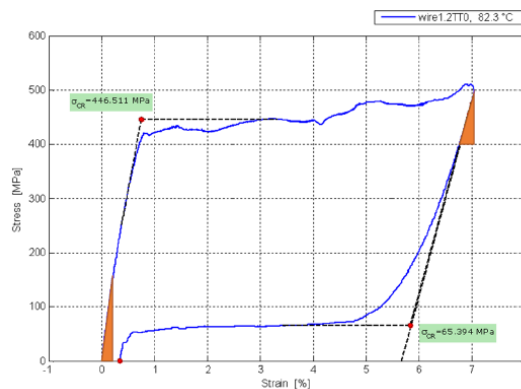
Figure 12: Curve obtained from isothermal test

1.1.8.3. Isobaric test

For the isobaric test (i.e., iso-stress), the material is stretched to apply a fixed preload and clamped to a machine capable of keep constant longitudinal tensions and finally heated by monitoring temperature and deformation. Thermal expansion coefficients of pure Austenite and Martensite can be derived from this test.
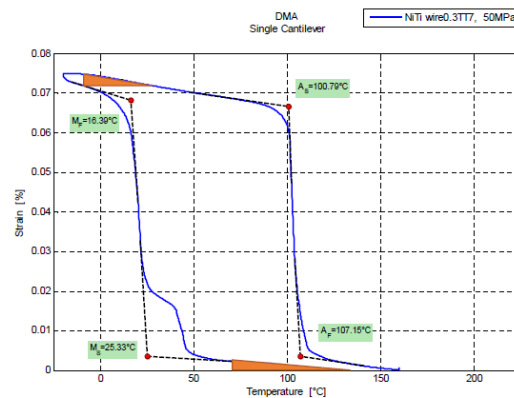
Figure 13: Curve obtained from isobaric test

The last important graph, representing the behavior of shape memory alloys, is obtained by varying the load and recalculating the characteristic temperatures. This results in different curves at different loads applied.
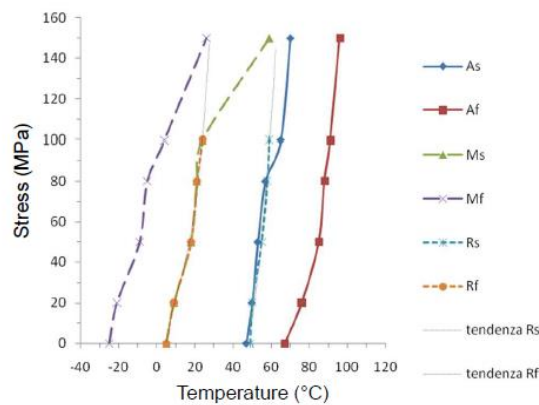
Figure 14: Variation curve of characteristic temperature with stress state

1.2. Problems in space environment

The spatial environment is very different from the terrestrial one, many phenomena can damage the structural integrity and mechanical behavior of the components. This requires the construction of structures resistant to degradation in space and the design of thermal protection systems. Some problems which need to be studied and kept under control are:

- Ionizing radiations
- Cycles of photonic radiations
- Contaminations, due to condensation and polymerization of volatile material
- Atomic oxigen
- Outgassing
- Micrometeorites, particles or objects coming directly from space
- Debris, particles or objects stemming from the degradation of artificial objects (other satellites, old components, propellant residues)

- Thermal cycles, due to cyclic temperature changes caused by radiations or internal heat generation
- High and low temperatures, due to sun or deep space exposure and internal heat generation

All these phenomena can cause changes in mechanical properties (embrittlement, strength reduction, thinning/consumption, deformability decrease), changes in thermo-optical properties (emissivity and absorbance change and, thus, changes in the heat transfer properties that affect the efficiency and functionality of the components), changes in electrical properties (loss of thermal power or loss of insulation capacity) and changes in surface properties (adhesion, friction). The phenomena suffered by the components also depend heavily on the material of which they are made.

1.2.1. Phenomena of degradation in space

1.2.1.1. Atomic oxygen effects

The Atomic Oxygen in the low Earth orbital environment (LEO) is formed by photo-dissociation of diatomic oxygen. Short-wavelength (<243 nm) solar radiations have sufficient energy to break the O_2 diatomic bond in an environment where the mean free path is sufficiently long. Thus, the probability of re-association or the formation of ozone (O_3) is low, which means that the rate of splitting of O_2 to the atomic oxygen species (AO) by UV is faster than the corresponding recombination. Oxygen atoms are known to be highly corrosive, once combined with most materials they encounter. In addition, the AO collision with the component surfaces can initiates numerous chemical and physical events on the surfaces: erosion of surface, embrittlement, strength reduction, deformability decrease, formation of surface cracks, loss in mass, variation of roughness, degradation in mechanical, thermal and optical properties and changes in chemical compositions of materials. Some solutions consist in the use of protective surface films (for example silica, alumina, silicon, fluorinated polymers with metal oxides, etc.), in the modification of the surface (i.e., the introduction of metals ions, silicon and phosphorous containing polymers) or the use of inorganic fillers introduced into polymers (metals, silica, alumina) [6].

1.2.1.2. Outgassing

Any material in a vacuum environment loses its mass. Some materials evaporate and the molecules absorbed on surfaces desorb. This phenomenon has a minimal effect on metals and ceramics. However, the same cannot be said for polymers on which the effect depends on the content of volatile matter. Volatile matter may be present in polymers after manufacturing or it may be present as a product of degradation/oxidation caused by exposure to the spatial environment. The main effects of outgassing are more evident on functional than mechanical properties. In fact, the material can settle on the optical surfaces not allowing the correct functioning,

it can settle and change the performance of surfaces such as solar panels (which are fundamental for their energy supply on satellites), cover and compromise the efficiency of electrical components or change the thermal exchange properties of the surfaces (which are crucial for the thermal dissipation processes). Some solutions may be choosing low outgassing materials, carrying out ground pre-treatments and avoiding proximity between contamination sources and sensitive components [7].

1.2.1.3. Radiations

There are different types of radiation depending on the height of the satellite:

- Solar spectrum radiations (UV, low energy radiations)
- Charged particles radiations (electrons, protons, ions)
- High energy photonic radiations (X rays, gamma rays)

Low energy radiation affects the behavior of polymers (scission of polymer chains, oxidation, generation of low molecular weight volatile substances) leading to loss of toughness/deformability of surface layers, breakage of films, surface cracks, failure of protective coatings, change of color or formation of chromophore compounds that induce a change of optical response of the surface. They can also lead to the reduction of the optical properties of ceramics. High-energy radiation, caused by solar flares, cosmic rays, solar proton events, radiation belts, are very dangerous for the GEO and HEO orbits, while they have a minor effect on those LEO thanks to the terrestrial magnetic field that acts as a shield. They can cause the degradation of materials, especially polymers that undergo a strong physical and mechanical degradation. A great exposure to these radiations can also have negative effects on the crew and on the electronics (electrostatic charges accumulation, high voltage discharges, radioactivity generation, modification of digital memories and reduction of solar cells and instrument efficiency). The effects of radiations can be mitigated by the appropriate selection of materials and by the use of protective coatings for sensitive materials. On the other hand, as for ionizing particles, the aforementioned effects can be limited by predicting the loss of functionality during the design phase or using metal shielding in Al or heavy metals.

1.2.1.4. Micrometeorites and debris

Even external bodies present in space have a great influence on the proper functioning of the equipment that is brought into orbit. In fact, micrometeorites, which are particles or objects coming from space, and debris, artificial objects coming from obsolete components, which constitute the so-called space junk, can impact space instrumentation causing the projectile vaporization and the production of craters larger than the impacting body. The phenomenon is so relevant that it is classified also on the basis of the frequency of impact, i.e., the expected time-span between two consecutive impacts as a function of the dimensions of the particles. To limit the problem caused by these foreign bodies, it is necessary to make a careful study of the

mission to be accomplished, foreseeing everything in the design phase. The creation of redundant systems is necessary to avoid the loss of control over the mission. In addition, the use of sandwich/multiwall protections (whose thickness and the choice to use single wall or double wall depend on the speed of the impacting bodies), multi-layer insulation covers reinforced with fiber and beta cloth (fabric made of silica fibers coated with PTFE layer, polytetrafluoroethylene, a polymer of fluorine and carbon) can help to avoid the aforementioned problems as well.

1.2.1.5. Temperature and thermal cycles

The thermal loads acting on the system depend on:

- Orientation with respect to Sun/Earth
- Orbit cycles
- Orientation with respect to other surfaces
- Internal sources
- Thermo-optical properties

The proper selection of emissivity, absorptivity (transmittance, conductivity), and the way these properties vary with temperature, allows to set the thermal balance. The choice of materials, thermal protections and paints used affects emissivity and absorptivity coefficients (white paint has α=0.21, while black paint has α=0.97). The time spent in space affects the value of the coefficients, changing the thermal cycles.

1.2.2. Use of SMA in the spatial environment

Shape memory alloys have been employed in space projects for over thirty years and the experience accumulated in the different missions has highlighted the advantages and disadvantages of these materials. Some advantages are: low shock upon actuation, lack of shock loading, high-energy and high-strain actuation, simplicity, reliability of low-cost devices, no contamination (no dust particles created, no loss of fluid), cyclic activation and deactivation capability, high yield strength, high power/weight ratio and frictionless, clean, silent and spark-free operations [8]. The possible uses of the SMA are:

- Operating components for deployable constructions. This is due to the fact that shape memory actuators allow easy control of the deployment process. In these structures, the use of shape memory alloys was foreseen both as functional and as construction material. The main problem was how to ensure the required geometrical dimensions of the objects after their deployment. For this reason, we have moved to the use of SMA only as a functional material. One of the first examples of such application can be considered a model of wire actuators of the flaps of the instrument container for satellite Nimbus [9].
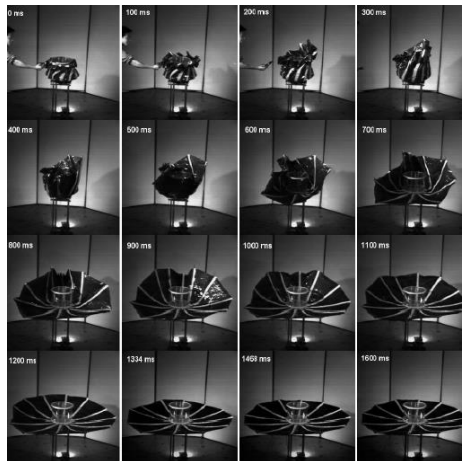
Figure 15: Deployable structure tested on the ground

- Tools for damping of vibrations. The ability of SMA to act as efficient vibration isolators comes from their pseudo-elastic capabilities as the hysteretic force versus displacement behavior allows for energy dissipation. An important use in this area is during launches. During launches, the payloads experience great transient and vibration acceleration loads. These loads are a major design constraint. Vibration isolations are designed to reduce these loads at the mounting interface, thus allowing to save in weight and launch costs as well as improve the system's reliability [10]. In addition to passive damping, an active damping system has also been studied and recently been applied to the isolation of vibration of the engine, transmission and rotor from the passenger space in a British designed helicopter. Another problem that requires the use of SMA dampers is the use of large facilities such as laboratories for astronauts. These very large truss-like structures will have problems of stability, as a result of induced vibrations from the manned activities, motions induced by docking of shuttles or other vehicles, or vibrations involving a shift in the platform position required in tactical maneuvering. Studies have shown that feedback control using small vectoring rockets will not be sufficient to provide positional stability and this has led to the use of SMA dampers [10], [11], [12].
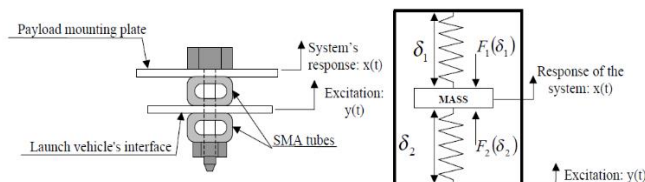

Figure 16: Vibration isolation design using SMA tubes and an equivalent mechanical system

- Composite materials with embedded SMA-elements which could be used as actuators, not only for damping and control of vibrations, but also for changing the stress and shape of the object made of these materials [9].

- Shape memory connectors are being developed to facilitate the joining of composite members [11]. The aim of another space experiment, called Sofora, was to develop techniques of assembling constructions in open spaces with the help of thermomechanical couplings, whose main element is a sleeve made of shape memory alloys. Other posting systems used consisted of bolts made of a high-strength titanium alloy, sleeves made of TiNi, and heaters [9], [11].
- Hermetic connection. The first "launch" of TiNi to an Earth orbit can be considered to have happened in 1982, when thermomechanical pipe couplings on the orbital station Salyut-7 were tested for their hermetic durability [9].
- The most common use of SMAs in space applications today is as part of release mechanisms. For this type of application, SMA have several advantages: low power consumption, multiple actuations allowing ground testing of the actual flight hardware, fast response (very important when release is performed simultaneously at several points), simplicity leading to savings in weight and low shock release. Fast response and low energy consumption make SMA superior to paraffin systems and low shock release eliminates the main problem related to the use of pyrotechnics. SMA-based release mechanisms were first tested during the Shape Memory Actuation Release Devices (SMARD) experiment mounted on the MightySat 1 spacecraft in May 1999. In January 2000, a second-generation SMA device called QWKNUT was successfully used on the US Air Force Academy's FalconSat [10], [11].
- SME seals. The very high recovery forces possible in shape memory alloys and the retention of these forces to high temperature argue for their consideration as protective seals [11].

The applications listed here are general such as the use of SMA as actuators. How these actuators are implemented depends on the various missions. In July 1997 the six-wheel solar power rover called "Sojourner" landed on Mars as part of the Mars Pathfinder mission. In this experiment, an SMA actuator was used to rotate a cover glass from its normal position. In another mission, a team of engineers at the Indian Space Research Organization's Satellite Application Centre developed a unique steeper motor used to rotate solar flaps, for attitude corrections, on INSAT-2E. The use of SMAs offers a lower mass, cheaper system than an electric motor, as well as a magnetically clean device. SMA hinge designs have also been tested in space during the Light Weight Solar Array Hinge (LFSAH) experiment on the space shuttle mission STS-93 in July 1999 and on the LFSA mounted on the New Millennium Earth Observer-1 (EO-1) satellite in November 2000. The last experiment mentioned is the development of a bistable composite panel with an SMA foil attached to its surface. Heating the SMA foil using a 5 W heater strip component forced the panel to go from one stable shape to another. This experiment, designed by a company named Luna Innovations, was

flown on the MightSat II.1 in July 2000 [10]. Over twenty years of experience of using materials with shape memory in space systems have proved their high efficiency, reliability and advantages in the situations where standard methods are unapplicable.

1.2.3. Disadvantages and problems of SMA in space

Practical challenges have hindered many of the SMA potential applications. Strain change actuation of the SMA material involves an intrinsic energy loss due to latent heat, resulting in a non-conservative activation. The SMA wires may also be susceptible to coupled thermos-mechanical interactions with the surroundings. Due to the thermo-mechanical nature of the SMAs, an increase in temperature is followed by a decrease in stress, which results in larger stress being required for the forward transformation for example. Also hysteresis have a direct effect on the SME and the pseudo-elastic phenomena. For this reason, hysteresis can be an advantage in certain applications, while a disadvantage in others [12]. There are also other limitations in the use of SMA that are not related to the external environment or the hysteresis of the material:

- Conventional resistive electric heating approaches trigger the SME by applying a small voltage to heat up the SMA. The magnitude of the applied voltage is determined according to the SMA resistivity. A major drawback of conventional activation is that the process is relatively slow (several minutes), and a major heat transfer usually occurs between the SMA and the ambient environment [12].
- Heating due to high-voltage joule effect activation of SMA generates instantaneous forces, leading to highly dynamic stroke because of the high accelerations and velocities. SMA wire geometric characteristics such as wire length and diameter change due to the contraction, together with other properties such as phase composition and temperature. Since these properties affect the wire's electrical resistance and, subsequently, the desired activation voltage, a variation of the electrical current would be necessary to supply a constant applied voltage [12].
- Activation time strongly depends on the power used for the Joule effect.
- There is a limit in the activation speed of SMA due to the austenite nucleation time that imposes a limit on the fastest possible shape memory actuation [12].
- Another issue is the slow cooling time that restricts the SMA material's frequency (SMA response time would consist of the heating and cooling time). Even though heating can be easily achieved by running current through the wire, cooling in a reasonable amount of time becomes an issue since it can only be achieved through radiation or conduction. This cooling constraint limits the spectrum of potential applications of multi-cycle SMA actuators in space [10].

- The cyclic loading behavior of SMA materials is usually associated with a functional and structural fatigue that directly affects the material's service life. Microstructural damage accumulated during cyclic loading results in structural fatigue failure. Functional fatigue involves a decrease in the functional properties, such as work displacement and contraction ability of the SMA and its energy dissipation characteristics. As seen in the figure, the maximum length recoverable by the sample decreases as the number of the thermal cycles increases, until eventually reaching a plateau. It is been observed that the temperature required for a phase change gets shifted to a higher temperature as the number of the cycles increases (and the energy dissipation capacity decreases), resulting in a functional fatigue deterioration. The equation in the graph comes from Costanza and al.'s studies [12].
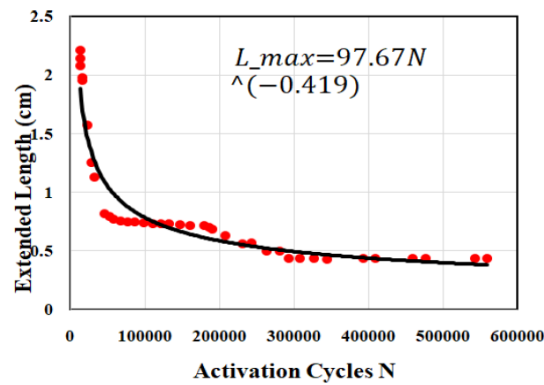

Figure 17: Maximum length vs. number of activation cycles.

- Relatively small efficiency of martensitic transformation. The coefficient of transformation of heat energy to mechanical work at shape recovery is estimated not to exceed 10% [9].
- The presence in space of radiations that affect the temperature of SMA. This problem requires considering the phenomenon already at the design stage and, possibly, using a temperature control system to prevent heating of the wires

Other secondary problems were found by carrying out experiments in the laboratory concerning this thesis. The first problem concerns the difficulty of using a removable locking system for very thin wires. The same problem also arises in the attempt to block the wires because they reach extremely high temperatures and can generate large forces. The second is the temperature detection of the wires, because, due to their extremely small radius, any temperature measurement is affected by the air around the wire, compromising the results. Despite the problems listed, the merits of SMA far exceed the defects and the continuous studies and experiments make it one of the most widely used materials in space.
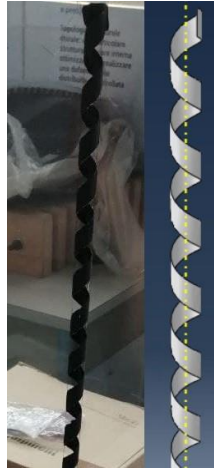
1.3. Prototype

Figure 18: Prototype structure

The prototype studied in the previous thesis and analyzed in detail in the present work is a composite helix [13]. The choice to use composite materials was due to:

- The respect of the constraint due to the realization;
- The innovative use of these materials in the structure of a borescope, something not yet available on the market
- The flexibility and lightness of the structure
- The behavior in the elastic field and the elastic modulus

These characteristics, together with the particular shape, allow to considerably deform the model, making it return to its initial configuration once the load is removed. Thanks to the simple form, one does not need to use joints to connect the different sections. The deformation of the structure takes place through NiTiNOL wires that could be directly embedded between the layers of composite, thanks to their extremely small diameter that makes them minimally invasive, or inserted in sheaths embedded in the structure. The wires can be more than one and are parallel to the axis of the spiral for the entire length of the composite helix. The geometric configuration of the structure was chosen in the initial design phase through finite element models with the Abaqus software. It is important to note that the outer part is not covered by shields: this made the thermal analysis fundamental for the intended use in the space environment, in which radiations play a decisive role on the temperature reached by the NiTiNOL wires.

1.3.1. Composite

The diameter of the helix was set to 10 mm and the length of the spiral to 500 mm. The layers of the composite material are made of carbon fiber fabric or glass fiber fabric, chosen because are among the most used materials in space applications. The material characteristics are as follows:

Table 1.1: Composites characteristics

	E_x	E_y	v_{12}	G_{12}	G_{13}	G_{23}
Carbon	55000 [MPa]	55000 [MPa]	0,09	2500 [MPa]	2500 [MPa]	2500 [MPa]
Glass	23000 [MPa]	23000 [MPa]	0,09	2000 [MPa]	2000 [MPa]	2000 [MPa]

The thickness of the plies could be 0.12 mm or 0.28 mm. The layers are arranged, in the Abaqus model, with the direction of the fibers rotated by 45° with respect to the horizontal direction.

1.3.2. NiTiNOL wire

The NiTiNOL wires employed have a preset deformation of 3% and have a diameter of 0.20 mm. The properties of the wires are:

Table 2.1: Physical characteristics of NiTiNOL wire

Conductivity	[S/m]	13,3
Specific Heat	[$J/{Kg\ K}$]	320
Density	[Kg/m]	6450
Electric Resistivity	[Kg/m]	$0,8\ 10^{-6}$
Young's modulus for austenite	[Pa]	$40,24\ 10^9$
Young's modulus for martensite	[Pa]	$24,067\ 10^9$
Poison's ratio		0.33
Thermal expansion coefficient of austenite	[K^{-1}]	$2,2\ 10^{-5}$
Thermal expansion coefficient of martensite	[K^{-1}]	$2,2\ 10^{-5}$
Martensitic start temperature	[K]	286,97
Martensitic finish temperature	[K]	265,5
Austenitic start temperature	[K]	333,77
Austenitic finish temperature	[K]	348,26
Maximum transformation strain		0,052
Martensitic stress influence coefficient	[$Pa\ K^{-1}$]	$-2,61863\ 10^5$
Austenitic stress influence coefficient	[$Pa\ K^{-1}$]	$-3,74944\ 10^5$

2 Thermal Analysis

2.1. Heat transfer mechanisms

Heat is a form of energy which occurs in the transfer from one body to another when they are at different temperatures. Heat transfer focuses on the description of the modes in which thermal energy can be transferred across vacuum and dense or rarefied media. Due to the complexity of the phenomenon, it is necessary to introduce approximations. If the Knudsen number, defined as the ratio of the molecular mean free path length and a representative physical length scale, is significantly less than one, it is possible to use a macroscopic approach, considering the material domain as a continuum and creating a model based on four fundamental equations:

- Balance equations, or when possible, conservation equations (mass, momentum and energy), derived from fundamental principles
- Constitutive relations, describing the properties of matter and how it reacts to interactions (with energy or with other matter)
- Jump conditions, across discontinuities or interfaces
- Boundary conditions and initial conditions, when the previous relations are written in a differential form

The Second Law of Thermodynamics states the direction of the spontaneous heat transfer, i.e., from higher- to lower-temperature bodies, whereas the First Law of Thermodynamics defines that systems continue to exchange energy until they both reach a certain temperature value, namely the temperature of equilibrium. Hence, the First Law of Thermodynamics is a form of energy balance, which is described by the equation (2.1):

$$\frac{dU}{dt} = Q - W \tag{2.1}$$

The total internal energy (U) of a system is a property of the thermodynamic system and its variation is determined by the balance of work (W) and heat (Q). The total net heat flux of the prototype is described by the difference between the heat flux entering the system (Q_{in}) and the heat flux leaving the system (Q_{out}):

$$Q_{net} = Q_{in} - Q_{out} \tag{2.2}$$

With thermal analysis, we refer to the activity of modelling, analyzing, designing and controlling systems from the point of view of heat transfer and temperature reached in the systems. Heat transfer can be carried out through:

- Conduction
- Convection
- Radiation

It is possible that one of these three mechanisms of heat transfer prevails over the others. This is the case of space heat transfer, where the vacuum environment nullifies convective phenomena, while conduction and, especially, radiation are the predominant ways of heat transfer [14].

2.1.1. Conduction

Conduction is a kind of energy transfer within a material (solid or fluid) involving the exchange of kinetic energy of molecules at different energy levels, in absence of macroscopic mass transport. This phenomenon occurs through the collision of adjacent molecules. In conductive materials, however, thermal transmission depends on the movement of free electrons. Since higher temperatures are associated with higher molecular energies, in the presence of a temperature gradient, the energy transfer by conduction must then occur in the direction of decreasing temperature. This can be described by a general equation (2.3) (which can be derived from the conservation of energy equation) …

$$\frac{dU}{d\tau} = \sum \dot{Q} + \dot{U} \tag{2.3}$$

…and the Fourier law (2.4), which is a constitutive equation written regarding the Second law of Thermodynamics:

$$\vec{Q} = -\Lambda_{\vec{p},\vec{d},T} \, \nabla T \tag{2.4}$$

Where $\vec{Q}$ is the thermal power flow, $\Lambda_{\vec{p},\vec{d},T}$ is the conductivity of the material and ∇T is the temperature gradient. Generally, the conductivity of the material is a tensor function of:

- Substance, and therefore of the point $\vec{p}$, for inhomogeneous domains
- Direction $\vec{d}$ under consideration, for anisotropic domains
- Temperature, and thus again the point $\vec{p}$, for all materials

Considering a closed system and assuming constant density (ρ), no device to extract mechanical work, electric work already converted into thermal energy (heat source) and constant conductivity (λ), the energy balance equation becomes:

$$\rho\,c\,\frac{dT}{d\tau} = \lambda\,\nabla^2 T + \dot{U} \tag{2.5}$$

In which c is the specific heat of the material and $\dot{U}$ is the thermal power source. Analytical solutions can be obtained for simplified cases, otherwise numerical solutions are needed. If the system is in steady-state conditions and temperature variants are significant along a single spatial direction only, the simplified Poisson equation (2.6) can be obtained:

$$\nabla^2 T = -\frac{\dot{U}}{\lambda} \tag{2.6}$$

If, in addition, no heat source is present, the Laplace equation (2.7) is obtained:

$$\nabla^2 T = 0 \tag{2.7}$$

As it can be observed, Poisson and Laplace equations have exactly the same form as the corresponding one in the study of Electromagnetism. Consequently, the results and resolution schemes will be completely analogous. The physical equation that regulates the rate of heat transfer by conduction for a one-dimensional plane wall is expressed by:

Table 3: Solutions of the conduction equation in different coordinate systems

Cartesian coordinates	Cylindrical coordinates	Spherical coordinates
$\dot{Q} = -\dfrac{T_2 - T_1}{\frac{s}{\lambda}}$	$\dot{Q} = -\dfrac{T_2 - T_1}{\frac{\ln(R_e/R_i)}{2\pi\lambda L}}$	$\dot{Q} = -\dfrac{T_2 - T_1}{\frac{R_e - R_i}{4\pi\lambda R_e R_i}}$

With cylindrical and spherical coordinates, $\dot{Q}$ is the heat transfer rate, not the heat flux. The relationships obtained have a physical significance only when the geometrical characteristics of the system and the thermal conditions along the boundaries considered (boundary conditions) are specified. In addition, if the system is not in steady state, it will be necessary to specify its thermal state at the initial moment of the observed phenomenon (initial conditions). The different types of conditions found in the experimental reality are reported:

- Constant surface temperature (Dirichlet condition).
- Constant surface thermal flux: finite flow or conditions of adiabaticity.
- Convective heat transfer to the surface.

2.1.2. Convection

Convection is a more complex phenomenon than conduction. Modelling it, we can assume that it is composed of two mechanisms that operate simultaneously:

- Energy transfer by conduction. There will always be a diffusion of energy associated with molecular motions.
- Energy transfer caused by the macroscopic motion of fluid associated with the movement of a large number of molecules.

Convection can therefore be present only for states of aggregation that allow internal mass motion, i.e., fluids. Heat transfer by convection can be classified following different lines:

- Single-phase (liquid or gas), two-phase (during boiling and condensation or for multicomponent mixtures), Marangoni/thermocapillary (due to surface tension gradients, concentration or temperature gradients)
- Internal (the solid surface of interest is completely enclosed by the fluid), external (one side of the domain is occupied by the fluid up to an "infinite" distance from the wall)
- Forced (the fluid motion is forced, not depending from temperature gradients), free (the fluid motion is only due to the temperature gradients), mixed (combination of free and forced)

The convection mechanism is caused by the viscosity of the fluid; therefore, its effects will be mainly felt within the boundary layer. In such region, velocity and temperature are different from the conditions "far" from the wall. The real engineering domains and conditions are complex, so the boundary layer theory is used to have a guideline for selecting the experimental correlations to be used. Being bound to the boundary layer, the heat exchange will depend on the fluid, the shape of the body, the field of motion and the boundary conditions. The relation that is commonly used is (2.8):

$$\dot{Q} = h(T_s - T_\infty) \tag{2.8}$$

The complexity of the phenomenon is thus hidden in the convective coefficient h, that will be evaluated from time to time using experimental formulas.

Table 4: Convective coefficient for several substances

$h \left[W / m^2 K \right]$	Liquids	Gases
Free convection	50-2000	2-25
Forced convection	100-20000	25-250
Convection with phase change (boiling, condensation)	2500-100000	

As h depends on many parameters, instead of using all the variables and in order to provide generality, correlations are developed in dimensionless terms. The dimensionless groups used in this thesis are:

- $Nu = \dfrac{h\,D_c}{\lambda_f} = \dfrac{convection\ heat\ transfer\ rate}{conduction\ heat\ transfer\ rate}$
- $Pr = \dfrac{c_f\,\mu_f}{\lambda_f} = \dfrac{diffusion\ of\ momentum}{thermal\ diffusivity}$
- $Re = \dfrac{\rho_f\,v\,D_c}{\mu_f} = \dfrac{inertia}{viscosity}$

A large number of correlations were developed during many years of theoretical and experimental research and can be found on textbooks, handbooks and literature papers. It is really important to understand very well how to properly select, use and check a correlation, because the error due to inappropriate use can be $\pm 30\%$ [15].

2.1.3. Radiation

With respect to conduction and convection, radiation heat transfer has some peculiar characteristics:

- It does not require the presence of matter; on the contrary, it optimally works in a vacuum environment
- The characteristic distances span from $10^{-10}\ m$ to more than $10^{12}\ m$
- Equations are integro-differentials
- The radiative properties of materials have extremely irregular behaviors with respect to temperature, wavelength and direction
- If the body is opaque, as in most solids and liquids, the radiation emitted by the innermost molecules is strongly absorbed by the surrounding molecules. For this reason, it can be considered that the phenomenon is linked to the surface characteristics of the body.

Any object with a temperature above the absolute zero emits energy and it is also able to absorb that radiation energy. So, two bodies can exchange energy between each other by thermal radiation. This way of heat transfer is governed by the amount of radiation energy emitted by an ideal black body (the black body is a model that absorbs all the incident radiations, emits more than any other body for every temperature and wavelength and the emission is not a function of the direction), also known as Planck's Distribution Law (2.9):

$$E_{b\lambda}(\lambda, T) = \frac{2\pi\,C_1}{\lambda^5\left(e^{\frac{C_2}{\lambda T}} - 1\right)} \tag{2.9}$$

$$C_1 = 2\pi h c_o^2 = 3.7418\ 10^{-16}\ W m^2 \tag{2.10}$$

$$C_2 = \frac{h c_o}{k} = 14.388\ \mu m\ K \tag{2.11}$$

where (E_b) is the energy emitted/absorbed by the black body, (λ) is the wavelength, (T) is the absolute temperature of the black body. Where the symbol (h) identifies the

Planck's constant, $6.6261 \ 10^{-34} \ Js$, c_o is the speed of light, $3 \ 10^8 \ m/s$, and k is the Boltzmann's constant, $1.3807 \ 10^{-23} \ J/K$. Integrating the equation of the energy emitted/absorbed by the black body over all wavelengths, we obtain the total black body emissive power:

$$E_b(T) = \int_0^\infty E_{b\lambda}(\lambda, T) \, d\lambda = kT^4 \quad \frac{W}{m^2} \tag{2.12}$$

Where σ is the Stefan-Boltzmann constant, $5.669 \ 10^{-8} \ W/m^2 \ K^4$, and the equation is called Stefan-Boltzmann Law (2.12). Each body emits thermal radiations, not only the black body. The mechanism is related to the transition of electrons from one quantum state to another. For the microscopic constituents of matter, interaction may be:

- Emission (spontaneous or stimulated by incident radiations)
- Absorption with or without ionization (i.e., with or without freeing of electrons)
- Scattering (dispersion/diffusion)

At the macroscopic level, the previous interactions originate the emission, absorption, reflection, transmission, refraction and sub-surface scattering phenomena [16]. Once the rays encounter the surfaces, just a part of them can pass through the surface when the other parts can be absorbed or reflected away. This depends on three radiative properties of the surface, which are ρ, reflectivity, α, absorption and τ, permeability. The sum of these three properties, can be described as [17]:
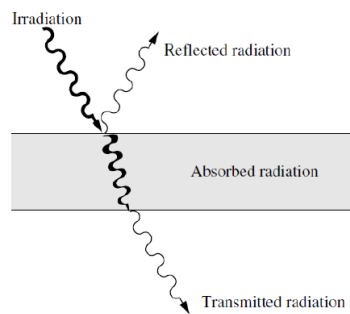
$$\rho + \alpha + \tau = 1 \tag{2.13}$$

Figure 19: Phenomena of radiation interaction with matter

Since, at a given temperature, the maximum possible energy emitted belongs to a black body, we can define a fourth nondimensional property, the emittance:

$$\varepsilon = \frac{energy \ emitted \ from \ a \ real \ body}{energy \ emitted \ by \ a \ black \ body \ at \ same \ temperature}$$

For real bodies, we have ε < 1, while for ideal black bodies ε = 1. At this point, we can calculate the total emissive energy of a real surface:

$$E = \varepsilon kT^4 \tag{2.14}$$

When a surface reaches the thermal equilibrium, the emissivity equals the absorptivity ($\alpha = \varepsilon$). This equality is known as Kirchhoff's Law and it requires the following two assumptions: the surface must be diffusive (i.e., surface properties are independent of direction) and grey (i.e., surface properties are independent of wavelength). A fundamental problem is the determination of the energy fraction that leaves a surface, intercepted by another surface and vice versa. The radiative view factor F_{ij} is defined as the fraction of the radiation leaving one surface that is intercepted by another. We consider the radiative energy exchange between two finite areas, A_i and A_j.
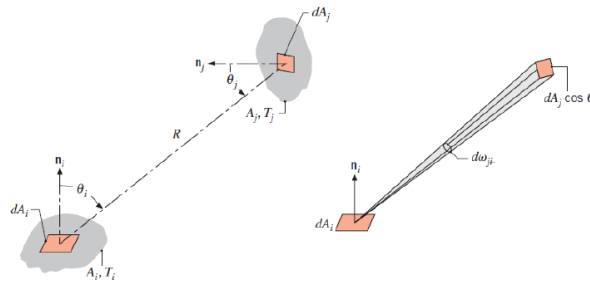
Figure 20: View factors between two finite surfaces A_i and A_j

We denoted with θ the angle formed by the normal vector at the surface with the distance R. Integrating over the two areas, A_i and A_j from an examination of the symmetry of the problem, it was possible to derive the Law of Reciprocity (2.15):

$$A_i F_{ij} = A_j F_{ji} \tag{2.15}$$

The sum of the view factors must be unity:

$$\sum_{j=1}^{N} F_{ij} = 1 \tag{2.16}$$

Summarizing the results obtained in the previous sections, we can conclude that radiative heat exchange between two surfaces is determined by three important parameters [14], [18]:

- The surface temperatures
- The radiative view factors (F_{ij})
- The surface properties (ε)

Therefore, considering diffusive surfaces, the amount of radiation leaving the surface i and absorbed by the surface j is:

$$Q_{ij} = A_i F_{ij} \varepsilon_{ij} \left(T_i^4 - T_j^4 \right) \tag{2.17}$$

2.2.   Heat sources in a spatial environment

The planets of the solar system, and therefore the Earth, can intercept only a fraction of the energy radiated by the Sun in space. It depends on the size of the planets and their distance from the Sun. The principal sources of environmental heating on geocentric orbits are direct sunlight, incident sunlight reflected off the Earth (albedo), and the planetary (i.e., Earth) IR radiation. All these heat fluxes from space, acting on the prototype, must be considered. The temperature surrounding the body in space is 2.7 K while the pressure is very close to the vacuum.

2.2.1.   Solar radiation source

Direct solar radiation is the greatest source of heat. Since the Earth's orbit around the sun is elliptical, the intensity of the solar radiation varies approximately by 3.5% throughout the year. The average value of the intensity of sunlight at the mean Sun-Earth distance (1 AU), called solar constant, has been set by the community's current agreement at the value of 1366.1 W/m^2. The solar spectrum can be schematically divided as follows:

Table 5: Spectrum of solar radiations

Wavelength	Spectrum	% Total energy
0.2-0.38 μm	Ultraviolet	7
0.38-0.78 μm	Visible	46
0.78-10 μm	Infrared (IR)	47

It is clear that the visible light, in the range between 380 nm and 760 nm, is responsible of the greatest percentage of the total solar radiation.
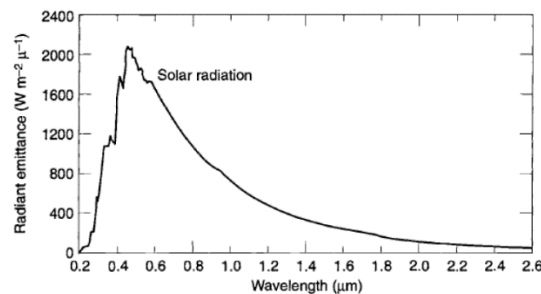
Figure 21: Spectrum of solar radiation

The heat flux generated by the Sun and absorbed by a component in geocentric orbit is defined as:

$$Q_{sun} = \alpha J_s A \cos \theta \qquad (2.18)$$

where J_s is the solar constant, α is the solar absorptance of the surface, A is the area of a flat surface, whose normal vector forms an angle θ with solar rays [14], [18], [19].

2.2.2. Albedo radiation source

A planet's albedo is usually expressed as the fraction of incident sunlight that is reflected back to space. Usually, it is expressed as a percentage of incident sunlight. Albedo is highly variable across the globe and depends on surface properties and cloud cover. The Earth albedo has an average value of 0.3, i.e., 30% of solar radiation is reflected in all directions, while the remaining 70% is absorbed. It can go from a value of 0.09 without clouds to 0.8 in the case of icy surfaces and clouds [18], [19].
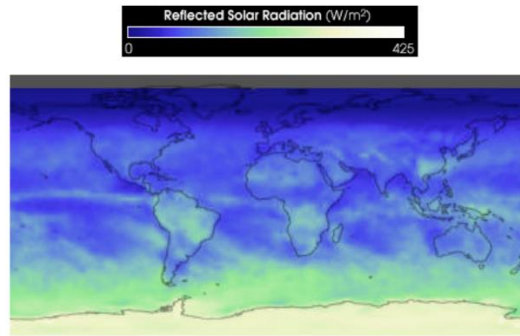
Figure 22: Distribution of albedo radiation on the Earth's surface

The fraction of albedo radiation absorbed by the component is:

$$Q_{albedo} = J_s a F_{comp-planet} \alpha \tag{2.19}$$

where a is the albedo factor and $F_{comp-planet}$ is the view factor between the surface of the component and the Earth, also known as visibility factor. Earth can be considered as a diffusive reflecting sphere: in this case, the visibility factor varies with the orbit altitude [14]:
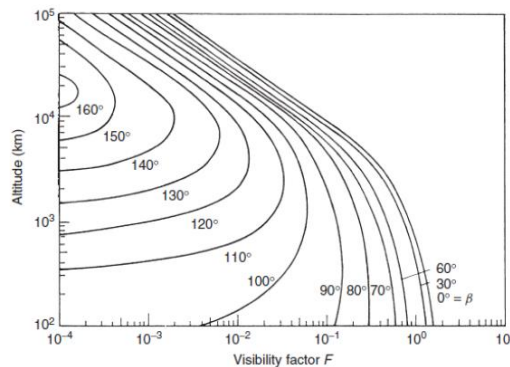
Figure 23: Variation of the visibility factor with the altitude of the orbit. β is the angle between the local vertical direction and the rays of the sun.

2.2.3. Planetary infrared radiation source

Solar radiations, which are not reflected, are absorbed by the Earth and emitted again as infrared heat. The energy spectrum is comparable to that of a black body at 288 K. At this temperature, the energy spectrum of the Earth's IR radiation is approximately in the same band of wavelengths as the prototype (considered at room temperature): for this reason, it is much more difficult to screen planetary radiations than solar radiations. The total IR radiation absorbed by the component is given by:

$$Q_{planet} = J_p A F_{comp-planet} \varepsilon \tag{2.20}$$

where ε is the infrared absorption coefficient of the surface, whereas J_p is the planet IR heat flux, which for Earth is defined as:

$$J_p = 237 \left(\frac{R_{rad}}{R_{orbit}} \right)^2 \tag{2.21}$$

with R_{rad} as the radius of the Earth's effective radiating surface and R_{orbit} as the orbit radius. The value 237 refers to the Earth's radiating intensity $[W/m^2]$ [14], [18], [19].

2.3. Strategies calculating temperature

The effect of shape memory alloys depends on the temperature and the state of stress to which they are subjected. Thermal analysis is fundamental to identify the correct amount of energy to be provided to the material in order to allow a correct activation. Moreover, the use of the prototype in a spatial environment, without thermal protection, could change its performance compared to the same operation carried out on earth. An analysis of thermal phenomena is therefore necessary. All the parameters were obtained through averages of values found in literature and on the websites of companies.

2.3.1. Simplification of the structure

2.3.1.1. NiTiNOL

The activation of the NiTiNOL wire embedded in the structure is achieved through the Joule effect. Some simplifying hypotheses of the model are necessary in order to study how the structure and the spatial environment affect the temperature reached by the wire and how the heat propagates in the system. Let us consider only one wire with the following characteristics:

Table 6: Characteristics of NiTiNOL wire

	ε	$\rho\ [Kg/m^3]$	$\lambda\ [W/m\ K]$	$c\ [J/Kg\ K]$	$L\ [m]$	$d\ [m]$	$\rho_e\ [\Omega m]$
NiTiNOL	0.75	6450	10	322	0.5	0.0002	$0.80\ 10^{-6}$

The composite layers surrounding the wire are approximated with cylinders 10 mm high. The area of their circular crown depends on the thickness of the layers of composite material and on the number of the layers. The reference pattern of the spiral has a pitch of 25 mm and wraps the wire 20 times. For this reason, 20 cylinders are arranged along the wire at a distance of 15 mm from each other.
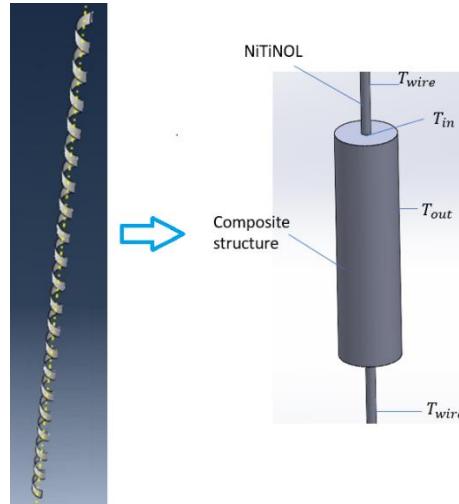

Figure 24: Approximation of the design prototype

In the figure above, T_{wire} is the temperature of the uncovered wire, T_{in} is the temperature of the wire covered by the composite material and T_{est} is the temperature of the outer surface of the composite structure. Another important hypothesis is that the wire is not subjected to a stress state after the production.

2.3.1.2. Composite material

The structure was obtained by overlapping layers of composite fabric with the lamination sequence $[0°]_4$ [13]. During the analysis, 4 different types of laminate structures were considered:

- Four layers of 0.28 mm thick carbon-fiber fabric (C_{28})
- Four layers of 0.12 mm thick carbon-fiber fabric (C_{12})
- Four layers of 0.12 mm thick glass-fiber fabric (V_{12-4})
- Six layers of 0.12 mm thick glass-fiber fabric (V_{12-6})

In this way, it is possible to see how the behavior of the structure varies by increasing the thickness of the composite layers or by increasing the number of layers (i.e., increasing the stiffness of the structure) and how it varies with the variation of the material used. In the case of composites, the basic parameters for stationary and transient thermal analysis varied in ranges defined as follows [20], [21]:

Table 7: Ranges of parameter validity of composite fabric constituent materials

	$\lambda\ [W/m\ K]$	ε	$\rho\ [Kg/m^3]$	$c\ [J/Kg\ K]$

Carbon fibers	8-375	0.53-0.96	1600-2150	710-930
Glass fibers	1-1.34	0.80-0.98	2500-2800	840-1030
Resin	0.22-1.44	0.5	1100-1460	837.36-2302.74

It's necessary to add the hypothesis, at least for this preliminary thermal analysis, that the properties of the material remain constant. The properties listed above are weighed considering a structure consisting of 70% fiber and 30% resin. In this way, reference values can be used for the various prototypes.
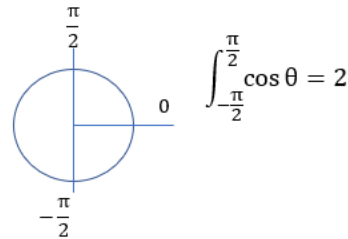
Table 8: Properties of composite materials

	$\lambda \, [W/m \, K]$	ε	$\rho \, [Kg/m^3]$	$c \, [J/Kg \, K]$
Carbon	5.6660-262.9320	0.5210-0.8220	1450-1943	748.1-1341.9
Glass	0.7660-1.37	0.71-0.8360	2080-2398	839.1-1411.9

Thanks to the table above, it was possible to distinguish between two limit cases: the worst possible (maximum $\lambda, \varepsilon, \rho, c$) and the best possible (minimum $\lambda, \varepsilon, \rho, c$).

2.3.2. Radiations

In order to calculate the radiations affecting the body, the worst-case scenario was taken into consideration, i.e., half of the model exposed to radiations. So as to vary the amount of radiations hitting the surface of the piece, coefficients, C_{sun}, C_{albedo}, C_{IR}, which can vary from 0 to 1 (0 for a surface completely in shadow and 1 for one exposed to radiations), were introduced.

Figure 25: Integral of the angle of incidence of solar radiation on the semi-circumference of the wire exposed to radiations

$$Q_{sun} = 2 \, \alpha \, J_s \, C_{sun} \, A \; [W] \tag{2.22}$$

$$Q_{albedo} = a \, \alpha \, J_s \, C_{albedo} \, A \, [W] \tag{2.23}$$

$$Q_{IR} = \varepsilon \, J_p \, F_{planet-comp} \, C_{IR} \, A \, [W] \tag{2.24}$$

Where $a = 0.30$, $F_{planet-comp} = 10^{-1}$ is the view factor selected considering the height of a low Earth orbit, LEO (because it is more affected by the radiations coming from

the Earth), and an angle between the incident rays and the normal at the surface of the body of 90° (values chosen as reference parameters); $J_p = 222.7968 \ W/m^2$ is the planet IR heat flux for a LEO orbit with the smallest possible radius (LEO orbits vary from 200 Km to 2000 Km).

$$A = \begin{cases} \dfrac{(A_{tot} - A_{hidden})}{2} & for \ NiTiNOL \ wire \\[2em] \dfrac{\left(\left((2\pi R_{est})0.01\right)20\right) + \left(\left((R_{est}^2 - R_{in}^2)\pi\right)40\right)}{2} & for \ the \ surface \ of \ the \ composite \end{cases} \qquad (2.25)$$

Where A_{tot} is the total surface of the wire, A_{hidden} is the surface of the wire hidden by the structure, R_{est} is the outer radius of the composite cylinder (which changes according to the number of layers and the thickness of the layers), R_{in} is the inner radius of the composite cylinder (considered to perfectly adhere to the wire).

2.3.3. Voltage optimization

The wire is activated via Joule Effect. It is necessary to calculate the optimal voltage for a correct activation of the wire. The threshold temperature for the activation of the shape memory effect is considered to be 75 °C. We take the temperature of the portion of wire embedded in the structure as a reference, since the temperature of the fully exposed wire is always higher. The aim of this analysis is to find the minimum voltage that allows the wire to exceed the activation temperature in the shortest time possible. The power calculation is carried out as follows:

$$R = \frac{4 \, \rho_e \, L}{\pi \left(\frac{d}{2}\right)} = 12.7324 \ [\Omega] \qquad (2.26)$$

$$P = \frac{V^2}{R} \ [W] \qquad (2.27)$$

$$q = \frac{P}{A_{tot}} \left[\frac{W}{m^2}\right] \qquad (2.28)$$

The evaluation of the optimal current takes place through two analyses. The first research looks for the minimum value of voltage that allows the heating of the wire over the activation temperature (a margin of safety was added to 75 °C bringing the threshold to 100 °C). The second research, on the other hand, highlights the relationship between the voltage and the activation time of the wire. Here, again, a threshold parameter had to be used and a maximum allowed activation time of 5 s was chosen. The average of the voltage obtained from the two analyses is considered as the optimal voltage. The evaluation process described above was applied using both the parameters of the worst-possible situation and those of the best, but the subsequent analyses of the stationary and the transient cases were carried out on the assumption of being in the worst-case scenario.

2.3.4. Stationary case

The Lumped parameter approach was employed for the calculation of the temperatures reached by the wire in the structure. This approach is based on the condition that the temperature within the solid can be assume as uniform. This happens when conduction inside the object is much faster than the exchanges (conduction, convection, radiation) with the surroundings. The Biot dimensionless group is used as an indicator to decide whether the lumped parameter approach can be used with a small error.

$$Bi = \frac{h\, D_c}{\lambda} \tag{2.29}$$

Indicatively, if $Bi < 0.05 - 0.1$, the error may be lower than 5%. In the expression of the Biot number, λ is the thermal conduction coefficient of the body, D_c is a characteristic dimension of the body, while h is:

- Convection coefficient for convection exchanges
- The inverse of the contact resistance for conduction exchanges
- An equivalent h_r, for radiation exchanges, thus defined:

$$h_r = \varepsilon\, \sigma\, (T_w + T_b)\big(T_w^2 + T_b^2\big) \left[\frac{W}{m^2\, K}\right] \tag{2.30}$$

Where T_b is the temperature of the body surface and T_w is the temperature of the surrounding environment. For the calculation of temperatures, a hypothesis, confirmed by the simulations carried out with Abaqus, was necessary: i.e., half of the thermal power flow, produced by the Joule effect, passed through the section of the wire covered by the composite and the other half passed through the section of the wire completely uncovered. Considering an external environment at $0\,K$, the external temperature of the composite coating is initially calculated through the equation:
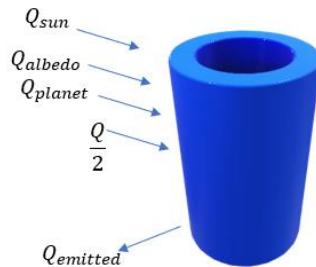
Figure 26: Thermal balance through the outer surface of the composite coating

$$\frac{Q}{2} + Q_{sun} + Q_{albedo} + Q_{planet} - \varepsilon\, \sigma\, A\, T_{out}^4 = 0 \tag{2.31}$$

Then, the temperature of the uncovered wire and, ultimately, the temperature of the wire embedded in the structure are calculated:
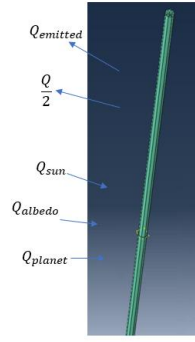
Figure 27: Thermal balance through the uncovered surface of the wire

$$Q_{sun} + Q_{albedo} + Q_{planet} + \frac{Q}{2} - \varepsilon \, \sigma \, A \, T_{wire}^4 = 0 \tag{2.32}$$

$$T_{in} = \left(\frac{Q}{2} \, R_{tot}\right) + T_{out} \tag{2.33}$$

R_{tot} is the composite internal conduction resistance in which the contact resistance of $0.005 \ K \, m^2/W$ was considered:

$$R_{tot} = \frac{\ln\left(\frac{R_{est}}{R_{int}}\right)}{2 \, \pi \, \lambda \, \frac{A_{hidden}}{2 \, \pi \, \frac{d}{2}}} + \frac{R_{contact}}{A_{hidden}} \left[\frac{K}{W}\right] \tag{2.34}$$

All equations were solved by applying two algorithms (the Newton-Rapshon method and the Bisection method [14]) and comparing the results obtained.

2.3.5. Transitional case

Also in this case, the Lumped parameter approach was applied. Here, two equations were considered (one for the wire temperature and one for the external temperature of the composite) and they had to be solved iteratively:

$$\rho_{NiTi} c_{NiTi} V_{NiTi} \frac{\partial T_{wire}}{\partial \tau} = Q + Q_{sun} + Q_{albedo} + Q_{planet} - \varepsilon \, \sigma \, A \, T_{wire}^4 - \frac{1}{R_{tot}} \Delta \tag{2.35}$$

$$\rho_c c_c V_c \frac{\partial T_{out}}{\partial \tau} = Q_{sun} + Q_{albedo} + Q_{planet} - \varepsilon \, \sigma \, A \, T_{out}^4 - \frac{1}{R_{tot}} \Delta \tag{2.36}$$

The terms with $NiTi$ index refer to the wire, whereas those with index c refer to the composite. The differential equations were approximated with a backward scheme. This scheme is part of finite-difference methods (FDM) which are a class of numerical techniques for solving differential equations by approximating derivatives with finite differences. Although with a higher approximation, the backward scheme was chosen for temporal discretization for greater stability of this method.

$$\frac{f^{k+1} - f^k}{\Delta t} = f(k+1) \tag{2.37}$$

Applying the approximation, the equations to be solved are:

$$T_{wire}^{k+1} = T_{wire}^{K} + \left(\frac{Q + Q_{sun} + Q_{albedo} + Q_{planet}}{\rho_{NiTi} c_{NiTi} V_{NiTi}} - \frac{\varepsilon \, \sigma \, A}{\rho_{NiTi} c_{NiTi} V_{NiTi}} \left(T_{wire}^{k+1} \right)^4 - \frac{\frac{1}{R_{tot}} \Delta}{\rho_{NiTi} c_{NiTi} V_{NiTi}} \right) \Delta t \tag{2.38}$$

$$T_{out}^{k+1} = T_{out}^{K} + \left(\frac{Q_{sun} + Q_{albedo} + Q_{planet}}{\rho_c c_c V_c} - \frac{\varepsilon \, \sigma \, A}{\rho_c c_c V_c} \left(T_{out}^{k+1} \right)^4 - \frac{\frac{1}{R_{tot}} \Delta}{\rho_c c_c V_c} \right) \Delta t \tag{2.39}$$

The chosen time step is $0.001 \, s$ with the initial temperature of $3 \, K$. At each iteration, the wire temperature is calculated and, subsequently, the external temperature of the composite and the thermal jump between the temperature of the covered wire and the external one of the composite are determined. The iterative cycle continues until the temperatures of the stationary case are reached.

2.3.6. Convective case

The case of wire activation in the lab was also analyzed, readjusting the equations listed above. The laboratory environment was simulated through a convection coefficient $h = 5 \, W/m^2 \, K$, considering a free convection, and an air temperature of $T_\infty = 15 \, °C$. Both stationary and transient analysis were performed using the Lumped parameter approach (always checking the Biot number).

$$\frac{Q}{2} - \varepsilon \, \sigma \, A \, (T_{out}^4 - T_\infty^4) - h \, A \, (T_{out} - T_\infty) = 0 \tag{2.40}$$

$$\frac{Q}{2} - \varepsilon \, \sigma \, A \, (T_{wire}^4 - T_\infty^4) - h \, A \, (T_{wire} - T_\infty) = 0 \tag{2.41}$$

$$T_{in} = \left(\frac{Q}{2} \, R_{tot} \right) + T_{out} \tag{2.42}$$

$$T_{wire}^{k+1} = T_{wire}^{K} + \left(\frac{Q}{\rho_{NiTi} c_{NiTi} V_{NiTi}} - \frac{\varepsilon \, \sigma \, A}{\rho_{NiTi} c_{NiTi} V_{NiTi}} \left(\left(T_{wire}^{k+1} \right)^4 - T_\infty^4 \right) - \frac{\frac{1}{R_{tot}} \Delta}{\rho_{NiTi} c_{NiTi} V_{NiTi}} - \frac{h \, A}{\rho_{NiTi} c_{NiTi} V_{NiTi}} \left(T_{wire}^{k+1} - T_\infty \right) \right) \Delta t \tag{2.43}$$

$$T_{out}^{k+1} = T_{out}^{K} + \left(-\frac{h \, A}{\rho_c c_c V_c} \left(T^{k+1} - T_\infty \right) - \frac{\varepsilon \, \sigma \, A}{\rho_c c_c V_c} \left(\left(T_{out}^{k+1} \right)^4 - T_\infty^4 \right) - \frac{\frac{1}{R_{tot}} \Delta}{\rho_c c_c V_c} \right) \Delta t \tag{2.44}$$

2.3.7. Length required for heat dissipation

After calculating the temperatures, it is necessary to check whether the composite can dissipate heat, by conduction and radiation, along its length without activating other wires that can be arranged along the circumference of the spiral. In order to calculate the length needed for the composite to dissipate the heat produced by the wire, it was necessary to start from the external temperature of the stationary case. A parallelepiped of the same material was added to the composite cylinder, with the same cylinder height, the same thickness and length $s = 10^{-5} \, m$. The choice of such a small length makes it possible to consider the whole piece at a uniform temperature. As for this additional element, the temperature of the surface farthest from the cylinder was calculated, after taking into account the dissipation by conduction and radiation. Other parallelepipeds were added, one behind the other along a straight line (always taking into consideration the previously added pieces), until the temperature fell below the activation temperature of the wire. A multiplicative coefficient allows to vary the portion of surface on which the radiations, perpendicular to the added surfaces, act.
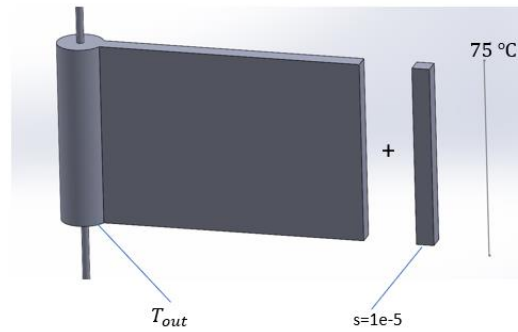
Figure 28: Calculation algorithm for the length needed to dissipate the external temperature of the composite

$$R = \frac{s}{\lambda \, A_{conduction}}$$

$$l_{new} = l_{old} + s$$

$$A_{emitted_{new}} = A_{emitted_{old}} + \left((2 \, s \, 0.01) + \left(2 \, s \, n_{plies} \, th \right) \right)$$

$$Q_{emitted_{new}} = Q_{emitted_{old}} + \varepsilon \, \sigma \left((2 \, s \, 0.01) + \left(2 \, s \, n_{plies} \, th \right) \right) T_{old}^4$$

$$-\frac{1}{R}(T_{new} - T_{old}) - Q_{emitted_{new}} + Q_{sun} + Q_{albedo} + Q_{planet} = 0$$

Figure 29: Calculation algorithm of heat dissipation length

Where n_{plies} is the number of plies, th is the thickness of the single ply, λ is the conduction coefficient of the composite and $A_{conduction}$ is the area that the power flow must pass through by conduction. During the calculation of the total dissipation length, it was assumed that a second wire was placed at a distance equal to 1/4 of the

length of the circumference of the prototype spiral. The temperature reached by the composite at this distance and then the temperature of the second wire was estimated in order to check whether it was activated or not. A second multiplicative coefficient allowed to vary the amount of radiations that affect the second wire.

2.4. Results of thermal analysis

For each structure previously mentioned, 3 different scenarios were taken into consideration:

- The model which is totally subjected to radiations and Joule heating effect (*JR*)
- The shadow model which is only subjected to Joule heating effect (*J*)
- The non-activated model which is only subjected to radiations (R)

Because of the large number of graphs, they are given as an example only in the first structure. In other cases, the data will be summarized in tables. However, missing graphs are given in appendix C.

2.4.1. Carbon-fibre fabric with 4 plies 0.28 *mm* thick

2.4.1.1. Calculation of the optimum voltage

Both the best possible case and the worst case are considered.

Table 9: Best- and worst-case possible properties

	Worst case	**Best case**
$\lambda\ [W/m^2\ K]$	262.9320	5.666
ε	0.822	0.521
$c\ [J/Kg\ K]$	1341.9	748.1
$\rho\ [Kg/m^3]$	1943	1450
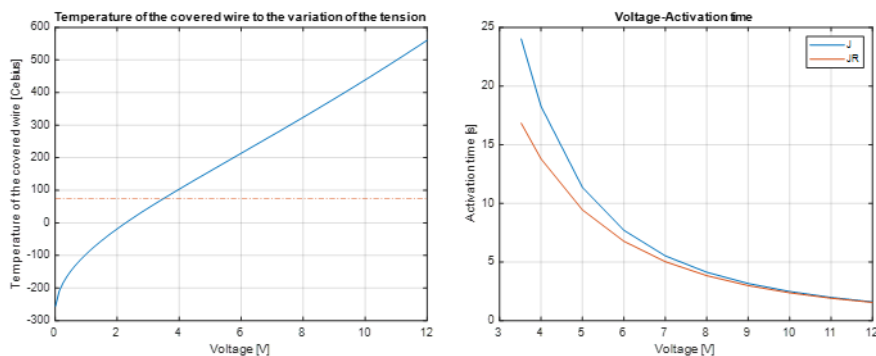
Figure 30: Temperature of the covered wire part varying with voltage (left) and activation time varying with voltage (right)

Table 10: Excellent voltage in the two scenarios considered

	Worst case	Best case
$V_{optimal}$ [V]	5.4278	5.1199

The voltages in both cases are very similar. In the following figure, it is shown how the temperatures vary with respect to the voltage, considering to be in the worst possible case.
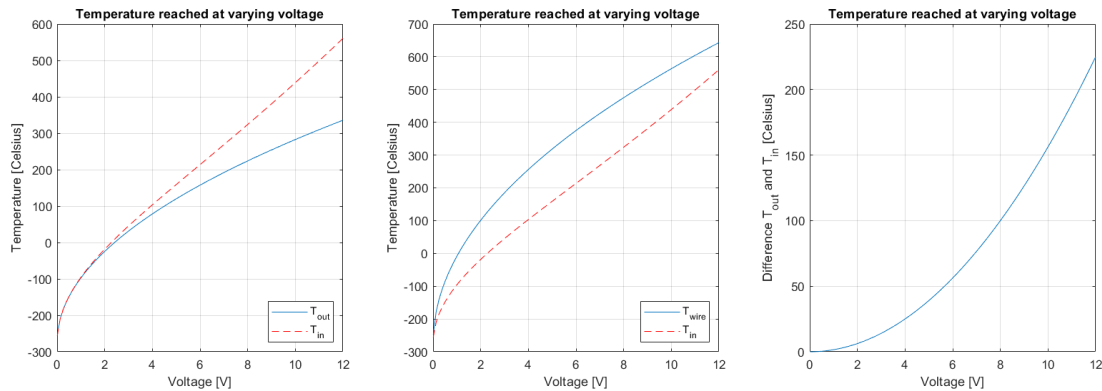
Figure 31: Temperatures variation with respect to voltage, considering being in the worst possible case

After this first part and for all the other analyses, only the worst-case scenario is considered, being the scenario perhaps less probable but more dangerous.

2.4.1.2. Stationary and transient case with Matlab
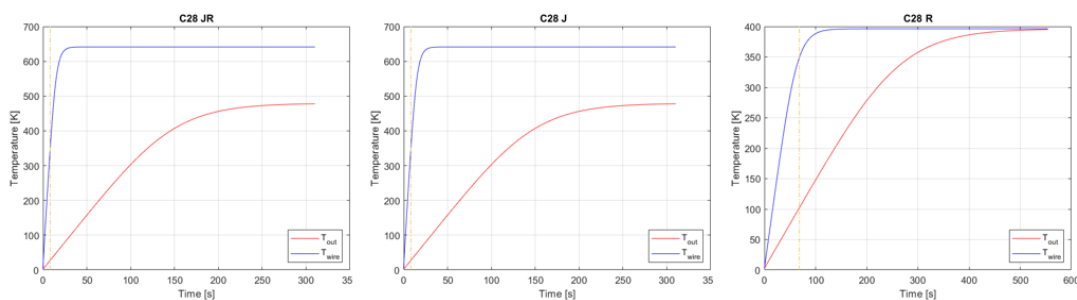
Figure 32: Transients for structure C_{28} in the 3 cases considered

Table 11: Stationary and transient case results with Matlab

$V = 5.4278$ [V]	T_{out} [°C]	T_{in} [°C]	T_{wire} [°C]	$t_{activation}$ [s]
JR	206.1331	252.1725	368.0018	8.1740
J	136.3367	182.3762	343.2186	9.5720
R	123.0917	123.0917	123.0917	68.3010

In all the cases reported, the number of Biot was calculated, and that confirmed the possibility of applying the Lumped Parameter approach. Temperatures are high and activation times are very short. The only presence of radiation activates the wire. This leads to consideration of mechanisms that counteract radiation. However, in case *R* the three temperatures are all similar and the transient longer.

2.4.1.3. Stationary and transient case with Abaqus

The same analyses implemented using Matlab were performed using Abaqus, so as to confirm the obtained results. The following images highlight the locations where the temperatures were recorded.
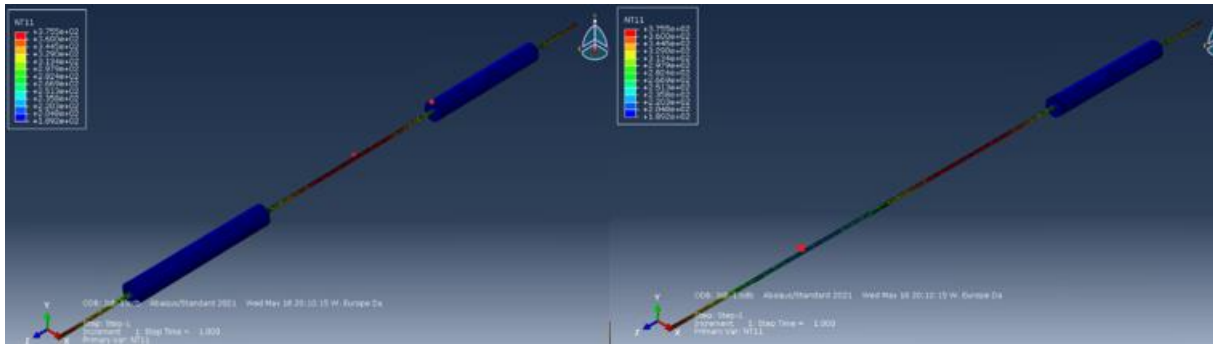
Figure 33: Points where the temperature is calculated in the Abaqus model

Table 12: Stationary and transient case results with Abaqus

$V = 5.4278\,[V]$	T_{out} [°C]	T_{in} [°C]	T_{wire} [°C]	$t_{activation}$ [s]
JR	187.93	229.8	370.397	<25
J	152.299	193.89	342.486	<25
R	70.5336	71.1112	94.7107	≈100
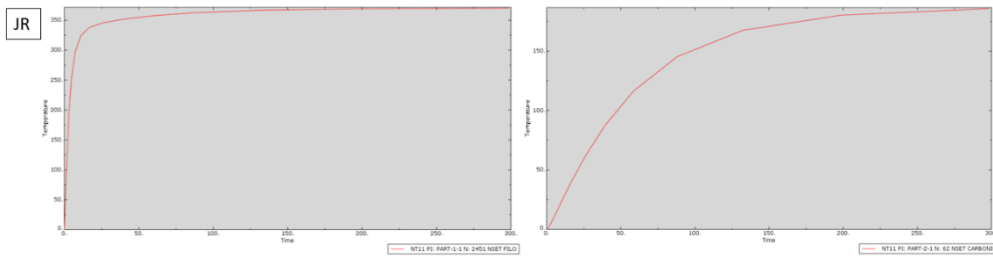
Figure 34: JR, transitional case for wire and composite
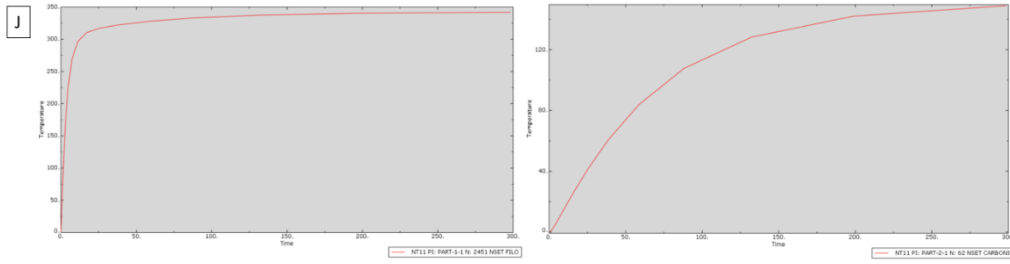
Figure 35: J, transitional case for wire and composite
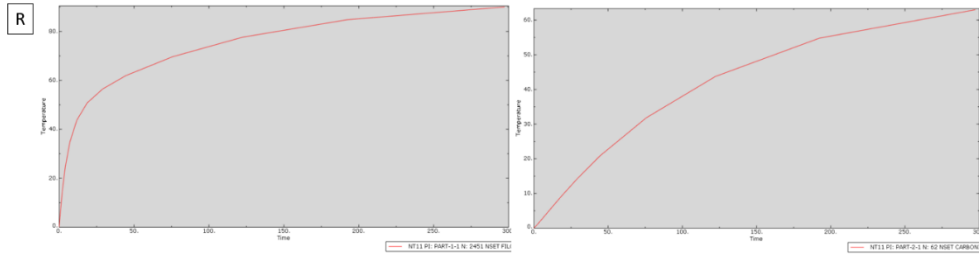
Figure 36: R, transitional case for wire and composite

The temperatures calculated with Abaqus are very similar to those obtained with Matlab. The difference is about 20 degrees for T_{out} and T_{in}, while the difference in the calculation of T_{wire} is negligible. Transients also have about the same duration. During the analysis, the flow of thermal power that passes through the fully uncovered wire and through the wire covered by the composite was also calculated. The following table shows the division of the thermal power flow in the simulations made with Abaqus. Considering the presence of approximations, the division is similar to the one proposed as a hypothesis at the beginning of the thermal analysis. Even the results, very similar between the two software, confirm the soundness of the initial hypothesis.

Table 13: Power division between wire and composite in Abaqus simulations

	$\%Q_{wire}$	$\%Q_{composite}$
JR	49.29%	44.07%
J	39.93%	43.77%

The differences between the Matlab and Abaqus models are due to:

- Temperatures distributed more evenly along the wire in the Abaqus model (whereas, in the Matlab model, temperatures have a step distribution)
- Different conduction resistors (39 Ω with Matlab and about 36 Ω with Abaqus)

The case with the mere presence of radiations in Abaqus differs significantly from that in Matlab because, in the first case, the wire is 0.45 mm long with the presence of 2 cylinders of composite material. This means that the surface exposed to radiations is considerably less than the real one (which, on the other hand, was taken into account in the analysis with Matlab). The effect of radiations is small if compared to that of the

Joule effect, so this problem occurs only in R case. However, the results confirm the small difference between the three temperatures in the presence of radiations only.

2.4.1.4. Convection in a laboratory environment

Free convection simulations were also carried out in an environment similar to the one of the laboratory ($T_\infty = 15\ °C$). The Biot number confirms the possibility of using the Lumped Parameter approach.
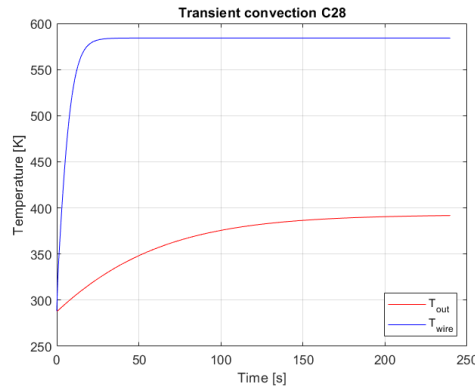
Figure 37: Case of transition for laboratory free convection

Table 14: Stationary and transient case results with Matlab for free convection in laboratory

Voltage [V]	T_{out} [°C]	T_{in} [°C]	T_{wire} [°C]	$t_{activation}$ [s]
5.4278	119.5862	165.6257	310.9826	1.3880
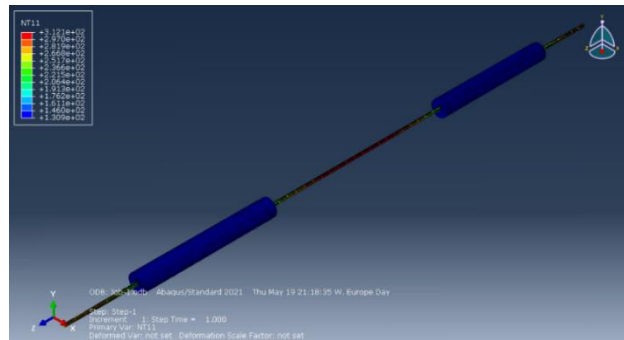
Figure 38: Simulation with Abaqus of free convection in the laboratory

Table 15: Results of the simulation with Abaqus of free convection in the laboratory

T_{out} [°C]	T_{in} [°C]	T_{wire} [°C]
130.91	172.61	312.124

Also in this case, the temperatures are similar and the results confirm that the Matlab simulation is able to predict the temperatures reached with the Joule effect.

2.4.1.5. Length for temperature dissipation

The last part of the analysis, relating to the carbon-fiber fabric with a 0.28 mm thickness, concerns the length necessary to bring the temperature of the outer surface of the composite cylinders wrapping the NiTiNOL wire below the threshold of the activation temperature. All results are collected in the tables below. The coefficient of length $0 \leq C_l \leq 1$ indicates how much surface area, of that addition, is invested by radiations with respect to the maximum allowed (that is, the length corresponding to that of the semi circumference of the spiral). The coefficient of the second wire $0 \leq C_2 \leq 1$, on the other hand, multiplies the number of radiations reaching the second wire of nitinol which is not activated and is placed at 1/4 of the length of the spiral circumference (the coefficient C_2 only concerns the radiations that arrive on the wire and not on the composite part).
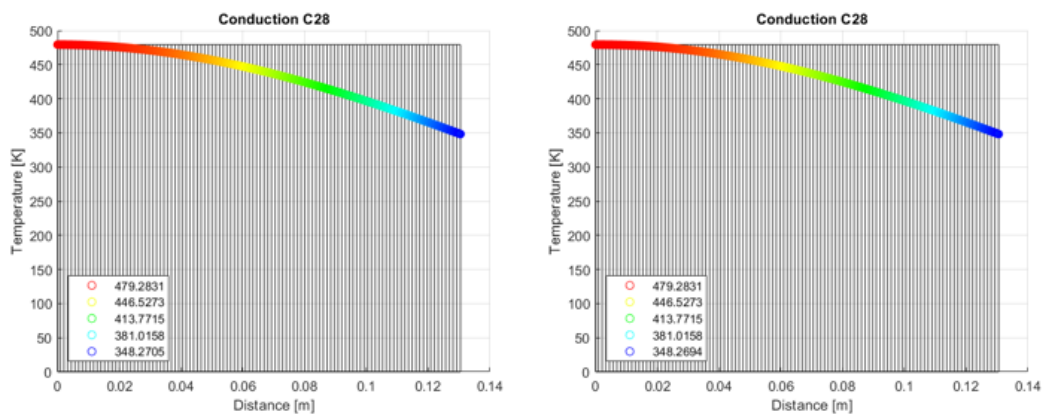
Figure 39: Temperature trend as the dissipation length increases (in case JR), without radiations (left) and with radiations (right)

Table 16: Temperature reached by the second wire in different cases of radiation exposure and length necessary to dissipate the temperature of the composite cylinders (in JR case)

JR			C_2	
			0	1
C_l	Length [m]	$T_{1/4\,circum}$ [°C]	T_{2-wire} [°C]	T_{2-wire} [°C]
0	0.1305	205.5459	190.7704	197.7273
0.5	0.1305	205.6826	190.8917	197.8480
1	0.1305	205.6861	190.8948	197.8511

Table 17: Temperature reached by the second wire in different cases of radiation exposure and length necessary to dissipate the temperature of the composite cylinders (in J case)

	C_2

J			0	1
C_l	Length $[m]$	$T_{1/4\ circum}$ [°C]	T_{2-wire} [°C]	T_{2-wire} [°C]
0	0.1170	136.0238	127.7815	135.0322
0.5	0.1171	136.1606	127.9079	135.1581
1	0.1173	136.1641	127.9111	135.1613

Table 18: Temperature reached by the second wire in different cases of radiation exposure and length necessary to dissipate the temperature of the composite cylinders (in R case)

R			C_2	
			0	1
C_l	Length $[m]$	$T_{1/4\ circum}$ [°C]	T_{2-wire} [°C]	T_{2-wire} [°C]
0	0.1096	122.8173	115.5367	122.8374
0.5	0.1097	122.9541	115.6639	122.9642
1	0.11	122.9576	115.6672	122.9674

With the C_{28} structure, the second wire is always activated because the temperature exceeds that of activation of nitinol wires. This is a big problem if the wires are inserted directly between the layers of composite. The composite length decreases the temperature by a negligible amount. In the passage between composite and second wire, the temperature decreases by a few degrees if the radiation hits the second wire, by a little more than 10 degrees if the second wire is completely in the shade.

2.4.1.6. Simulation of curve dissipation length

Simulations were made with Abaqus with a second wire placed at 1/4 of the circumference of the spiral to see if the activation of the first wire also involved the activation of the second. In this analysis, the second wire is always considered without radiations to heat it (in order to consider the worst possible case).
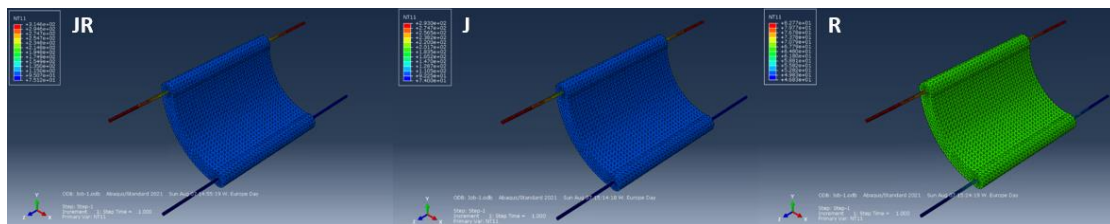
Figure 40: Temperature distribution with curved length and $C_l = 1$

Table 19: Temperatures in the curved case

| | C_l | | | | | | | |
| | 0 | | | | 1 | | | |
	$T_{1_{in}}$ [°C]	$T_{1_{out}}$ [°C]	$T_{1/_4\ circum}$ [°C]	$T_{2_{in}}$ [°C]	$T_{1_{in}}$ [°C]	$T_{1_{out}}$ [°C]	$T_{1/_4\ circum}$ [°C]	$T_{2_{in}}$ [°C]
JR	72.5584	21.8795	21.7878	21.3098	151.838	103.041	102.952	101.8
J	68.3174	18.523	18.4353	17.9477	149.689	101.551	101.468	100.331
R	-115.653	-117.329	-117.335	-117.381	67.1383	66.476	66.4709	65.6729

Compared to the other cases, the temperatures are lower but the behavior of the system is the same. The parameter that makes this analysis particular is the internal temperature reached by the wire. The lower temperature could be due to the small model created on Abaqus (Matlab refers to the entire structure, while on Abaqus we are always forced to consider smaller models or local behaviors). The radiation area on the active wire is very small and this greatly reduces the contribution of radiations to the temperature reached by the wire (for this reason, the temperature difference between JR and J case in Matlab is greater than in Abaqus). The composite that joins the two wires, on the other hand, has a large surface area compared to the one of the wire and this makes the radiations, which impact on this surface, extremely relevant in the calculation of the temperatures. Therefore, even though the temperatures are lower, because of the differences due to the creation of the model, the behavior of the structure with Abaqus is similar to that of the calculations with Matlab:

- Through both software, it is possible to notice a temperature jump of, at most, 50 °C between the internal temperature of the activated wire and the external temperature of the composite outside the wire.
- For the entire length of the composite between the first and second wire, the temperature slightly decreases. This is because the carbon-fiber fabric retains little heat and is not able to isolate well the two wires.
- The temperature jump between the temperature of the composite at 1/4 of the circumference and the one of the second wire is very small: a few degrees on Matlab, whereas, on Abaqus, the difference is even smaller.

The influence of radiations is fundamental in this analysis. This emphasizes the need to study measures to avoid radiations.

2.4.2. Carbon-fibre fabric with 4 plies 0.12 mm thick

2.4.2.1. Calculation of the optimum voltage

The analysis is the same as that of the $0.28 - mm - thick$ carbon-fiber fabric, with the same considerations. For this reason, data and graphs are reported below.

Table 20: Best- and worst-case possible properties

	Worst case	Best case
$\lambda \, [W/m^2 \, K]$	262.9320	5.666
ε	0.822	0.521
$c \, [J/Kg \, K]$	1341.9	748.1
$\rho \, [Kg/m^3]$	1943	1450

Table 21: Excellent voltage in the two scenarios considered

	Worst case	Best case
$V_{optimal} \, [V]$	4.9938	4.7415

The optimum voltage is slightly lower than in the C_{28} case.

2.4.2.2. Stationary and transient case with Matlab

Table 22: Stationary and transient case results with Matlab

$V = 4.9938 \, [V]$	$T_{out} \, [°C]$	$T_{in} \, [°C]$	$T_{wire} \, [°C]$	$t_{activation} \, [s]$
JR	245.4802	284.4495	345.8631	9.4760
J	194.1801	233.1494	318.0633	11.4150
R	123.0917	123.0917	123.0917	68.3010

In all the cases reported, the number of Biot was calculated, and that confirmed the possibility of applying the Lumped Parameter approach. Compared to the previous case, the T_{out} and T_{in} have increased, and therefore the T_{wire} have decreased. The transition times have increased. The situation in case R remained unchanged. The higher temperatures can be due to the decrease of the surfaces that exchange the energy with the deep space, which represent the most significant cooling phenomenon. If the surfaces decrease, then the exchanged energy also decreases.

2.4.2.3. Stationary and transient case with Abaqus

Table 23: Stationary and transient case results with Abaqus

$V = 4.9938 \, [V]$	T_{out} [°C]	T_{in} [°C]	T_{wire} [°C]	$t_{activation}$ [s]
JR	228.801	263.594	353.533	<25
J	200.841	235.559	325.58	<25
R	76.713	77.215	98.3128	≈ 50

Table 24: Power division between covered and uncovered wire in Abaqus simulations

	$\%Q_{wire}$	$\%Q_{composite}$
JR	53.01%	44.64%
J	42.48%	44.55%

In this case, the analysis with Abaqus is even closer to the results obtained with Matlab and the division of the thermal power flow in Abaqus is similar to that foreseen by the initial hypothesis of the analysis.

2.4.2.4. Convection in a laboratory environment

The Biot number confirms the possibility of using the Lumped Parameter approach.

Table 25: Stationary and transient case results with Matlab for free convection in laboratory

Voltage [V]	T_{out} [°C]	T_{in} [°C]	T_{wire} [°C]	$t_{activation}$ [s]
4.9938	168.6721	207.6414	285.3313	1.72

Table 26: Results of the simulation with Abaqus of free convection in the laboratory

T_{out} [°C]	T_{in} [°C]	T_{wire} [°C]
173.519	208.114	293.935

The results are very similar. The activation time of the wire is extremely short and the temperatures are high again in this case. This confirms that the free convection with the air is not able to counteract the temperatures reached by the NiTiNOL wires.

2.4.2.5. Length for temperature dissipation

Table 27: Temperature reached by the second wire in different cases of radiation exposure and length necessary to dissipate the temperature of the composite cylinders (in JR case)

JR	C_2	
	0	1

C_l	Length [m]	$T_{1/4\ circum}$ [°C]	T_{2-wire} [°C]	T_{2-wire} [°C]
0	0.0874	243.7123	224.1967	230.9740
0.5	0.0874	244.0126	224.4562	231.2320
1	0.0874	244.0203	224.4629	231.2387

Table 28: Temperature reached by the second wire in different cases of radiation exposure and length necessary to dissipate the temperature of the composite cylinders (in J case)

J			C_2	
			0	1
C_l	Length [m]	$T_{1/4\ circum}$ [°C]	T_{2-wire} [°C]	T_{2-wire} [°C]
0	0.0876	193.0139	179.6103	186.6234
0.5	0.0877	193.3144	179.8790	186.8907
1	0.0878	193.3221	179.8859	186.8975

Table 29: Temperature reached by the second wire in different cases of radiation exposure and length necessary to dissipate the temperature of the composite cylinders (in R case)

R			C_2	
			0	1
C_l	Length [m]	$T_{1/4\ circum}$ [°C]	T_{2-wire} [°C]	T_{2-wire} [°C]
0	0.0739	122.4886	115.2312	122.5328
0.5	0.0740	122.7892	115.5109	122.8115
1	0.0745	122.7969	115.5181	122.8186

The second wire is always activated. The composite dissipates little heat and the temperature differences between the various parts of the model are similar to those of the previous case. The temperatures of the second wire are higher because those of the first are higher. Instead, the lengths needed to dissipate the heat are decreased. This is due to higher temperatures (even of the composite) which make the term heat exchange for radiation more significant.

2.4.2.6. Simulation of curve dissipation length
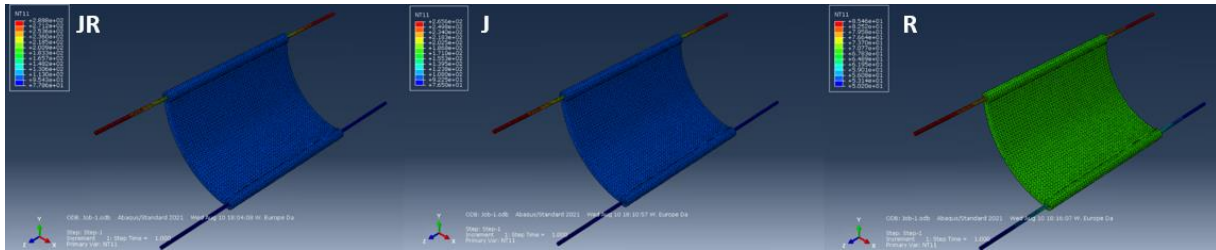
Figure 41: Temperature distribution with curved length and $C_l = 1$

Table 30: Temperatures in the curved case

	C_l							
	0				1			
	$T_{1_{in}}$ [°C]	$T_{1_{out}}$ [°C]	$T_{1/4\,circum}$ [°C]	$T_{2_{in}}$ [°C]	$T_{1_{in}}$ [°C]	$T_{1_{out}}$ [°C]	$T_{1/4\,circum}$ [°C]	$T_{2_{in}}$ [°C]
JR	63.6349	23.4738	23.2393	22.84	144.924	106.218	105.998	105.048
J	58.5908	19.3132	19.0901	18.6999	142.26	104.397	104.186	103.19
R	-109.768	-111.23	-111.248	-111.288	70.8255	70.2821	70.2677	69.5681

The same considerations can be made as in the previous case.

2.4.3. Glass-fibre fabric with 4 plies 0.12 mm thick

2.4.3.1. Calculation of the optimum voltage

For the calculation of the optimal voltage for the wire activation, both the parameters of the best possible case and those of the worst case are considered.

Table 31: Best- and worst-case possible properties

	Worst case	Best case
λ [$W/m^2\,K$]	1.37	0.766
ε	0.8360	0.71
c [$J/Kg\,K$]	1411.9	839.1
ρ [Kg/m^3]	2398	2080

Table 32: Excellent voltage in the two scenarios considered

	Worst case	Best case
$V_{optimal}$ [V]	4.9938	4.9282

It's important to note that the difference between the two voltages in the case of using a glass-fiber fabric is less than that for a carbon-fiber fabric. In both cases, however, the two voltages are very similar. The voltage in this case is similar to that of the case C_{12}.

2.4.3.2. Stationary and transient case with Matlab

Table 33: Stationary and transient case results with Matlab

$V = 4.9938 \, [V]$	T_{out} [°C]	T_{in} [°C]	T_{wire} [°C]	$t_{activation}$ [s]
JR	244.0428	283.7046	345.8631	9.4780
J	192.2112	231.8730	318.0633	11.4130
R	123.0917	123.0917	123.0917	68.3010

In all the cases reported, the number of Biot was calculated, and that confirmed the possibility of applying the Lumped Parameter approach. The temperatures are slightly lower than those of the case C_{12}, the difference is negligible. The timing of transients between the two structures is also similar.

2.4.3.3. Stationary and transient case with Abaqus

Table 34: Stationary and transient case results with Abaqus

$V = 4.9938 \, [V]$	T_{out} [°C]	T_{in} [°C]	T_{wire} [°C]	$t_{activation}$ [s]
JR	229.735	260.761	353.689	<25
J	201.069	232.461	325.732	<25
R	77.1381	76.4765	98.6394	≈ 50

Table 35: Power division between covered and uncovered wire in Abaqus simulations

	$\%Q_{wire}$	$\%Q_{composite}$
JR	53.07%	39.11%
J	42.53%	39.57%

In this case, the analysis with Abaqus is even closer to the results obtained with Matlab and the division of the thermal power flow in Abaqus is similar to that foreseen by the initial hypothesis of the analysis.

2.4.3.4. Convection in a laboratory environment

The Biot number confirms the possibility of using the Lumped Parameter approach.

Table 36: Stationary and transient case results with Matlab for free convection in laboratory

Voltage $[V]$	T_{out} [°C]	T_{in} [°C]	T_{wire} [°C]	$t_{activation}$ $[s]$
4.9938	167.5083	207.1701	285.3313	1.7180

The results obtained with Abaqus are as follows:

Table 37: Results of the simulation with Abaqus of free convection in the laboratory

T_{out} [°C]	T_{in} [°C]	T_{wire} [°C]
174.224	205.818	294.188

The difference in temperatures calculated with the two software is negligible and this confirms the results obtained with Matlab. Activation times are very short.

2.4.3.5. Length for temperature dissipation

Table 38: Temperature reached by the second wire in different cases of radiation exposure and length necessary to dissipate the temperature of the composite cylinders (in JR case)

JR			C_2	
			0	1
C_l	Length $[m]$	$T_{1/_4\ circum}$ [°C]	T_{2-wire} [°C]	T_{2-wire} [°C]
0	0.0063	-	-	-
0.5	0.0071	-	-	-
1	0.0071	-	-	-

Table 39: Temperature reached by the second wire in different cases of radiation exposure and length necessary to dissipate the temperature of the composite cylinders (in J case)

J			C_2	
			0	1
C_l	Length $[m]$	$T_{1/_4\ circum}$ [°C]	T_{2-wire} [°C]	T_{2-wire} [°C]
0	0.0063	-	-	-
0.5	0.0076	-	-	-
1	0.0076	-	-	-

Table 40: Temperature reached by the second wire in different cases of radiation exposure and length necessary to dissipate the temperature of the composite cylinders (in R case)

R			C_2	
			0	1
C_l	Length $[m]$	$T_{1/_4\ circum}$ [°C]	T_{2-wire} [°C]	T_{2-wire} [°C]
0	0.0053	-	-	-
0.5	0.0079	75.0535	70.5246	78.1138
1	0.0080	75.3096	70.7679	78.3563

The wire allows, in most cases, the insulation of the second wire with respect to the first wire. In some cases, the temperature of the second wire is not reported because the material allowed the temperature to drop below the threshold of activation of NiTiNOL before reaching the second wire. It is worth noting that the length needed to dissipate the temperature increases from the *JR* case to the *J* case. This is because, even though the initial temperature is lower in case *J*, the only way the energy is subtracted from the system is by radiation, which has a greater effect where the temperature is higher, while at lower temperature the emission becomes much less significant (since one is always considering the same material and configuration). The great insulating properties of the glass-fiber fabric make it the ideal candidate for the realization of the prototypes, from a thermal point of view.

2.4.3.6. Simulation of curve dissipation length
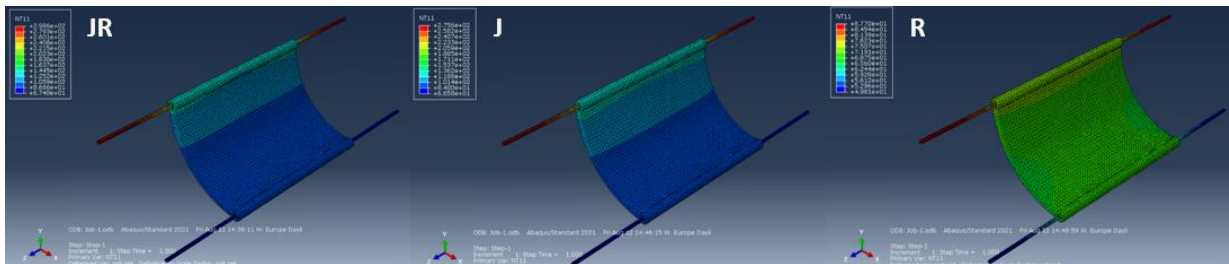
Figure 42: Temperature distribution with curved length and $C_l = 1$

Table 41: Temperatures in the curved case

	C_l							
	0				1			
	$T_{1_{in}}$ [°C]	$T_{1_{out}}$ [°C]	$T_{1/_4\ circum}$ [°C]	$T_{2_{in}}$ [°C]	$T_{1_{in}}$ [°C]	$T_{1_{out}}$ [°C]	$T_{1/_4\ circum}$ [°C]	$T_{2_{in}}$ [°C]
JR	83.5343	41.8816	3.90063	3.52534	164.842	125.476	93.9671	92.5243

J	77.959	37.3553	0.7475	0.4087	161.322	123.312	92.9123	91.5054
R	-108.376	-110.275	-113.64	-113.685	73.8518	73.5193	71.2468	70.0775

2.4.4. Glass-fibre fabric with 6 plies 0.12 mm thick

2.4.4.1. Calculation of the optimum voltage

For the calculation of the optimal voltage for the wire activation, both the parameters of the best possible case and those of the worst case are considered.

Table 42: Best- and worst-case properties

	Worst case	Best case
$\lambda \, [W/m^2 \, K]$	1.37	0.766
ε	0.8360	0.71
$c \, [J/Kg \, K]$	1411.9	839.1
$\rho \, [Kg/m^3]$	2398	2080

Table 43: Best and worst possible scenario

	Worst case	Best case
$V_{optimal} \, [V]$	5.1805	5.1149

The voltage is increased, even if slightly, because the surface that allows to exchange heat with the space environment has increased.

2.4.4.2. Stationary and transient case with Matlab

Table 44: Stationary and transient case results with Matlab

$V = 5.1805 \, [V]$	$T_{out} \, [°C]$	$T_{in} \, [°C]$	$T_{wire} \, [°C]$	$t_{activation} \, [s]$
JR	224.837	267.7052	355.4467	8.8840
J	164.9815	207.8495	329.0135	10.56
R	123.0917	123.0917	123.0917	68.3010

In all the cases reported, the number of Biot confirmed the possibility of applying the Lumped Parameter approach. T_{est} and T_{in} temperatures have decreased, so T_{wire} has increased. Wire activation times have also decreased. The temperature difference between V_{12-4} and V_{12-6} cases is smaller than in the transition from C_{28} to C_{12}. Case R has always remained similar in all analyses, a sign that the temperatures reached with

the presence of radiation alone are not affected by the two materials we used (or that the difference in the use of these two materials is minimal).

2.4.4.3. Stationary and transient case with Abaqus

Table 45: Stationary and transient case results with Abaqus

$V = 5.1805\,[V]$	T_{out} [°C]	T_{in} [°C]	T_{wire} [°C]	$t_{activation}$ [s]
JR	227.567	262.34	363.302	<25
J	178.49	213.856	332.606	<25
R	114.984	114.281	118.732	≈ 100

Table 46: Power division between wire and composite in Abaqus simulations

	$\%Q_{wire}$	$\%Q_{composite}$
JR	57.04%	43.65%
J	44.99%	44.39%

The difference with Matlab and Abaqus is very small and the thermal power flow confirms the initial hypothesis of the analysis.

2.4.4.4. Convection in a laboratory environment

The Biot number confirms the possibility of using the Lumped Parameter approach.

Table 47: Stationary and transient case results with Matlab for free convection in laboratory

Voltage [V]	T_{out} [°C]	T_{in} [°C]	T_{wire} [°C]	$t_{activation}$ [s]
5.1805	143.6314	186.4993	296.47	1.5620

The results obtained with Abaqus are as follows:

Table 48: Results of the simulation with Abaqus of free convection in the laboratory

T_{out} [°C]	T_{in} [°C]	T_{wire} [°C]
153.895	189.343	301.546

The temperatures reached in case V_{12-6} considering the convection in the laboratory are lower than those of case V_{12-4} (T_{wire} remains similar instead). The same thing happened when we switched from C_{28} to C_{28}. The results lead to the same considerations: high temperatures and very fast activation times. Free convection with air does not significantly decrease temperatures.

2.4.4.5. Length for temperature dissipation

Table 49: Temperature reached by the second wire in different cases of radiation exposure and length necessary to dissipate the temperature of the composite cylinders (in JR case)

JR			C_2	
			0	1
C_l	Length [m]	$T_{1/4\ circum}$ [°C]	T_{2-wire} [°C]	T_{2-wire} [°C]
0	0.0076	-	-	-
0.5	0.0086	97.4451	91.6696	99.2142
1	0.0089	98.4716	92.6348	100.1758

Table 50: Temperature reached by the second wire in different cases of radiation exposure and length necessary to dissipate the temperature of the composite cylinders (in J case)

J			C_2	
			0	1
C_l	Length [m]	$T_{1/4\ circum}$ [°C]	T_{2-wire} [°C]	T_{2-wire} [°C]
0	0.0074	-	-	-
0.5	0.0088	97.1727	91.4135	98.9590
1	0.0095	98.1993	92.3788	99.9207

Table 51: Temperature reached by the second wire in different cases of radiation exposure and length necessary to dissipate the temperature of the composite cylinders (in R case)

R			C_2	
			0	1
C_l	Length [m]	$T_{1/4\ circum}$ [°C]	T_{2-wire} [°C]	T_{2-wire} [°C]
0	0.0064	-	-	-
0.5	0.0086	87.5662	82.3582	89.9371
1	0.0097	88.5928	83.3277	90.9031

With 6 layers of fiber-glass fabric, there is less insulation between the two wires due to the larger size of the composite on which the radiations act. This highlights the importance of the radiations acting on the composite structure because when there are no radiations on the length, the material perfectly insulates as in the structure with 4

layers. Also in this case, the length, passing from JR to J, increases. This is due to lower temperature and, therefore, less energy loss through radiations. Due to the lower insulating capacity, it is preferable to use 4 layers of material.

2.4.4.6. Simulation of curve dissipation length
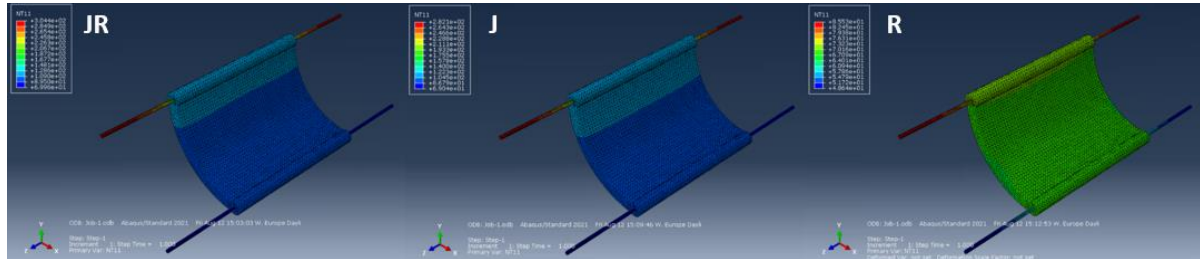
Figure 43: Temperature distribution with curved length and $C_l = 1$

Table 52: Temperatures in the curved case

| | C_l | | | | | | | |
| | 0 | | | | 1 | | | |
	$T_{1_{in}}$ [°C]	$T_{1_{out}}$ [°C]	$T_{1/4 \, circum}$ [°C]	$T_{2_{in}}$ [°C]	$T_{1_{in}}$ [°C]	$T_{1_{out}}$ [°C]	$T_{1/4 \, circum}$ [°C]	$T_{2_{in}}$ [°C]
JR	77.9019	34.8656	10.9233	10.6098	159.608	118.016	97.0657	95.7222
J	72.2774	30.8612	7.71454	7.40592	155.307	116.138	95.8627	94.5308
R	-111.729	-113.373	-115.226	-115.258	71.1757	70.9718	69.6117	68.4326

The thermal behavior of all the 4 structures considered is very similar. The required voltage is always around 5 V and the temperatures are over 150 °C. Also, the activation times are very similar (slightly greater in the case of glass fibers) and differ little passing from the JR case to the J one. The radiations play an important role because, even though it takes more time, they still lead the wires to activation. This requires protection from external radiations. The problem of heat dissipation inside the structure was also analyzed. The insulating capacity of the fiber-glass fabric makes this material the optimal choice from a thermal point of view. In fact, the temperature difference is small, but this material is able to avoid the heating of the second wire placed at a distance of 1/4 of the circumference, without the need of additional thermal protections such as insulating sheaths.

3 Cooling

Thermal analysis confirmed the need to avoid radiations, which can activate NiTiNOL wires. In order not to compromise the functionality of the structure and its control, thermal protection must be used. For such a flexible structure, with the need to make large movements, a flexible and lightweight protection is needed. According to literature, the component that meets the needed requirements is a protection with multi-layer insulation (MLI).

3.1. Multi-layer insulation

Figure 44: MLI for the thermal protection

Multi-layer insulation (MLI) is thermal insulation composed of multiple layers of thin sheets and is often used on spacecrafts and cryogenics. MLI is one of the main items of the spacecraft thermal design, primarily intended to reduce heat loss by thermal radiation. It is therefore commonly used on satellites and other applications in vacuum where conduction and convection are much less significant and radiation dominates. It consists of multiple foils (made of Kapton or Mylar coated with a highly reflective metal) which are placed parallel to each other and low thermal conductive spacers which are arranged in between the foils to avoid direct contact with the foils. These spacers are made in Dacron (synthetic fiber obtained by polymerization from ethylene glycol and terephthalic acid) in order to reduce as much as possible the heat exchanged by conduction [22].
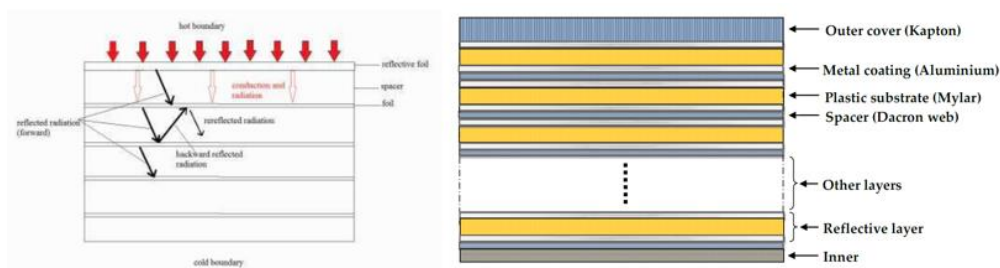
Figure 45: Scheme and components of MLI

Multi-layers insulations are capable of maintaining hundreds of temperature gradients across a thin insulation. The effective thickness of a typical MLI is within few millimeters. The radiation heat from the outer space strikes on the first reflective layer

where a part is reflected back to the environment, and the remaining radiation energy heats up the first layer of spacer. As the temperature of the layer increases, solid conduction, gas conduction and radiation take place through the spacer material to the next foil. Thus, the temperature of the second foil will increase. The second foil reflects some radiations back to the first foil and the remaining energy transfers to the third foil. This process continues down to the bottom layer [23]. In the area of multi-layer thermal insulation, a great deal of survey results has been generated in recent decades. The ability to have a radiation protection that is flexible and lightweight is crucial for the prototype under development.

3.2. Cooling strategies

In addition to the MLI covering of the structure, there are other mechanisms and devices that can counteract the biggest disadvantage of shape memory alloys: the control of the cooling of the material. The use of the structure as a system for the refueling of space equipment makes it possible to consider convection as one of the phenomena that allow temperature control. The use of liquids or gases, whether for refueling or just for thermal control, is therefore one of the possible mechanisms to be considered. A preliminary analysis of how the structure subjected to convection behaves in space is necessary.

3.2.1. Substances

For the study of cooling by convection, it is necessary to consider that the spiral structure is enclosed by an outer casing. The thermal protection with MLI therefore allows to protect against radiations and to give the shape necessary for the passage of liquids or gases for cooling. In these analyses, 4 cases are considered: forced convection with a liquid, forced convection with 2 types of gas and, ultimately, free convection with a liquid. In all cases, the 4 structures of the previous analysis are considered. The fluids considered are:

- Liquid Hydrogen Peroxide H_2O_2 for forced convection. This liquid was chosen because it is a green propellant and minimizes the loss of performance due to the replacement of toxic propellants. It can be used as monopropellant, bipropellant (as oxidizer) and as propellant in the case of hybrid-type propulsion [24]. We use the linear coefficient of thermal expansion because we assume that the liquid can only dilate in the direction of the spiral axis.

Table 53: Parameters of hydrogen peroxide

	Hydrogen Peroxide H_2O_2
$\rho \, [Kg/m^3]$	1280

Molar mass [g/mol]	34.0147
Boiling point [℃]	150.2
c [J/K mol]	89.1
μ [Pa s]	$1.02 \ 10^{-3}$
β [GPa]	2.2
α [K^{-1}]	$158.15 \ 10^{-6}$

- Methane and air in the case of forced convection with gas. The choice fell on these two gases because methane is widely used in the aerospace field and air is taken as a general reference.

Table 54: Parameters of methane and air

	Methane CH_4	Air
ρ [Kg/m^3]	0.657	1.225
Molar mass [g/mol]	16.04	28.9633
c [J/K mol]	2201.37	1005
μ [Pa s]	$0.012 \ 10^{-3}$	$1.18 \ 10^{-5}$
λ [W/m K]	0.03205228	0.0286098
P_c [atm]	45.8	37.36
T_c [K]	190.7	132.63
γ (at 20℃)	1.320	1.4

3.2.2.   Convection with hydrogen peroxide

The structure is approximated with a rough tube whose input conditions are known and selected a priori. In aerospace plants, tanks are always under pressure. Moreover, considering a LEO orbit (similar to the one of the ISS at $408 \ Km$), the pressure must counteract the gravity force, because the constant of gravity at $408 \ Km$ has decreased, but has still a great influence. The structure was approximated with a $500 \ mm$ long tube with a $10 \ mm$ diameter. The conditions at the inlet of the tube are:

- $P_1 = 50 \ [atm] = 5.066 \ [MPa]$
- $T_1 = 15 \ [℃] = 288.15 \ [K]$ (Temperature at which H_2O_2 is liquid)
- $v_1 = 5 \ [m/s]$

The pressure and temperature at the outlet of the tube are not known and depend on the losses that the structure generates. However, the output and the inlet speed are set to be equivalent, because we want the structure to exchange heat by convection in the most uniform way possible for the whole length of the tube.
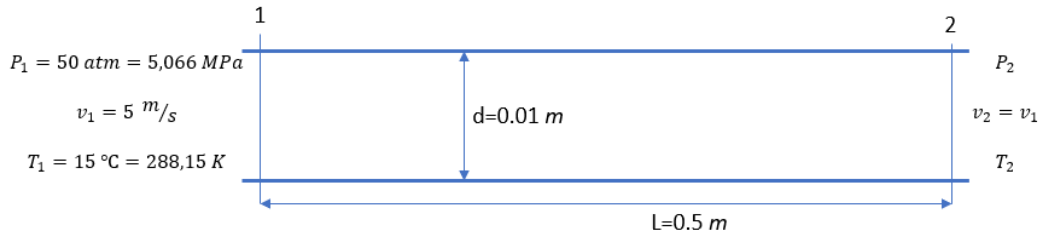
Figure 46: Summary diagram of convection with hydrogen peroxide

The first part of the analysis concerns the study of the conditions at the exit of the structure and the calculation of the convective coefficient.

3.2.2.1. Conditions at the exit of the structure

The initial assumptions in this situation are:

- $\rho = cost \ [Kg/m^3]$
- $v_1 = v_2$
- Forced convection
- 1D (single predominant size)
- $\lambda = 0.6 \ [W/m \ K]$ (For liquids)
- $e = 0.02325 \ [mm]$ (Roughness)

In the structure, the presence of 3 wires is assumed. Therefore, the generated thermal power is:

$$\dot{Q} = 3\frac{V^2}{R} \ [W] \tag{3.1}$$

The tube has a constant section and the mass flow is derived from the formula:

$$\dot{m} = \rho v A \ \left[\frac{Kg}{s}\right] \tag{3.2}$$

The energy conservation equation is used to derive the conditions at the exit of the structure. For the formulation of the equation of energy conservation for a fluid, we start from the first principle of thermodynamics that establishes the equivalence between the various forms of energy.

$$\int_{V_0} \frac{\partial \rho \varepsilon}{\partial t} dV + \int_{S_0} \rho \varepsilon u \cdot n dS = \dot{L} + \dot{Q} \tag{3.3}$$

The equation (3.3) is the energy conservation equation in integral form, where $\dot{L}$ and $\dot{Q}$ respectively the work done on the system and the heat introduced in the system. The

specific total energy can be written by highlighting the kinetic, potential and internal energy contribution. Considering that the volume of the system does not change, in the case considered, in which the constant velocity hypothesis allows to eliminate the term linked to the velocity and the reduced length of the structure with respect to the radius of the LEO orbit allows to neglect the term linked to the acceleration of gravity, the equation becomes:

$$\dot{m}\left[\left(c_v T_2 + \frac{p_2}{\rho}\right) - \left(c_v T_1 + \frac{p_1}{\rho}\right)\right] = \dot{Q} \tag{3.4}$$

The problem with this equation (3.4) is that we do not know the temperature and the pressure at the exit of the structure. This is why the equation of state for liquids is considered. It is not possible to have a simple form of this equation, therefore we resort to a linearization.

$$\frac{\Delta V}{V} = -\frac{1}{\beta}\Delta p + \alpha \Delta T \tag{3.5}$$

β is the compressibility module and α is the coefficient of thermal expansion. Considering that the volume remains constant $\Delta V = 0$ and replacing the equation of state (3.5) in the equation of conservation of energy (3.4), we obtain:

$$T_2 = T_1 + \frac{\frac{\dot{Q}}{\dot{m}}}{c_v + \frac{\beta\alpha}{\rho}} \tag{3.6}$$

After calculating the temperature at the exit section of the structure, since the temperature change due to the thermal power is small, the pressure losses are calculated by the relationship:

$$p_1 = p_2 + \frac{1}{2}\alpha\rho v^2 \tag{3.7}$$

The intensity of the pressure losses is greatly affected by the presence of a *laminar motion*, characterized by individual particles whose speed has the same direction as the axis of the duct, or a *turbulent motion*, with components of speed in all directions. The transition of motion from laminar to turbulent is dominated by the ratio of mass forces to viscous forces, expressed by the Reynolds number:

$$Re = \frac{\rho v D_c}{\mu} \tag{3.8}$$

where ρ is the density, v the average speed, D_c the hydraulic diameter and μ viscosity. The hydraulic diameter is defined as:

$$D_c = \frac{4\,A}{P} \tag{3.9}$$

where A is the area of the section and P the perimeter. In the case of pipes, the following expression of α was determined experimentally:

$$\alpha = \lambda \frac{L}{D_c} \tag{3.10}$$

Where λ is a coefficient of distributed losses and L is the length of the. The pressure drop on the entire pipe is therefore given by the Darcy-Weisbach law (3.11):

$$p_1 - p_2 = \lambda \frac{L}{D_c} \frac{1}{2} \rho v^2 \tag{3.11}$$

The coefficient λ depends on the type of motion, indicated by the Reynolds number, and on the surface roughness of the duct, defined as the ratio between the average thickness of the irregularities, ε, and the diameter of the tube. The Moody diagram shows the trend of the coefficient.
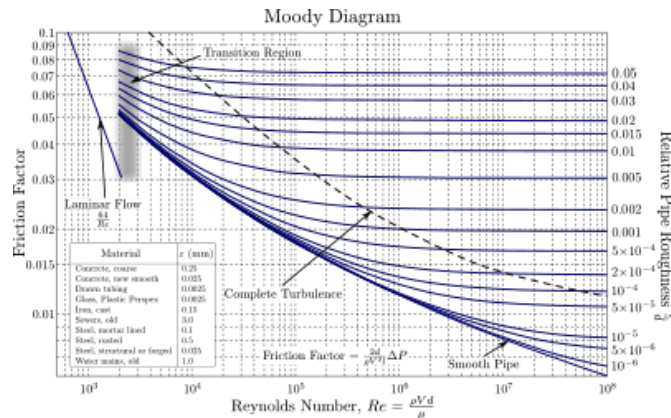
Figure 47: Moody diagram

It is known that for $Re < 2000$ the motion is laminar. In laminar motion, not only is the pressure loss linearly dependent on geometric parameters, but it is also dependent on the viscosity and the velocity of the fluid. When the Reynolds number exceeds 4000, the motion becomes turbulent. In this case, the values of λ are derived from experimental curves or empirical formulas. For very high Reynolds number, λ is significantly independent of the Reynolds number and only depends on roughness. In this range of motion, the pressure loss is therefore dependent on the square of the speed and independent of the viscosity of the fluid. For values of the Reynolds number between 2000 and 4000, the transition zone is not well defined, since the transition from the laminar to the turbulent state is a phenomenon of instability that can therefore have a certain margin of uncertainty. Among the relationships used in the calculation, it is possible to find those for rough tubes and fully developed turbulent flows [25]:

$$\frac{1}{\sqrt{\lambda}} = 1.14 - 2\log_{10}\left(\frac{e}{D}\right) \tag{3.12}$$

Concentrated pressure losses are also calculated. The pressure drop for a curved section, such as the prototype after activation, can be calculated with:

$$\Delta p = \left[\lambda\frac{L}{D} + \beta K_g\right]\frac{1}{2}\rho v^2 \tag{3.13}$$

Where $\lambda\frac{L}{D}$ expresses the losses distributed in the elbow section and βK_g indicates the losses due to the change in direction of the velocity vector. K_g and β are derived from the diagrams:
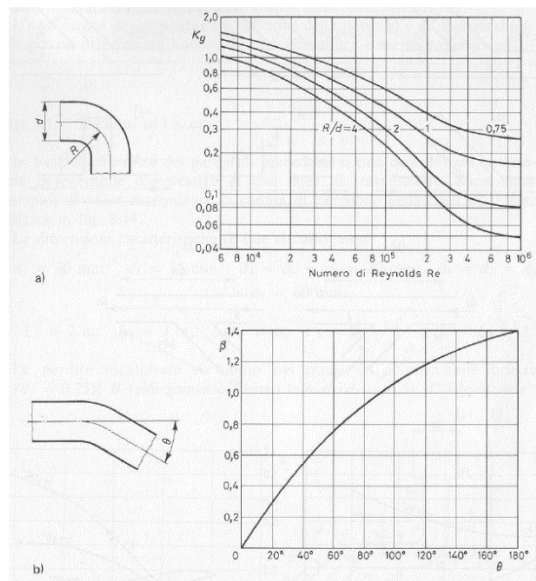
Figure 48: Coefficients for the calculation of pressure losses in curved sections

Assuming a radius of curvature of $30\ cm$, representing the displacement of the structure during activation, the coefficients are obtained: $\beta = 0.4$ and $K_g = 0.8$.

3.2.2.2. Convective coefficient

After calculating the physical quantities at the exit of the structure, the convective coefficient is calculated in the case of convection with liquid in turbulent motion. The coefficient is derived from empirical relationships that bind the dimensionless groups which are representative of the phenomenon.

$$Re = \frac{\rho v D_c}{\mu} > 10000 \qquad\qquad Nu = 0{,}023\ Re^{0,8}\ Pr^n$$

$$0.6 < Pr = \frac{\mu\ c_p}{\lambda} < 160 \qquad\qquad h = \frac{Nu\ \lambda}{D}\left[\frac{W}{m^2\ K}\right]$$

$$n = 0{,}4 \quad per\ T_s > T_m$$

$$\frac{L}{D} > 10 \qquad\qquad\qquad n = 0{,}3 \quad per\ T_s < T_m$$

Figure 49: Empirical expression for the calculation of the Nusselt number, with the conditions of validity

3.2.3. Convection with methane and air

The initial conditions in the case of cooling by convection with gas are chosen considering a fuel supply system for methane (as we previously did for hydrogen peroxide), and a simple cooling system for air. In the case of methane:

- $P_{1_{CH4}} = 10 \, [atm] = 1.013 \, [MPa]$
- $T_{1_{CH4}} = 25 \, [°C] = 298.15 \, [K]$
- $v_{1_{CH4}} = 5 \, [m/s]$
- $M_{1_{CH4}} = \dfrac{v}{c} = \dfrac{v}{\sqrt{\gamma RT}} = 0.0221$

In the case of air:

- $P_{1_{air}} = 1 \, [atm] = 101325 \, [MPa]$
- $T_{1_{air}} = 25 \, [°C] = 298.15 \, [K]$
- $v_{1_{air}} = 10 \, [m/s]$
- $M_{1_{air}} = \dfrac{v}{c} = \dfrac{v}{\sqrt{\gamma RT}} = 0.0289$
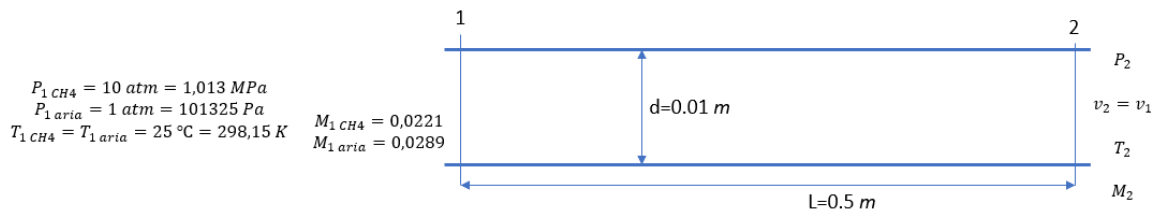
Figure 50: Approximate scheme of gas convection

In order to use the equation of the state of the ideal gases, the compressibility factor must be:

$$Z = \frac{Pv}{RT} \approx 1 \tag{3.14}$$

In this case, the reduced temperature and the reduced pressure (dependent on critical temperature and critical pressure) are calculated:

$$P_r = \frac{P}{P_c} \qquad T_r = \frac{T}{T_c} \tag{3.15}$$

Considering the initial conditions, Z is very close to the unit, so the condition of ideal gas can be used [26].

3.2.3.1. Conditions at the exit of the structure

The initial assumptions in this situation are:

- 1D
- Non-reacting flow
- Single phase

- Single-component mixture
- Calorically perfect gas
- Constant area
- $e = 0.02325 \, [mm]$
- Spiral with 3 wires and $V = 5 \, [V]$

Two models, Fanno flow and Rayleigh flow [27], are used for the calculation of pressure losses and the conditions at the exit of the structure. One takes into account losses by friction, whereas the other considers the losses due to the introduction of heat into the flow. These two models require the definition of total quantities. Total quantities are defined for the quantities of pressure, enthalpy, temperature and density. Total quantities represent the value that the given magnitude would have if the fluid in motion stopped isoentropically.

$$h_T = h + \frac{v^2}{2} \qquad\qquad p_T = p + \frac{v^2}{2}\rho \qquad\qquad T_T = T + \frac{v^2}{2c_p} \qquad (3.16)$$

The relation between total quantities and their static quantities are functions of the Mach number only.

$$\frac{T_T}{T} = 1 + \frac{\gamma - 1}{2}M^2 \qquad \frac{p_T}{p} = \left(1 + \frac{\gamma - 1}{2}M^2\right)^{\frac{\gamma}{\gamma-1}} \qquad \frac{\rho_T}{\rho} = \left(1 + \frac{\gamma - 1}{2}M^2\right)^{\frac{1}{\gamma-1}} \qquad (3.17)$$

The Fanno flow considers the presence of friction, but the duct must have a constant section and there must be no addition of heat in the system. The model allows to calculate the pressure loss at the outlet of the duct (total and, then, static). For any condition at the inlet, the system tends, through the friction, to converge the number of Mach to 1 towards the outlet of the tube. This never happens inside the tube due to thermodynamic reasons. The achievement of the sonic conditions involves the adjustment of the quantities in the initial section because of this new situation of equilibrium. Then, some quantities such as mass flow or pressure could be changed, completely affecting the operation of the system. Therefore, proper design is needed so that the length required to get the sonic sizes, property only of the flow, is longer than the tube. Subsequently, one obtains a completely unchocked tube. For the calculation of the physical quantities at the output, we must consider the Fanning friction factor, C_f, that corresponds to a quarter of the Darcy friction factor, f, which can be obtained from the Moody diagram.

$$C_f = \frac{f\left(Re, \frac{e}{d}\right)}{4} \qquad (3.18)$$

In the case of air, in the transition zone between smooth and rough pipes with $Re > 4000$, the bisection method is used to calculate f:

$$\frac{1}{\sqrt{f}} = 1.14 - 2\ \log_{10}\left(\frac{e}{d} + \frac{9.35}{Re\ \sqrt{f}}\right) \qquad (3.19)$$

Whereas in the case of methane, with rough tubes and fully developed turbulent flow:

$$\frac{1}{\sqrt{f}} = 1.14 - 2\ \log_{10}\left(\frac{e}{d}\right) \qquad (3.20)$$

The equation that allows to compute the losses in a duct of defined diameter D, Fanning Friction Factor C_f and length L, passing from the input section to the output section, is:

$$4C_f\frac{L}{D} = 4C_f\frac{L^*}{D}\bigg|_1 - 4C_f\frac{L^*}{D}\bigg|_2 \qquad (3.21)$$

The amount in section 1 is tabulated and, then, known, as it depends only on the γ, the adiabatic coefficient of expansion, of the flow and the input section Mach.

M	$4C_tL^*/D$	T/T^*	p/p^*	ρ/ρ^*	p_o/p_o^*	I/I^*	$\Delta s/R$
1.60	1.7233E−01	7.9365E−01	5.5679E−01	7.0156E−01	1.2502E+00	1.0635E+00	2.2333E−01
1.62	1.7950E−01	7.8695E−01	5.4759E−01	6.9584E−01	1.2666E+00	1.0665E+00	2.3636E−01
1.64	1.8664E−01	7.8027E−01	5.3862E−01	6.9029E−01	1.2836E+00	1.0695E+00	2.4963E−01
1.66	1.9373E−01	7.7363E−01	5.2986E−01	6.8489E−01	1.3010E+00	1.0725E+00	2.6315E−01
1.68	2.0078E−01	7.6703E−01	5.2131E−01	6.7965E−01	1.3190E+00	1.0755E+00	2.7690E−01
1.70	2.0777E−01	7.6046E−01	5.1297E−01	6.7455E−01	1.3376E+00	1.0785E+00	2.9088E−01

Figure 51: Table Fanno flow

The only unknown is the term in section two. After calculating it from the equation, one can use the tables again to find the quantities in the output section of the tube. After the Fanno flow, the Rayleigh model, which considers a tube with a constant section, is used adding heat to the system but neglecting the friction. The relationship which allows to pass from the input section to the output section is:

$$\frac{T_{T_2}}{T_{T_1}} = \frac{T_{T_2}}{T_T^*}\bigg|_2 \frac{T_T^*}{T_{T_1}}\bigg|_1 \qquad (3.22)$$

Also in this case, the term in section 1 is tabulated and known, as it depends only on γ of the flow and Mach number at the inlet.

M	p/p^*	T/T^*	ρ/ρ^*	T_o/T_o^*	p_o/p_o^*	$\Delta s/R$
1.60	5.2356E−01	7.0174E−01	7.4609E−01	8.8419E−01	1.1756E+00	5.9259E−01
1.62	5.1346E−01	6.9190E−01	7.4210E−01	8.7922E−01	1.1877E+00	6.2250E−01
1.64	5.0363E−01	6.8219E−01	7.3825E−01	8.7429E−01	1.2002E+00	6.5265E−01
1.66	4.9405E−01	6.7259E−01	7.3454E−01	8.6939E−01	1.2131E+00	6.8303E−01
1.68	4.8472E−01	6.6312E−01	7.3096E−01	8.6453E−01	1.2264E+00	7.1360E−01
1.70	4.7562E−01	6.5377E−01	7.2751E−01	8.5971E−01	1.2402E+00	7.4436E−01
1.72	4.6677E−01	6.4455E−01	7.2418E−01	8.5493E−01	1.2545E+00	7.7529E−01
1.74	4.5813E−01	6.3545E−01	7.2096E−01	8.5019E−01	1.2692E+00	8.0636E−01

Figure 52: Table of the Rayleigh flow

The total temperature in the output section (once the thermal power introduced in the system is known), in the case of calorically perfect gas, is calculated from the expression:

$$Q = \dot{m} c_p \left(T_{T_2} - T_{T_1} \right) \tag{3.23}$$

Once these two quantities are known from the equation of Rayleigh flow, we can derive the ratio of T_T^* (total temperature in the section where Mach=1, an intrinsic property of flow) and T_{T_2}. Going back to consulting the tables, we then obtain all the quantities in the output section of the structure.

3.2.3.2. Convective coefficient

After calculating the physical quantities at the exit of the structure, the convective coefficient is calculated in the case of convection with gas for several numbers of Reynolds. In the case of methane, the empirical expression that allows to calculate the Nusselt number and then the convection coefficient is:

$$Re = \frac{\rho v D}{\mu} > 10000$$
$$0.6 < Pr = \frac{\mu c_p}{\lambda} < 160$$
$$\frac{L}{D} > 10$$

$$Nu = 0.023 \, Re^{0.8} \, Pr^n$$
$$h = \frac{Nu \, \lambda}{D} \left[\frac{W}{m^2 \, K} \right]$$
$$n = 0.4 \quad per \; T_s > T_m$$
$$n = 0.3 \quad per \; T_s < T_m$$

Figure 53: Empirical expression for the calculation of the Nusselt number

In the case of air, on the other hand, the empirical expressions are:

$$Re < 2100$$
$$Pr > 0.7$$
$$\frac{L}{D} \gg 0.05 \, Re \, Pr$$
$$q = cost$$

$$Nu = 4.36$$

$$Re > 6000$$
$$Pr > 0.7$$
$$\frac{L}{D} > 10$$

$$Nu = 0.023 \, Re^{0.8} \, Pr^{0.33}$$

$$h = \frac{Nu \, \lambda}{D} \left[\frac{W}{m^2 \, K} \right]$$

$$Re = \frac{\rho v D}{\mu} > 10000$$
$$0.6 < Pr = \frac{\mu c_p}{\lambda} < 160$$
$$\frac{L}{D} > 10$$

$$Nu = 0.023 \, Re^{0.8} \, Pr^n$$

$$n = 0.4 \quad per \; T_s > T_m$$
$$n = 0.3 \quad per \; T_s < T_m$$

Figure 54: Empirical expression for the calculation of the Nusselt number

3.2.4.   Calculation of temperature

3.2.4.1. Stationary case

The second part of the analysis concerns the calculation of temperature reached by the wire in the structure. The same strategy of thermal analysis was also used in this case, with the same assumptions. Considering the average temperature T_∞, obtained from the first part of the analysis, the external temperature of the composite coating is calculated through the equation:

$$\frac{Q}{2} - hA(T - T_\infty) = 0 \tag{3.24}$$

Then the temperature of the uncovered wire and, ultimately, the temperature of the wire embedded in the structure are calculated:

$$\frac{Q}{2} - hA(T - T_\infty) = 0 \tag{3.25}$$

$$T_{in} = \left(\frac{Q}{2} R_{tot}\right) + T_{out} \tag{3.26}$$

The areas considered are respectively:

$$A = \begin{cases} \dfrac{(A_{tot} - A_{hidden})}{2} & for\ NiTiNOL\ wire \\[2ex] \dfrac{\left(\left((2\pi R_{est})0.01\right)20\right) + \left(\left((R_{est}^2 - R_{in}^2)\pi\right)40\right)}{2} & for\ the\ surface\ of\ the\ composite \end{cases} \tag{3.27}$$

Where A_{tot} is the total surface of the wire, A_{hidden} is the surface of the wire hidden by the structure, R_{est} is the outer radius of the composite cylinder, R_{in} is the inner radius of the composite cylinder.

3.2.4.2. Transitional case

Also in this case, the Lumped parameter approach was applied. Here the equations considered were two (one for the wire temperature and one for the external temperature of the composite) and they had to be solved iteratively:

$$\rho_{NiTi} c_{NiTi} V_{NiTi} \frac{\partial T_{wire}}{\partial \tau} = Q - hA(T_{wire} - T_\infty) - \frac{1}{R_{tot}}\Delta \tag{3.28}$$

$$\rho_c c_c V_c \frac{\partial T_{out}}{\partial \tau} = -hA(T_{out} - T_\infty) - \frac{1}{R_{tot}}\Delta \tag{3.29}$$

The terms with $NiTi$ index refer to the wire, while those with index c refer to the composite. The differential equations have been approximated by a backward scheme.

$$T_{wire}^{k+1} = T_{wire}^{K} + \left(\frac{Q}{\rho_{NiTi}c_{NiTi}V_{NiTi}} - \frac{hA}{\rho_{NiTi}c_{NiTi}V_{NiTi}} \left(T_{wire}^{k+1} - T_{\infty} \right) - \frac{\frac{1}{R_{tot}}\Delta}{\rho_{NiTi}c_{NiTi}V_{NiTi}} \right) \Delta t \qquad (3.30)$$

$$T_{out}^{k+1} = T_{out}^{K} + \left(-\frac{hA}{\rho_{c}c_{c}V_{c}} \left(T_{out}^{k+1} - T_{\infty} \right) - \frac{\frac{1}{R_{tot}}\Delta}{\rho_{c}c_{c}V_{c}} \right) \Delta t \qquad (3.31)$$

The resolution scheme is the same as described in Chapter 2.

3.2.5. Free convection with water

In the last part of the analysis, it was decided to consider also the water with a free convection, as if the structure (covered with MLI) contained the liquid without it flowing away. The parameters used in this case are:

Table 55: Parameters of water

	Water H_2O
$\rho \; [Kg/m^3]$	997
$c_p \; [J/K \; mol]$	4187
$\beta \; [GPa]$	2.2
$\alpha \; [K^{-1}]$	153 10^{-6}
$T_1 \; [K]$	288.15
$P_1 \; [Pa]$	101325

The equations used are the same as in the previous case, considering a wire activation period of 5 minutes:

$$T_2 = T_1 + \frac{\frac{3 \, Q \, \Delta t}{\rho \, V_{structure}}}{c_p + \frac{\beta \, \alpha}{\rho}} \qquad (3.32)$$

$$0 = -\frac{1}{\beta}\Delta p + \alpha \Delta T \qquad (3.33)$$

With the temperature and pressure of the fluid after 5 minutes, the convection coefficient necessary to cool the temperature of the wires down below the activation limits of the shape memory effect is calculated. With this coefficient, the temperatures reached by the structure during cooling are estimated (using the same equations as described above).

3.2.6. Addition of sheaths

Another strategy, to cool the composite, could be the addition of sheaths between the NiTiNOL wires and the composite layers. Many prototypes produced in the laboratory contain sheaths that allow the wire not to be bound along the spiral and, therefore, allow to obtain a greater displacement when the wires are activated. In the model, the sheath cylinders are considered perfectly adherent to the wires and the characteristic parameters of this material are:

Table 56: Table of the characteristics of the sheaths

	PTFE
Thickness $[mm]$	0.3
c_p $[J/Kg\ K]$	1000
ρ $[Kg/m^3]$	2150
ε	0.895

The strategies and the calculation model of temperatures is the same as used in previous analyses: only a few terms of the equations change. The addition of the sheaths in the model increases the conduction resistance by about 27% compared to the total resistance. For this reason, two analyses were carried out. The first always considering the flow of thermal power divided into 50%-50% for the uncovered and for the covered wire. The second analysis was carried out decreasing the flow of thermal power passing through the covered part by 27%. An important hypothesis to consider is that the surface exposed to the outer environment of the sheath and the surface of the composite are at the same temperature. The new conductive resistance shall contain two contact resistances and the resistance due to the sheaths. It shall be calculated as follows:

$$R_{tot} = \frac{\ln\left(\frac{R_{est_{comp}}}{R_{int_{comp}}}\right)}{2\,\pi\,\lambda\,\dfrac{A_{hidden}}{2\,\pi\,\dfrac{d}{2}}} + \frac{R_{contact}}{A_{hidden}} + \frac{\ln\left(\frac{R_{est_G}}{R_{int_G}}\right)}{2\,\pi\,\lambda_G\,\dfrac{A_{hidden}}{2\,\pi\,\dfrac{d}{2}}} + \frac{R_{contact}}{\left(2\,\pi\,R_{est_G}\,0.01\right)20}\left[\frac{K}{W}\right] \qquad (3.34)$$

The terms with the indices G indicate the quantities that refer to the sheaths.

3.3. Results of the cooling analysis

As in the case of thermal analysis, also the cooling was studied on the 4 structures considered before:C_{28}, C_{12}, V_{12-4}, V_{12-6}. The characteristic parameters of the composite have been described above. Also in this case, we chose to show the results obtained considering one structure at a time. Before calculating temperatures, it is necessary to

see the results of the study on the losses, caused by the structure, and on the coefficient of convection.

3.3.1. Convection with hydrogen peroxide

In this case, a flow of hydrogen peroxide in the liquid state is considered. This allows to cool the structure during the flow of the fuel, while the wires are active. The conditions chosen in the entrance section of the structure are:

- $P_1 = 50 \,[atm] = 5.066 \,[MPa]$
- $T_1 = 15 \,[°C] = 288.15 \,[K]$
- $v_1 = 5 \,[m/s]$

At the exit of the structure, which is $500 \, mm$ long and has a diameter of $10 \, mm$, after the above calculations, the same parameters have become:

- $P_2 = 5.0465 \,[MPa]$
- $T_2 = 288.1541 \,[K]$
- $v_2 = v_1 = 5 \,[m/s]$

The following tables summarizes the losses and the basic parameters of the calculation of the convection coefficient.

Table 57: Summary table of pressure losses in the case of convection with hydrogen peroxide

Distributed losses	19487.658
Concentrated losses	24.607.658
Percentage of distributed losses	0.38%
Percentage of concentrated losses	0.49%

Table 58: Parameters related to the calculation of the convection coefficient in the case of hydrogen peroxide

$\dot{m} \,[Kg/s]$	0.5027
Re	62745.098
Pr	4.453082
Nu	287.91
$h \,[W/m^2 \, K]$	17274.568

The same analysis is performed by varying the parameters in the input section of the structure as shown in the table below.

	Minimo	Massimo
$v_1 \left[{}^m\!/_s \right]$	2	20
$p_1 \, [atm]$	20	80
$T_1 \, [°C]$	0	30

Figure 55: Parameter change in the input section

Considering the presence of 3 wires simultaneously activated with a voltage of about $10 \, V$ (about twice the voltage of a single wire in the previous thermal analysis), the conditions at the exit of the structure are recalculated.
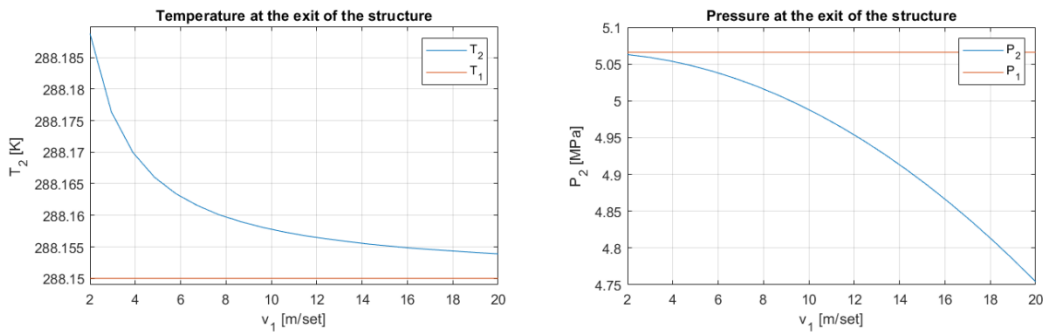
Figure 56: Output conditions by varying speed

The conditions at the exit do not significantly differ from the conditions at the entrance, because the structure is short and with a constant section. Even if the conditions at the entrance (pressure and temperature) vary, the conditions at the exit vary linearly with them. The biggest variation is in the pressure if the speed is increased too much. The convection coefficient and the pressure loss with respect to the speed change are recalculated. Losses are always small, almost negligible.

Table 59: Convection coefficient and pressure losses varying speeds

$v_1 \, [m/s]$	Re	$h \, [W/m^2 K]$	% Loss
2	25098	8299.6	0.0615
20	250980	52366.7	6.1548

3.3.2. Convection with methane and air

Applying the Fanno model to methane and air, there is no noticeable variation in physical parameters caused by friction alone. The Rayleigh model produced more significant results than the previous case, yet still negligible considering the small variations that are detected. However, this shows the greater importance of the addition of heat compared to the friction mechanism.

$$T_{T1_{CH4}} = 298.17 \, [K] \ \rightarrow \ T_{T2_{CH4}} = 298.6947 \, [K] \tag{3.35}$$

$$T_{T1_{air}} = 298.1998 \, [K] \; \rightarrow \; T_{T2_{air}} = 304.454 \, [K] \tag{3.36}$$

$$M_{1_{CH4}} \cong M_{2_{CH4}} \; (con \; M < 0.3) \tag{3.37}$$

$$M_{1_{air}} \cong M_{2_{air}} \; (con \; M < 0.3) \tag{3.38}$$

$$P_{T_1} \cong P_{T_2} \; \rightarrow \; P_1 \cong P_2 \tag{3.39}$$

$$T_{T_1} \cong T_{T_2} \; \rightarrow \; T_1 \cong T_2 \tag{3.40}$$

Specifically, the most noticeable variations are obtained considering the air. To have the same mass flow, the velocity at the exit of the structure and the density in the case of air are:

$$v_2 = 10.21 \, [m/s] \tag{3.41}$$

$$\rho_2 = 1.15 \, [Kg/m^3] \tag{3.42}$$

The speed is increased by 2.14% in the case of air. As for methane, the change of speed and density is negligible. For the calculation of the convection coefficient, the velocity and density for both substances are considered constant and equal to those at the entrance (because the variations are negligible). Also in this case, the same analysis was carried out by varying the input speed from $2 \, m/s$ to $20 \, m/s$. In all cases the differences are negligible and the Mach number remains below the value 0.3.

$v \, [m/s]$	$M_{1\,CH4}$	$M_{1\,aria}$	Re_{CH4}	Re_{aria}	$h_{CH4} \left[\frac{W}{m^2 K}\right]$	$h_{aria} \left[\frac{W}{m^2 K}\right]$
2	0,0044	0,0058	10924	1308	116	12
2,95	0,0065	0,0085	16099	1928	158	24
3,89	0,0086	0,0113	21274	2547	198	30
4,84	0,011	0,014	26449	3167	235	36
5,79	0,013	0,017	31623	3788	272	41
6,74	0,015	0,019	36798	4406	307	47
7,68	0,017	0,022	41973	5026	341	52
8,63	0,019	0,025	47148	5646	374	57
9,58	0,021	0,028	52322	6265	406	62
10,53	0,023	0,030	57497	6885	438	67
11,47	0,025	0,033	626712	7505	470	71
12,42	0,028	0,036	67847	8124	500	76
13,37	0,030	0,039	73021	8744	531	81
14,32	0,032	0,041	78196	9364	560	85
15,26	0,034	0,044	83371	9983	590	90
16,21	0,036	0,046	88546	10603	619	91
17,16	0,038	0,050	93720	11222	648	95
18,11	0,040	0,052	98895	11842	676	100
19,05	0,042	0,055	104070	12462	704	104
20	0,044	0,058	109245	13081	732	108

Figure 57: Variation of the convection coefficient by varying the entry velocity in the structure

Once the convection coefficient is obtained, the analysis focuses on obtaining the temperatures reached by the wire during activation, considering the presence of this cooling mechanism. The reference conditions for this thermal analysis (in which T_m is the average temperature along the structure) are:

Table 60: Parameters for the thermal analysis

	$h\ [W/m^2K]$	$v\ [m/s]$	$P\ [atm]$	$T_m\ [°C]$	$\dot{m}\ [Kg/s]$	Re
$H_2O_2\ (l)$	17275	5	50	15	0.5027	62745
$CH_4\ (g)$	241.5824	5	10	25	0.0026	27311
$Air\ (g)$	61.9547	10	1	28.152	0.00092981	6540.7

Due to the large number of graphs, only those in the case C_{28} are given as an example, while in the other cases they are shown in the appendix D.

3.3.3. 4 Carbon layers 0.28 mm thick

During the analysis, the activation temperature of NiTiNOL wires of 90 ℃ and the presence of only one wire are considered. The convection coefficient which has just been calculated and the voltage obtained from the thermal analysis are benchmarks. The Biot number confirmed the possibility of using the Lumped parameter approach also in this case. The temperatures reached during cooling are:

Table 61:Calculation of temperatures in the stationary case with Matlab

	$h[W/m^2K]$	$V[V]$	$v[m/s]$	$T_m[°C]$	$T_{wire}[°C]$	$T_{in}[°C]$	$T_{out}[°C]$	$t_{wire}[s]$	$t_{out}[s]$
$H_2O_2\ (l)$	17275	5.4278	5	15	15.3553	61.1153	15.0759	<0.1	<0.22
$CH_4\ (g)$	241.5824	5.4278	5	25	50.4063	76.4638	30.4244	<5	<16
$Air\ (g)$	61.9547	5.4278	10	28.152	127.2197	95.3429	49.3034	<20	<60
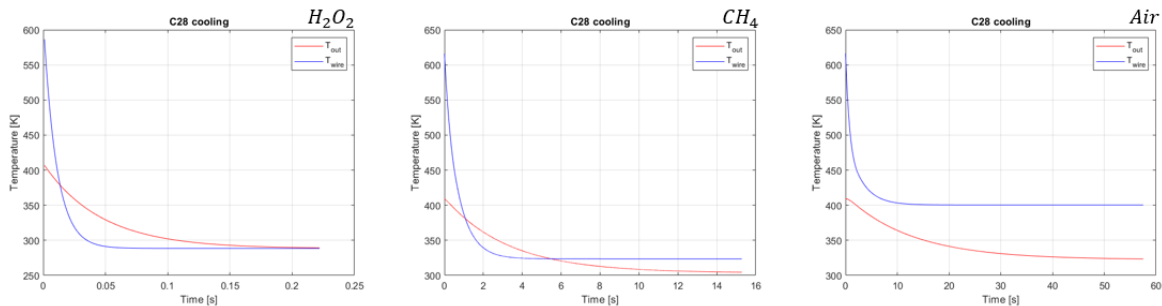
Figure 58: Transient of simulations with Matlab

Temperatures have fallen so much, in a very short time. The temperature reached by the structure during cooling depends on the activation voltage of the wires and the convection coefficient (which varies if the speed in the structure is changed). Two

studies were carried out: one by varying the activation voltage of the wires while maintaining the convection coefficient constant, the other by varying the convection coefficient while maintaining the supply voltage constant. The results are shown below.
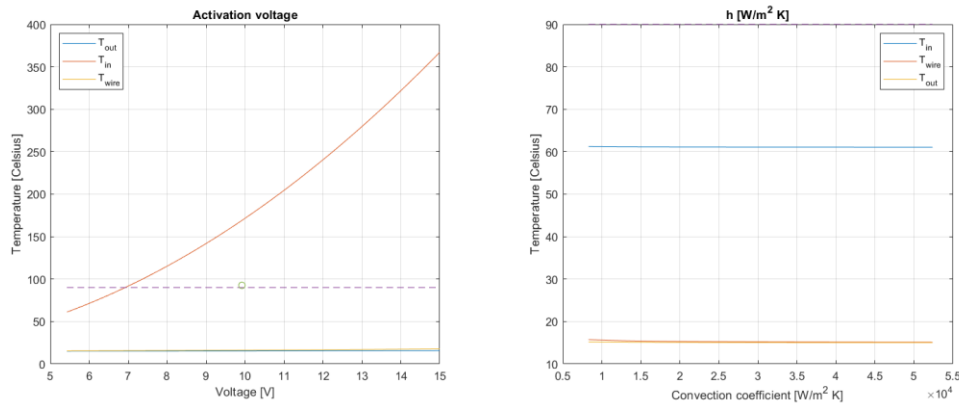
Figure 59: Temperature variation with voltage and convection coefficient using hydrogen peroxide

It is necessary to choose a temperature limit value that can indicate whether or not the wire exceeds the activation temperature. Since in the analysis with Matlab the temperature is considered concentrated and not distributed, the average temperature between the one of the uncovered wires and that of the wire covered by the composite is chosen as the threshold value ($T_{average}$). The voltage graph shows that the average temperature exceeds the activation temperature in the case of:

Table 62: Voltage needed to activate the wire using hydrogen peroxide

H_2O_2	$Voltage$ [V]	T_{wire} [°C]	T_{in} [°C]	T_2 [K]
$T_{average} > 90$ [°C]	9.9209	16.1870	169.0626	288.1660

Again, the temperature change at the exit of the structure is negligible. By varying the coefficient of convection in the range obtained from the previous analysis (varying the speed from 2 m/s to 20 m/s), the wire is never activated. So, the use of a fluid in turbulent motion brings down temperatures. This abrupt decrease in temperatures can be an advantage, once known the problems of thermal control of shape memory alloys, but also an issue, because the properties of NiTiNOL are completely cancelled. The same calculation was made considering methane and air. Two situations were distinguished, one in which $T_{average}$ was considered and the other in which both temperatures, both of the covered and uncovered wires, were above the activation threshold (T_{single}).
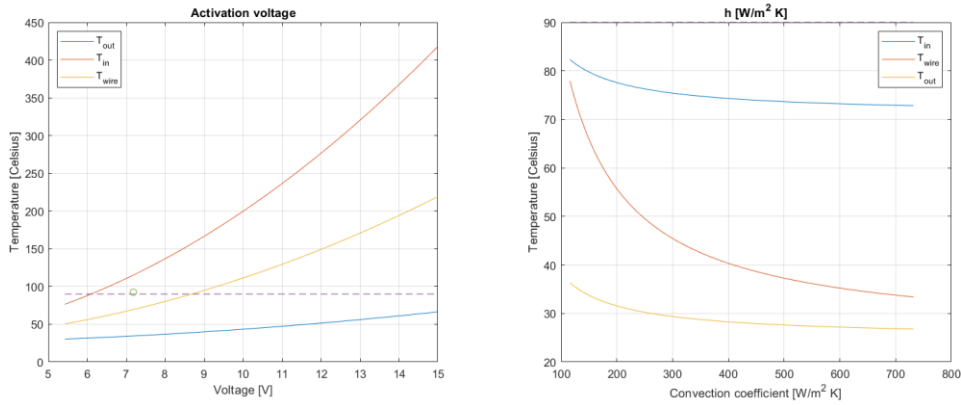
Figure 60: Temperature variation with voltage and convection coefficient using Methane

Also in this case, for any value of the convection coefficient, there is a cooling that does not allow the activation of the wire.

Table 63: Voltage needed to activate the wire using methane

CH_4	Voltage [V]	T_{wire} [°C]	T_{in} [°C]	T_2 [K]	v_2 [m/s]	ρ_2 [Kg/m³]
$T_{average} > 90$ [°C]	7.1860	69.5311	115.2036	300.2972	5.0360	6.5078
$T_{single} > 90$ [°C]	8.7488	91.0066	158.7051	301.3328	5.0534	6.4855

The voltage is lower than with H_2O_2. Considering the convection with air:
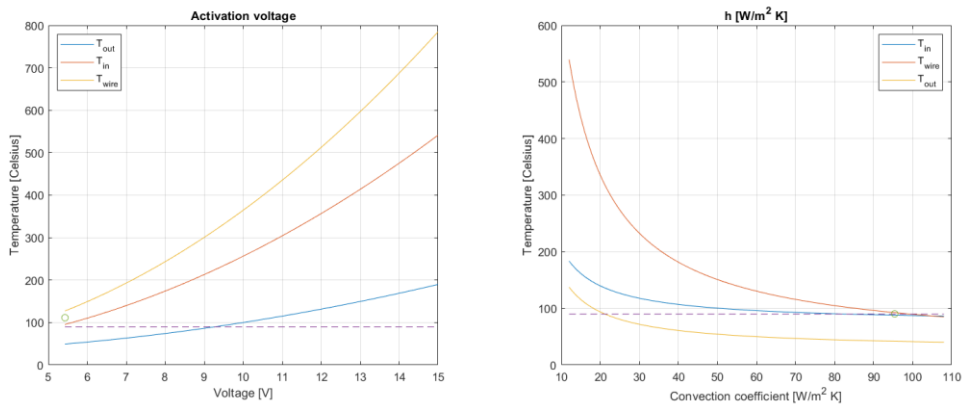
Figure 61: Temperature variation with voltage and convection coefficient using Air

In this case, we always have the two situations considered before, but also a limit value of the convection coefficient beyond which temperatures ($T_{average}$) drop below the activation threshold of the wire.

Table 64: Voltage needed to activate the wire using air

Air	Voltage [V]	T_{wire} [°C]	T_{in} [°C]	T_2 [K]	v_2 [m/s]	ρ_2 [Kg/m³]	T_m [°C]
$T_{average} > 90$ [°C]	5.4278	127.2197	95.3429	305.5785	10.2492	1.1551	28.71
$T_{single} > 90$ [°C]	5.4278	127.2197	95.3429	305.5785	10.2492	1.1551	28.71

In this case, the reference voltage obtained from the thermal analysis is sufficient to activate the wires and to have a good cooling as well. Considering the hydrogen peroxide and methane, the voltage must grow so much to be able to activate the NiTiNOL wires (in the case of H_2O_2 the voltage is almost double of the optimal voltage of the thermal analysis). The parameters in the output section of the structure have grown, albeit slightly. Moreover, there is a limit convection coefficient beyond which the wires are cooled until deactivation. This limit coefficient (between 90 and 100) can be obtained by always considering the same temperature input to the system (in order to have about the same average temperature), but bringing the speed in the range between 15.26 m/s and 18.11 m/s. Abaqus models were created as an alternative to simulations with Matlab. The results are shown below.
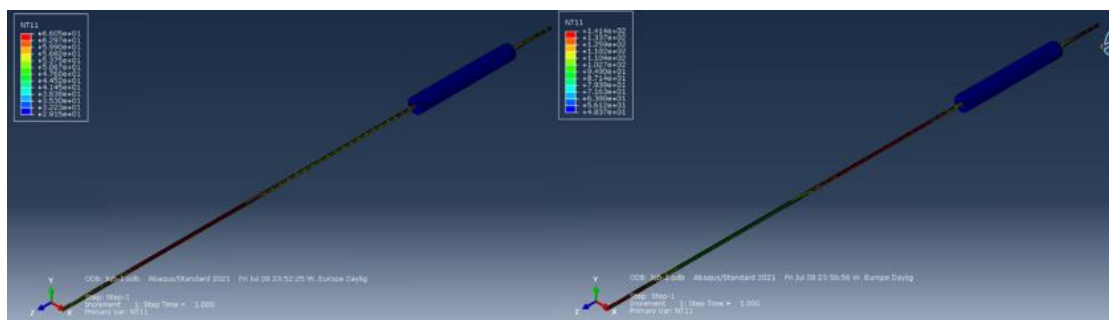
Figure 62: Simulation of cooling with methane (left) and air (right)

Table 65: Temperatures from simulation with Abaqus

C_{28}	h $[W/m^2K]$	$Voltage$ $[V]$	T_{out} [°C]	T_{in} [°C]	T_{wire} [°C]
H_2O_2 (l)	17275	5.4278	15.0329	49.4372	15.4264
CH_4 (g)	241.5824	5.4278	29.1535	65.9342	55.5618
Air (g)	61.9547	5.4278	48.3707	87.6329	141.426

The large cooling capacities of liquids have led to the consideration of a liquid such as water that by free convection cools the considered wire. This system, being static, does not need the use of a fluid flowing in the structure. For this reason, the heating of the liquid depends on the time in which the wire is kept active. For the analysis, the duration of activation of the wire was considered to be 5 minutes (chosen because from thermal analysis and experimental tests, it was noted that the activation lasts a few seconds). Different coefficients of convection have been considered to see which allows to deactivate the wire. The conditions of the liquid after activation and the optimal convection coefficient are shown below.
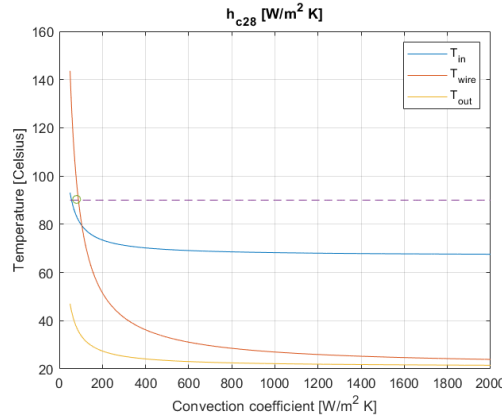
Figure 63: Cooling through free water convection

Table 66: Condition of the liquid after 5 minutes and optimum convection coefficient

$Voltage$ [V]	T_2 [K]	P_2 [MPa]	h [W/m^2K]
5.4278	299.9056	4.0582	80.2401

The temperature increased by about 10 degrees, while the pressure increased more. The system with voltage $V = 5.4278\ V$ is considered deactivated with a convection coefficient of $h = 80.2401\ W/m^2K$. The same analysis of the transient, done with the voltage obtained from the thermal analysis, is carried out considering the higher voltage in the case of $T_{average} > 90\ ℃$. The times of the transient are tabulated below. All transient graphs with Matlab and Abaqus are shown in appendix D.

Table 67: Transient duration with Abaqus and Matlab

						Abaqus		Matlab	
	h [W/m^2K]	V [V]	T_m[K]	$T_{i_{out}}$[℃]	$T_{i_{wire}}$[℃]	t_{wire}[s]	t_{out}[s]	t_{wire}[s]	t_{out}[s]
H_2O_2 (l)	17275	9.9209	288.15	136.3367	343.2186	<0.5	<1	<0.1	<0.22
CH_4 (g)	241.5824	7.1860	299.2236	136.3367	343.2186	<10	<35	<5	<16
Air (g)	61.9547	5.4278	301.86	136.3367	343.2186	<35	<120	<20	<60
H_2O (l)	80.2401	5.4278	294.0278	136.3367	343.2186	<35	<80	<15	<45

The times are saved with inequalities because it is not possible to trace the exact times through the graphs (especially if the graphs used are obtained with Abaqus). So even increasing the voltage, the cooling times with these 4 mechanisms are extremely short. Matlab tends to underestimate the cooling time, but with both software the time is very short. The longest cooling time is about 2 minutes.

3.3.4. 4 Carbon layers 0.12 mm thick

The temperatures reached during cooling are:

Table 68: Calculation of temperatures in the stationary case with Matlab

	$h[W/m^2K]$	$T[V]$	$v[m/s]$	$T_m[°C]$	$T_{wire}[°C]$	$T_{in}[°C]$	$T_{out}[°C]$	$t_{wire}[s]$	$t_{out}[s]$
$H_2O_2\ (l)$	17275	4.9938	5	15	15.3007	54.0980	15.1287	<0.08	<0.12
$CH_4\ (g)$	241.5824	4.9938	5	25	46.5058	73.1714	34.2021	<5	<9
$Air\ (g)$	61.9547	4.9938	10	28.152	112.0104	103.0032	64.0339	<20	<35

Temperatures and times are slightly higher than in the C_{28} case. Considering the hydrogen peroxide, the voltage graph (in appendix D) shows that the average temperature exceeds the activation temperature in the case of:

Table 69: Voltage needed to activate the wire using hydrogen peroxide

H_2O_2	$Voltage\ [V]$	$T_{wire}\ [°C]$	$T_{in}\ [°C]$	$T_2\ [K]$
$T_{average} > 90\ [°C]$	9.8948	16.1807	168.4991	288.1659

The required voltage is lower than that of C_{28}. Again, the temperature change at the exit of the structure is negligible. By varying the coefficient of convection in the range obtained from the previous analysis, the wire is never activated. The same calculation was made considering methane and air. Also with methane, for any value of the convection coefficient, the cooling does not allow the activation of the wire.

Table 70: Voltage needed to activate the wire using methane

CH_4	$Voltage\ [V]$	$T_{wire}\ [°C]$	$T_{in}\ [°C]$	$T_2\ [K]$	$v_2\ [m/s]$	$\rho_2\ [Kg/m^3]$
$T_{average} > 90\ [°C]$	6.8317	65.2483	115.1531	300.0907	5.0325	6.5123
$T_{single} > 90\ [°C]$	8.8738	92.9060	177.1043	301.4244	5.0549	6.4835

Considering the convection with air:

Table 71: Voltage needed to activate the wire using air

Air	$Voltage\ [V]$	$T_{wire}\ [°C]$	$T_{in}\ [°C]$	$T_2\ [K]$	$v_2\ [m/s]$	$\rho_2\ [Kg/m^3]$	$T_m\ [°C]$
$T_{average} > 90\ [°C]$	4.9938	112.0104	103.0032	304.438	10.21	1.1594	28.152
$T_{single} > 90\ [°C]$	4.9938	112.0104	103.0032	304.438	10.21	1.1594	28.152

The conditions at the exit are similar to those at the entrance. The voltage required for the activation of the wires with methane is slightly higher than $5\ V$, while with the air the nominal one is sufficient. There is a limit convection coefficient beyond which the wires are cooled until deactivation. This limit coefficient (between 80 and 90) can be obtained by always considering the same temperature input to the system (in order to have about the same average temperature), but bringing the speed in the range

between 13 m/s and 16 m/s. Abaqus models were created as an alternative to simulations with Matlab.

Table 72: Temperatures from simulation with Abaqus

C_{12}	h [W/m^2K]	$Voltage$ [V]	T_{out} [°C]	T_{in} [°C]	T_{wire} [°C]
H_2O_2 (l)	17275	4.9938	15.0489	44.4899	15.3609
CH_4 (g)	241.5824	4.9938	31.8633	63.3291	50.8758
Air (g)	61.9547	4.9938	60.6891	93.8407	125.518

The results are very similar to those obtained from the analysis with Matlab. As described above, free convection with water has also been considered. In this case, the optimal convection coefficient is:

Table 73: Condition of the liquid after 5 minutes and optimum convection coefficient

$Voltage$ [V]	T_2 [K]	P_2 [MPa]	h [W/m^2K]
4.9938	298.1008	3.45	72.4362

The system with voltage $V = 4.9938 \, V$ is considered deactivated with a convection coefficient of $h = 72.4362 \, W/m^2K$. The same analysis of the transient, done with the voltage obtained from the thermal analysis, is carried out considering the higher voltage in the case of $T_{average} > 90$ °C. The times of the transient are tabulated below. The graphs are given in appendix D.

Table 74: Transient duration with Abaqus and Matlab

						Abaqus		Matlab	
	h [W/m^2K]	V [V]	$T_m[K]$	$T_{i_{out}}$[°C]	$T_{i_{wire}}$[°C]	$t_{wire}[s]$	$t_{out}[s]$	$t_{wire}[s]$	$t_{out}[s]$
H_2O_2 (l)	17275	9.8948	288.158	194.1801	318.0633	<0.20	<0.5	<0.08	<0.12
CH_4 (g)	241.5824	6.8317	299.1204	194.1801	318.0633	<5	<5	<5	<9
Air (g)	61.9547	4.9938	301.302	194.1801	318.0633	<20	<20	<20	<35
H_2O (l)	72.4362	4.9938	293.1254	194.1801	318.0633	<20	<10	<15	<30

3.3.5. 4 Glass layers 0.12 mm thick

With air, methane and water, the Lumper parameter approach was used and it was confirmed by the Biot number. As for hydrogen peroxide, the Lumped parameter approach was used in continuity to the previously used calculation scheme, even though the Biot number is at the limit. Possible model errors greater than 5% are then accepted. The temperatures reached during cooling are:

Table 75: Calculation of temperatures in the stationary case with Matlab

	$h[W/m^2 K]$	$T[V]$	$v[m/s]$	$T_m[°C]$	$T_{wire}[°C]$	$T_{in}[°C]$	$T_{out}[°C]$	$t_{wire}[s]$	$t_{out}[s]$
H_2O_2 (l)	17275	4.9938	5	15	15.3007	54.7905	15.1287	<0.08	<0.16
CH_4 (g)	241.5824	4.9938	5	25	46.5058	73.8639	34.2021	<5	<12
Air (g)	61.9547	4.9938	10	28.152	112.0104	103.6957	64.0339	<20	<40

Considering hydrogen peroxide, the voltage graph (in appendix D) shows that the average temperature exceeds the activation temperature in the case of:

Table 76: Voltage needed to activate the wire using hydrogen peroxide

H_2O_2	Voltage [V]	T_{wire} [°C]	T_{in} [°C]	T_2 [K]
$T_{average} > 90$ [°C]	9.6906	16.1325	164.8364	288.1652

The required voltage is lower than cases C_{28} and C_{12}. This is due to the insulating properties of the glass fibers that allow not to disperse the heat produced by Joule effect. Again, the temperature change at the exit of the structure is negligible. By varying the coefficient of convection in the range obtained from the previous, the wire is never activated. The same calculation was made considering methane and air. Also with methane, for any value of the convection coefficient, the cooling does not allow the activation of the wire.

Table 77: Voltage needed to activate the wire using methane

CH_4	Voltage [V]	T_{wire} [°C]	T_{in} [°C]	T_2 [K]	v_2 [m/s]	ρ_2 [Kg/m³]
$T_{average} > 90$ [°C]	6.8317	65.2483	116.4492	300.0907	5.0325	6.5123
$T_{single} > 90$ [°C]	8.8738	92.9060	179.2910	301.4244	5.0549	6.4835

Considering the convection with air:

Table 78: Voltage needed to activate the wire using air

Air	Voltage [V]	T_{wire} [°C]	T_{in} [°C]	T_2 [K]	v_2 [m/s]	ρ_2 [Kg/m³]	T_m [°C]
$T_{average} > 90$ [°C]	4.9938	112.0104	103.6957	304.438	10.2109	1.1594	28.144
$T_{single} > 90$ [°C]	4.9938	112.0104	103.6957	304.438	10.2109	1.1594	28.144

With methane, the voltages are similar to those of case C_{12}. There is a limit convection coefficient for air beyond which the wires are cooled until deactivation. This limit coefficient (between 85 and 90) can be obtained by always considering the same temperature input to the system but bringing the speed in the range between 13 m/s

and 16 m/s. Abaqus models were created as an alternative to simulations with Matlab.

Table 79: Temperatures from simulation with Abaqus

C_{12}	h $[W/m^2K]$	$Voltage$ $[V]$	T_{out} $[°C]$	T_{in} $[°C]$	T_{wire} $[°C]$
H_2O_2 (l)	17275	4.9938	15.007	44.929	15.3609
CH_4 (g)	241.5824	4.9938	30.7406	64.1314	50.8766
Air (g)	61.9547	4.9938	60.6701	94.0021	125.482

Results with Matlab and Abaqus are very similar. Again, free convection with water has been considered. The optimal convection coefficient is:

Table 80: Condition of the liquid after 5 minutes and optimum convection coefficient

$Voltage$ $[V]$	T_2 $[K]$	P_2 $[MPa]$	h $[W/m^2K]$
4.9938	298.1008	3.45	73.4117

The system with voltage $V = 4.9938\ V$ is considered deactivated with a convection coefficient of $h = 73.4117\ W/m^2K$. The same analysis of the transient, done with the voltage obtained from the thermal analysis, is carried out considering the higher voltage in the case of $T_{average} > 90\ ℃$. The times of the transient are tabulated below. The graphs are shown in appendix D.

Table 81: Transient duration with Abaqus and Matlab

						Abaqus		Matlab	
	h $[W/m^2K]$	V $[V]$	$T_m[K]$	$T_{i_{out}}[°C]$	$T_{i_{wire}}[°C]$	$t_{wire}[s]$	$t_{out}[s]$	$t_{wire}[s]$	$t_{out}[s]$
H_2O_2 (l)	17275	9.6906	288.1576	192.2112	318.0633	<0.20	<0.20	<0.08	<0.16
CH_4 (g)	241.5824	6.8317	299.1204	192.2112	318.0633	<5	<2.5	<5	<12
Air (g)	61.9547	4.9938	301.294	192.2112	318.0633	<20	<20	<20	<40
H_2O (l)	73.4117	4.9938	293.1254	192.2112	318.0633	<20	<7	<15	<35

3.3.6.   6 Glass layers 0.12 mm thick

The convection coefficient just calculated and the voltage obtained from the thermal analysis are benchmarks. For hydrogen peroxide, the Lumped parameter approach was used in continuity to the previously used calculation scheme, even though the Biot number is at the limit. Possible model errors greater than 5% are then accepted. The temperatures reached during cooling are:

Table 82: Calculation of temperatures in the stationary case with Matlab

	$h[W/m^2K]$	$T[V]$	$v[m/s]$	$T_m[°C]$	$T_{wire}[°C]$	$T_{in}[°C]$	$T_{out}[°C]$	$t_{wire}[s]$	$t_{out}[s]$
H_2O_2 (l)	17275	5.1805	5	15	15.3237	57.9690	15.1011	<0.1	<0.23
CH_4 (g)	241.5824	5.1805	5	25	48.1439	75.0980	32.2301	<5	<15
Air (g)	61.9547	5.1805	10	28.152	118.3980	99.2124	56.3445	<30	<55

The temperatures are intermediate compared to those of the case C_{28} and those of the cases V_{12-4} and C_{12}. The temperature reached by the structure during cooling depends on the activation voltage of the wires and the convection coefficient (which varies if the speed in the structure is changed). Considering hydrogen peroxide, the voltage graph (in the appendix D) shows that the average temperature exceeds the activation temperature in the case of:

Table 83: Voltage needed to activate the wire using hydrogen peroxide

H_2O_2	$Voltage$ [V]	T_{wire} [°C]	T_{in} [°C]	T_2 [K]
$T_{average} > 90$ [°C]	9.7897	16.1558	168.4429	288.1655

By varying the coefficient of convection in the range obtained from the previous analysis, the wire is never activated. The same calculation was made considering methane and air. Also with methane, for any value of the convection coefficient, the cooling does not allow the activation of the wire.

Table 84: Voltage needed to activate the wire using methane

CH_4	$Voltage$ [V]	T_{wire} [°C]	T_{in} [°C]	T_2 [K]	v_2 [m/s]	ρ_2 [Kg/m³]
$T_{average} > 90$ [°C]	6.9841	67.0641	116.0533	300.1783	5.0340	6.5104
$T_{single} > 90$ [°C]	8.7877	91.5948	169.1530	301.3611	5.0539	6.4848

Considering the convection with air:

Table 85: Voltage needed to activate the wire using air

Air	$Voltage$ [V]	T_{wire} [°C]	T_{in} [°C]	T_2 [K]	v_2 [m/s]	ρ_2 [Kg/m³]	T_m [°C]
$T_{average} > 90$ [°C]	5.1805	118.3980	99.2124	304.917	10.2270	1.1576	28.3835
$T_{single} > 90$ [°C]	5.1805	118.3980	99.2124	304.917	10.2270	1.1576	28.3835

There is a limit convection coefficient beyond which the wires are cooled until deactivation. This limit coefficient (between 90 and 95) can be obtained by always considering the same temperature input to the system (in order to have about the same

average temperature), but bringing the speed in the range between 16.21 m/s and 17.16 m/s. Abaqus models were created as an alternative to simulations with Matlab.

Table 86: Temperatures from simulation with Abaqus

V_{12}	h [W/m^2K]	$Voltage$ [V]	T_{out} [°C]	T_{in} [°C]	T_{wire} [°C]
H_2O_2 (l)	17275	5.1805	15.0051	46.8188	15.3884
CH_4 (g)	241.5824	5.1805	29.5571	64.7802	52.836
Air (g)	61.9547	5.1805	54.3639	90.3053	132.179

As described above, free convection with water was also considered. In this case, the optimal convection coefficient is:

Table 87: Condition of the liquid after 5 minutes and optimum convection coefficient

$Voltage$ [V]	T_2 [K]	P_2 [MPa]	h [W/m^2K]
5.1805	298.8588	3.7059	75.3627

The system with voltage $V = 5.1805\ V$ is considered deactivated with a convection coefficient of $h = 75.3627\ W/m^2K$. The same analysis of the transient, done with the voltage obtained from the thermal analysis, is carried out considering the higher voltage in the case of $T_{average} > 90$ ℃. The times of the transient are tabulated below. The graphs are shown in appendix D.

Table 88: Transient duration with Abaqus and Matlab

						Abaqus		Matlab	
	h [W/m^2K]	V [V]	T_m[K]	$T_{i_{out}}$[°C]	$T_{i_{wire}}$[°C]	t_{wire}[s]	t_{out}[s]	t_{wire}[s]	t_{out}[s]
H_2O_2 (l)	17275	9.7897	288.1578	164.9815	329.0135	<0.20	<1	<0.1	<0.25
CH_4 (g)	241.5824	6.9841	299.1642	164.9815	329.0135	<10	<35	<5	<15
Air (g)	61.9547	5.1805	301.5335	164.9815	329.0135	<35	<80	<30	<55
H_2O (l)	75.3627	5.1805	293.5044	164.9815	329.0135	<20	<80	<20	<50

Cooling times are very short, even with the wire activated with the maximum voltage. In all analyses, the difference between the various structures in terms of temperature is minimal. The activation voltage varies by a few degrees. In cases where air is considered, the boundary convection coefficient varies in a range between 80 W/m^2K and 100 W/m^2K. The analysis shows that using liquids drastically lowers temperatures, but can be a problem from the point of view of control. Liquids can impair the activation of the wire and cause an excessive increase in the voltage necessary for the proper functioning of the structure. The use of gas in turbulent

motion allows optimal cooling and greater control. The air allows to use the voltage obtained from the thermal analysis and reduces the temperatures enough. The problem is a correct designing of the system that allows the air flow to cool the prototype. Considering the prototype as a system for refueling fuel, high pressure could represent another problem because only layers of MLI, an extremely flexible protection, give shape to the structure.

3.3.7. Cooling with sheaths

Another mechanism that allows to reduce the temperature of the composite part is represented by the use of sheaths inserted between the wires and the structure. PTFE cylinders are used and they are considered to be perfectly adherent to the wires in the analysis. The internal resistance of the structure is increased by 27%. Two situations are analyzed: one in which the flow of thermal power is divided into 50%-50% between the covered and the uncovered wire and the other in which the flow of thermal power that passes through the covered wire is reduced by 27% (similar to the electric current flowing in a branch of the circuit where the resistance is increased). Moreover, the use of sheaths was already foreseen in the work of the previous thesis [13], because they allow to bind the nitinol wires only at the ends of the spiral and, therefore, the wires are free to entirely contract increasing the movement of the prototype. Considering a 50%-50% division of thermal power flow, in the case C_{28}:

Table 89: Reduction of temperatures with sheaths in case 50%-50%

$V = 5.4278 \, [V]$	T_{out} [°C]	T_{in} [°C]	T_{wire} [°C]	$t_{activation}$ [s]
JR	182.8376 (-11.3%)	245.9308 (-2.48%)	368.0018	8.06 (-1.39%)
J	96.9815 (-28.87%)	160.0747 (-12.2%)	343.2186	9.4260 (-1.53%)
R	122.3383 (-0.61%)	122.3383 (-0.61%)	122.4121 (-0.55%)	68.3010

In the case of $0.12 - mm -$ thick carbon-fiber fabric:

Table 90: Reduction of temperatures with sheaths in case 50%-50%

$V = 4.9938 \, [V]$	T_{out} [°C]	T_{in} [°C]	T_{wire} [°C]	$t_{activation}$ [s]
JR	197.1112 (-19.7%)	250.5169 (-11.9%)	345.8631	9.372 (-1.1%)
J	122.6548 (-36.8%)	176.0605 (-24.5%)	318.0633	11.277 (-1.2%)
R	121.9261 (-0.95%)	121.9261 (-0.95%)	122.04 (-0.85%)	68.3010

In the case of $0.12 - mm -$ thick glass-fiber fabric with 4 plies:

Table 91: Reduction of temperatures with sheaths in case 50%-50%

$V = 4.9938 \, [V]$	T_{out} [°C]	T_{in} [°C]	T_{wire} [°C]	$t_{activation}$ [s]

JR	196.1549 **(-19.6%)**	249.8265 **(-11.9%)**	345.8631	9.376 **(-1.08%)**
J	121.0267 **(-37%)**	174.6984 **(-24.7%)**	318.0633	11.277 **(-1.2%)**
R	121.9452 **(-0.93%)**	121.9452 **(-0.93%)**	122.0578 **(-0.84%)**	68.3010

In the case of $0.12 - mm -$ thick glass-fiber fabric with 6 plies:

Table 92: Reduction of temperatures with sheaths in case 50%-50%

$V = 5.1805\,[V]$	$T_{out}\,[°C]$	$T_{in}\,[°C]$	$T_{wire}\,[°C]$	$t_{activation}\,[s]$
JR	190.0897 **(-15.5%)**	247.9548 **(-7.38%)**	355.4467	8.778 **(-1.2%)**
J	110.3689 **(-33.1%)**	168.2340 **(-19.1%)**	329.0135	10.42 **(-1.33%)**
R	122.1377 **(-0.78%)**	122.1377 **(-0.78%)**	122.2316 **(-0.7%)**	68.3010

As confirmation of the results obtained, simulations were made with Abaqus in the 3 cases JR, J and R. The material considered C_{28}.

Table 93: Abaqus simulation of C_{28} structure with embedded sheaths

$V = 5.4278\,[V]$	$T_{out}\,[°C]$	$T_{in}\,[°C]$	$T_{wire}\,[°C]$
JR	156.851 **(-16.5%)**	221.182 **(-3.8%)**	370.077 **(-0.09%)**
J	111.77 **(-27%)**	176.723 **(-8.9%)**	339.712 **(-0.8%)**
R	68.0366 **(-3.5%)**	69.3495 **(-2.5%)**	94.2905 **(-0.44%)**

From the simulation, it is found that all the temperatures are lowered, except the temperature of the uncovered wire that remains almost unchanged. The biggest difference in temperature is the external temperature of the composite, in the case of activation with Joule effect, without radiations (case J). All materials show the same similar behaviors. Activation times are also reduced by little. Considering a 77%-23% division of thermal power flow, in the case of $0.28 - mm -$ thick carbon-fiber fabric:

Table 94: Reduction of temperatures with sheaths in case 77%-23%

$V = 5.4278\,[V]$	$T_{out}\,[°C]$	$T_{in}\,[°C]$	$T_{wire}\,[°C]$	$t_{activation}\,[s]$
JR	168.8446 **(-18.1%)**	214.9027 **(-14.8%)**	402.1413 **(+9.3%)**	6.7 **(-18%)**
J	68.9765 **(-49.4%)**	115.0346 **(-37%)**	381.1719 **(+11.1%)**	7.601 **(-20.6%)**
R	122.3383 **(-0.61%)**	122.3383 **(-0.61%)**	122.4121 **(-0.55%)**	68.3010

In the case of $0.12 - mm -$ thick carbon-fiber fabric:

Table 95: Reduction of temperatures with sheaths in case 77%-23%

$V = 4.9938\,[V]$	T_{out} [°C]	T_{in} [°C]	T_{wire} [°C]	$t_{activation}$ [s]
JR	180.3013 **(-26.6%)**	219.2875 **(-22.9%)**	378.0350 **(+9.3%)**	7.796 **(-17.7%)**
J	92.7073 **(-52.3%)**	131.6935 **(-43.5%)**	354.4676 **(+11.4%)**	9.047 **(-20.7%)**
R	121.9261 **(-0.95%)**	121.9261 **(-0.95%)**	122.04 **(-0.85%)**	68.3010

In the case of $0.12 - mm -$ thick glass-fiber fabric with 4 plies:

Table 96: Reduction of temperatures with sheaths in case 77%-23%

$V = 4.9938\,[V]$	T_{out} [°C]	T_{in} [°C]	T_{wire} [°C]	$t_{activation}$ [s]
JR	179.5265 **(-26.4%)**	218.7068 **(-22.9%)**	378.035 **(+9.3%)**	7.798 **(-17.7%)**
J	91.2025 **(-52.6%)**	130.3828 **(-43.8%)**	354.4676 **(+11.4%)**	9.047 **(-20.7%)**
R	121.9452 **(-0.93%)**	121.9452 **(-0.93%)**	122.0578 **(-0.84%)**	68.3010

In the case of $0.12 - mm -$ thick glass-fiber fabric with 6 plies:

Table 97: Reduction of temperatures with sheaths in case 77%-23%

$V = 5.1805\,[V]$	T_{out} [°C]	T_{in} [°C]	T_{wire} [°C]	$t_{activation}$ [s]
JR	174.6438 **(-22.3%)**	216.8853 **(-19%)**	388.4812 **(+9.29%)**	7.297 **(-17.9%)**
J	81.351 **(-50.7%)**	123.5925 **(-40.5%)**	366.0921 **(+11.3%)**	8.378 **(-20.7%)**
R	122.1377 **(-0.78%)**	122.1377 **(-0.78%)**	122.2316 **(-0.7%)**	68.3010

In this case, the temperature of the covered wire and the temperature of the composite decreased, more significantly than in the previous case. On the other hand, the temperature of the uncovered wire increased, although slightly. The timing of transients changed drastically, making the phenomenon even faster. It is always the case *J* that creates the greatest difference in temperatures compared to the case without sheaths (in particular, the biggest variation is that of the temperature of the composite). These results confirm the usefulness of the sheaths not only as an element that allows the wire to contract more and generate a greater displacement: in fact, sheaths are also recommended from a thermal point of view because they reduce temperatures. In the second case, in fact, the increase in the temperature of the uncovered wire is much smaller than the decrease in the temperature of the composite and the covered wire. Therefore, the advantages far exceed the disadvantages and, for this reason, it is convenient to use the sheaths.

4 Mechanical optimization

4.1. Strategies for structural optimization

Thermal analysis, for the cooling and heating of the structure, allowed to determine the thermal behavior of the prototype. This thesis aims to optimize the prototype not only from the thermal point of view, but also mechanically. For this reason, several geometric parameters have been modified to understand how they affect the structure. The modified geometric sizes are:

- <u>Pitch of the spiral structure</u>. Changing the pitch of the structure, its height changes as well. For this reason, the analysis of the pitch change was divided into two parts. In the first, the pitch and the number of revolutions of the structure are changed to keep the height of the prototype constant. In the second, it is accepted that the structure becomes longer, but the number of turns of the spiral is kept constant.
- <u>Diameter of the structure</u>
- <u>Width of the composite layers</u>

The geometrical characteristics of the structure (already studied and previously used) are maintained as reference quantities and are as follows:

- Nominal pitch: 25 *mm*
- Nominal diameter: 10 *mm*
- Nominal width: 10 *mm*

The analysis was performed using the Abaqus software. The creation of the laminate was carried out by the command "*composite layup*", setting the orientation of the fibers. The fibers were arranged at an angle of 45° with respect to the horizontal direction: this was because, during the creation of the prototypes in the laboratory, it was noticed that wrapping the strips of composite on the mold, the direction of the fibers was not that of the axis of the structure. The Abaqus model was then constrained (*U1=0, U2=0, U3=0*) to several points up to a height of 30 *mm* to simulate the locking of the structure during experiments. Ultimately, the forces were modeled with "*connector forces*" on "*wires*" (with two reference systems at the end) to which the property "*connection type: cylindrical*" was assigned. This allows the forces not only to be created in equal and opposite pairs in every area where the wire was present, but it also allows the forces to always point at each other throughout the movement of the structure.
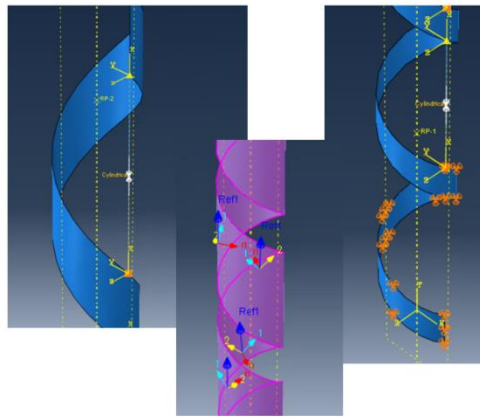
Figure 64: Structure model details with Abaqus

Then, from the simulations, the displacements (*U1*, *U2*, *U3*) were extrapolated on three points of the spiral at each step of the simulation: one at the free end (A), one at the center (B) and the last at the end of the constraint (C). Subsequently, the parameters on which the choice of the final configuration was based were:

- Curvature and radius of curvature of the structure with activated wire. The structure has a complex movement that never takes place on a single plane. This may be due to the lack of symmetry given by the spiral shape and inaccuracies during the production of the prototypes. For this reason, both the curvature on the *XY* plane and the curvature on the *ZY* plane were also recorded. The reference system is shown in the figure below (the three points from which the movements along the three main axes are extrapolated are also highlighted in red).
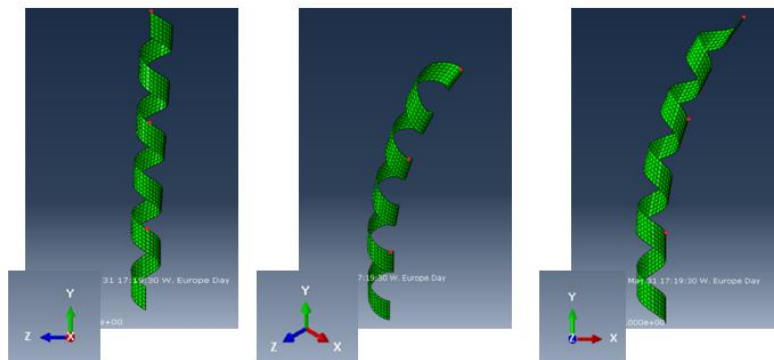
Figure 65: Reference system with highlighted XY and ZY planes

- Angle of curvature, again with curvature angle in *XY* plane and *ZY* plane
- Distance between the point on the free end (A) of the structure and the point on the constraint (C) of the structure. This parameter allows one to understand how much the structure is crushing on itself. Also, in this case, both the distance on the *XY* plane and the one on the *ZY* plane are recorded

A fourth parameter is also recorded, that is the difference, at each step of the simulation, between $U3$ of the free end of the structure (A) and $U3$ of the point located in the middle of the structure (B). This is because the movement of the structure is very complex and coupled with respect to all 3 axes. For this reason, it can happen that the free end, after a greater displacement than that of the central part, comes back. The analysis is carried out on C_{28}, C_{12}, V_{12-6} structures. The glass structure with $0.12 - mm -$ thick fiber-glass fabric with 4 plies was not considered because the structure crushed on itself not allowing any meaningful analysis. At each step of the simulation, displacements along the three main axes are recorded as shown in the example below.

c28 spessore 20							c12 spessore 20							v12 spessore 20						
Time	U1a	U2a	U3a	U1b	U2b	U3b	Time	U1a	U2a	U3a	U1b	U2b	U3b	Time	U1a	U2a	U3a	U1b	U2b	U3b
0.001	0.001676	-0.00046	-0.00015	0.000494	-0.00023	-3E-05	0.001	0.014623	-0.00439	-0.0007	0.004347	-0.00222	-6.7E-05	0.001	0.009469	-0.00287	-0.00042	0.002802	-0.00144	-4.6E-05
0.002	0.003353	-0.00092	-0.00031	0.000988	-0.00047	-6E-05	0.002	0.029247	-0.00879	-0.00139	0.008694	-0.00443	-0.00013	0.002	0.018937	-0.00574	-0.00084	0.005604	-0.00289	-9.2E-05
0.0035	0.005868	-0.00161	-0.00054	0.001728	-0.00081	-0.0001	0.0035	0.051181	-0.01539	-0.00243	0.015214	-0.00776	-0.00023	0.0035	0.03314	-0.01006	-0.00147	0.009807	-0.00505	-0.00016
0.00575	0.00964	-0.00265	-0.00088	0.002839	-0.00134	-0.00017	0.00575	0.084081	-0.0253	-0.00398	0.024994	-0.01275	-0.00039	0.00575	0.054443	-0.01653	-0.0024	0.016111	-0.00831	-0.00026
0.009125	0.015297	-0.00421	-0.0014	0.004506	-0.00212	-0.00027	0.009125	0.133427	-0.04019	-0.00629	0.039664	-0.02025	-0.00062	0.009125	0.086395	-0.02625	-0.0038	0.025567	-0.01318	-0.00042
0.014187	0.023784	-0.00655	-0.00218	0.007005	-0.0033	-0.00042	0.014187	0.20744	-0.06259	-0.00973	0.061666	-0.0315	-0.00096	0.014187	0.134319	-0.04085	-0.00588	0.03975	-0.02051	-0.00065
0.021781	0.036513	-0.01005	-0.00334	0.010755	-0.00507	-0.00065	0.021781	0.318445	-0.09632	-0.01481	0.094666	-0.04841	-0.00149	0.021781	0.206197	-0.06282	-0.00895	0.061022	-0.0315	-0.001
0.033172	0.055605	-0.01532	-0.00508	0.016378	-0.00772	-0.00099	0.033172	0.484919	-0.14724	-0.02226	0.144159	-0.07383	-0.0023	0.033172	0.313992	-0.0959	-0.01348	0.092924	-0.04802	-0.00152
0.050258	0.084239	-0.02323	-0.00769	0.024812	-0.0117	-0.0015	0.050258	0.734563	-0.22431	-0.03305	0.218384	-0.11211	-0.00354	0.050258	0.475638	-0.14581	-0.02007	0.140766	-0.07285	-0.00231
0.075887	0.127183	-0.03511	-0.01159	0.037461	-0.01767	-0.00227	0.075887	1.108779	-0.34148	-0.04845	0.329669	-0.16983	-0.0055	0.075887	0.718009	-0.22134	-0.0295	0.212506	-0.11023	-0.0035
0.11433	0.191583	-0.05297	-0.01742	0.05643	-0.02664	-0.00342	0.11433	1.669729	-0.52081	-0.06971	0.496529	-0.25711	-0.00862	0.11433	1.081262	-0.3361	-0.04268	0.320047	-0.16659	-0.00529
0.171995	0.288145	-0.07987	-0.0261	0.084871	-0.04011	-0.00514	0.171995	2.510194	-0.79783	-0.09763	0.746664	-0.38965	-0.01375	0.171995	1.625601	-0.51159	-0.06022	0.481242	-0.25178	-0.00801
0.258493	0.432902	-0.12044	-0.03898	0.127508	-0.06035	-0.00774	0.258493	3.768707	-1.23157	-0.13098	1.121594	-0.59211	-0.02246	0.258493	2.440779	-0.78235	-0.08169	0.722771	-0.38105	-0.01214
0.388239	0.649849	-0.18181	-0.05801	0.191407	-0.09081	-0.01165	0.388239	5.651268	-1.9236	-0.16308	1.68357	-0.90422	-0.03791	0.388239	3.660447	-1.20553	-0.10331	1.084521	-0.57833	-0.01852
0.582859	0.974848	-0.27502	-0.08588	0.287132	-0.1367	-0.01755	0.582859	8.462648	-3.05653	-0.17476	2.526255	-1.39196	-0.06666	0.582859	5.482559	-1.87888	-0.11305	1.626078	-0.88197	-0.02854
0.874788	1.461291	-0.41738	-0.12627	0.430425	-0.20599	-0.02648	0.777478	11.25732	-4.30605	-0.14761	3.369376	-1.90425	-0.10235	0.777478	7.294607	-2.59894	-0.09646	2.166392	-1.1951	-0.03898
1	1.669619	-0.4794	-0.14303	0.491792	-0.23589	-0.03034	0.972098	14.03274	-5.67547	-0.08656	4.213587	-2.44228	-0.14518	0.972098	9.097528	-3.36634	-0.0568	2.706197	-1.51795	-0.05049
							1	14.42889	-5.88182	-0.07529	4.334742	-2.5216	-0.15193	1	9.355737	-3.48067	-0.04857	2.783625	-1.5651	-0.05206

Figure 66: Data collection of point movements along the three main axes

The first part of the analysis consists of the decoupling between the XY plane and the ZY plane. Data is then divided into two groups.
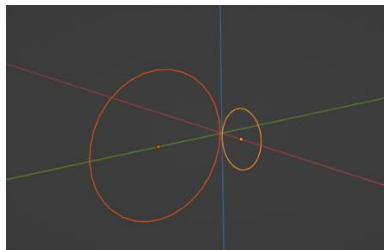
Figure 67: Two circumferences on two perpendicular planes

On each plane, there are 3 points that uniquely identify a circumference. At each step of the simulation, the parameters that identify the circumference are calculated through a linear system of 3 equations in 3 unknowns which is solved through the command "*fsolve*" of Matlab.

$$\begin{cases} x_A^2 + y_A^2 + \alpha\,x_A + \beta\,y_A + \gamma = 0 \\ x_B^2 + y_B^2 + \alpha\,x_B + \beta\,y_B + \gamma = 0 \\ x_C^2 + y_C^2 + \alpha\,x_C + \beta\,y_C + \gamma = 0 \end{cases} \longrightarrow \text{fsolve} \longrightarrow \alpha, \beta, \gamma$$

Figure 68: System of equations for the unique identification of the circumference

The obtained parameters are: the radius of curvature through the coefficients that identify the circumference, the curvature (i.e., the inverse of the radius of curvature), the angle of curvature through the long circumference arc as the part of the structure

that moves (*L* is the total height of the structure and *bc* the total height of the constraint) and the distance between the two extreme points *A* and *C*.

$$r = \sqrt{\frac{\alpha^2}{2} + \frac{\beta^2}{2} - \gamma} \, [mm]$$

$$\theta = \frac{(L - bc) \, 360}{2 \, \pi \, r} \, [Degree]$$

$$d = \sqrt{(x_C - x_A)^2 + (y_C - y_A)^2} \, [mm]$$

Figure 69: Parameters derived from the circumference in the plane

These calculations are made for both the *XY* and *ZY* planes. In the general case, that is, when the plane on which the points move is not generated by the three main axes, the calculations are much more complex because the structure does not move on a plane but has a complex movement instead. In this case, for each step of the simulation, the plane on which the 3 points lie is uniquely calculated.

$$\vec{v}_{BA} = \vec{B} - \vec{A}$$
$$\vec{v}_{CA} = \vec{C} - \vec{A}$$

$$a = \det\begin{pmatrix} y_{\vec{v}_{BA}} & z_{\vec{v}_{BA}} \\ y_{\vec{v}_{CA}} & z_{\vec{v}_{CA}} \end{pmatrix}$$

$$b = -\det\begin{pmatrix} x_{\vec{v}_{BA}} & z_{\vec{v}_{BA}} \\ x_{\vec{v}_{CA}} & z_{\vec{v}_{CA}} \end{pmatrix}$$

$$c = \det\begin{pmatrix} x_{\vec{v}_{BA}} & y_{\vec{v}_{BA}} \\ x_{\vec{v}_{CA}} & y_{\vec{v}_{CA}} \end{pmatrix}$$

$$d = -(a \, x_A) - (b \, y_A) - (c \, z_A)$$

$$\longrightarrow a \, x + b \, y + c \, z + d = 0$$

Figure 70: Search for the plane on which the three points lie in space
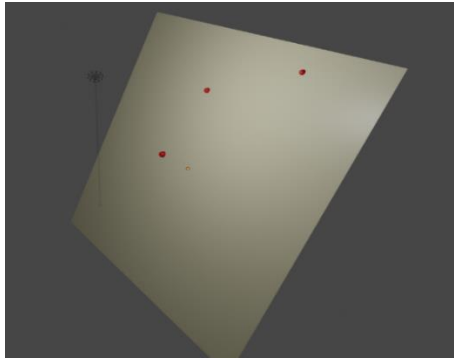
Figure 71: Identified plane of the 3 points of the spiral

The circumference in space is identified as the intersection of the newly calculated plane and the sphere on which the points lie. However, the 3 points are not enough to unambiguously define the sphere. So, one has to introduce another constraint to get a system of 4 equations in 4 unknowns. The chosen constraint equation is the one that connects the center of the sphere to the plane on which the 3 points lie. The system of equations is always solved through the algorithm "*fsolve*" and from the obtained

quantities, one can obtain: the curvature, the radius of curvature, the angle of curvature and the distance between the two extreme points.

$$\begin{cases} x_A^2 + y_A^2 + z_A^2 + \alpha\, x_A + \beta\, y_A + \gamma\, z_A + \delta = 0 \\ x_B^2 + y_B^2 + z_B^2 + \alpha\, x_B + \beta\, y_B + \gamma\, z_B + \delta = 0 \\ x_C^2 + y_C^2 + z_C^2 + \alpha\, x_C + \beta\, y_C + \gamma\, z_C + \delta = 0 \\ \left(-\dfrac{\alpha}{2}\, a\right) + \left(-\dfrac{\beta}{2}\, b\right) + \left(-\dfrac{\gamma}{2}\, c\right) + d = 0 \end{cases} \longrightarrow \text{fsolve} \longrightarrow \alpha, \beta, \gamma, \delta$$

Figure 72: Solution system for sphere identification in 3D

$$center = \begin{bmatrix} -\dfrac{\alpha}{2} \\ -\dfrac{\beta}{2} \\ -\dfrac{\gamma}{2} \end{bmatrix} \qquad r = \frac{1}{2}\sqrt{\alpha^2 + \beta^2 + \gamma^2 - 4\,\delta} \; [mm]$$

Figure 73: Calculation of the center and radius of the sphere

$$\theta = \frac{(L - bc)\,360}{2\,\pi\,r} \; [Degree] \qquad d = \sqrt{(x_C - x_A)^2 + (y_C - y_A)^2 + (z_C - z_A)^2} \; [mm]$$

Figure 74: Calculation of the angle of curvature and the distance between the extreme points of the structure
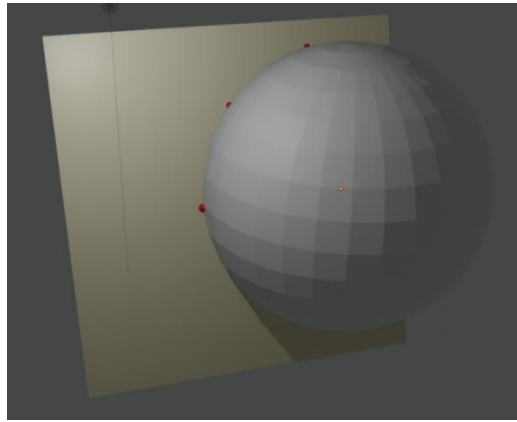
Figure 75: Image of plane and sphere intersected in 3D

For each pitch, diameter and width, we calculate the radius of curvature, the angle of curvature and the distance of the ends of the structure for each step of the simulation. An example is given below.
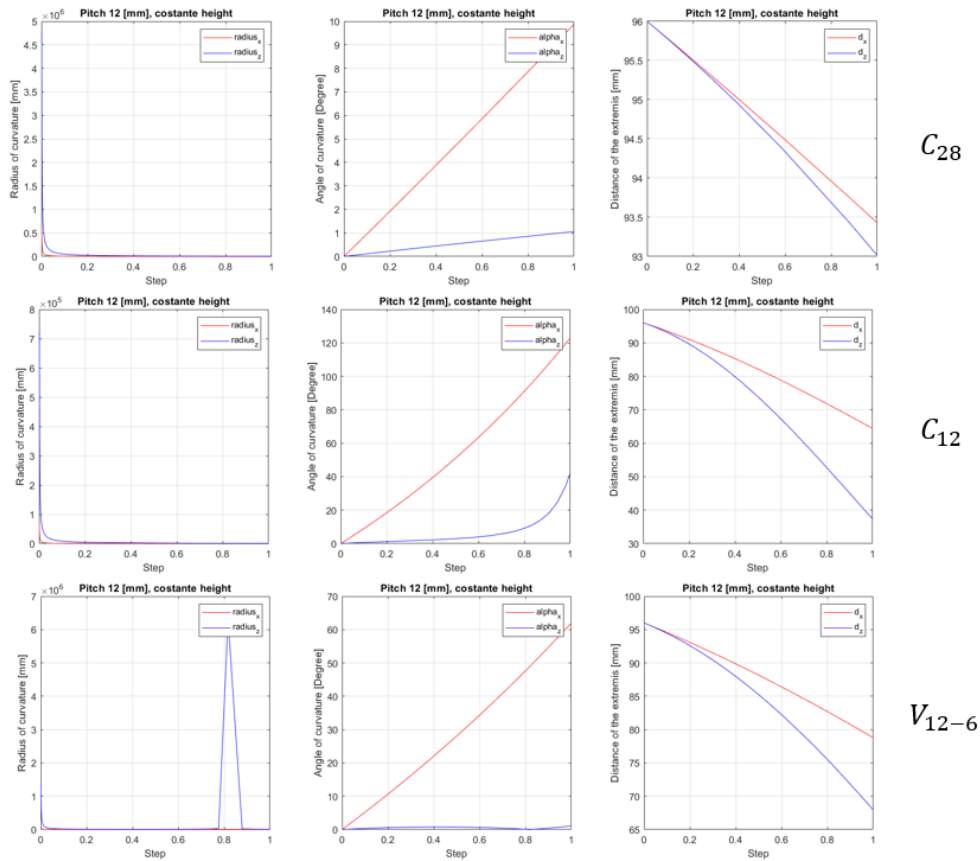
Figure 76: Example of calculation of the quantities for each step of the simulation in the case of pitch 12 mm and constant structure height

The torsion (difference between U3 of point A and point B) is also calculated for each structure at each simulation step. An example is given below.
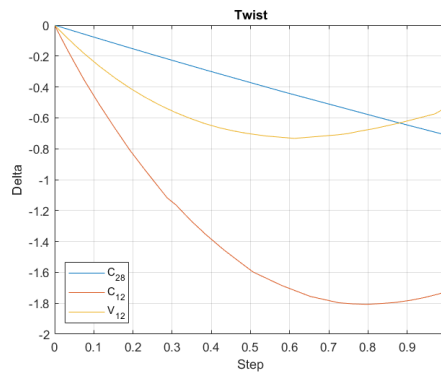
Figure 77: Torsion calculation example for each simulation pitch in the case of pitch 12 mm and constant structure height

All these graphs are not reported in the optimization analysis results as they do not have a physical relevance, because the simulation step does not refer to time (so the graphs are not transient phenomena) but only indicates the progress of the calculation towards the simulation solution.

4.2. Results of the optimization

The simulations with Abaqus are always local or on small models. Because of that, a reduced model, which is 130 mm high and has 5 turns of the spiral, was chosen for simulations. The height of the base constraint is 30 mm (as in the case of experiments). The first part of the optimization analysis concerns the change of pitch of the structure. As explained above, two cases are considered:

- Structure with a constant height (130 mm). For this reason, when the pitch varies, the number of turns of the spiral also changes.
- Constant number of revolutions (5 revolutions). In this case, it is accepted that the structure increases or decreases its height according to the analyzed pitch.

From a design point of view, a binding parameter could be the height of the prototype, for this reason keeping the height constant could be more relevant.

4.2.1. Terminology in the calculations

- "*Pitch*", is the pitch of the spiral, in [mm]
- "*# revolutions*", is the number of turns of the spiral
- "*Diameter*", is the diameter of the structure, in [mm]
- "*Width*", is the width of the composite fabric strips, in [mm]
- "*r*", is the radius of curvature, in [mm]
- "r_x", is the radius of curvature on the XY plane, in [mm]
- "r_y", is the radius of curvature on the ZY plane, in [mm]
- "Curvature", is the inverse of the radius of curvature
- "*Delta*", is calculated as:

$$Delta = \frac{1}{r} - \left(\frac{1}{r_x} + \frac{1}{r_z}\right) \tag{4.1}$$

- "$\%r_x$" and "$\%r_z$", are the percentages of r_x and r_z calculated as follows:

$$\%r_x = 100\left(\frac{\frac{1}{r_x}}{\frac{1}{r_x} + \frac{1}{r_z}}\right) \tag{4.2}$$

$$\%r_z = 100\left(\frac{\frac{1}{r_z}}{\frac{1}{r_x} + \frac{1}{r_z}}\right) \tag{4.3}$$

- "*alpha*", is the angle of curvature, in [$Degree$]
- "$alpha_x$", is the angle of curvature on the XY plane, in [$Degree$]
- "$alpha_y$", is the angle of curvature on the ZY plane, in [$Degree$]
- "*d*", is the distance between the ends of the spiral that has moved, in [mm]

- "d_x", is the distance between the ends of the spiral that has moved on the *XY* plane, in [*mm*]
- "d_y", is the distance between the ends of the spiral that has moved on the *ZY* plane, in [*mm*]
- "*Twist*", is the difference between U3 of point A and U3 of point B, in [*mm*]

4.2.2.   Constant height of the spiral

The colors used in the tables below identify the structure to which reference is made:

- Yellow, for a $0.28 - mm -$ thick carbon-fiber fabric structure with 4 plies
- Blue, for $0.12 - mm -$ thick carbon-fiber fabric structure with 4 plies
- Green, for $0.12 - mm -$ thick glass-fiber fabric structure with 6 plies

Whereas, orange identifies the reference structure (the one on the basis of which the prototypes were previously created). The images of the simulations of the different cases are shown in Appendix E.

Pitch [*mm*]	# revolutions	r [*mm*]	Curvature	Delta	r_x [*mm*]	r_z [*mm*]	% rx	% rz	Twist
12	10	553.87	0.00181	0.00018	556.8348723	5201.703894	90%	10%	-0.711702228
15	8	678.75	0.00147	0.00020	685.5573002	4740.695182	87%	13%	-0.673124224
17	7	747.26	0.00134	0.00020	757.172437	4573.534812	86%	14%	-0.641314328
20	6	832.74	0.00120	0.00020	846.893917	4506.593089	84%	16%	-0.894811302
22	6	884.55	0.00113	0.00020	901.8099398	4470.503221	83%	17%	-1.095083356
25	5	942.46	0.00106	0.00022	969.9902443	3938.038073	80%	20%	-1.048866391
27	5	963.41	0.00104	0.00024	996.828491	3703.780192	79%	21%	-1.314699292
30	4	957.36	0.00104	0.00025	996.9597576	3393.501266	77%	23%	-1.019386709
32	4	956.57	0.00105	0.00027	1003.797395	3115.914141	76%	24%	-1.269842267
35	4	925.43	0.00108	0.00031	982.6917656	2706.161728	73%	27%	-1.765117526
37	3	881.78	0.00113	0.00037	968.6284606	2113.644	69%	31%	-1.263257205
40	3	854.18	0.00117	0.00041	956.8633049	1876.884455	66%	34%	-1.697242379

Figure 78: Calculation of curvature, radius of curvature and twist in case C_{28}

Pitch [*mm*]	# revolutions	alpha [Degree]	alpha_x [Degree]	alpha_z [Degree]	d [*mm*]	d_x [*mm*]	d_z [*mm*]
12	10	9.93	9.87796402	1.05742175	93.43518656	93.42971483	93.01560273
15	8	7.60	7.52179308	1.087735017	88.03107997	88.02604396	87.80596631
17	7	6.52	6.432010755	1.06485278	83.32795685	83.32339907	83.1766137
20	6	6.88	6.765402179	1.271376811	98.2140928	98.20608408	98.01641328
22	6	7.13	6.988762785	1.409804542	108.14	108.1285518	107.910557
25	5	6.08	5.906840801	1.454932087	98.41282984	98.40160039	98.26046175
27	5	6.42	6.207631747	1.670710427	106.32	106.3017219	106.1391013
30	4	5.39	5.17234534	1.519557458	88.61	88.59346115	88.50541175
32	4	5.75	5.47958668	1.765258792	94.50	94.4764971	94.37817452
35	4	6.50	6.122018174	2.223095829	103.27	103.2243777	103.1079846
37	3	4.81	4.377207419	2.005961119	72.75	72.72115693	72.68594838
40	3	5.37	4.790300075	2.442165445	78.56	78.5183654	78.48594848

Figure 79: Calculation of the angles of curvature and of the distance of extremes in case C_{28}

Pitch [mm]	# revolutions	r [mm]	Curvature	Delta	r_x [mm]	r_z [mm]	% rx	% rz	Twist
12	10	44.88559653	0.022278862	0.007736359	44.74267452	130.4598514	74%	26%	-1.721415043
15	8	56.81	0.017603965	0.002171489	56.58983627	475.1864654	89%	11%	-2.144737244
17	7	63.98	0.015630688	0.001495672	63.76551673	692.5675649	92%	8%	-2.322814822
20	6	73.45	0.013613976	7.82194E-05	73.32402666	18484.01979	100%	0%	-1.632719278
22	6	79.26	0.012616133	0.000943544	79.32663644	1048.689868	93%	7%	-0.715712309
25	5	85.90	0.011641977	0.000446134	85.85758675	2268	96%	4%	-1.148250341
27	5	89.15	0.011216987	0.000929726	89.27441653	1057.87035	92%	8%	-0.689600945
30	4	86.74	0.011529269	0.000398737	86.44099595	2782.250224	97%	3%	-1.98639369
32	4	86.46	0.011566459	0.000263609	86.10965822	4608.972815	98%	2%	-2.185717344
35	4	82.67	0.012095595	6.38831E-05	82.25374534	505782.0079	100%	0%	-2.522102833
37	3	75.36	0.01326886	0.002923173	74.70099955	356.4642449	83%	17%	-4.283747196
40	3	68.48	0.014603539	0.004273738	67.14100842	251.0512324	79%	21%	-5.859009266

Figure 80: Calculation of curvature, radius of curvature and twist in case C_{12}

Pitch [mm]	# revolutions	alpha [Degree]	alpha_x [Degree]	alpha_z [Degree]	d [mm]	d_x [mm]	d_z [mm]
12	10	122.54	122.9339751	42.16159052	64.53646024	64.4073406	37.36833288
15	8	90.78	91.12272621	10.85178247	66.52872632	66.38911763	49.76250377
17	7	76.12	76.37578284	7.032008869	65.54474856	65.42336924	53.70453872
20	6	78.00	78.14052518	0.309974671	78.49110331	78.39673123	63.15747608
22	6	79.51	79.45043468	6.009913833	87.09371026	87.03551375	69.41358305
25	5	66.70	66.73350799	2.526280893	81.3730167	81.30538436	69.21927725
27	5	69.41	69.31374551	5.849435318	88.00270274	87.9458468	73.89612604
30	4	59.45	59.65479804	1.853399134	74.21051902	74.07553841	65.50221235
32	4	63.62	63.87663064	1.193410127	78.70975232	78.52694407	68.41539813
35	4	72.77	73.1402178	0.011894565	84.41959224	84.11854513	70.77709812
37	3	56.26	56.7581118	11.89428602	60.01977107	59.57833754	54.30204768
40	3	66.94	68.26919149	18.25787636	63.03646715	62.21199668	55.41662317

Figure 81: Calculation of the angles of curvature and of the distance of extremes in case C_{12}

Pitch [mm]	# revolutions	r [mm]	Curvature	Delta	r_x [mm]	r_z [mm]	% rx	% rz	Twist
12	10	88.75	0.01127	0.00021	88.74420248	4888.794632	98%	2%	-0.531944633
15	8	111.44	0.00897	0.00001	111.3969329	171971.8536	100%	0%	-0.711099982
17	7	124.80	0.00801	0.00010	124.7558066	10411.10264	99%	1%	-0.787956774
20	6	142.27	0.00703	0.00015	142.2727974	6732.99288	98%	2%	-0.569125175
22	6	152.21	0.00657	0.00031	152.328488	3219.167628	95%	5%	-0.270788491
25	5	164.57	0.00608	0.00010	164.5492457	9626.278642	98%	2%	-0.683377683
27	5	170.46	0.00587	0.00018	170.4898627	5661.13291	97%	3%	-0.68861866
30	4	169.17	0.00591	0.00014	169.023279	7625.610572	98%	2%	-1.199310899
32	4	170.09	0.00588	0.00011	169.8664334	9337.927228	98%	2%	-1.452691197
35	4	166.69	0.00600	0.00005	166.3377258	25094.01681	99%	1%	-1.876755476
37	3	158.61	0.00630	0.00079	158.9493565	1250.029005	89%	11%	-2.307575822
40	3	152.12	0.00657	0.00091	152.1752143	1093.405344	88%	12%	-3.135818958

Figure 82: Calculation of curvature, radius of curvature and twist in case V_{12}

Pitch [mm]	# revolutions	alpha [Degree]	alpha_x [Degree]	alpha_z [Degree]	d [mm]	d_x [mm]	d_z [mm]
12	10	61.97	61.98032862	1.125102453	78.80	78.78439559	67.93846917
15	8	46.27	46.29050389	0.029985257	77.22	77.20667367	71.05389435
17	7	39.02	39.03739146	0.467783426	74.37	74.35915941	70.14206606
20	6	40.27	40.27177406	0.850970446	88.53	88.51346475	83.11714688
22	6	27.24	41.37463601	1.957815334	97.90	97.90353428	91.64452012
25	5	34.82	34.81983722	0.595201756	90.05	90.03616555	85.87107011
27	5	36.30	36.29508576	1.093057571	97.42	97.40509646	92.56571955
30	4	30.48	30.50834291	0.676223905	81.58	81.54532321	78.71794656
32	4	32.34	32.38070479	0.589038092	86.91	86.85480788	83.54487795
35	4	36.09	36.16772335	0.239740688	94.49	94.38684068	90.09525033
37	3	26.73	26.67445642	3.391831444	66.74	66.63072093	65.03176469
40	3	30.13	30.12095223	4.192098004	71.56	71.36154189	69.35685644

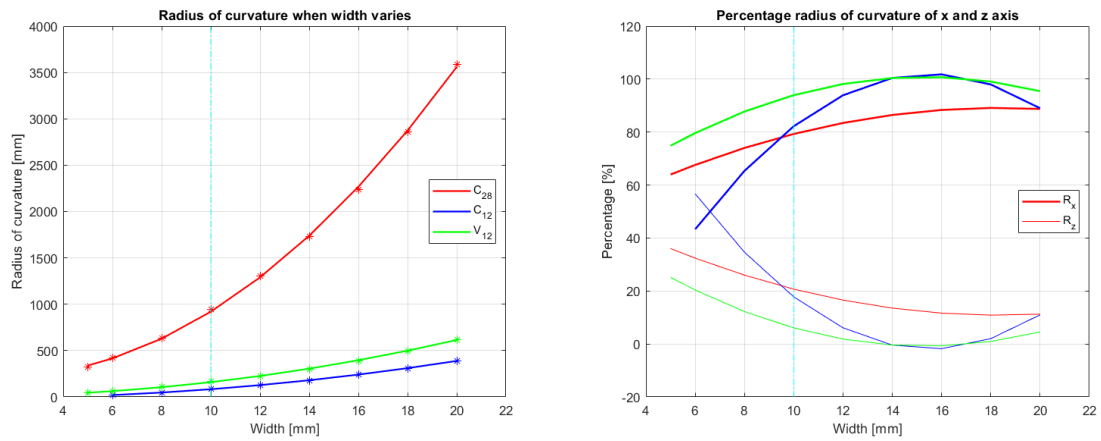Figure 83: Calculation of the angles of curvature and of the distance of extremes in case V_{12}
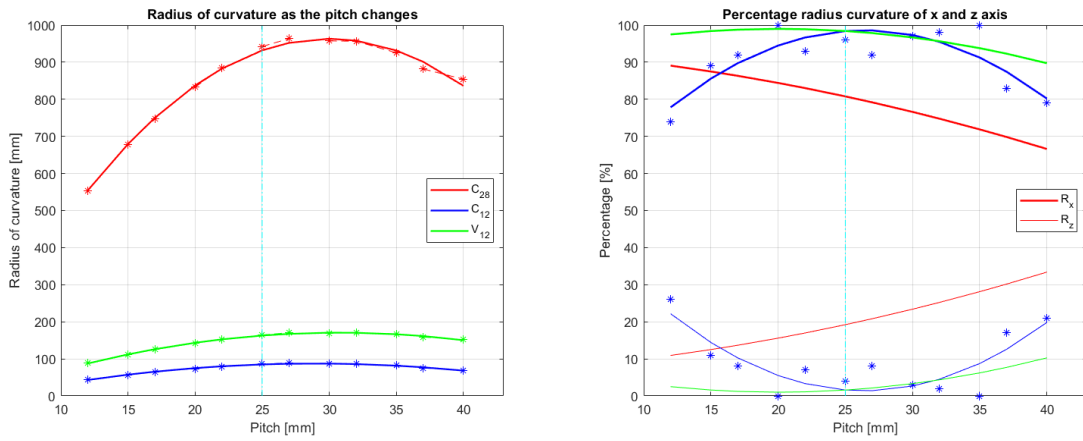
Figure 84: Variation of the radius of curvature with the pitch and relative percentages
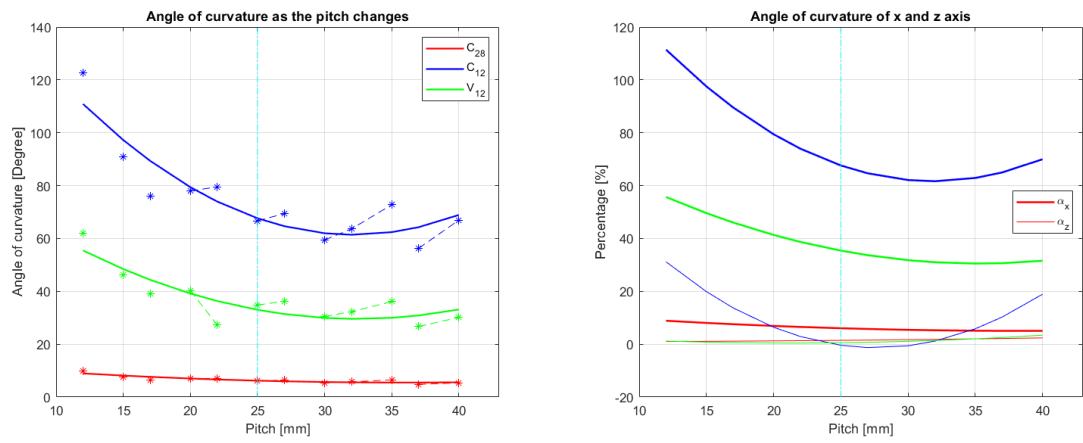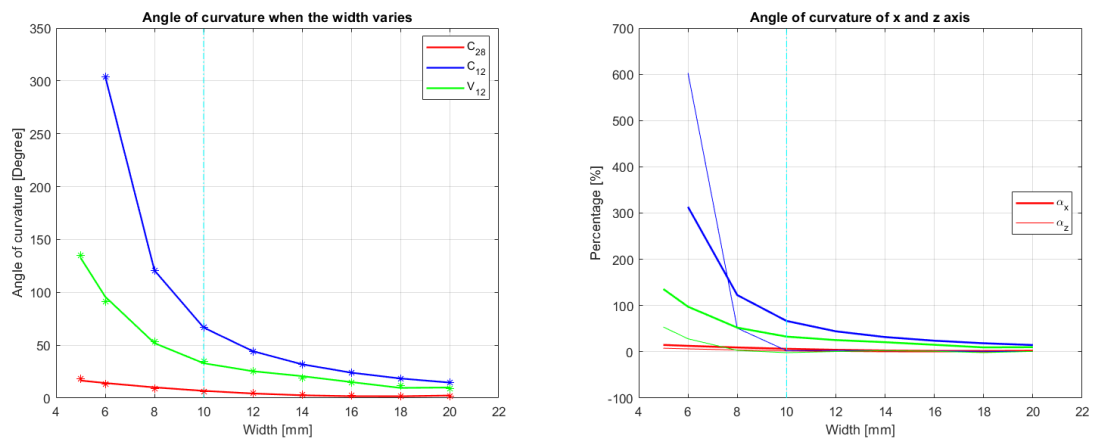

Figure 85: Variation of the angle of curvature with the pitch and relative percentages
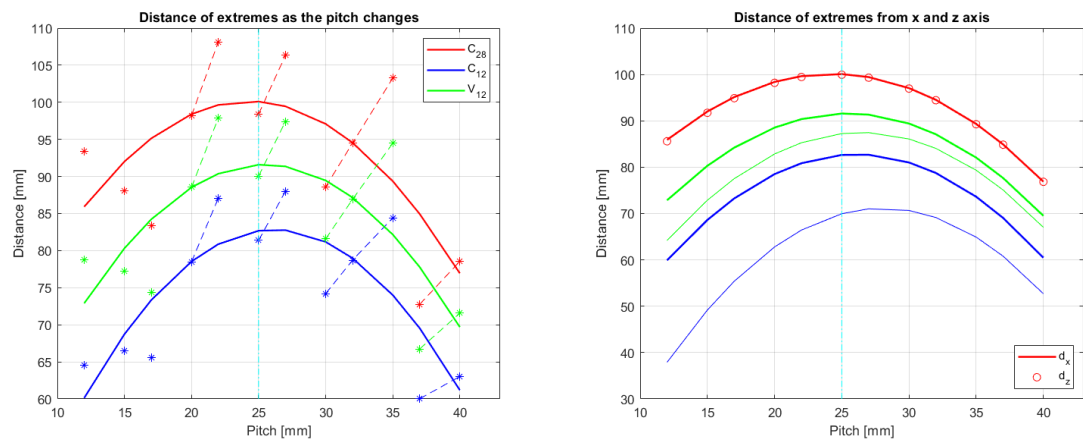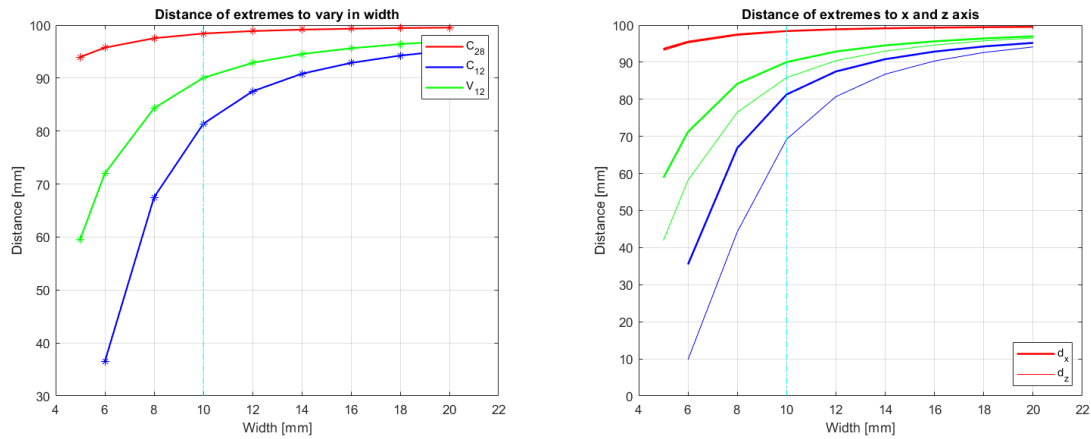

Figure 86: Variation of distance of extremes with pitch and relative percentages
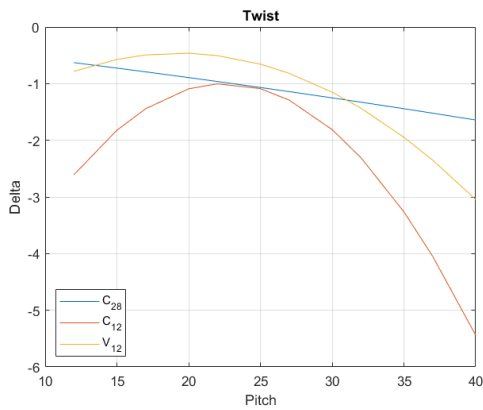
Figure 87: Twisting as the pith changes

Theoretically a monotonic trend is expected. By increasing the pitch, the structure should be more flexible and, for this reason, the radius of curvature should always decrease, while the angle should increase and the distance should decrease. From the analysis, the radius of curvature first increases and then decreases, while the angle of curvature first decreases and then increases. The twist varies but the difference always remains negative. The worst case, in this specific situation, is with a pitch between 25 mm and 35 mm because the structure is as stiff as possible. The bell pattern of this analysis (especially with a small pitch) is counterintuitive. The explanation could be the number of forces that are placed on the structure. If, for every pitch, we placed the same number of forces, the behavior of the radius of curvature would be as expected. However, by decreasing the pitch, the number of forces on the structure increases (because there are more laps in order to have the same height). This increase in the number of the forces is not compensated by the increase in material of the spiral and, therefore, the radius of curvature decreases (if the pitch decreases).

4.2.3. Constant number of revolutions

Pitch [mm]	r [mm]	Curvature	Delta	r_x [mm]	r_z [mm]	% rx	% rz	Twist
12	527.98	0.00189	0.00021	531.7628098	4390.609742	89%	11%	-0.225621544
15	655.54	0.00153	0.00022	663.4770674	4212.287933	86%	14%	-0.340561599
17	732.45	0.00137	0.00022	743.3905892	4246.805912	85%	15%	-0.429515362
20	831.59	0.00120	0.00021	847.5696535	4261.457911	83%	17%	-0.599573597
22	880.03	0.00114	0.00021	899.7630003	4181.742214	82%	18%	-0.747653037
25	942.46	0.00106	0.00022	969.9902443	3938.038073	80%	20%	-1.048866391
27	963.41	0.00104	0.00024	996.828491	3703.780192	79%	21%	-1.314699292
30	972.89	0.00103	0.00026	1018.082669	3250.972949	76%	24%	-1.872113824
32	965.34	0.00104	0.00029	1020.829589	2916.610792	74%	26%	-2.386057615
35	936.72	0.00107	0.00032	1003.447537	2555.176794	72%	28%	-3.307321429
37	912.18	0.00110	0.00035	989.8706885	2290.210146	70%	30%	-4.124677777
40	881.41	0.00113	0.00039	973.2233201	2015.771057	67%	33%	-5.506523609

Figure 88: Calculation of curvature, radius of curvature and twist in case C_{28}

Pitch [mm]	alpha [Degree]	alpha_x [Degree]	alpha_z [Degree]	d [mm]	d_x [mm]	d_z [mm]
12	5.21	5.171849866	0.62638166	46.6970305	46.69588152	46.62721548
15	5.24	5.181410089	0.816123405	58.6647222	58.66277704	58.58526115
17	5.32	5.24100394	0.917421961	66.63677187	66.63408163	66.54870549
20	5.51	5.408006695	1.075608972	78.57862796	78.57415243	78.47235171
22	5.73	5.603729644	1.205724394	86.52	86.51425893	86.39761464
25	6.08	5.906840801	1.454932087	98.41282984	98.40160039	98.26046175
27	6.42	6.207631747	1.670710427	106.32	106.3017219	106.1391013
30	7.07	6.753374508	2.114903338	118.13	118.10385	117.9039533
32	7.60	7.18421552	2.51451438	125.98	125.9308047	125.7037753
35	8.56	7.993850038	3.139277545	137.67	137.5834902	137.3080202
37	9.30	8.566548608	3.702618899	145.42	145.301347	144.9972619
40	10.40	9.41954897	4.54780055	157.01	156.8070529	156.4687941

Figure 89: Calculation of the angles of curvature and of the distance of extremes in case C_{28}

Pitch [mm]	r [mm]	Curvature	Delta	r_x [mm]	r_z [mm]	% rx	% rz	Twist
12	42.70268698	0.02341773	0.003933129	42.59792788	258.0286587	86%	14%	-1.438141584
15	54.54	0.018336346	0.002899494	54.36241339	352.0163369	87%	13%	-1.98743391
17	62.47	0.016008582	0.002093477	62.26378023	489.8700415	89%	11%	-2.104599476
20	73.19	0.013662939	0.001044127	72.96708937	997.7474022	93%	7%	-1.995062351
22	78.50	0.012738424	0.000467049	78.30610601	2298.445863	97%	3%	-1.780066729
25	85.90	0.011641977	0.000446134	85.85758675	2268	96%	4%	-1.148250341
27	89.15	0.011216987	0.000929726	89.27441653	1057.87035	92%	8%	-0.689600945
30	90.80	0.011013052	0.001623986	91.19984393	598.0475718	87%	13%	-0.043445349
32	89.40	0.011185152	0.002160893	89.96609711	448.2803174	83%	17%	0.32837534
35	87.45	0.011434634	0.003409162	88.38443159	283.3193481	76%	24%	1.278514385
37	82.48	0.012124361	0.004883428	83.50811529	198.6923744	70%	30%	1.781212807
40	75.00	0.013333076	0.010925058	76.29547013	89.67647618	54%	46%	3.388700962

Figure 90: Calculation of radius of curvature and twist in case C_{12}

Pitch [mm]	alpha [Degree]	alpha_x [Degree]	alpha_z [Degree]	d [mm]	d_x [mm]	d_z [mm]
12	64.40	64.56176517	10.65849596	34.46579075	34.38468404	28.99643273
15	63.04	63.23756721	9.765872803	45.49004453	45.3692016	39.05839978
17	62.37	62.57430873	7.953360436	52.89655587	52.77425172	45.7858673
20	62.63	62.81821572	4.59401082	63.88658995	63.77884624	55.34103746
22	64.23	64.38870293	2.193668634	70.94464496	70.84988742	61.06586579
25	66.70	66.73350799	2.526280893	81.3730167	81.30538436	69.21927725
27	69.41	69.31374551	5.849435318	88.00270274	87.9458468	73.89612604
30	75.72	75.38931258	11.49656627	97.17664197	97.12196275	79.11330065
32	82.03	81.51803861	16.35998614	102.5205	102.4550668	80.79276274
35	91.72	90.75590562	28.31225324	109.76292	109.6849503	82.18000269
37	102.81	101.544327	42.67791047	112.78298	112.6671401	78.81779661
40	122.23	120.1555572	102.2266386	115.34027	115.1670188	70.40690953

Figure 91: Calculation of the angles of curvature and of the distance of extremes in case C_{12}

Pitch [mm]	r [mm]	Curvature	Delta	r_x [mm]	r_z [mm]	% rx	% rz	Twist
12	85.71	0.01167	0.00062	85.72770597	1602.413583	95%	5%	-0.578943968
15	108.46	0.00922	0.00047	108.4788198	2137.968654	95%	5%	-0.749961555
17	123.22	0.00812	0.00029	123.2078385	3427.248716	97%	3%	-0.732677221
20	141.81	0.00705	0.00013	141.7686518	7653.123002	98%	2%	-0.747999132
22	151.36	0.00661	0.00003	151.3126461	31520.51821	100%	0%	-0.72845751
25	164.57	0.00608	0.00010	164.5492457	9626.278642	98%	2%	-0.683377683
27	170.46	0.00587	0.00018	170.4898627	5661.13291	97%	3%	-0.68861866
30	174.45	0.00573	0.00024	174.5347985	4065.185509	96%	4%	-0.850756168
32	173.62	0.00576	0.00026	173.6829519	3837.183342	96%	4%	-1.134093046
35	172.43	0.00580	0.00038	172.630579	2562.765056	94%	6%	-1.284497499
37	167.45	0.00597	0.00040	167.585297	2444.137107	94%	6%	-1.750460863
40	160.44	0.00623	0.00050	160.5525012	2000.965448	93%	7%	-2.331417561

Figure 92: Calculation of curvature, radius of curvature and twist in case V_{12}

Pitch [mm]	alpha [Degree]	alpha_x [Degree]	alpha_z [Degree]	d [mm]	d_x [mm]	d_z [mm]
12	32.09	32.08061368	1.716284388	40.22	40.20408414	38.33110622
15	31.70	31.6904883	1.607950034	51.88	51.86114721	49.67292301
17	31.62	31.62228195	1.136804863	59.65	59.63910833	57.21811324
20	32.32	32.33198809	0.598927047	71.19	71.18103792	68.2456248
22	33.31	33.32192468	0.159960206	78.77	78.75565201	75.36308045
25	34.82	34.81983722	0.595201756	90.05	90.03616555	85.87107011
27	36.30	36.29508576	1.093057571	97.42	97.40509646	92.56571955
30	39.41	39.39325337	1.691311141	108.17	108.1422475	101.9596409
32	42.24	42.22555926	1.911261236	115.06	115.0098427	107.6186354
35	46.52	46.46574888	3.129982249	125.02	124.9498607	115.539404
37	50.64	50.59975739	3.469435223	131.17	131.055622	119.6545171
40	57.14	57.09861044	4.581450785	139.89	139.6873054	124.8334893

Figure 93: Calculation of the angles of curvature and of the distance of extremes in case V_{12}
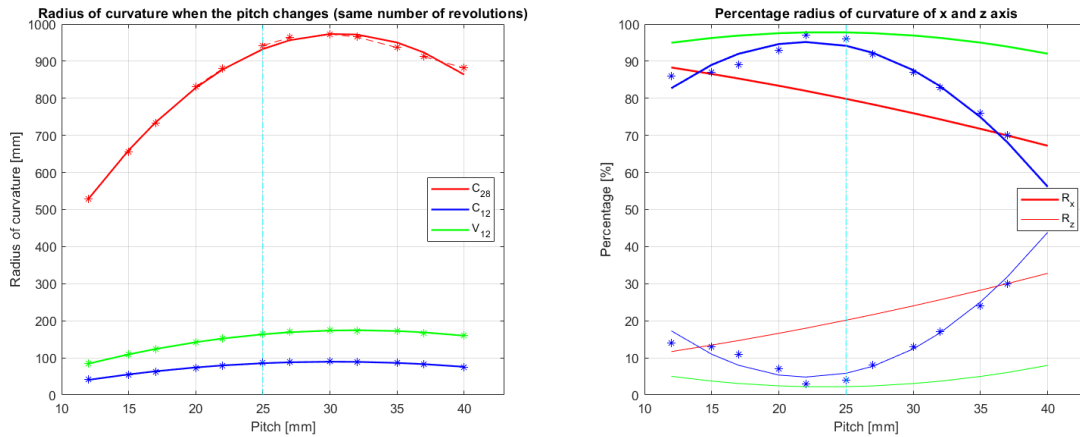
Figure 94: Variation of the radius of curvature with the pitch and relative percentages
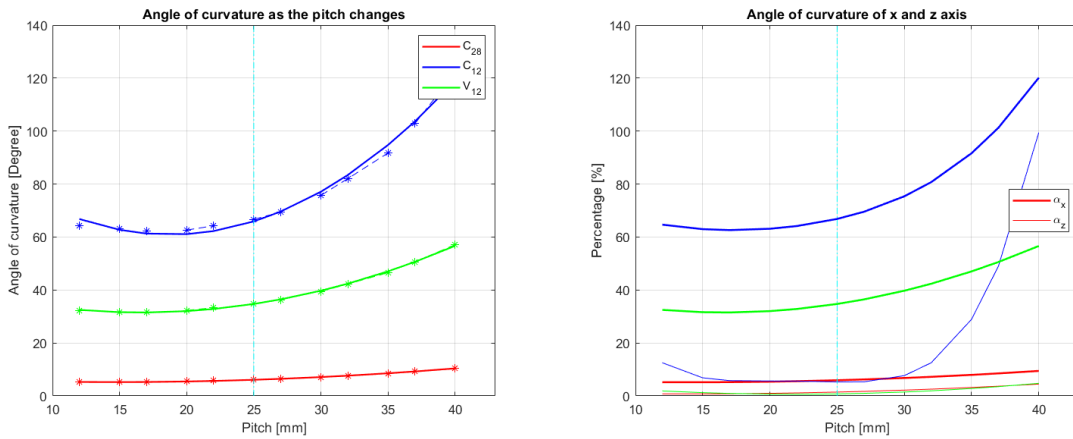
Figure 95: Variation of the angle of curvature with the pitch and relative percentages
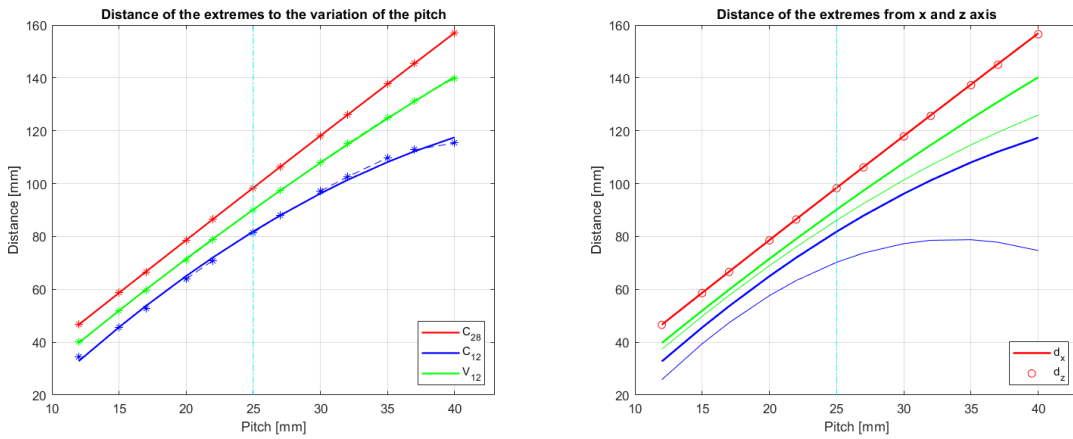
Figure 96: Variation of distance of extremes with pitch and relative percentages
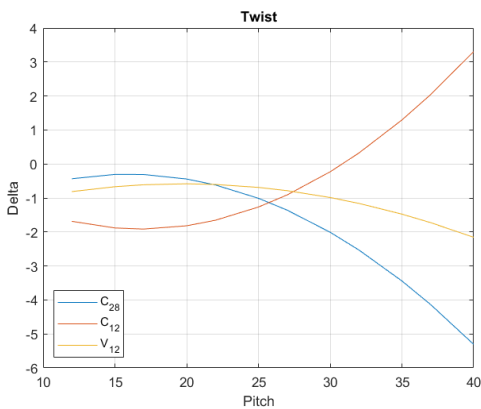
Figure 97: Twisting as the pitch changes

The graph of the change of radius of curvature is similar to that of the previous case (with constant height). The behavior of the radius is different from the one wanted because the height of the structure changes a lot with the variation of the pitch. The angle, on the other hand, constantly increases because the structure becomes more flexible, while the distance always increases (less with high pitches) because the height of the structure is increasing. It is important to note that the percentage on the *XY* plane is greater at small pitches and decreases by increasing the pitch. Thus, increasing the pitch, the structure tends to move more towards the *ZY* plane. The torsion increases if the pitch increases, the effect is seen especially in case C_{12} where the tip of the prototype goes back after the initial displacement. In all cases, the most flexible structure is C_{12}. On the other hand, the least flexible structure is C_{28}.

4.2.4. Variation of diameter

Diameter [mm]	r [mm]	Curvature	Delta	r_x [mm]	r_z [mm]	% rx	% rz	Twist
5	1634.43	0.00061	0.00018	1748.102066	4590.054478	72%	28%	-0.9648
6	1552.49	0.00064	0.00018	1648.641311	4594.025015	74%	26%	-0.94228
8	1251.91	0.00080	0.00019	1300.537306	4590.835046	78%	22%	-0.92047
10	942.46	0.00106	0.00022	969.9902443	3938.038073	80%	20%	-1.048866391
12	698.56	0.00143	0.00029	717.141655	3025.101036	81%	19%	-1.32529
14	515.79	0.00194	0.00039	528.6960999	2263.210307	81%	19%	-1.70744
16	393.35	0.00254	0.00052	402.8251513	1715.543735	81%	19%	-2.13248
18	311.61	0.00321	0.00068	319.0992643	1316.544519	80%	20%	-2.58424
20	245.89	0.00407	0.00086	251.043365	1056.322915	81%	19%	-2.91723

Figure 98: Calculation of curvature, radius of curvature and twist in case C_{28}

Diameter [mm]	alpha [Degree]	alpha_x [Degree]	alpha_z [Degree]	d [mm]	d_x [mm]	d_z [mm]
5	3.51	3.277599211	1.248259248	99.58073347	99.57102238	99.53351277
6	3.69	3.475333241	1.247180399	99.46242097	99.45329302	99.40887416
8	4.58	4.405546789	1.24804701	99.07421528	99.06557607	98.98795283
10	6.08	5.906840801	1.454932087	98.41282984	98.40160039	98.26046175
12	8.20	7.989464719	1.894012095	97.40	97.38209873	97.13203872
14	11.11	10.83718596	2.531615349	95.90	95.86941123	95.43512185
16	14.57	14.22348613	3.339802906	93.89	93.84443411	93.14157442
18	18.39	17.95547214	4.351981924	91.25	91.17813912	90.12410781
20	23.30	22.82306067	5.424078066	87.94	87.84587986	86.29101831

Figure 99: Calculation of the angles of curvature and of the distance of extremes in case C_{28}

Diameter [mm]	r [mm]	Curvature	Delta	r_x [mm]	r_z [mm]	% rx	% rz	Twist
5	279.11	0.00358	0.00016	279.1103834	6310.194255	96%	4%	-1.42114
6	232.11	0.00431	0.00002	232.0258207	64016.34863	100%	0%	-0.90103
8	146.48	0.00683	0.00050	146.7870932	1963.535123	93%	7%	-0.07089
10	85.90	0.01164	0.00045	85.85758675	2268	96%	4%	-1.148250341
12	47.55	0.02103	0.01010	46.82972004	102.2314036	69%	31%	-4.22712
14	23.87	0.04189	0.10645	22.90395267	9.552299812	29%	71%	-4.32627
16	NaN	#VALORE!	#VALORE!	NaN	NaN	#VALORE!	#VALORE!	NaN
18	NaN	#VALORE!	#VALORE!	NaN	NaN	#VALORE!	#VALORE!	NaN
20	NaN	#VALORE!	#VALORE!	NaN	NaN	#VALORE!	#VALORE!	NaN

Figure 100: Calculation of curvature, radius of curvature and twist in case C_{12}

Diameter [mm]	alpha [Degree]	alpha_x [Degree]	alpha_z [Degree]	d [mm]	d_x [mm]	d_z [mm]
5	20.53	20.528	0.907987571	97.14006408	97.10726931	95.41012099
6	24.69	24.69370837	0.089501792	95.79325673	95.77478964	93.31899802
8	39.11	39.03325441	2.917991069	90.908322	90.90128123	85.3736729
10	66.70	66.73350799	2.526280893	81.3730167	81.30538436	69.21927725
12	120.50	122.3491822	56.04518525	65.11	64.53626534	42.9696884
14	240.03	250.1567321	599.8113611	42.15	40.95275354	14.79854152
16	NaN	NaN	NaN	NaN	NaN	NaN
18	NaN	NaN	NaN	NaN	NaN	NaN
20	NaN	NaN	NaN	NaN	NaN	NaN

Figure 101: Calculation of the angles of curvature and of the distance of extremes in case C_{12}

Diameter [mm]	r [mm]	Curvature	Delta	r_x [mm]	r_z [mm]	% rx	% rz	Twist
5	398.70	0.00251	0.00018	399.5323412	5275.666388	93%	7%	-1.23384
6	349.55	0.00286	0.00013	349.7593307	7379.563393	95%	5%	-1.01788
8	245.34	0.00408	0.00002	245.3016808	41295.56703	99%	1%	-0.60433
10	164.57	0.00608	0.00010	164.5492457	9626.278642	98%	2%	-0.683377683
12	109.40	0.00914	0.00011	109.2727238	10198.54307	99%	1%	-1.40637
14	72.04	0.01388	0.00107	71.79140811	983.5720297	93%	7%	-2.2724
16	46.53	0.02149	0.00636	46.13540161	161.9291055	78%	22%	-3.06866
18	28.16	0.03552	0.05626	27.68071703	17.96916058	39%	61%	-3.22142
20	12.80	0.07815	0.24119	12.1944828	4.21337411	26%	74%	-3.02403

Figure 102: Calculation of curvature, radius of curvature and twist in case V_{12}

Diameter [mm]	alpha [Degree]	alpha_x [Degree]	alpha_z [Degree]	d [mm]	d_x [mm]	d_z [mm]
5	14.37	14.34071128	1.086038716	98.07075542	98.04960399	97.21188033
6	16.39	16.38148707	0.776411509	97.30300402	97.28743076	96.18870444
8	23.35	23.35727148	0.138745593	94.68202252	94.67327212	92.54214301
10	34.82	34.81983722	0.595201756	90.05	90.03616555	85.87107011
12	52.37	52.43374332	0.561803575	82.76	82.71017668	75.19980277
14	79.53	79.80868605	5.825275403	72.17	72.02988832	60.03426428
16	123.13	124.1904861	35.38324957	58.33	58.04464099	41.55744313
18	203.49	206.9880613	318.8561828	41.63	41.20451484	22.56372616
20	447.79	469.8500172	1359.855024	22.28	21.5578993	6.370875719

Figure 103: Calculation of the angles of curvature and of the distance of extremes in case V_{12}
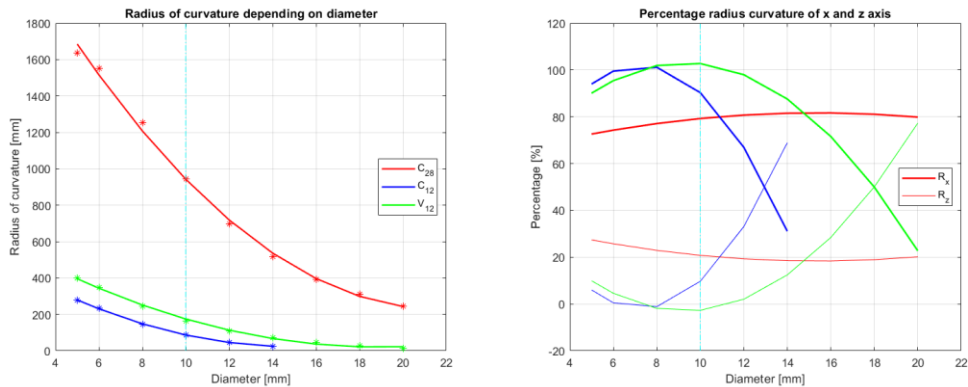
Figure 104: Variation of the radius of curvature with the diameter and relative percentages
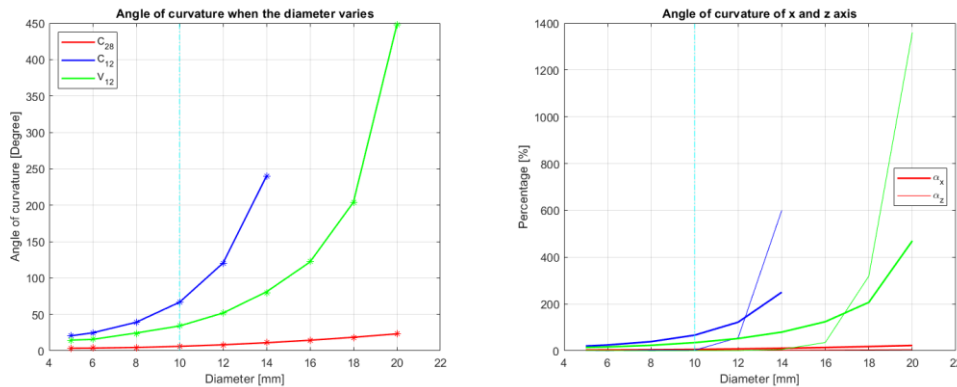
Figure 105: Variation of the angle of curvature with the diameter and relative percentages
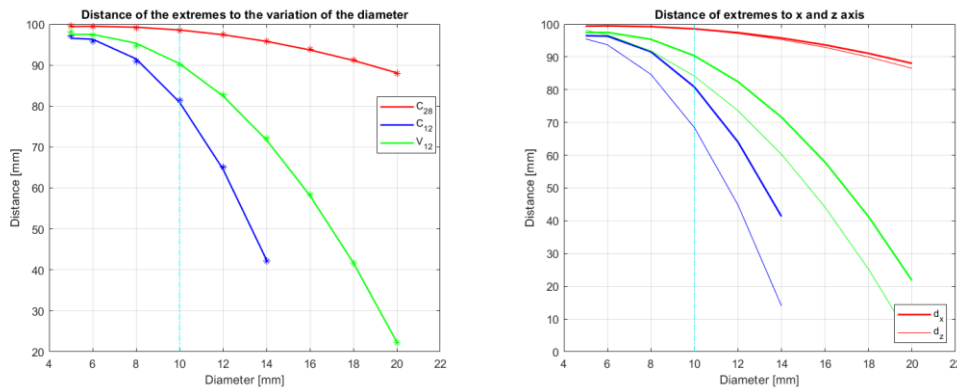
Figure 106: Variation of distance of extremes with diameter and relative percentages
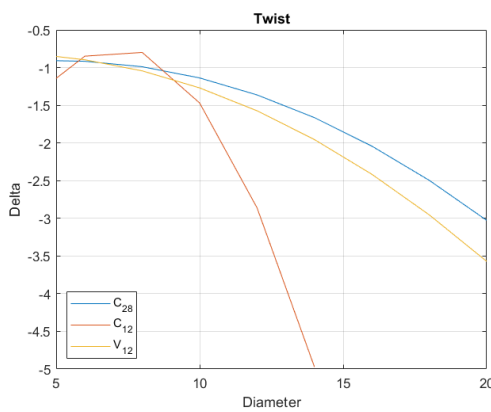
Figure 107: Twisting as the diameter changes

In this case, increasing the diameter of the structure, the radius of curvature decreases and the angle of curvature increases. The behavior of the structure is monotonous as expected. The structure, beyond a certain diameter, becomes so flexible that it crushes on itself making any calculation insignificant (calculations with non-physical relevance are highlighted in red). The percentages in the graphs intersect in the points that do not have a physical relevance. For this reason, the calculations stop after a certain diameter. The most flexible structure is always C_{12}, while the least flexible is C_{28}.

4.2.5. Variation of the width of composite

In this case, the height of the structure and of the constraint at the base change a little. The distances, however, remain similar to those of the nominal case.

Width [mm]	r [mm]	Curvature	Delta	r_x [mm]	r_z [mm]	% rx	% rz	Twist
5	319.20	0.00313	0.00118	355.5129106	666.6811217	65%	35%	-5.92114
6	422.50	0.00237	0.00086	471.0237453	910.0393165	66%	34%	-4.48767
8	635.17	0.00157	0.00043	669.7709467	1952.70073	74%	26%	-2.15315
10	942.46	0.00106	0.00022	969.9902443	3938.038073	80%	20%	-1.048866391
12	1302.02	0.00077	0.00013	1325.165161	6955.123723	84%	16%	-0.56447
14	1728.89	0.00058	0.00008	1750.640018	10965.76719	86%	14%	-0.33832
16	2239.23	0.00045	0.00006	2261.442678	15987.84826	88%	12%	-0.22071
18	2857.06	0.00035	0.00004	2880.595847	22370.66241	89%	11%	-0.15328
20	3584.57	0.00028	0.00003	3610.296567	30060.78069	89%	11%	-0.1127

Figure 108: Calculation of curvature, radius of curvature and twist in case C_{28}

Width [mm]	alpha [Degree]	alpha_x [Degree]	alpha_z [Degree]	d [mm]	d_x [mm]	d_z [mm]
5	17.95	16.11637097	8.594180583	93.9847447	93.58355105	93.16444224
6	13.56	12.16409578	6.29596749	95.74767826	95.52519125	95.21970952
8	9.02	8.554533426	2.934181293	97.52663279	97.47721025	97.23416518
10	6.08	5.906840801	1.454932087	98.41282984	98.40160039	98.26046175
12	4.40	4.323670831	0.823792384	98.88	98.87270214	98.78902229
14	3.31	3.272847582	0.522496772	99.15	99.14542361	99.09420179
16	2.56	2.533594155	0.358370799	99.32	99.32186352	99.28945726
18	2.01	1.989025277	0.256120174	99.45	99.4455054	99.42462958
20	1.60	1.587010331	0.190599772	99.53	99.53460502	99.52070352

Figure 109: Calculation of the angles of curvature and of the distance of extremes in case C_{28}

Width [mm]	r [mm]	Curvature	Delta	r_x [mm]	r_z [mm]	% rx	% rz	Twist
5	NaN	#VALORE!	#VALORE!	NaN	NaN	#VALORE!	#VALORE!	NaN
6	18.84	0.05308	0.10681	18.28736838	9.504980616	34%	66%	-1.15521
8	47.44	0.02108	0.00925	46.71657601	112.0978871	71%	29%	-4.09327
10	85.90	0.01164	0.00045	85.85758675	2268	96%	4%	-1.148250341
12	129.17	0.00774	0.00050	129.3670097	1934.545513	94%	6%	-0.07915
14	179.33	0.00558	0.00036	179.6533616	2668.190423	94%	6%	0.215708
16	238.34	0.00420	0.00024	238.71022	4007.06616	94%	6%	0.22465
18	309.41	0.00323	0.00016	309.76602	6141.09716	95%	5%	0.15689
20	390.61	0.00256	0.00010	390.90733	9717.15144	96%	4%	0.07663

Figure 110: Calculation of curvature, radius of curvature and twist in case C_{12}

Width [mm]	alpha [Degree]	alpha_x [Degree]	alpha_z [Degree]	d [mm]	d_x [mm]	d_z [mm]
5	NaN	NaN	NaN	NaN	NaN	NaN
6	304.10	313.3079528	602.7974367	36.51052482	35.46577983	9.808402571
8	120.77	122.6455027	51.11227426	67.49958259	66.87423375	44.25278536
10	66.70	66.73350799	2.526280893	81.3730167	81.30538436	69.21927725
12	44.36	44.2893282	2.961717836	87.50	87.49674862	80.728009
14	31.95	31.89240602	2.147364709	90.82	90.81799208	86.77958044
16	24.03906	24.00223	1.42987	92.86444	92.86442	90.33237
18	18.51795	18.49647	0.93299	94.25209	94.25208	92.62488
20	14.66833	14.65713	0.58964	95.21780	95.21777	94.11821

Figure 111: Calculation of the angles of curvature and of the distance of extremes in case C_{12}

Width [mm]	r [mm]	Curvature	Delta	r_x [mm]	r_z [mm]	% rx	% rz	Twist
5	42.39	0.02359	0.01019	41.44136104	103.6925171	71%	29%	-4.57106
6	62.86	0.01591	0.00479	61.65073003	223.1653488	78%	22%	-5.93221
8	107.01	0.00935	0.00049	106.6870503	2179.249183	95%	5%	-2.49314
10	164.57	0.00608	0.00010	164.5492457	9626.278642	98%	2%	-0.683377683
12	228.37	0.00438	0.00013	228.4607624	7486.154887	97%	3%	-0.13281
14	302.58	0.00330	0.00010	302.7249086	9519.031881	97%	3%	0.033181
16	390.39	0.00256	0.00007	390.528556	14284.27773	97%	3%	0.05494
18	497.45	0.00201	0.00004	497.5606502	23205.61312	98%	2%	0.031472
20	618.79	0.00162	0.00002	618.8509738	42063.19906	99%	1%	0.003489

Figure 112: Calculation of curvature, radius of curvature and twist in case V_{12}

Width [mm]	alpha [Degree]	alpha_x [Degree]	alpha_z [Degree]	d [mm]	d_x [mm]	d_z [mm]
5	135.15	138.2574753	55.25546211	59.62936686	58.83454408	41.92522672
6	91.14	92.93609254	25.67413795	72.02275534	71.21508725	58.19445754
8	53.54	53.70453053	2.629152277	84.32722148	84.19218431	76.51207608
10	34.82	34.81983722	0.595201756	90.05	90.03616555	85.87107011
12	25.09	25.07904593	0.765356587	92.88	92.87877592	90.40639447
14	18.94	18.92668158	0.601907633	94.54	94.54298912	92.99815153
16	14.68	14.67134186	0.401110792	95.63	95.6335833	94.63206612
18	11.52	11.51533577	0.246904829	96.42	96.41499339	95.75726043
20	9.26	9.258413081	0.136213557	96.97	96.97169906	96.51933986

Figure 113: Calculation of the angles of curvature and of the distance of extremes in case V_{12}

Figure 114: Variation of the radius of curvature with the width and relative percentages

Figure 115: Variation of the angle of curvature with the width and relative percentages

Figure 116: Variation of distance of extremes with width and relative percentages
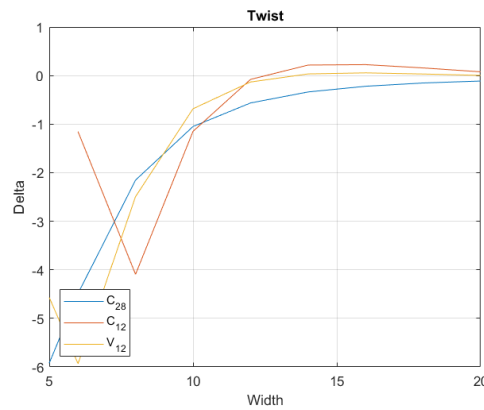
Figure 117: Twisting as the width changes

In this case, the trend of the graphs is monotonous, with the radius of curvature that increases if the width increases (because the structure becomes more rigid). The angle of curvature decreases as the distance increases. The twist is always negative (slightly positive with larger width). With a small width, the structure is very flexible and this great flexibility compromises the results. The most flexible structure remains C_{12}, while the least flexible one remains C_{28}. From the analyses conducted, it is clear that the most flexible structure possible is obtained by increasing the pitch and diameter and decreasing the thickness. Although C_{12} seems to be the best structure from this analysis, V_{12} has a very similar behavior and is better from a thermal point of view. Considering the analyses, both thermal and mechanical, it is more convenient to choose a structure with 6 layers of glass-fiber fabric with a thickness of 0.12 mm.

5 Experiments

5.1. Production of the prototypes

In order to test the prototypes, it was necessary to make them. A mold has been created that can support the particular structure of the prototypes during the autoclave cycle. The mold consists of a $10-mm-$ diameter cylinder on which the spiral is wound. At the ends, there are four supports (two on each side) that allow to place and lock the NiTiNOL wires. The bar is 1000 mm long. This length has been chosen to contain the $500-mm-$ long spiral structure, to contain the four supports and to make the vacuum bag. The mold structure is illustrated below.

Figure 118: Complete mold

The composite layers are cut into $10-mm-$ wide strips and wrapped on the mold using a jig.
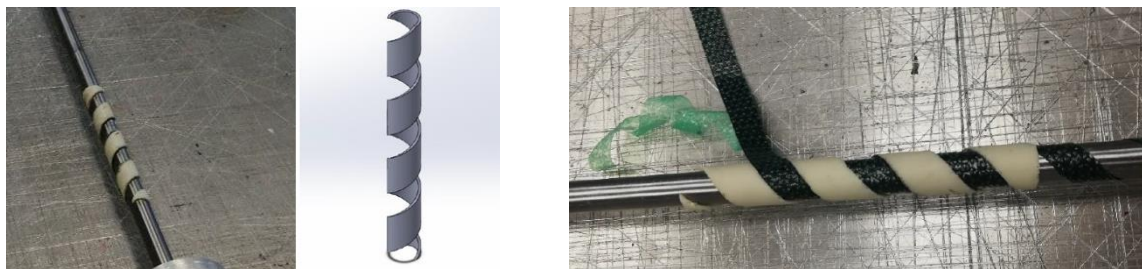
(a) Jig on the mold

(b) Use of the jig to arrange the composite layers on the mold

Figure 119: How to use the jig when creating prototypes

The jig was produced using 3D printing. It has a diameter of 10 mm and is 100 mm long. The jig was created in such a way that the empty spaces correspond to the area where the composite strips should be placed. As the layers of composite are arranged, the jig is moved forward. This allows prototypes to be made with a constant pitch. After placing half of the overall layers of composite fabric, NiTiNOL wires are inserted. These can be directly incorporated into the structure or inserted into PTFE sheaths that are incorporated into the structure.

Figure 120: NiTiNOL wires directly embedded in the structure (left) and NiTiNOL wires inside sheaths embedded in the structure (right)

At one end of the mold there are two supports. In the first support, the wires pass through half-holes, with a diameter of 2 mm, arranged along the central circumference, with a diameter of 9 mm. This support is used to hold the wires in the correct position. In the second support, the wires pass through holes, with a diameter of 2 mm, and then are wrapped on screws coupled with M3 threaded holes. The second support is therefore used to hold the wires in tension and lock them through the screws on which they are wound. In the first prototypes, it was observed that the residual torsion stresses present in the helix when it is removed from the mold caused a partial torsion that led to a misalignment of the inserted wires. For this reason, the wires have been constrained on one side with a rotation of 60° in the opposite direction to that of the winding of the helix (to reduce this effect). The two supports are bound to the bar by two screws positioned below.
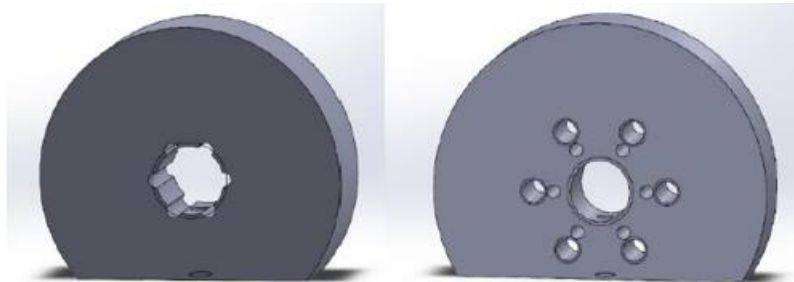
Figure 121: Support to hold the wires in place (left) and support to hold in tension and blocked wires (right)

Figure 122: Two supports together holding the wires in the correct position and stress state

After the prototype has been correctly positioned on the mold, the vacuum bag for the autoclave cycle is created. The layers of materials used in the vacuum bag, written in order from the innermost to the outermost, are:

- Peel ply: it makes the surfaces on which it is applied rough and opaque. This creates faces on the laminate, ready for subsequent gluing and lamination.
- PTFE layer: it allows the passage of excess resin, air and other volatile substances that are released from the laminate. It prevents the laminate and the bag from adhering, by making separation easier at the end of the production cycle.
- Bleeder: it can be made of cotton or, in other cases, polyester or fiberglass. Its function is to absorb the excess resin flowing through the holes in the previous film to prevent them from closing due to the pressure applied. It also has the function of protecting the bag from sharp edges in the mold that may cause cuts or breakages in the bag itself.
- Bag: it can expand to fit the mold and laminate assembly.
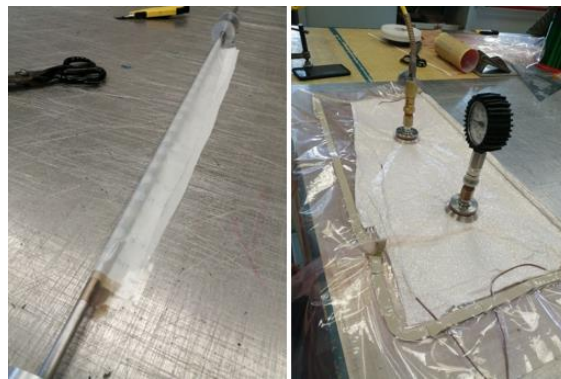
Figure 123: Creation of the vacuum bag

Once the vacuum bag is made, the material can be placed in autoclave to allow the polymerization of the resin and thus obtain the final characteristics of the laminate. The autoclave is a system that allows to control temperature and pressure in order to bring the resin to cross-linking. The advantage of the autoclave is that it is possible to exercise a hydrostatic pressure on the pieces, therefore a load perpendicular to the laminate at any point. This allows to reduce the presence of voids and, thus, to improve the mechanical characteristics of the laminate. The autoclave installed in the *DAER laboratories* has an internal diameter of 1.5 m, of which the useful diameter without insulation is 1.2 m, the useful length is 2.2 m; it can reach a maximum of 15 bar and 450 ℃, with a maximum temperature gradient of 10 ℃/min. The cycle, with the respective pressures and temperatures, is defined on the basis of the parameters in the technical data sheet provided by the manufacturer of the pre-impregnated [28]. The values of the various phases of the autoclave cycle used for the prototypes are shown in the figure below.

Temperature [°C]	Pressure [bar]	Vol	Delta_time [min]
75	0.1	-1	23
125	4	-1	25
125	2	-1	30
60	4	-1	33
58	0.4	-0.4	5

Figure 124: Cycle in autoclave

5.2.   Strategy for experiments

The experimental part of this work aims to examine the real three-dimensional movement of the prototype, in addition to the transient with the relative phases of activation and deactivation of the wires. The results are influenced by the manual production of the prototype. Different structures are then subjected to analysis:

- C_{12} structure with an embedded wire
- C_{12} structure with two wires in the sheaths
- C_{12} structure with two embedded wires
- C_{12} structure with three wires in the sheaths
- C_{12} structure with six embedded wires
- V_{12-6} structure with three wires in the sheaths

The geometry of the reference structure is: 500 mm height, 10 mm diameter, 25 mm pitch and width of the composite strips of 10 mm. The analysis therefore allows to distinguish between various types of structures and choose the optimal one from an experimental point of view. The instrumentation for monitoring the movement of the spiral tip requires:

- A power supply with crocodile clamps to heat NiTiNOL wires by Joule effect
- An anchor tool to lock the lower part of the structure
- A system that collects and analyzes data

5.2.1.   Power supply system

The current supply system in the laboratory allows to set a limit to the voltage and current (respectively 10 V and 1.5 A). Once the crocodile clamps are connected to the passive user (in our case the wire), one of the two parameters reaches the limit and the other adjusts according to the resistance. In the resistance, in addition to that proper to the NiTiNOL wire, we must also consider: the length of the wires of the supply system (with the material and the size) and the way the clamps are connected to the wires. The positive crocodile clamp starts from the power supply and is connected to the bottom of the spiral. The crocodile negative clamp, on the other hand, should reach

the tip of the spiral, but the direct connection cannot be done because the crocodile clamp weighs too much (and that may bend the structure). In order to minimize this phenomenon, a wire is added: one end of this wire is attached to the crocodile clamp and the other is connected to a line of nitinol on the tip of the spiral through a clamp with a screw. Moreover, the connecting wire is passed inside the structure to reduce as much as possible the weight that bends the structure.
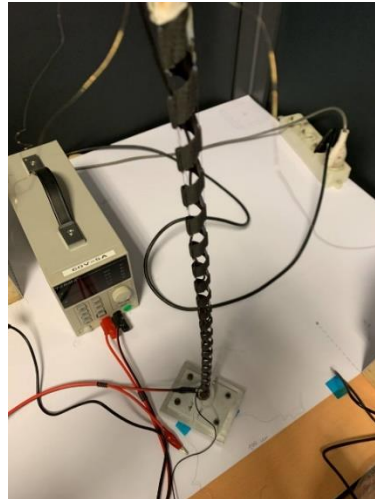
Figure 125: Additional wire passing through the structure

5.2.2.   Constraint at the basis of the structure

It is necessary to block the structure on one end in order to have a bending movement. The characteristics required for the constraint are:

- It must not compromise the functionality of the structure
- It must be removable and reusable (which therefore allows to save money and time)
- It must not deform/modify the structure or break the wires
- It must be rigid enough not to be moved due to activation of nitinol wires
- It must insulate the wires from each other
- It must electrically and thermally insulate the wires

The proposed solution is a constraint composed of aluminum base with a central cylinder on which the lower part of the structure is threaded. After placing the prototype, it is wrapped by an insulating rubber and then clamped by two pieces as shown below.
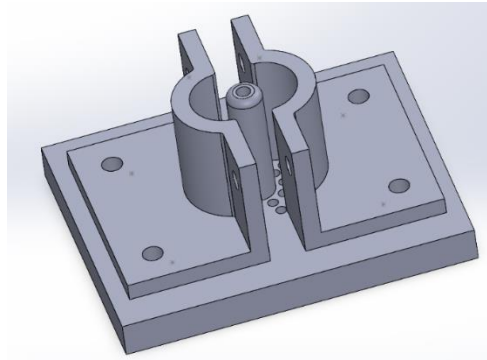
Figure 126: 3D model of the constraint

The base is a parallelepiped $10\,mm$ high, $100\,mm$ long and $80\,mm$ wide. On the surface, there are four slotted holes, $10\,mm$ long with a radius of $2.90\,mm$, near the four vertices of the rectangle. These holes are necessary to bind at different distances the two clamps from the structure. At the center of the surface, there is a $30-mm-$ high cylinder on which the prototype must be placed. At the base of this cylinder, there are 20 holes arranged on two circumferences, with different radii, concentric with respect to the central cylinder. The central cylinder has a radius of $9\,mm$ and the holes have a diameter of $3\,mm$. The distance between the holes is 36°. When the structure is placed, each wire should be passed through each hole at the base of the cylinder; moreover, the wires are locked separated from each other at the bottom of the parallelepiped. After placing the structure on the central cylinder, the prototype is clamped with two symmetrical pieces, created through additive manufacturing.
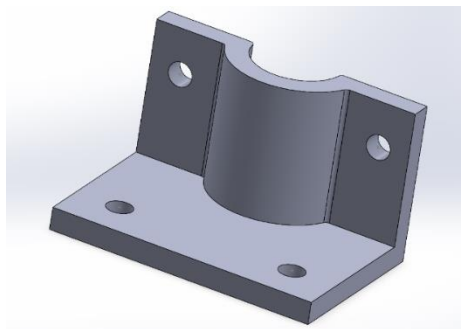
Figure 127: One of the pieces to clamp the structure

The lower part of the pieces has two holes so that the pieces are fixed with bolts on the base parallelepiped. The other two holes on the vertical walls block the structure by tightening the two pieces with bolts. The central half-circumference has a radius of $10\,mm$ and embraces a part of the structure with the insulating plastic. The workpiece has a thickness of $5\,mm$, a width of $60\,mm$ and a length of $40\,mm$. The vertical walls are $35\,mm$ high.

5.2.3. System for data collection

The most difficult part of the experiments was the realization of a system capable of keeping track of the three-dimensional movements of the tip of the spiral. Since there

was no machinery available to carry out the analysis, it was necessary to devise the data acquisition system before being able to analyze it. In the previous thesis, the movement of the spiral was followed by a camera that framed the prototype with a millimeter grid behind it. The displacement was then derived from the analysis of the video frames. In order to improve the accuracy of the system, different systems were considered that included the use of Arduino (receivers and transmitters, photo-resistances, etc.). But, among all the solutions designed, the most convenient was to use a tracking software that would allow to follow the movement of a marker placed on the tip of the spiral. The algorithm code was written in Python using Visual Studio Code. Two cameras were then used, placed on orthogonal planes, which framed the prototype from the front and side. The video frames were transmitted to the computer, which allowed them to be simultaneously viewed. After placing the marker on the tip of the spiral, the algorithm followed its movement and recorded its coordinates. The algorithm used is the Lucas-Kanade method [29].
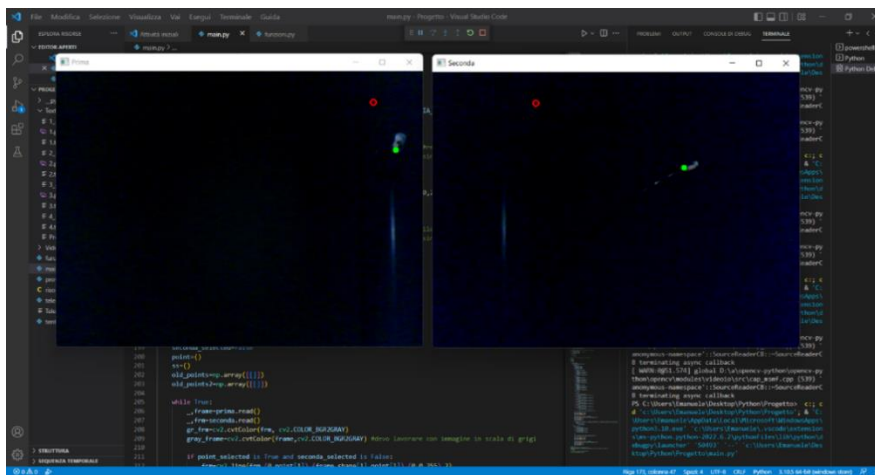
Figure 128: Pursuit of the tip of the spiral by the Lukas-Kanade method

5.2.3.1. Method of Lucas-Kanade

In the study of image sequences, an important role is played by the estimation of the movement that an object has performed between one frame and the next. In this regard, we talk about optical flow: it is a matter of determining vectors of motion on each pixel (or a subset of them). This is what the Lucas-Kanade method aims to do [30].
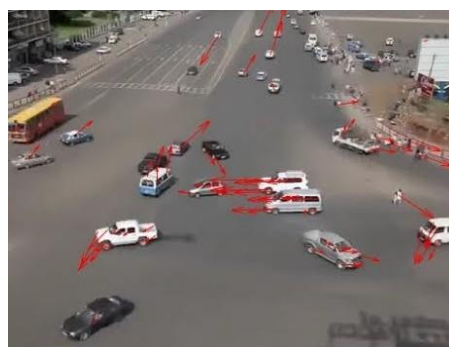
Figure 129: Example of the use of the Lucas-Kanade method

The assumptions behind the algorithm are as follows [30], [31]:

- Constant brightness: a pixel of a moving object does not change between frames; this means that in gray images, which will be the input of the implemented algorithm, the brightness does not change. Considering $I(x, y, t)$, the brightness of the pixel in the position (x, y) at instant t:

$$I(x, y, t) = I(x + dx, y + dy, t + dt) \rightarrow \frac{\partial I(x, y)}{\partial t} = 0 \tag{5.1}$$

- Small movements: the time intervals between one frame and the next are small enough so that the object in question does not move too far from the previous position. Starting from the equation of brightness we can write:

$$\frac{\partial I}{\partial x}\Big|_t \left(\frac{\partial x}{\partial t}\right) + \frac{\partial I}{\partial y}\Big|_t \left(\frac{\partial y}{\partial t}\right) + \frac{\partial I}{\partial t} = 0 \rightarrow I_x u + I_y v + I_t = 0 \tag{5.2}$$

The problem is that, in this case, we have more unknowns (u, v) than equations (one for each pixel). To overcome this obstacle, we need a third hypothesis.

- Spatial coherence: close points that belong to the same object have a similar movement and are projected at close points in the plane of the image. Then, if a group of pixels (p_i) confirms this hypothesis, it is possible to create a redundant system of equations that allows to overcome the stalemate of the previous point. For example, if one sets a 5x5 window around the reference pixel for brightness values, it is possible to set 25 equations.

$$0 = I_t(p_i) + \nabla I(p_i) \cdot [u \quad v] \tag{5.3}$$

$$\begin{bmatrix} I_x(p_1) & I_y(p_1) \\ I_x(p_2) & I_y(p_1) \\ \vdots & \vdots \\ I_x(p_{25}) & I_y(p_1) \end{bmatrix} \begin{bmatrix} u \\ v \end{bmatrix} = - \begin{bmatrix} I_t(p_1) \\ I_t(p_2) \\ \vdots \\ I_t(p_{25}) \end{bmatrix} \rightarrow Ax = b \tag{5.4}$$

This system can be solved by minimizing the least squares and, thus, the solution that is obtained is represented by the equation [32]:

$$\begin{bmatrix} u \\ v \end{bmatrix} = (A^T A)^{-1} A^T b \tag{5.5}$$

Specifically, the optical flux equation (5.2) defines a line in the velocity plane u and v, for each pixel. Considering all lines defined by all pixels nearby the reference one, it is assumed that the lines are not parallel, but defined by a similar 2D motion, so they will intersect close to the true 2D motion. The Lucas-Kanade optical flow algorithm uses a least-square linear method to analyze intersections of more than two lines. This method is used when the system is over-determined. So, a solution for (u, v) should

lie on these lines and it will be at the point of their intersection. This is illustrated in the image below.
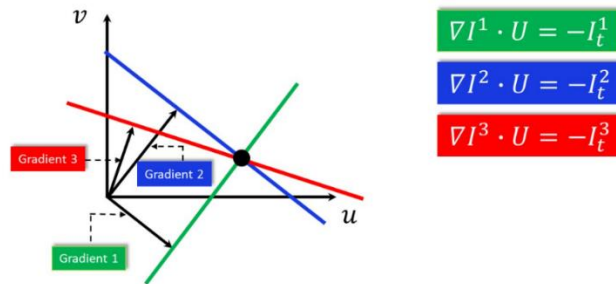
Figure 130: Solution of the over-determined Lucas-Kanade system

Of course, the equation can be solved when $A^T A$ is invertible, that is, when it has full rank equal to two, which happens in windows that include objects that are moving in two directions. $A^T A$ is not invertible also if the pixel (x, y) is located in a region with no structure (for example, if I_x; I_y and I_t are all zero for all pixels in the nearby areas). Even if the matrix is invertible, it can be ill conditioned. One way of testing how good the inverse of $A^T A$ is to look at the eigenvalues of this matrix. $A^T A$ is a symmetrical matrix, and, as such, can be diagonalized and written in the form:

$$A^T A = U \begin{bmatrix} \lambda_1 & 0 \\ 0 & \lambda_2 \end{bmatrix} U^T \tag{5.6}$$

Where U is a unitary 2x2 matrix. If $A^T A$ is not invertible, λ_1 or λ_2, or both, are zero. If one of them, or both, are very small, then the inverse matrix is ill-conditioned. Although one eigenvalue is much larger than the other, the matrix is ill-conditioned. It is possible to test the size of the eigenvectors by solving the characteristic equation:

$$det(A^T A - \lambda I) = 0 \tag{5.7}$$

Visual examples of cases where the $A^T A$ matrix is ill-conditioned are shown below.
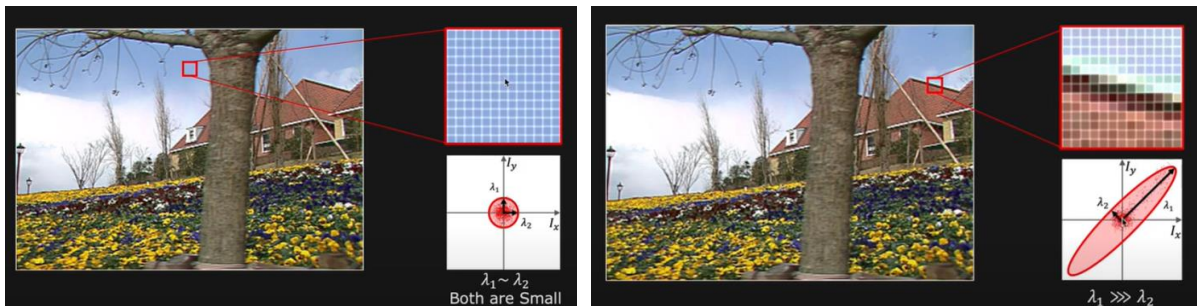
(a) Eigenvalues similar or close to zero   (b) An eigenvalue much greater than the other

Figure 131: Examples of an ill-conditioned matrix

Another problem to be considered is also the fact that often not even the hypothesis of small movements is valid. The algorithm described above would not work well in real cases and that is why the pyramidal image technique is commonly used.
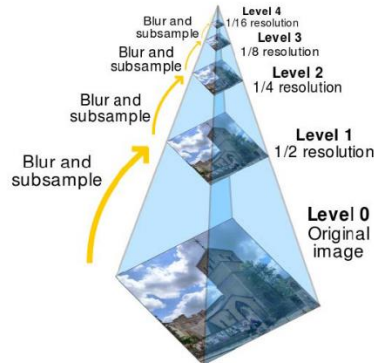
Figure 132: Pyramidal image technique

The starting image is blurred and subsampled several times, so as to obtain multiple images of different resolutions from the same scene. At this point, starting from the highest level of the pyramid, that is the one with the least detail, the optical flow is calculated and the resulting movement is used as a starting point for the next level, that is the one below, up to level 0. This way, it is possible to keep track of faster and wider movements.

5.2.3.2. Program for the analysis of movement

Through Visual Studio Code and the Python programming language, we created a program [33] that uses the two cameras connected to the computer and the Lucas-Kanade method to follow the movement of the tip of the structure. Before doing the experiments, it is necessary to calibrate the cameras, because the resolution in the movements depends on the distance of the cameras from the spiral. The semi-angle of the optical cone of the spiral has been obtained experimentally and turns out to be $\alpha = 24.1022°$. The cameras used have a resolution of 640x480 pixels. From these parameters, it is possible to derive how many millimeters correspond to the displacement of a pixel and then to find the accuracy of the calculated movements.
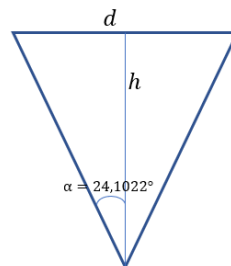
Figure 133: Angle of view cone

$$i = \frac{h}{\cos\alpha} \longrightarrow d = 2\,(i\,\sin\alpha) \longrightarrow risoluzione = \frac{d}{640}$$

Figure 134: Calculation for the accuracy

After connecting the power supply to the structure and placing the prototype in the correct position, the program is ready to start.
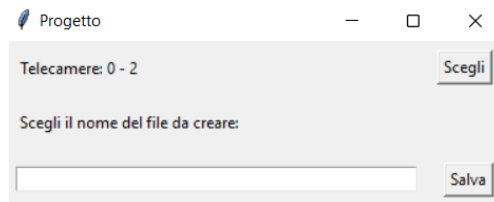
Figure 135: Home page of the program

The starting page of the program requires to enter the name of the text file to be created, on which the coordinates of the tip of the spiral will be saved, and requires to save it with the "Salva" button in order to continue. If a name that was already used is chosen, the program will not allow to go ahead without changing it. It also keeps track of the cameras used the previous times. The computer assigns a number to each output on which there is a camera (the maximum number of outputs allowed is 5). From the image, it is possible to see that, previously, the output 0 and output 2 cameras were used. If one wants to change cameras, it is necessary to press the "Scegli" button.
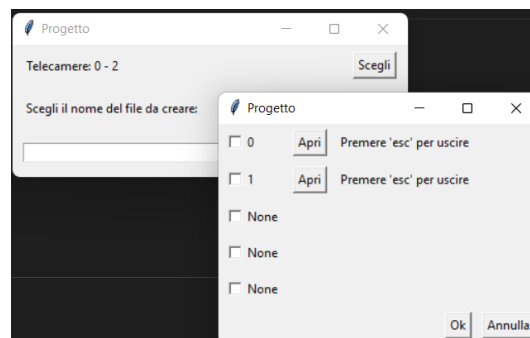
Figure 136: Window to choose the cameras

Pressing the "Scegli" button will open a window that will allow to choose the cameras to use. On the exits where there are no cameras there is no output number, but the word "None". It is possible to view the camera connected to a number by pressing the "Apri" button. This will open a window that will show the frames from the camera connected to that output number. After choosing the cameras, marking them with a tick (no more than two, otherwise an error message will appear), one has to press "Ok" and return to the previous window with the number of cameras updated. Once the text file to save the data is created, the frames of both cameras will be projected at the same time. It is therefore necessary to select on the two windows the point that the tracker must follow, that is, the tip of the spiral (whose initial position will be marked with a red circumference, while the dot that follows the tip in the movement will be a green circle).
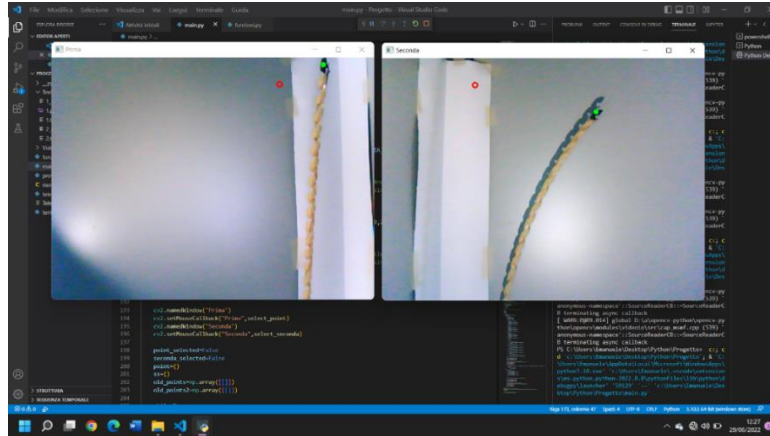
Figure 137: Tracer of the tip of the spiral

At this point, the power supply system is activated and the wire will heat up by Joule effect, moving the structure. The Lucas-Kanade algorithm, thus, takes the incoming coordinates of the point in a frame and returns the coordinates of the point on the next frame. For each frame, the coordinates of the point and the distance of the point from the initial position are shown in the created document. While the program continues to operate, the power supply system is turned off and the wire is turned off as well to record the movement of the cooling phase. When the experiment is considered to be finished, the space bar is pressed in order to move forward. The program will thus create a graph with, on the x-axes, the period of the experiment and, on the y-axes, the displacements. It is also created a fast-paced 3D video which simulates the movement of the structure. Every time a single wire is analyzed, the power supply system must be connected and then disconnected. Each wire is activated and deactivated 10 times (in order to have a statistically acceptable number of data) and each time the data is recorded as described above.

5.2.3.3. Post-processing

The previous analysis allows to obtain the vector of the displacements of the traced point with respect to the initial position. However, the program does not allow to obtain the corresponding time vector. In order to analyze the results, it is necessary to create a vector, with the same number of elements of the vector of the displacements, but ranging from 0 to 1. In this way, one does not have the true period of the experiment, but the portions of the vector in which there is activation or deactivation of the wire in percentage terms can be compared. It must be chosen a limit beyond which to consider that the activation of the wire is initiated and one beyond which to consider that it is over. This also applies to the deactivation phase. To do this, we use a smoothing technique of the displacement curve and we calculate the difference between each element and the next one of the vector of the displacements (the vector thus obtained is called the vector of differences). In this way, we obtain a second graph with the period between 0 and 1 on the x-axes and the difference of the displacements on the y-axes (the vector of differences). 5% of the maximum difference of the last

graph was chosen as a threshold to consider that the wire is being activated. The wire is activated if more than 5 elements of the vector of differences are greater than the threshold value. The activation phase is considered to be finished after more than 5 elements of the vector of differences are less than 5% of the maximum difference (after the activation has started). On the other hand, it is considered that the wire is deactivated after more than 5 elements of the vector of differences are less than 5% of the minimum difference (after the end of the activation). The deactivation phase shall be deemed to have ended after more than 5 elements of the vector of differences are greater than 5% of the minimum difference (after the start of deactivation). The graphs described are shown below:
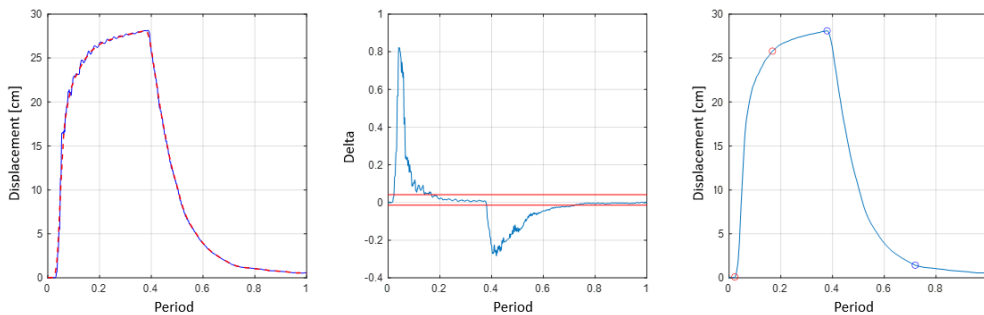
Figure 138: Vector of displacements and vector of differences graphs

On the left, there is the graph of the vector of displacements, compared to the period 0 to 1, before and after the smoothing of the curve. In the center, there is the graph of the vector of differences, compared to the period from 0 to 1. On the right, there is the graph of displacements with the activation phase highlighted (with 2 red dots) and deactivation (with 2 blue dots).

5.3.   Results of the experiments

Before doing the experiments, the accuracy of the results obtained with this data acquisition system was tested. We analyzed one camera at a time. After defining the distance between the moving object and the camera and calculating the resolution, a path of 20 *cm* is marked. The movement of the object along this path is tracked by the program that uses the Lucas-Kanade algorithm. The motion was repeated 30 times for each camera. The results are shown below, with the mean value and the standard deviation.

Camera	Y	Average	Stn. Dev.
18.9	0.24447282	19.88316	0.907851
19.488	0.39971989		
21.7794	0.04960645		
20.07376	0.42985655		
19.765	0.43572973		
19.618	0.42108695		
20.645	0.30901355		
21.156	0.16445411		
22.0146	0.02792243		
20.25416	0.40423193		
19.278	0.35189307		
19.05648	0.29029849		
19.23	0.33923266		
19.79	0.4371284		
18.58797	0.15882897		
21.3161	0.126448		
19.899	0.43936878		
19.44937	0.39202978		
19.68	0.42856981		
20.4498	0.36165951		
20.2837	0.39868124		
18.297	0.09550894		
21.23455	0.14512271		
19.06977	0.29416256		
19.1558	0.31879375		
19.3341	0.36599105		
20.0919	0.42797159		
19.55649	0.41188963		
19.5776	0.41523803		
19.4631	0.39482781		

Figure 139: Data accuracy of data acquisition system

The results obtained confirm the accuracy of the method used. Then, the instrument can be calibrated with the distances of the cameras from the prototype. Subsequently, the wires, connected to the power supply system, are tested one at a time on the different structures. In order to distinguish the tip from the rest of the structure, the tip was colored white for the carbon structure and black for the glass structure. The colored portion is 2 cm high. Since the program sees a uniform portion on the tip, the tracker (green dot) can move within this area. This leads to an error that could be at most 1 cm on the position of the tip of the spiral. Due to the large amount of data, only a few graphs are given as an example. The complete data collection is however reposted in the appendix F.

5.3.1. Structure with an embedded wire

The considered structure is composed of 4 layers of $0.12 - mm - $ thick carbon-fiber fabric C_{12}). Only one wire of NiTiNOL is embedded into the structure. An example of the graph through the created program is proposed below:
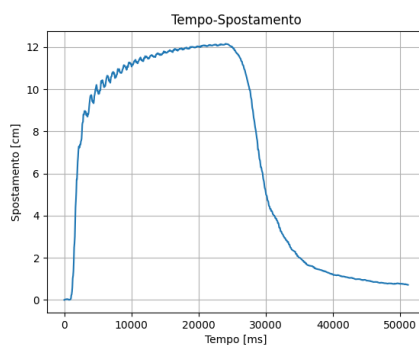
Figure 140: Graph of the second wire activation with Python at the ninth activation

The activation and deactivation phases are clearly distinguished. The oscillations are due to the elasticity of the structure that is opposed to the force generated by the shape memory alloys. Analyzing the displacement vector as described above with Matlab, we have:
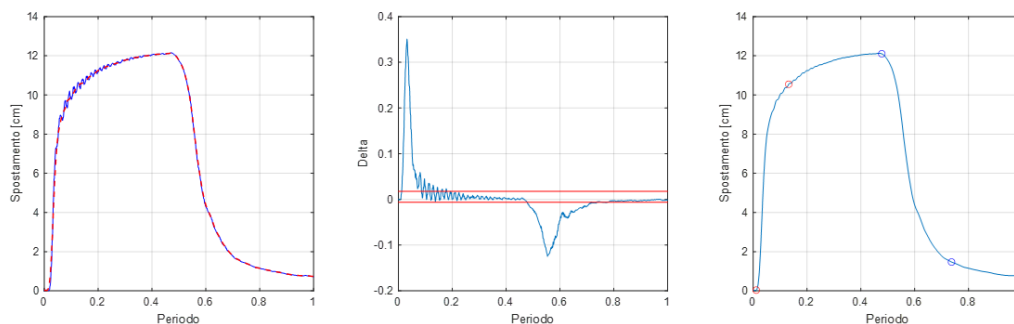
Figure 141: Analysis of the above graph with Matlab at the ninth activation

Table 98: Table of averaged quantities

	Max displacement [*cm*]	Residual displacement [*cm*]	% Activation	% De-activation
1st wire	12.18439	0.680322	10.5	28.8

The activation rate is one third of the deactivation rate. The maximum displacement achieved by the structure is about 12 *cm* and the residual deviation from the initial position is almost negligible. The slope of the activation part is very steep, so the wire is activated very quickly.

5.3.2. Structure with 2 wires with sheaths

There are two wires of NiTiNOL inside sheaths that are embedded into the C_{12} structure. In this particular case, there was a considerable difference in the movements between one wire and another. By replacing the wire that generated the minor displacements with a new wire (this process was possible thanks to the presence of sheaths in the structure which do not bind the wire to the composite), displacements were obtained in line with those of the other wire. This confirms the fatigue problem

caused by the activation and deactivation cycles of the shape memory alloys (in fact, the prototype had been already used in the previous thesis).

1st old wire 1st new wire 2nd wire
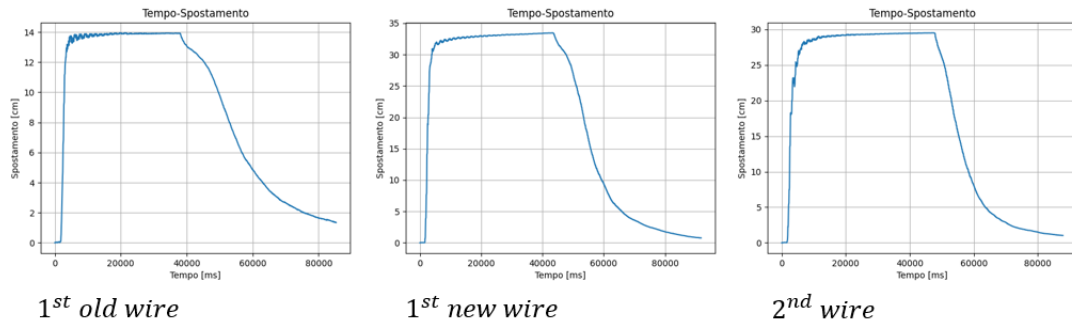
Figure 142: Experimentally obtained movements at the ninth activation
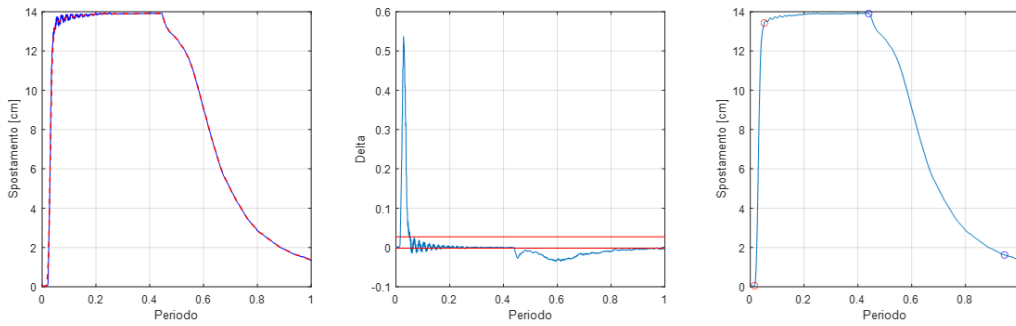
Figure 143: Analysis with Matlab of the old wire at the ninth activation
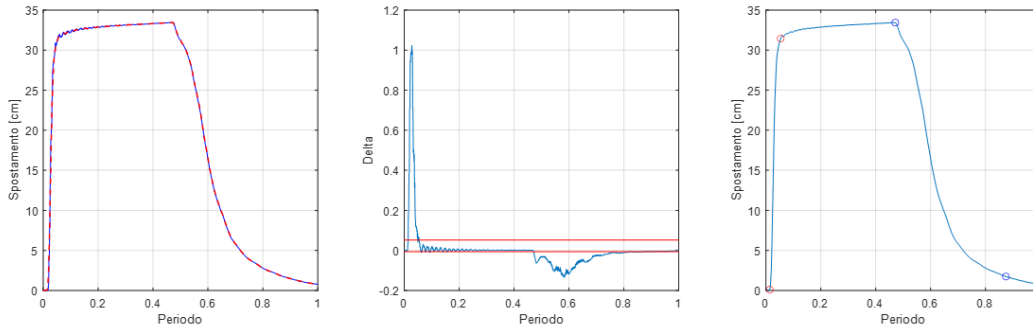
Figure 144: New wire analysis with Matlab at the ninth activation
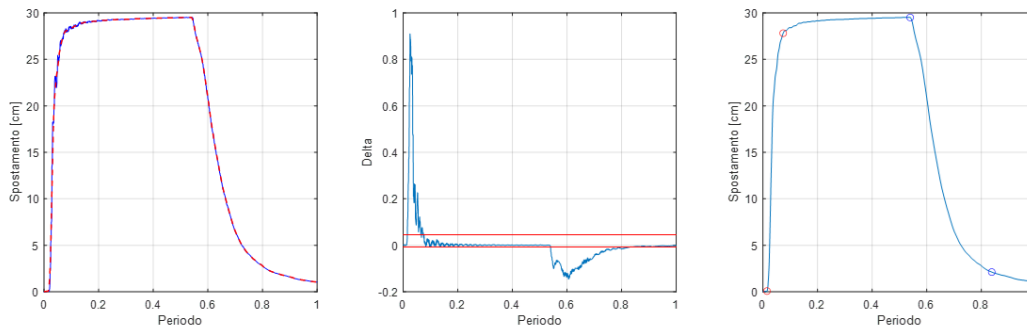
Figure 145: Matlab analysis of the second wire at the ninth activation

Table 99: Table of averaged quantities

	Max displacement [*cm*]	Residual displacement [*cm*]	% Activation	% De-activation
1st old wire	14.36037	1.089225	3.7	51.7
1st new wire	34.43166	1.139566	5	42.1
2nd wire	30.05163	0.886102	7.7	32.5

The old wire allows a displacement that is half of the displacement allowed by the new wire. The old wire always activates faster, but deactivates more slowly than the new wire. Also this time, the oscillations could be due to the elasticity of the structure. The maximum displacement obtained with the new wires is about $30\,cm$. The ratio between the percentage of activation and deactivation of the old wire is about 1/2 of the percentages of the new wires.

5.3.3. Structure with 2 embedded wires

The considered structure is composed of 4 layers of $0.12-mm-$ thick carbon-fiber fabric. There are two wires of NiTiNOL directly embedded into the structure.

1st wire 2nd wire
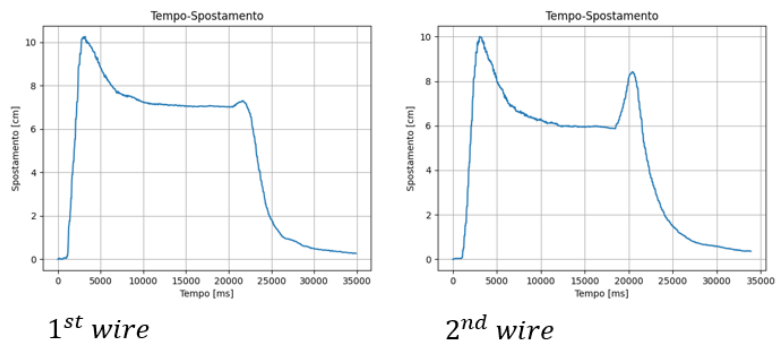
Figure 146: Experimentally obtained movements at the ninth activation
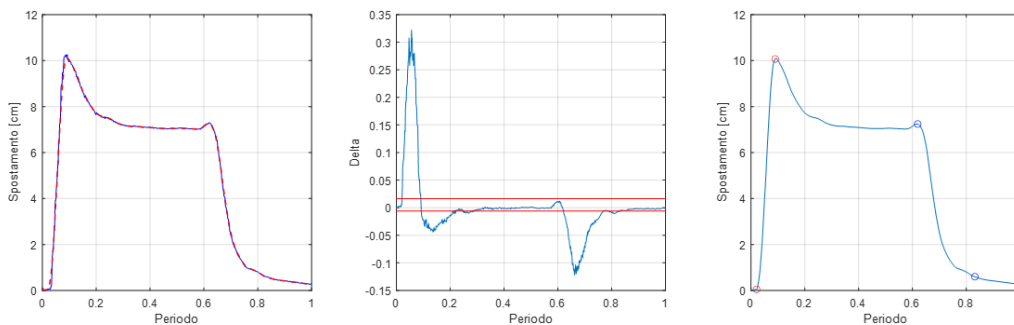
Figure 147: First wire analysis with Matlab at the ninth activation
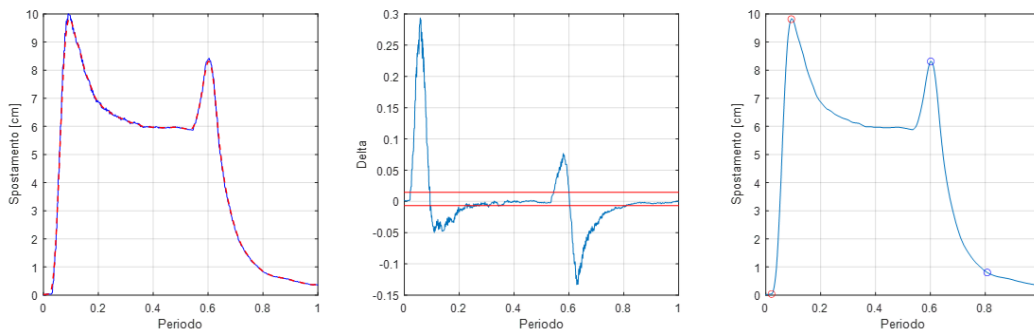
Figure 148: Second wire analysis with Matlab at the ninth activation

Table 100: Table of averaged quantities

	Max displacement [*cm*]	Residual displacement [*cm*]	% Activation	% De-activation
1st wire	10.30181	0.459974	7.3	21.6
1st wire	9.979267	0.46571	6.2	23

This is the only structure that behaves abnormally during the activation and deactivation of the wires. After the very fast activation, the structure goes back and settles to a displacement of about 2%-4% smaller than the maximum displacement during activation. The deactivation phase, on the other hand, starts when the power supply is turned off, the structure first increases the displacement and then returns to the initial position. This anomalous behavior is due to errors in the production of the structure itself. The calculation of the percentages of activation and deactivation times is also affected by these phenomena. This is why the activation and deactivation percentages are slightly higher than those calculated. The maximum displacement is about 10 *cm* and the residual one is negligible. Also in this case, the activation time (which turns out to be very fast because the graphs have a great slope) is about 1/3 of the deactivation time.

5.3.4. Structure with 3 wires with sheaths

The considered structure is composed of 4 layers of $0.12 - mm - thick$ carbon-fiber fabric. There are three wires of NiTiNOL inside sheaths embedded into the structure.

1st wire 2nd wire 3rd wire
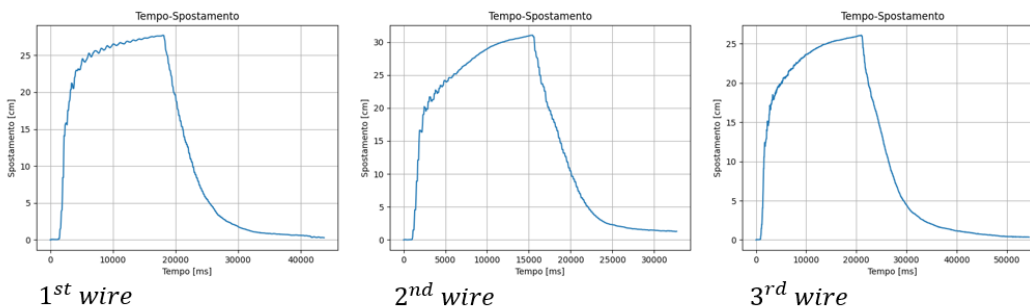
Figure 149: Experimentally obtained movements at the ninth activation
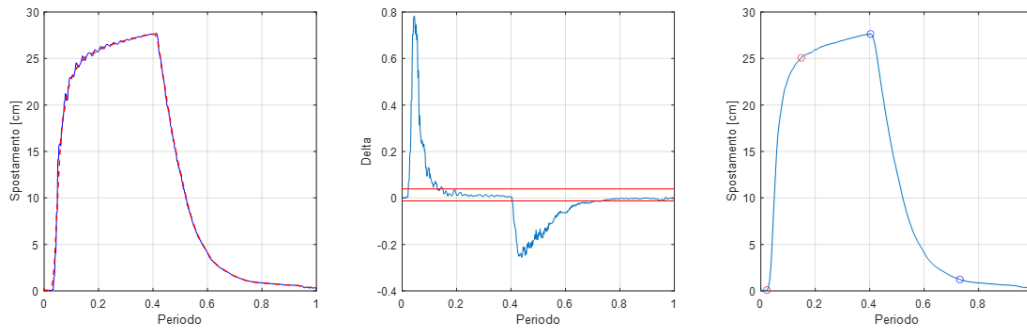
Figure 150: First wire analysis with Matlab at the ninth activation
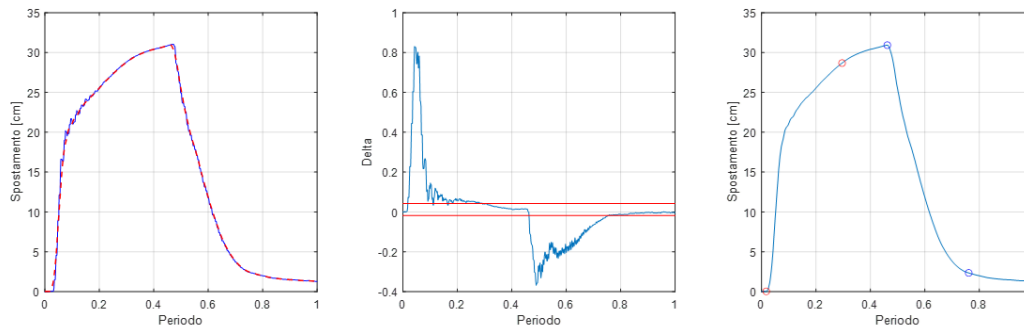
Figure 151: Second wire analysis with Matlab at the ninth activation
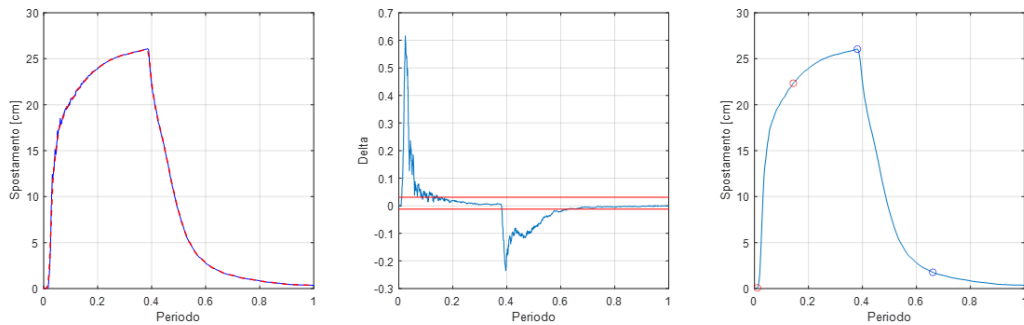
Figure 152: Third wire analysis with Matlab at the ninth activation

Table 101: Table of averaged quantities

	Max displacement [*cm*]	Residual displacement [*cm*]	% Activation	% De-activation
1st wire	28.62141	0.589505	11.20087	30.29782
2nd wire	30.86154	0.866888	23.8977	27.32522
3rd wire	26.68996	0.827506	19.80538	28.81014

The maximum displacement is about 30 *cm*. Also in this case, there are small oscillations that can be due to the created program or the elasticity of the structure. The activation phase can be divided into two parts: the first part has a great slope and is very fast, the second part has a low slope and allows a slow achievement of the maximum displacement. The activation time is shorter than the deactivation time, but

the slow transition to the maximum displacement makes the times of the two phases comparable.

5.3.5. Structure with 6 embedded wires

The considered structure is composed of 4 layers of $0.12 - mm - thick$ carbon-fiber fabric. There are six wires of NiTiNOL directly embedded into the structure.
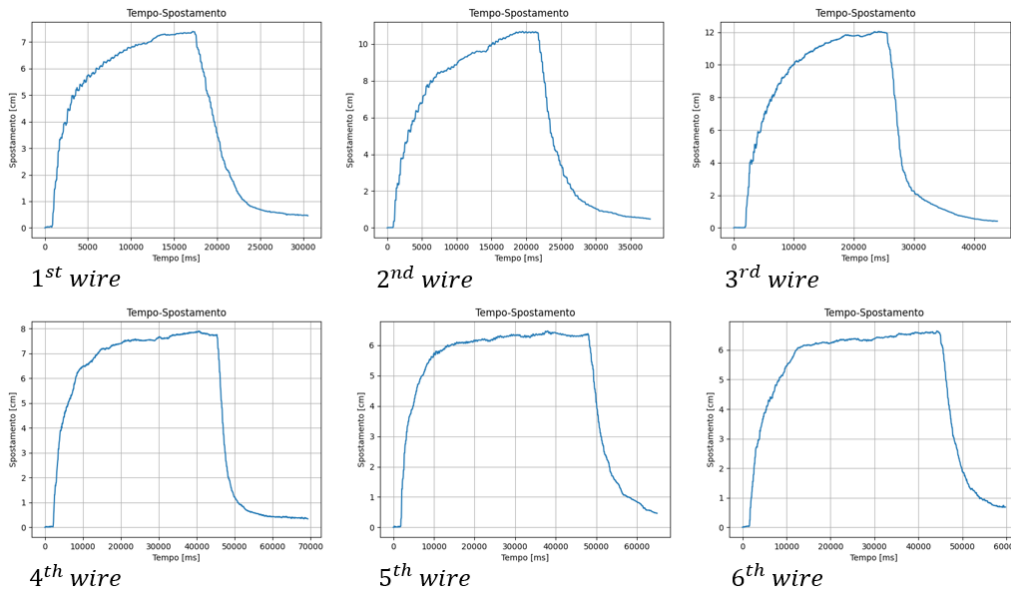
Figure 153: Results obtained experimentally at the seventh activation
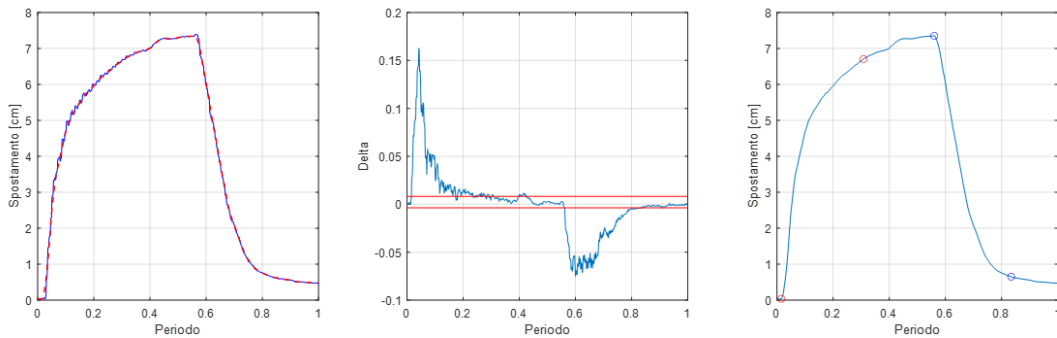
Figure 154: First wire analysis with Matlab at the seventh activation
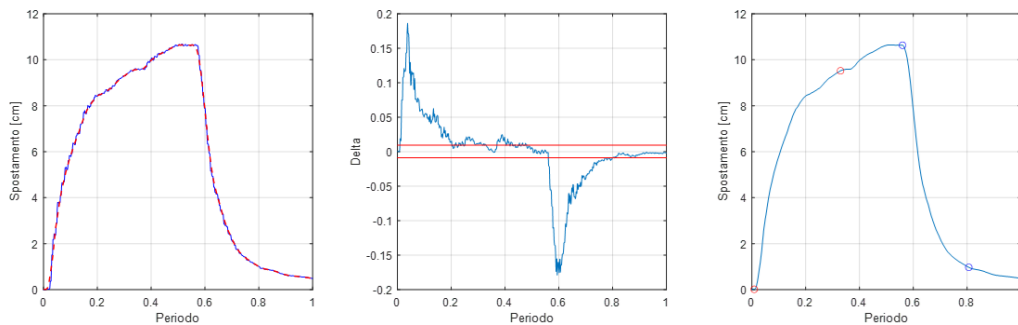
Figure 155: Second wire analysis with Matlab at the seventh activation
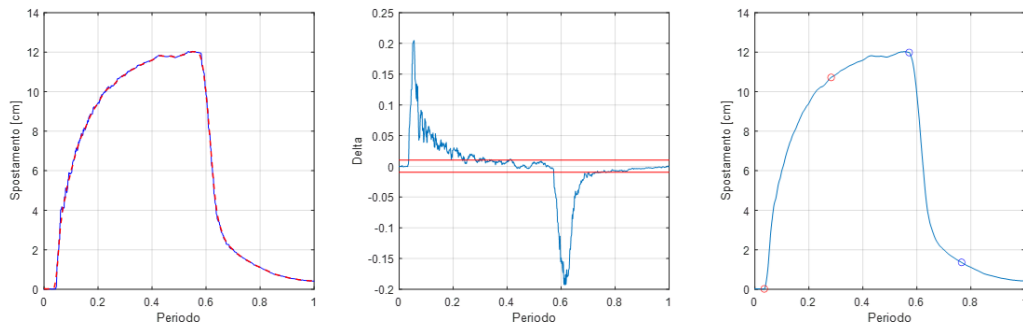
Figure 156: Third wire analysis with Matlab at the seventh activation
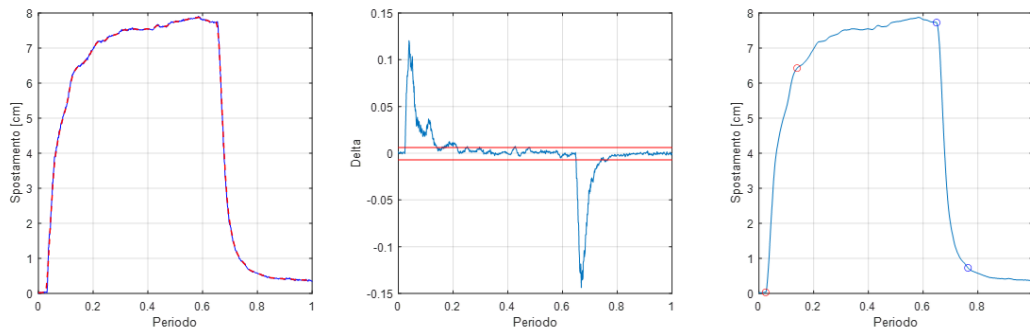
Figure 157: Fourth wire analysis with Matlab at the seventh activation
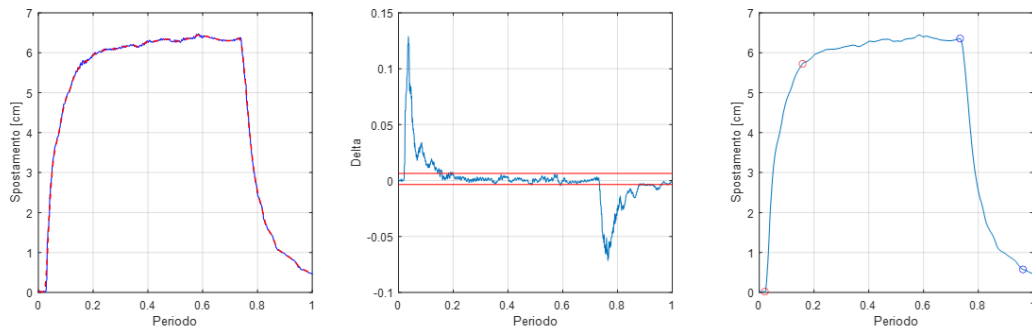
Figure 158: Fifth wire analysis with Matlab at the seventh activation
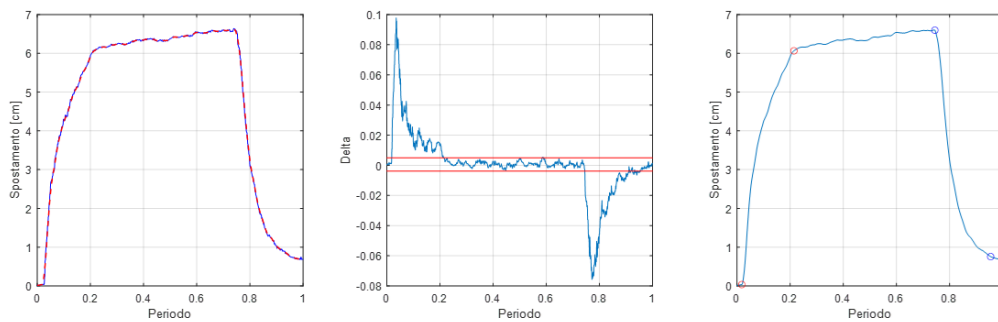
Figure 159: Sixth wire analysis with Matlab at the seventh activation

Table 102: Table of averaged quantities

	Max displacement [*cm*]	Residual displacement [*cm*]	% Activation	% De-activation

1st wire	7.409339	0.393498	22.7	29.4
2nd wire	10.61826	0.454563	24	23
3rd wire	12.21585	0.561323	22.6	22.4
4th wire	7.845275	0.387306	21.8	16.9
5th wire	6.569035	0.465062	16.2	21.4
6th wire	6.589329	0.510426	18.6	21.2

In this structure, the displacement for all wires is about $10\ cm$. The activation and deactivation times are comparable and the low slope implies a long transient for the achievement of the maximum displacement. Moreover, the curves are richer in oscillations, especially towards the maximum displacement value.

5.3.6. Structure with 3 wires with sheaths

The considered structure is composed of 6 layers of $0.12 - mm -$ thick glass-fiber fabric. There are three wires of NiTiNOL inside sheaths that are embedded into the structure. During the production of this prototype, the excess resin entered the sheaths binding the wires after solidifying. For this reason, even though the structure has the sheaths inserted, the wires still remain stuck in the composite.

$1^{st}\ wire$ $2^{nd}\ wire$ $3^{rd}\ wire$
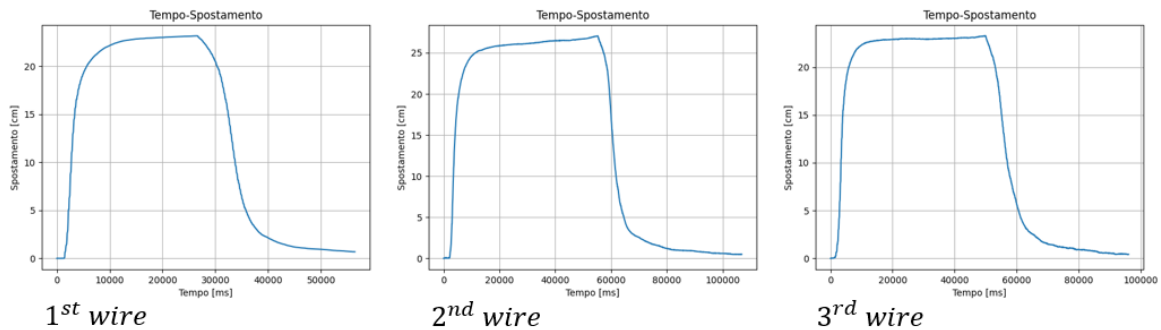
Figure 160: Results obtained experimentally at the fifth activation
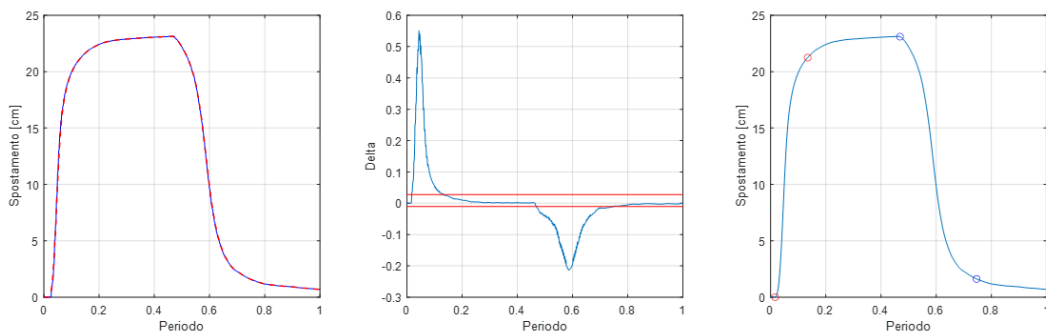
Figure 161: First wire analysis with Matlab at the fifth activation
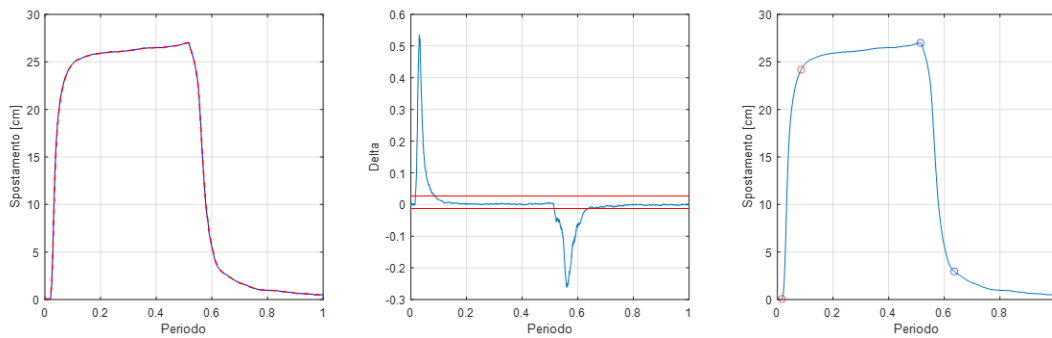
Figure 162: Second wire analysis with Matlab at the fifth activation
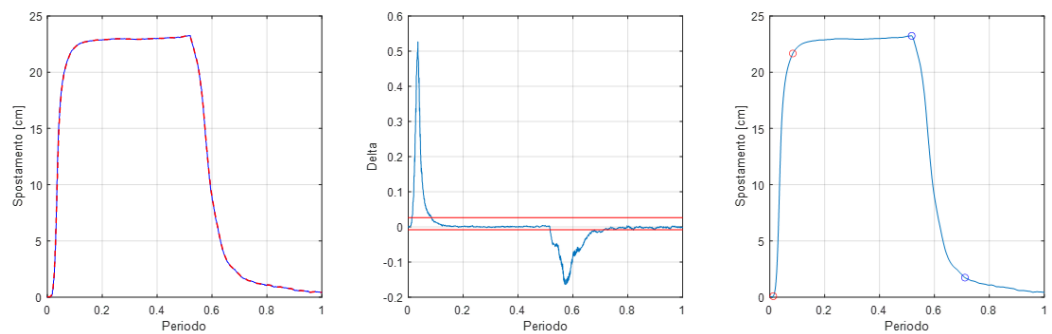
Figure 163: Third wire analysis with Matlab at the fifth activation

Table 103: Table of averaged quantities

	Max displacement [cm]	Residual displacement [cm]	% Activation	% De-activation
1st **wire**	23.36544	0.792598	11	27.3
2nd **wire**	25.72886	1.417794	9.7	17.8
3rd **wire**	24.17042	1.096841	9.1	21

The maximum displacement is about 25 cm. The activation is very fast with a steep slope, the deactivation is about twice the activation. The deactivation has two different gradients: the first is smaller, which implies more time, while the second is greater. All the curves are very clean and regular, without oscillations and with very noticeable plateaus. The analysis showed that the structures containing the sheaths allow a greater displacement (almost double) and have longer deactivation times than the structures without sheaths. There are no major differences between glass and carbon structures for both maximum and residual displacement. Glass has the advantage of better insulation; this allows the structure to be activated very quickly. For this reason, the first part of the wire deactivation has a lower slope. In addition, the glass structure has no oscillations, while the structure that has the highest number of oscillations is the one with only one wire incorporated. Then, decreasing the number of wires increases the flexibility of the structure. From all the analyses it emerged that the optimal structure must be made of glass fiber fabric, maybe of 6 layers.

6   Conclusions and future

The aim of this thesis was to optimize, from a thermo-mechanical point of view, the prototype obtained after the initial design phase. Four structures of different thickness and different materials were considered. The mechanical analysis has allowed to vary the characteristic geometric parameters of the structure and to see how the flexibility of the structure is affected, during the activation phase of the NiTiNOL wires, and the stiffness of the structure, during the wire deactivation phase. The experiments were necessary in the study of the actual movement of the structure. Moreover, aspects that had never been taken into consideration were evaluated: the influence of the number of NiTiNOL wires and the influence of the use of sheaths in the displacement of the structure. Thermal analysis, on the other hand, allowed to see the behavior of the structure directly in the environment in which it will operate. Also in this study, having considered different structures, allows you to choose the solution that best meets the design needs. Various cooling mechanisms of the structure have also been proposed that can be used for the thermal control of the prototype or to reduce the high temperatures that can be reached in space (which can also affect the behavior of shape memory alloys). In addition, certain methods of thermal protection against radiation have been proposed.

The four analyses carried out yielded different results. The thermal analysis confirmed the great insulating capacity of the glass fiber fabric compared to the carbon fabric, which allows the high temperatures of the composite to be contained around the wire. The structure with 4 layers appeared to be the most convenient because less affected by radiation. The analysis of cooled then confirmed the advantages of the use of sheaths (both thermal and mechanical, then confirmed by experiments). Moreover, among the various cooling mechanisms for convection those with air (forced convection) and water (free convection) were the most convenient. Mechanical analysis has provided important information for the realization of even more flexible or rigid structures. The experiments then gave the results obtained and highlighted other problems (such as fatigue) to be addressed in subsequent work.

One aspect to be analyzed, which has not been considered, is the effect of fatigue and aging on shape memory alloys. As seen from an experiment, wires can reduce their ability to move the structure by half if they are used repeatedly or if they are stored incorrectly. Another aspect that has been noticed during the work is the complex movement of the structure that during the movements, does not move on the axes but

tends to twist and fold on itself. The structures should also be tested in a space-like environment to confirm the results obtained from thermal analysis.

The Abaqus model and the calculation models used with Matlab are not very detailed, but useful for this first thermal analysis and optimization. In the future, it will be necessary to create more detailed and accurate calculation models. This will be useful especially in the creation of a system of control of the movement of the structure as some aspects treated, such as the diffusion of heat in the structure and therefore the influence of the activation of a wire on the other wires, will be fundamental.

The use of prototypes as fuel refueling systems has been considered, but the use of the structure as a tool for the control and inspection of inaccessible areas can also be studied. So, in addition to the control of the structure is necessary to adapt it to a weight like a camera to be placed on the tip of the spiral.

The next steps are therefore the development of more complex and accurate models, simulations in a space-like environment and the creation of a system to control the movements of the structure.

7 Bibliography

[1] K. Lygin, P. Labenda and T. Sadek, "Prediction of Transformation Behavior of R-phase SMA actuators by the application of Fuzzy Logic," *Materials Science Forum*, pp. 584-588, January 2013.

[2] V. Valentina, P. Franco and T. Enrico, "Meteriali a memoria di forma: caratterizzazione e applicazioni nel campo dei Beni Culturali," *ALMA Master Studiorum-Università di Bologna*, 2008.

[3] P. Lucio, S. Giuseppe and A. Alessandro, "Progetto di un rivestimento flessibile attuato per strutture con capacità di variazione di forma," *Politecnico di Milano*, 2012.

[4] L. L. Salvatore and S. Giuseppe, "Progettazione e sperimentazione di un dispositivo di sicurezza basato su attuatori in lega a memoria di forma," *Politecnico di Milano*, 2010.

[5] A. S. o. T. a. Materials, "ASTM E111-97 Standard Test Method for Young's Modulus, Tangent Modulus, and Chord Modulus," in *A.I. Standard*.

[6] S.W.Samwel, "Low Earth Orbital Atomic Oxygen Erosion Effect on Spacecraft Materials," *Space Research Journal* , vol. 7, pp. 1-13, 2014.

[7] Z. J. e. al, "Outgassing Environment of Spacecraft: An Overview," *IOP Conference Series: Materials Science and Engineering*, vol. 611, 2019.

[8] C. Menna, F. Auricchio and D. Asprone, "Applications of Shape Memory Alloys," in *Shape Memory Alloy Engineering*, Elsevier Ltd, 2015.

[9] A. Razov and A. Cherniavsky, "Applications of shape memory alloys in space engineering: past and future," *8th European Space Mechanisms and Tribology Symposium*, vol. 438, p. 141, 1999.

[10] O. J. Godard, M. Z. Lagoudas and D. C. Lagoudas, "Design of space systems using shape memory alloys," *Smart Structures and Materials 2003: Smart Structures and Integrated Systems,* vol. 5056, pp. 545-558, 2003.

[11] L. McDonald and Schetky, "Shape memory alloy applications in space systems," *Materials & Design,* vol. 12.1, pp. 29-32, 1991.

[12] E. Naggar, Abdelmoneim and M. A. Youssef, "Shape memory alloy heat activation: State of the art review," *AIMS Materials Science,* vol. 7.6, pp. 836-858, 2020.

[13] T. Biasutti, P. Bettini and D. Rigamonti, "Hingeless arm for space robotics actuated through shape memory alloys," *Politecnico di Milano,* 2021.

[14] L. Casonato, E. Angelini, S. Grassini, F. Tessarin and T. Schillaci, "Bio inspired smart materials applied to Spacecraft Thermal Control," *Politecnico di Torino,* 2018.

[15] R. B. Bird, W. E. Stewart and E. N. Lightfoot, Transport Phenomena, John Wiley & Sons, Inc., 2002.

[16] U. D. o. Energy, Doe Fundamentals Handbook - Thermodynamics, Heat Transfer, and Fluid, Lulu.com, 2016.

[17] A. Raid, M. Benzohra, M. Mansouri and A. Alhamany, "Radiation effect on shape memory alloy," *Preprints,* 2018.

[18] N. Giorgi and A. Gregorio, "Studio dell'analisi termica e dell'assetto per il satellite didattico Atmocube," *Università degli studi di Trieste,* 2009.

[19] G. Sguotti, A. Francesconi and A. Lorenzetti, "Modellazione termica e valutazione sperimentale delle fasi di riscaldamento e raffreddamento di uno SMP per applicazioni spaziali," *Università degli studi di Padova,* 2014.

[20] G. Sardano, C. F. Badini and A. Caradonna, "Compositi conduttivi a matrice polimerica contenenti filler carboniosi," *Politecnico di Torino.*

[21] B. Tuberosa, E. Troiani , S. Sangiorgi, M. Scafè and P. Marabini, "Proprietà meccaniche a trazione di compositi polimerici rinforzati con fibre lunghe di carbonio di interesse per il settore automotive," *ALMA Mater Studiorum-Università di Bologna,* 2012.

[22] G. D. Di Leone, P. Maggiore , M. D. L. Dalla Vedova and J. D. Luca, "Confronto tra più architetture di circuito a fluido bifase meccanicamente pressurizzato e relativo progetto perliminare per MMRTG di rover marziano," Politecnico di Torino, Torino.

[23] P. Sutheesh and A. Chollackal, "Thermal performance of multilayer insulation: A review," *IOP Conf. Series: Materials Science and Engineering,* vol. 396, 2018.

[24] B. M. S. Rose, G. Srilochan and L. Galfetti, "Hydrogen peroxide based green propellants for future space propulsion applications," *Politecnico di Milano,* 2021.

[25] T. L. Bergman, A. S. Lavine, F. P. Incropera and D. P. Dewitt, Foundamentals of heat and mass transfer, Jefferson City: John Wiley & Sons, 2011.

[26] R. Giorgio, A. Carpignano, R. Gerboni and G. Ballocco, "Conversione di una piattaforma petrolifera in dismissione e del relativo reservoir in sito di stoccaggio temporaneo per una miscela di idrogeno e gas naturale. Progettazione preliminare.," *Politecnico di Torino,* 2021.

[27] P. H. Oosthuizen and W. E. Carscallen, Introduction to Compressible Fluid Flow, Boca Raton: CRC Press/Taylor & Francis, 2015.

[28] L. Nele, A. Caggiano and R. Teti, "Autoclave Cycle Optimization for High Performance Composite Parts Manufacturing," *Procedia CIRP,* vol. 57, pp. 241-246, 2016.

[29] B. D. Lucas and T. Kanade, "An iterative Image Registration Technique with an Application to Stereo Vision," in *Proceedings of the 7th International Joint Conference on Artificial Intelligence (IJCAI '81),* April 1981.

[30] C. Fantozzi and S. Mazzocca, "Stima della posizione in dispositivi mobili, con applicazione a uno strumento musicale virtuale," *Università degli Studi di Padova,* 2015.

[31] A. Romanoni, M. Matteucci and D. Rizzi, "Ricostruzione 3D delle traiettorie veicolari da immagini di una o più telecamere," *Politecnico di Milano,* 2011.

[32] N. Peters, F. Toschi and A. Corbetta, "Optical flow in Pedestrian Tracking, Turbolence and Vortex Dynamics," *Eindhoven University of technology ,* 2019.

[33] G. Casciola and P. Varano, "Elaborazione di immagini con la libreria OpenCV," *ALMA Master studiorum, Università degli studi di Bologna,* 2009.

A Appendix A

A.1. Theoretical experimental setup

A power supply, which was directly connected to the wires through clamps, was employed in order to activate the wires through the Joule effect during the experiments. The auto-ranging power supply system in laboratory was set with a maximum voltage of $10\ V$ and a current of $1.5\ A$. The voltage and current present on the wire depend on the resistance of the wire (which depends on the wire itself, on how the wire is embedded in the structure, how the wire is bound to the structure and how the power supply is connected to the wire). If one of the two parameters reaches the maximum, the other adapts according to the resistance. The problem with this type of activation is the constraint of the activation of one wire at a time (or, at most, two). Each time one has to activate a different wire, it is necessary to disassemble the system and reassemble it on the new wire. To overcome this obstacle, we devised a system that can be connected to several wires and can allow them to be activated separately or simultaneously. In the initial design phase, a layout was chosen with a dedicated display and potentiometer for each wire to be controlled. The control circuit of a single wire is shown below. The nitinol wire is modeled as a $12\ \Omega$ resistance. There is a $12\ V$ transformer (directly connected to power outlets), slightly higher than the voltage previously used to compensate all the losses due to the construction material of the model. A theoretical image of the piece and a representation of a circuit proposed as a solution is shown below:
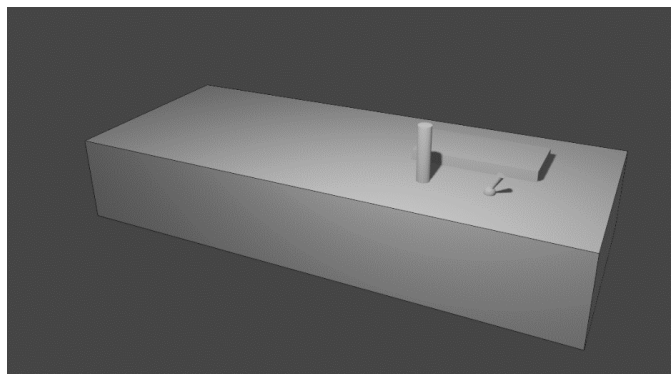
Figure 164: Theoretical representation of the instrument
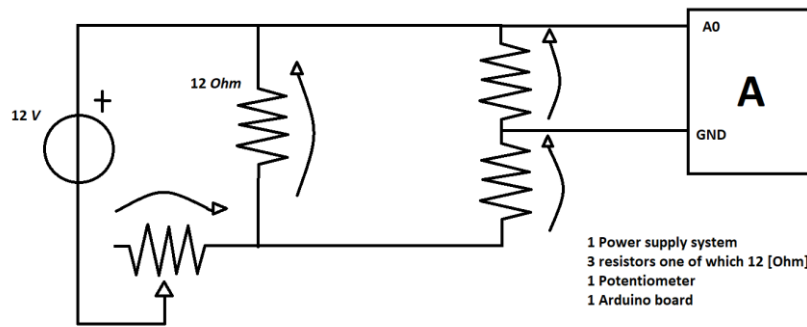
Figure 165: Ideal circuit

A $12\,V$ transformer, a $12\,\Omega$ resistor representing the NiTiNOL wire, a $10\,K\Omega$ potentiometer, two additional resistors and an Arduino board are employed. We choose to take the additional resistors with high values to prevent the Arduino board from being damaged by the high current, as it is only able to withstand a maximum of $40\,mA$. We also choose the two resistors with a ratio of 0.67, so that on the analog pin of Arduino, the maximum voltage does not exceed $5\,V$, beyond which the card would show a constant value (i.e., on the A0 pin, one would have a value of 1023 constant for any voltage above $5\,V$). For the description of the model, it is necessary to distinguish 2 limit cases: potentiometer with maximum resistance and potentiometer with minimum resistance.

A.1.1. Potentiometer with maximum resistance

Let's set the two additional resistors to 4000 Ω and 6000 Ω and solve the resistance configuration:
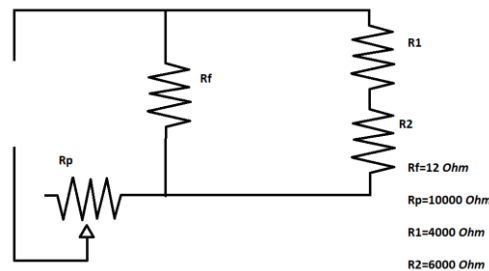
Figure 166: Configuration with only resistors

$$R_{eq} = R_p + \frac{R_f(R_1 + R_2)}{R_f + (R_1 + R_2)} = 10011.985\ [\Omega]$$

We find the current circulating in the equivalent circuit, remembering that the voltage coming from the transformer is $V = 12\,V$:

$$i = \frac{V}{R_{eq}} = 1.2\ [mA]$$

In this case, we calculate the voltage present on the potentiometer and on the resistances in parallel:

$$V_p = i \, R_p = 11.9 \, [V]$$

$$V_{parallelo} = 0.0144 \, [V]$$

Ultimately, we derive the current circulating on the representative resistance of the nitinol wire, since we know the voltage and the value of the resistance, the current on the branch of resistors to which Arduino is connected and the voltage that Arduino reads:

$$i_f = \frac{V_{parallela}}{R_f} = 0.001198561725929 \, [A]$$

$$i_{Arduino} = i - i_f = 0.001438 \, [mA]$$

$$V_{Arduino} = 0.0058 \, [V]$$

In this case, the wire is not active and the structure does not move.

A.1.2. Potentiometer with minimum resistance

With the same calculations, we find the quantities in case the potentiometer has the minimum resistance, supposedly 0.5 Ω:

Table 104: Sizes in the case with the potentiometer with minimum resistance

R_{eq}	12.4856 [Ω]
i	0.9611 [A]
V_p	0.48055 [V]
$V_{parallelo}$	11.5194 [V]
i_f	0.9599 [A]
$i_{Arduino}$	0.0012 [A]
$V_{Arduino}$	4.8000 [V]

Calculations are made on a single branch of the circuit. It is supposed to have equal circuits in parallel, in order to have several wires simultaneously connected.

A.1.3. Arduino code

The last step is the code design on Arduino that reads the voltage on the A0 pin and shows it on a digital display. In this way, the voltage present on the wire is controlled

through the potentiometer and, simultaneously, Arduino shows on the display the voltage that is present on the wire. The display used to show the voltage value is a seven-segment TM1637 display:

Figure 167: TM1637 display

We connect the display to pin 2 and 3 of Arduino and download the library that allows us to interface with the device. The code to be used is:

```
#include "TM1637.h"
#define CLK 2
#define DIO 3

TM1637 tm1637(CLK,DIO);

void setup(){
  tm1637.init(); //Inizializzo l'oggetto
  tm1637.set(BRIGHT_TYPICAL); //Iposto la luminosità
}

void loop(){
  float valore=map(analogRead(A0),0,1023,0,0.0144,11.5194);
  shownumber(valore);
}

void shownumber(float val){
  int n1=val%10;
  int n2=(val/10)%10;
  int n3=(((val-((n2*10)+n1))*100)/10)%10;
  int n4=((val-((n2*10)+n1))*100)%10;

  tm1637.display(0,n1);
  tm1637.display(1,n2);
  tm1637.display(2,n3);
  tm1637.display(3,n4);
}
```

Figure 168: Code Arduino for the prototype designed

B   Appendix B

B.1.   New mold
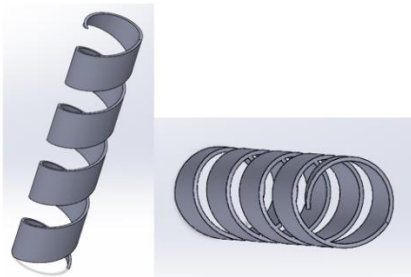
Figure 170: Guide with 25 mm pitch and 20 mm diameter
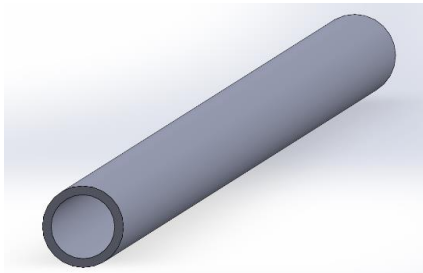
Figure 169: Cylinder in which to insert the mold bar

The prototypes created are all with the same diameter, pitch and width of the composite fabric strips. They differ only in the number of embedded wires and the material used. To analyze a greater number of structures it is necessary to change the diameter of the mold and the pitch of the guide obtained through the 3D printing. The problem of the change of pitch of the guide is solved by printing again other guides (varying if it needs also the diameter). To increase the diameter of the mold, a cylinder is created in which to insert the mold. The difference between the two diameters must then be filled with foam or rubber (the choice must also consider the autoclave cycle that the mold must withstand). The ends of the cylinder are critical points as they represent a net difference in altitude that the nitinol wires must overcome. To avoid this problem, cones have been created to be inserted in the ends of the cylinder, which prevent the generation of critical points that can break the wires during the cycle in an autoclave.
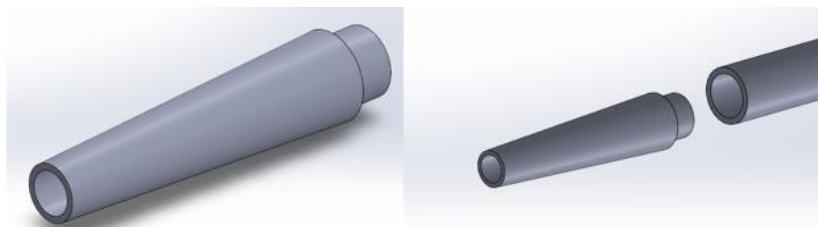
Figure 171: Cones to be inserted at the end of the cylinder

C   Appendix C

This section shows all the graphs that could not be inserted in the thesis. In the case of the structure consisting of 4 layers of $0.28 - mm -$ thick carbon fiber fabric, all data are given as an example in Chapter 2. In this part of the work of insert the graphs of the structures:

- Structure composed of 4 layers of $0.12 - mm -$ thick carbon fiber fabric (C_{12})
- Structure composed of 4 layers of $0.12 - mm -$ thick glass fiber fabric (V_{12-4})
- Structure composed of 6 layers of $0.12 - mm -$ thick glass fiber fabric (V_{12-6})

C.1.   Carbon-fibre fabric with 4 plies $0.12 \ mm$ thick

The graphs related to the activation voltage are:
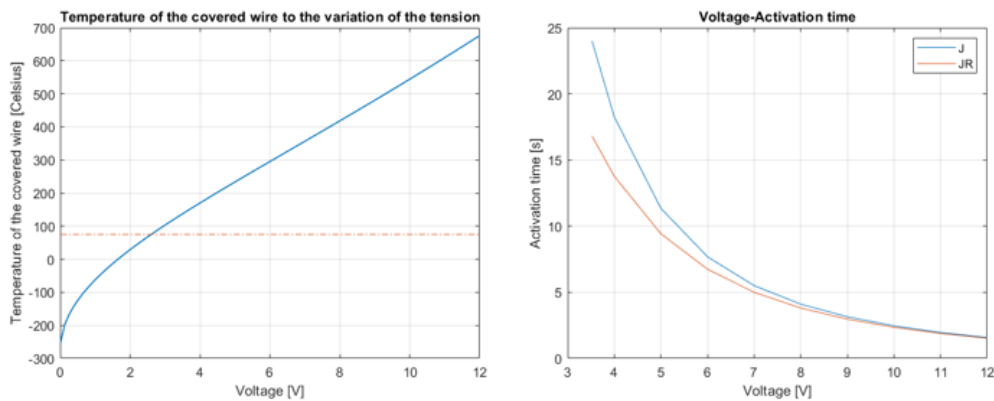
Figure 172: Search for the optimal voltage
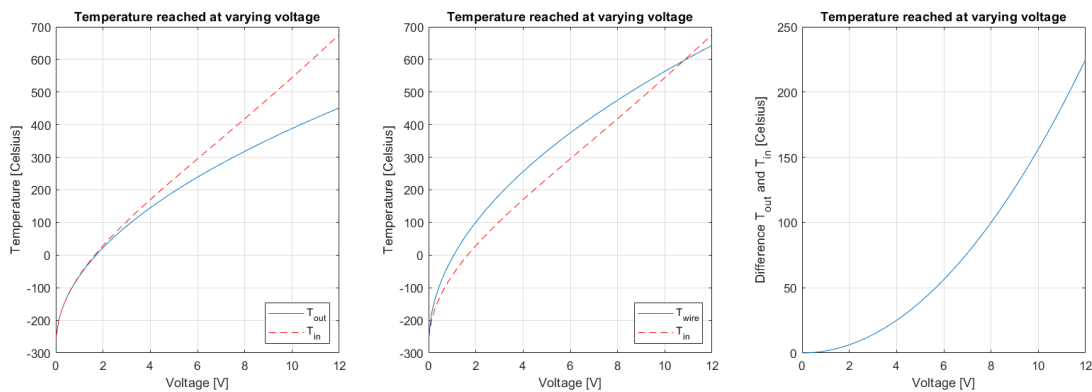
Figure 173: Temperature variation with respect to voltage, considering being in the worst possible case

C.1.1. Transient case with Matlab

Below are the graphs of the transients obtained through Matlab:
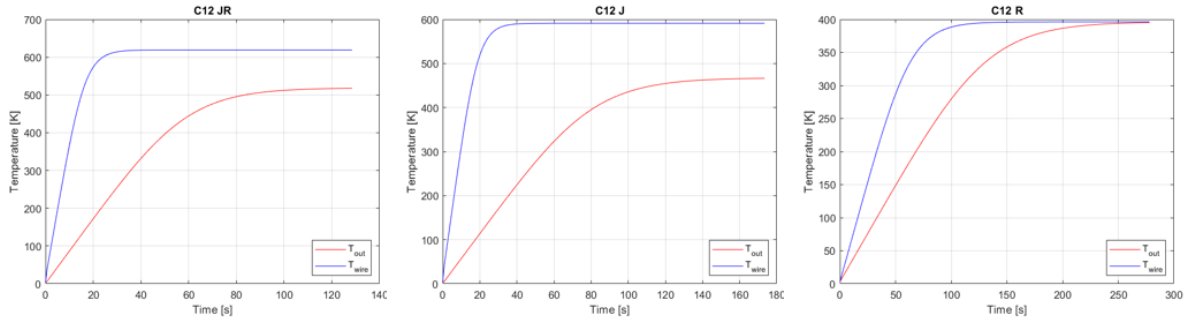
Figure 174: Transients for structure C_{12} in the 3 cases considered

C.1.2. Convection in a laboratory environment
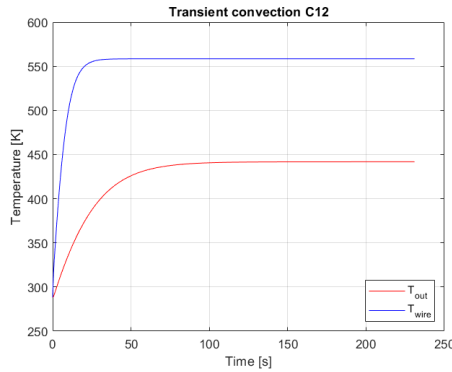
Figure 175: Case of transition for laboratory free convection

C.1.3. Transient case with Abaqus

Below are the graphs of the transients obtained through Abaqus:
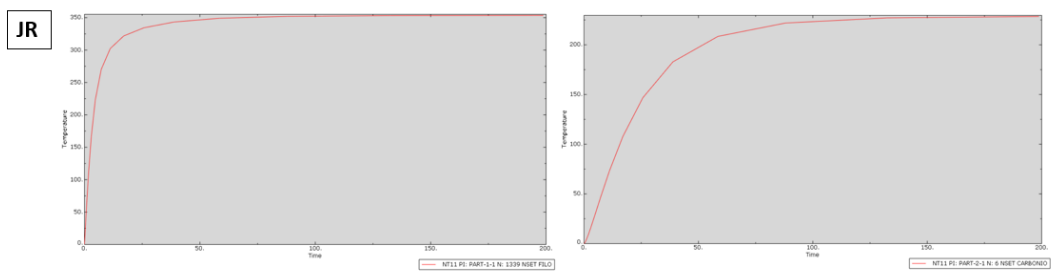
Figure 176: JR, transitional case for wire and composite
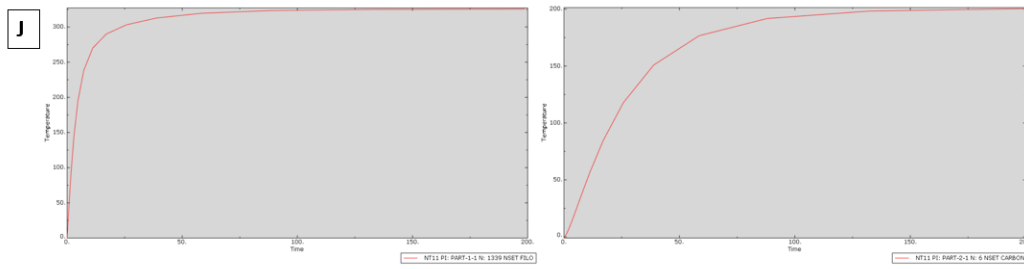
Figure 177: J, transitional case for wire and composite
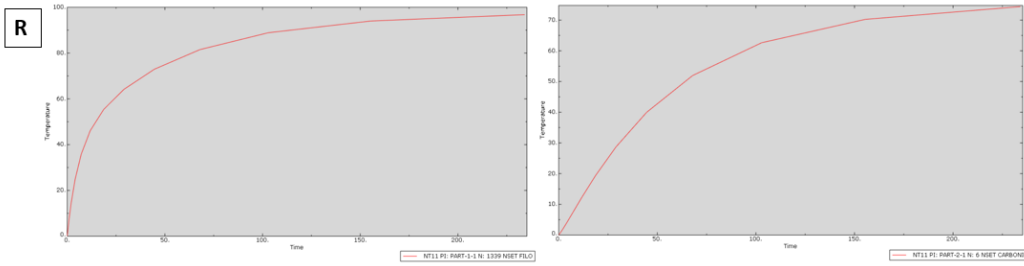
Figure 178: R, transitional case for wire and composite

C.1.4. Length for temperature dissipation

Two graphs of the required length for temperature dissipation are given below:
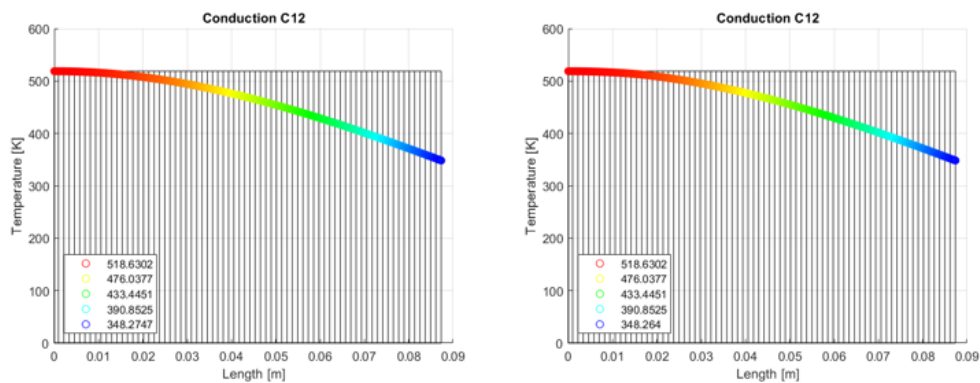
Figure 179: Temperature trend as the dissipation length increases in JR case, not considering the radiations (left) and considering the radiations (right)

C.2. Glass-fibre fabric with 4 plies $0.12\ mm$ thick

The graphs related to the activation voltage are:
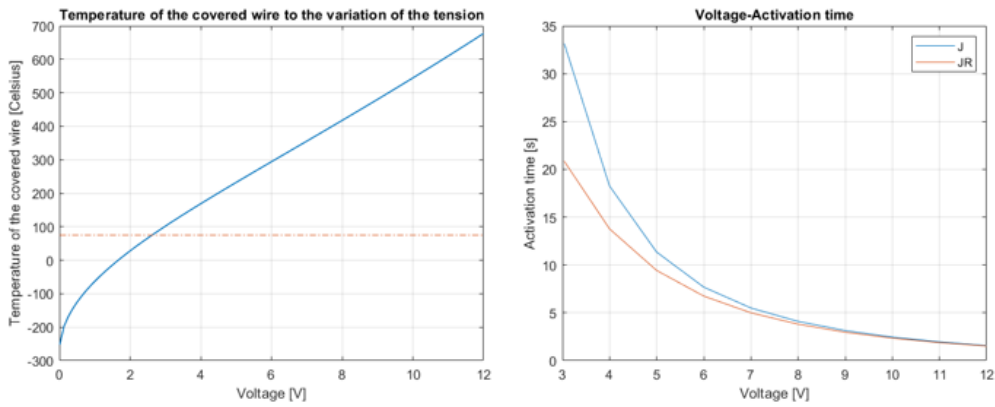
Figure 180: Search for the optimal voltage
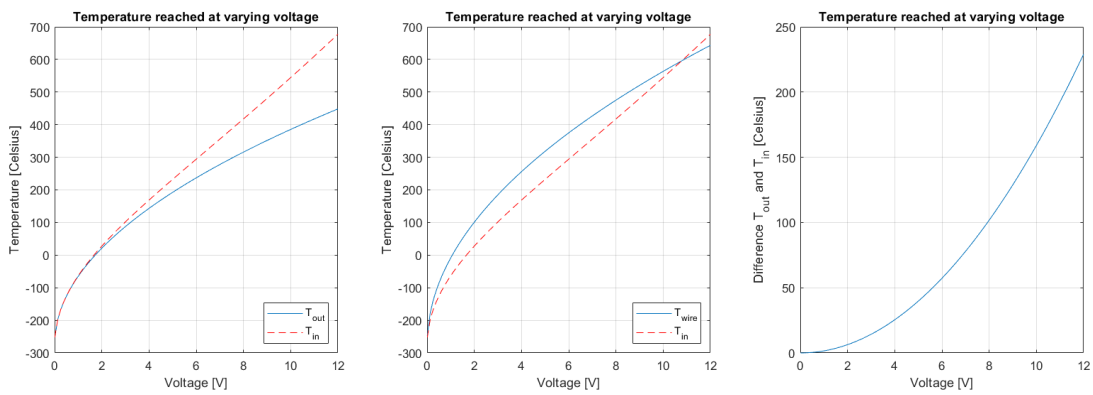
Figure 181: Temperature variation with respect to voltage, considering being in the worst possible case

C.2.1. Transient case with Matlab

Below are the graphs of the transients obtained through Matlab:
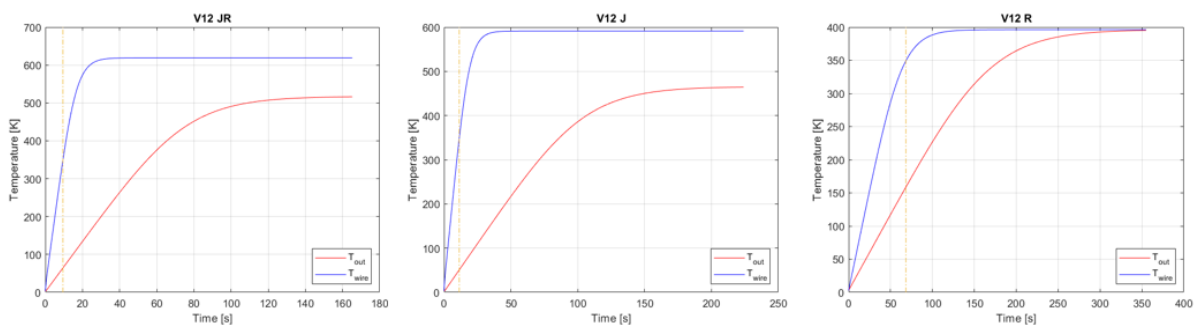
Figure 182: Transients for structure V_{12-4} in the 3 cases considered

C.2.2. Convection in a laboratory environment
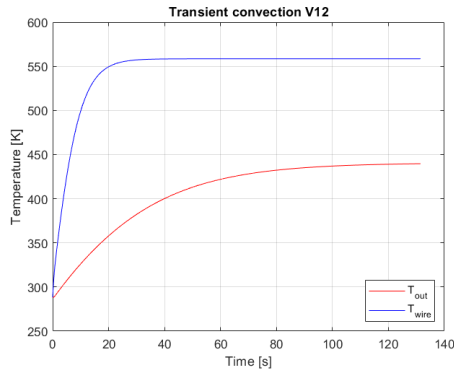
Figure 183: Case of transition for laboratory free convection

C.2.3. Transient case with Abaqus

Below are the graphs of the transients obtained through Abaqus:
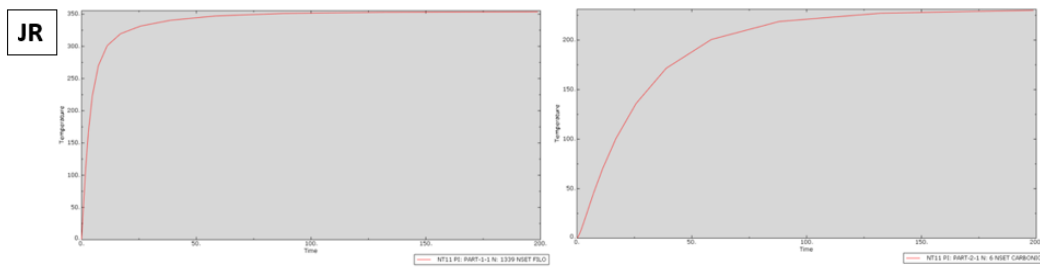
Figure 184: JR, transitional case for wire and composite
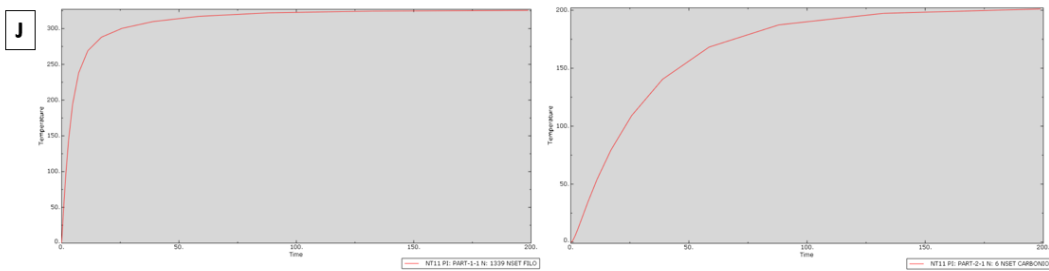
Figure 185: J, transitional case for wire and composite
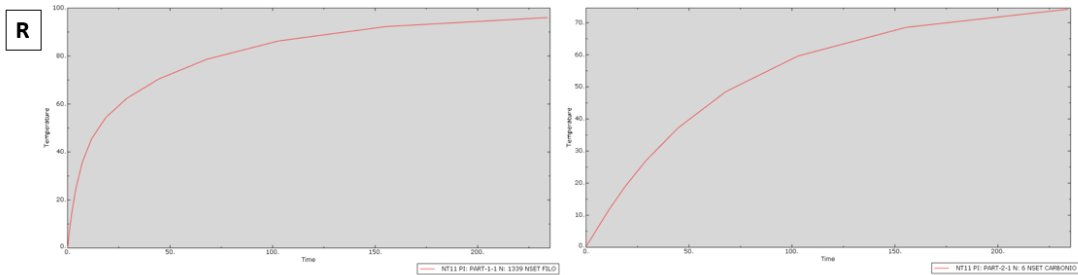
Figure 186: R, transitional case for wire and composite

C.2.4. Length for temperature dissipation

Two graphs of the required length for temperature dissipation are given below:
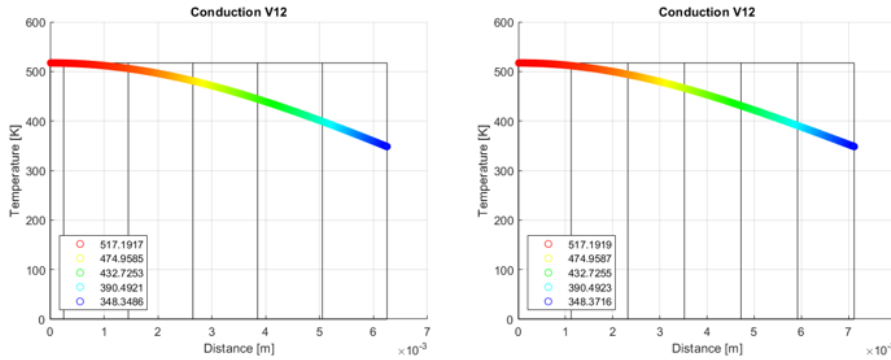
Figure 187: Temperature trend as the dissipation length increases in JR case, not considering the radiations (left) and considering the radiations (right)

C.3. Glass-fibre fabric with 6 plies 0.12 *mm* thick

The graphs related to the activation voltage are:
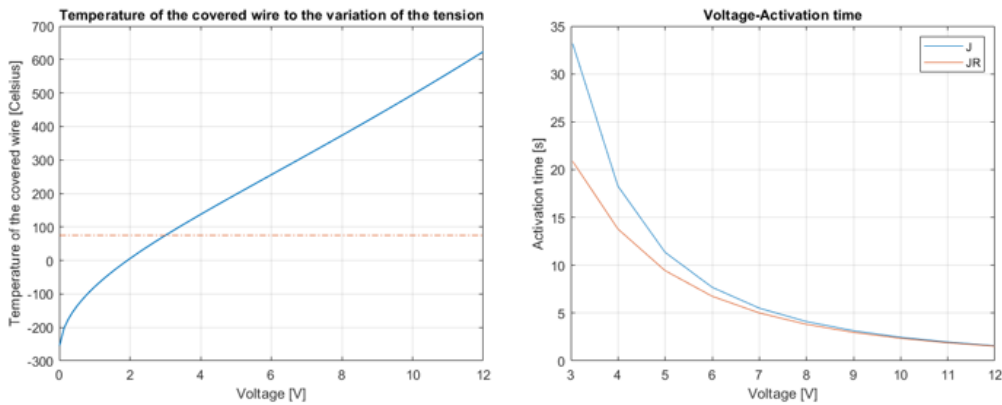
Figure 188: Search for the optimal voltage
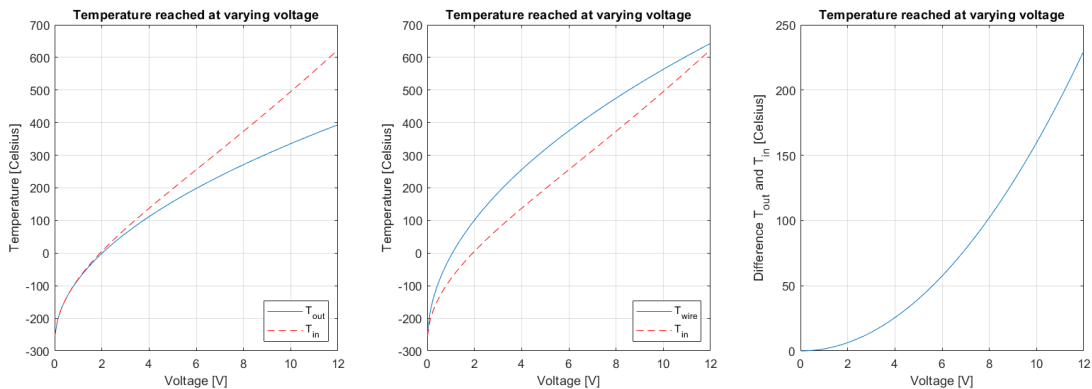
Figure 189: Temperature variation with respect to voltage, considering being in the worst possible case

C.3.1. Stationary and transient case with Matlab
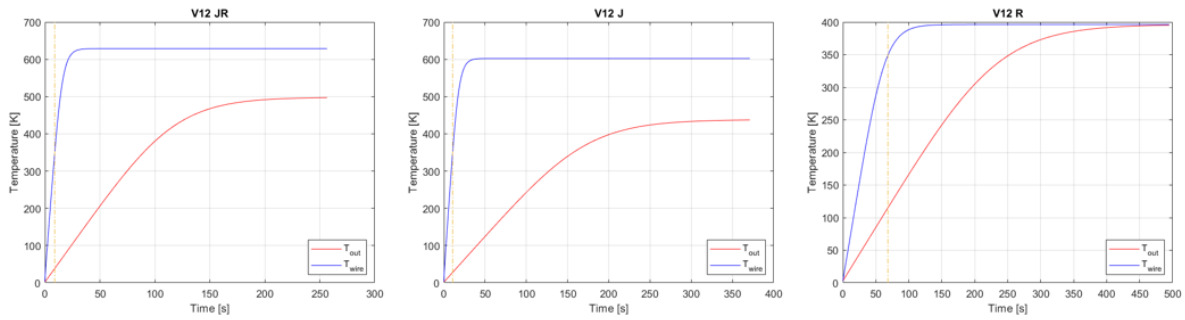
Figure 190: Transients for structure V_{12-6} in the 3 cases considered

C.3.2. Convection in a laboratory environment
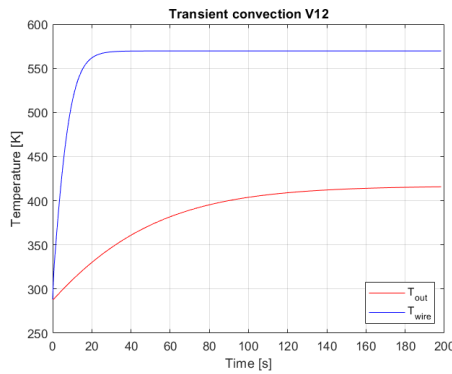
Figure 191: Case of transition for laboratory free convection

C.3.3. Transient case with Abaqus

Below are the graphs of the transients obtained through Abaqus:
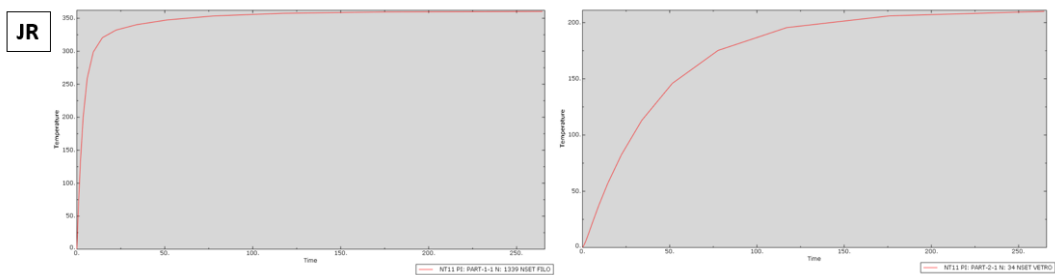
Figure 192: JR, transitional case for wire and composite
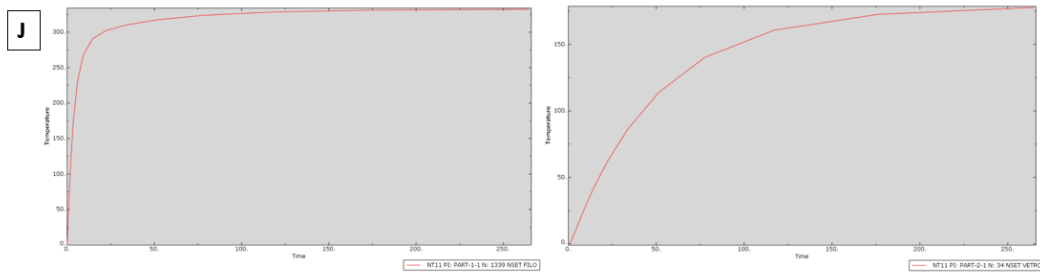
Figure 193: J, transitional case for wire and composite
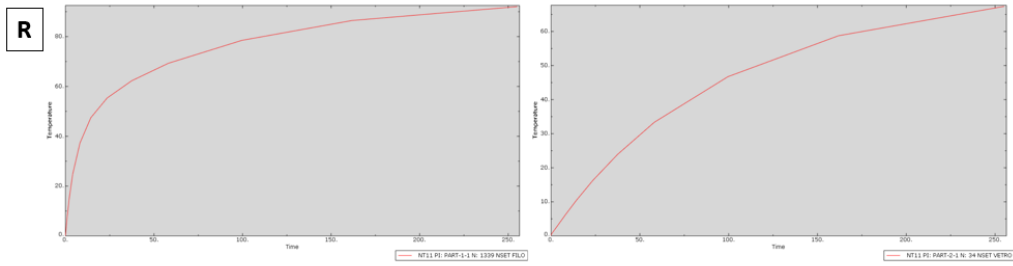
Figure 194: R, transitional case for wire and composite

C.3.4. length for temperature dissipation

Two graphs of the required length for temperature dissipation are given below:
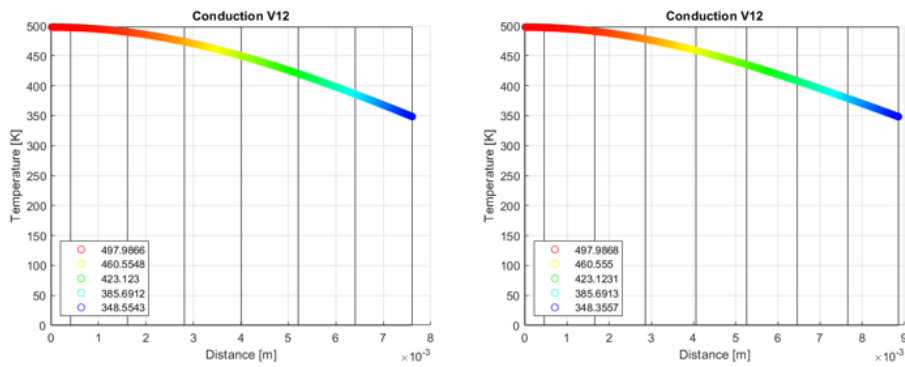
Figure 195: Temperature trend as the dissipation length increases in JR case, not considering the radiations (left) and considering the radiations (right)

D Appendix D

D.1. 4 Carbon layers 0.28 *mm* thick

Transient charts with Matlab and Abaqus are shown below:
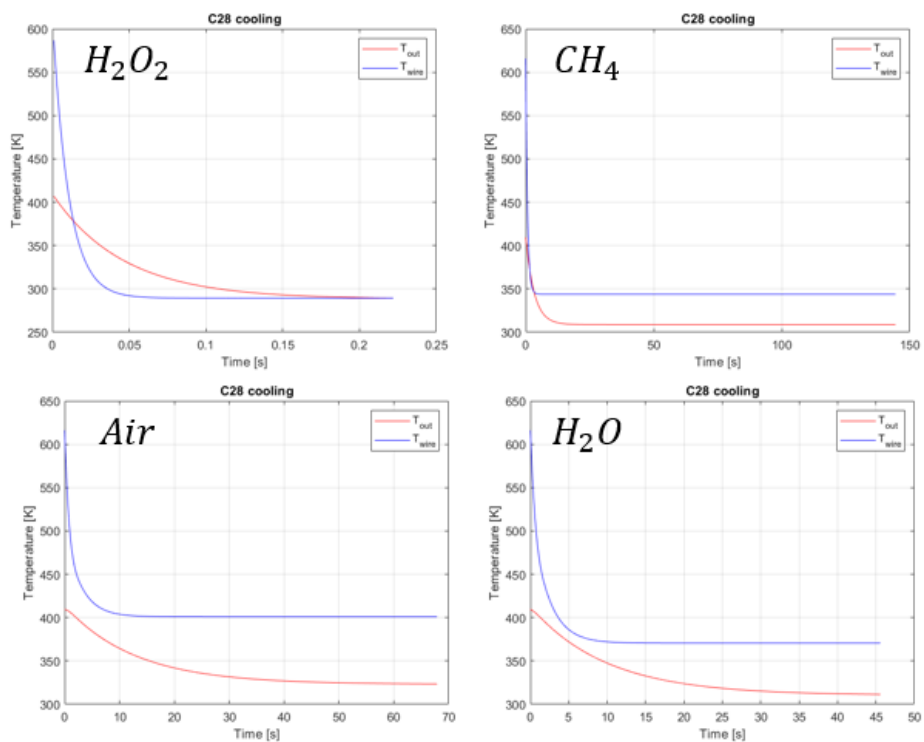
Figure 196: Results obtained with Matlab
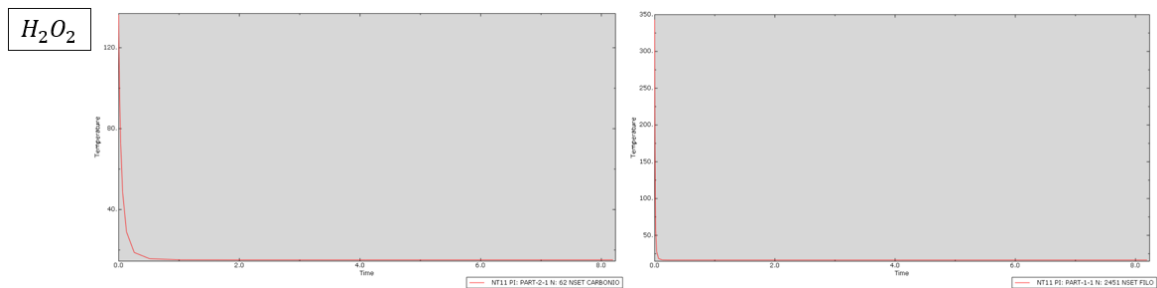
Figure 197: Hydrogen peroxide transient using Abaqus
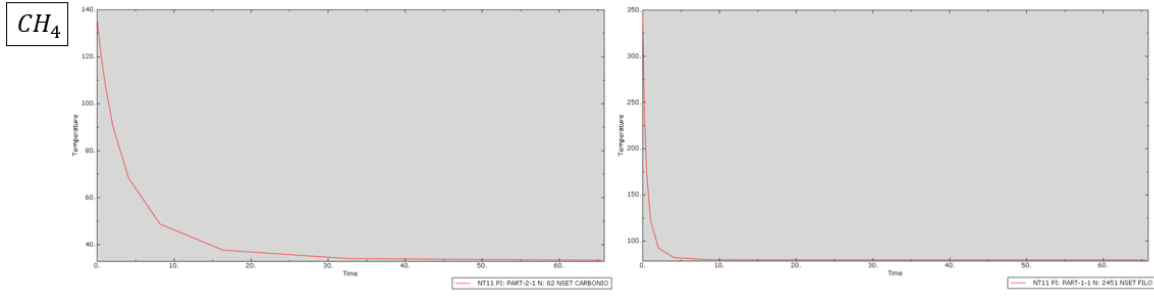
Figure 198: Methane transient using Abaqus
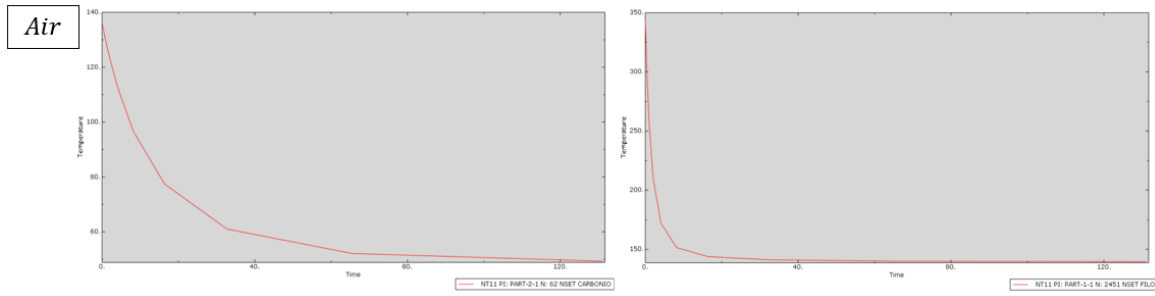
Figure 199: Air transient using Abaqus
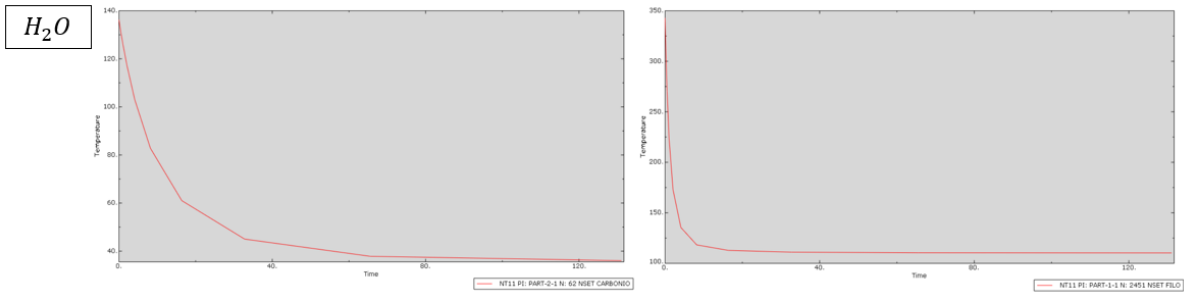
Figure 200: Water transient using Abaqus

D.2. 4 Carbon layers 0.12 *mm* thick
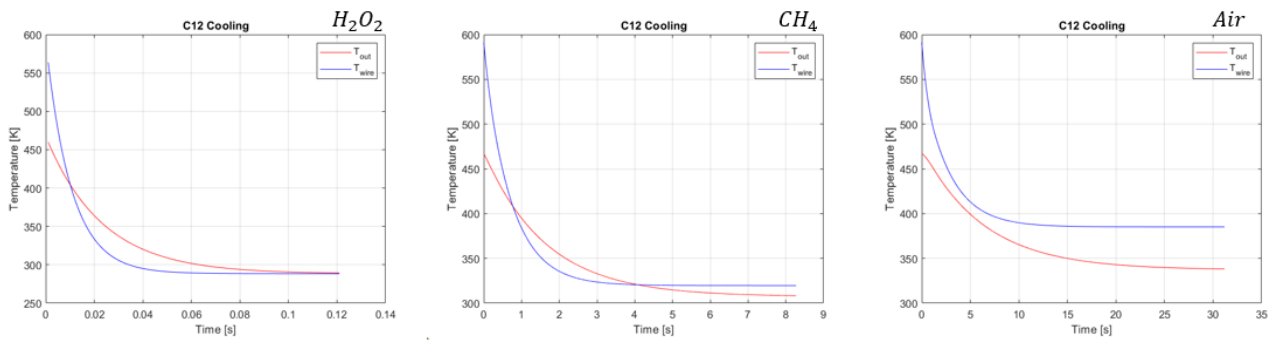
Figure 201: Transient of simulations with Matlab
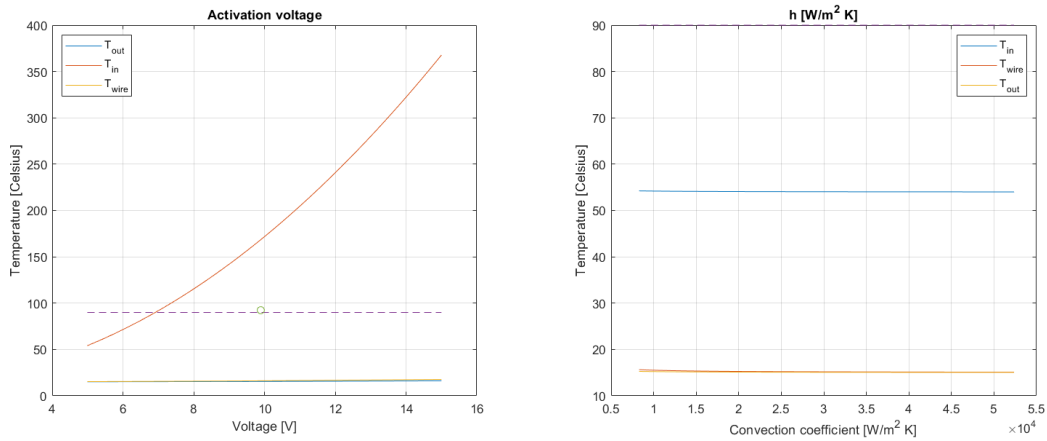
Figure 202: Temperature variation with voltage and convection coefficient using hydrogen peroxide
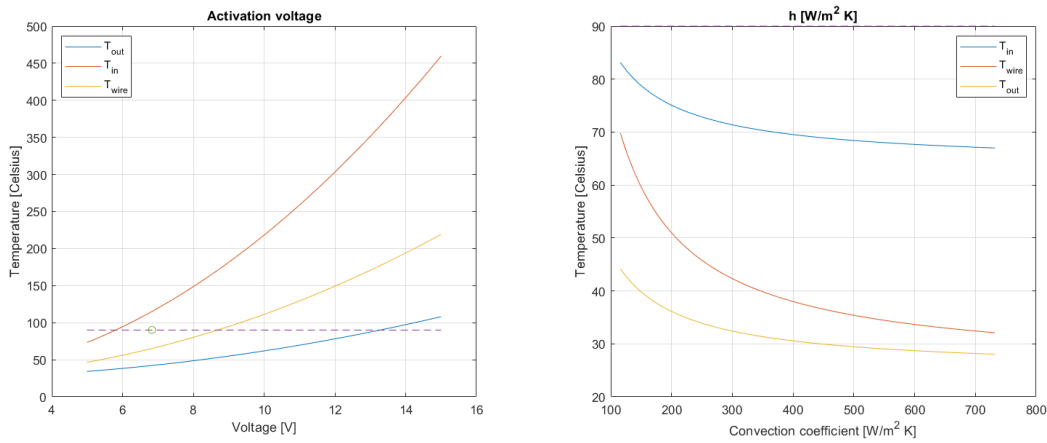
Figure 203: Temperature variation with voltage and convection coefficient using Methane
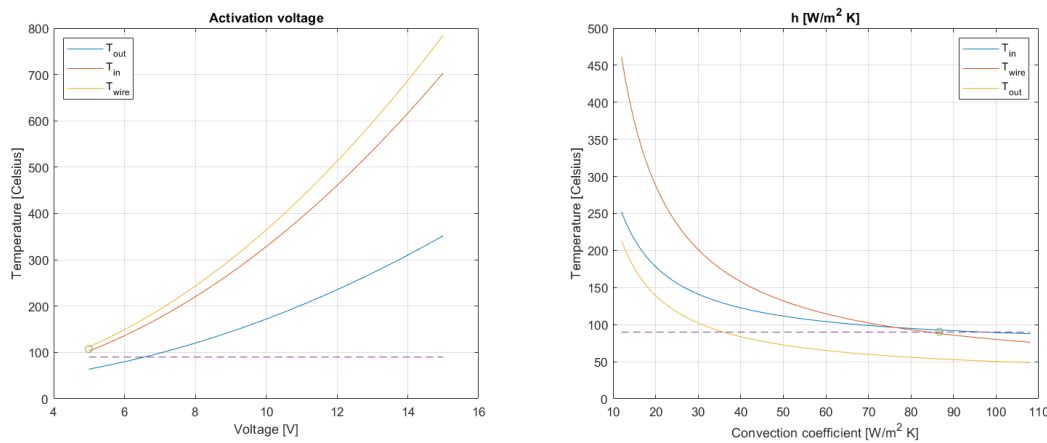
Figure 204: Temperature variation with voltage and convection coefficient using Air

In the case of free convection with water, the optimum convection coefficient is obtained from the graph:
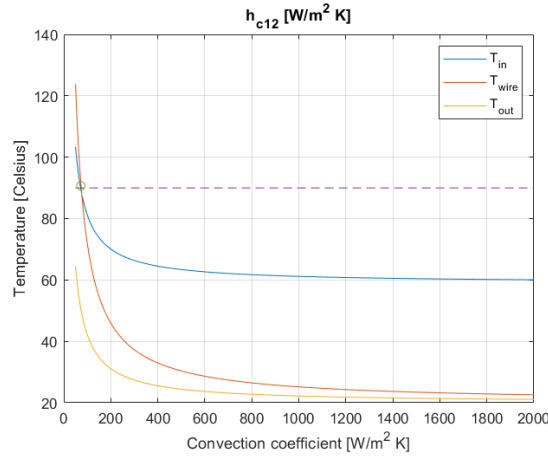
Figure 205: Cooling through free water convection

Transient charts with Matlab and Abaqus are shown below:
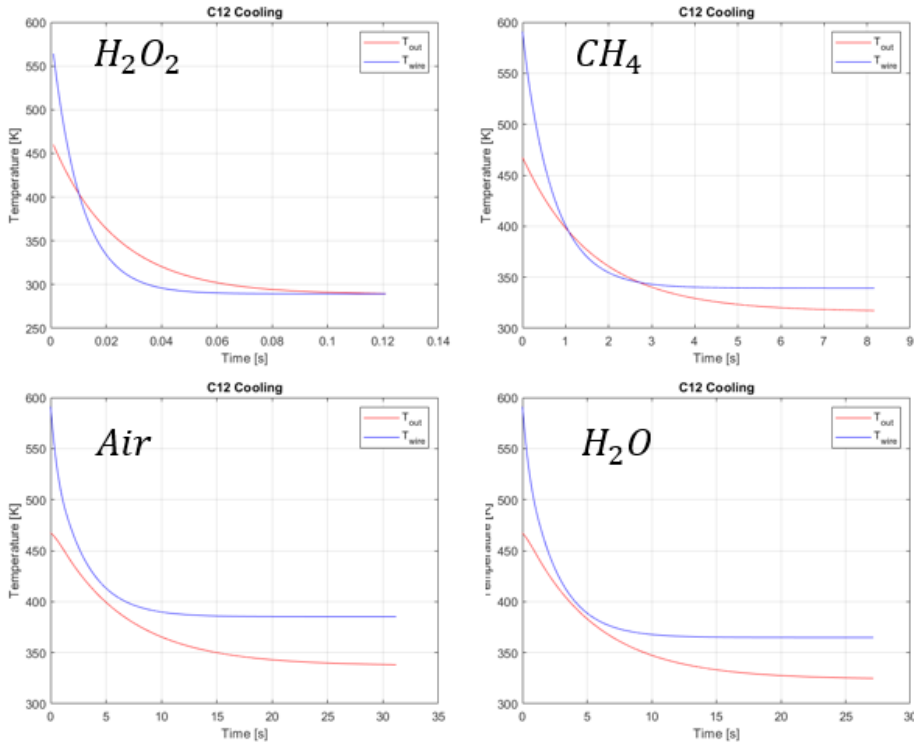
Figure 206: Results obtained with Matlab
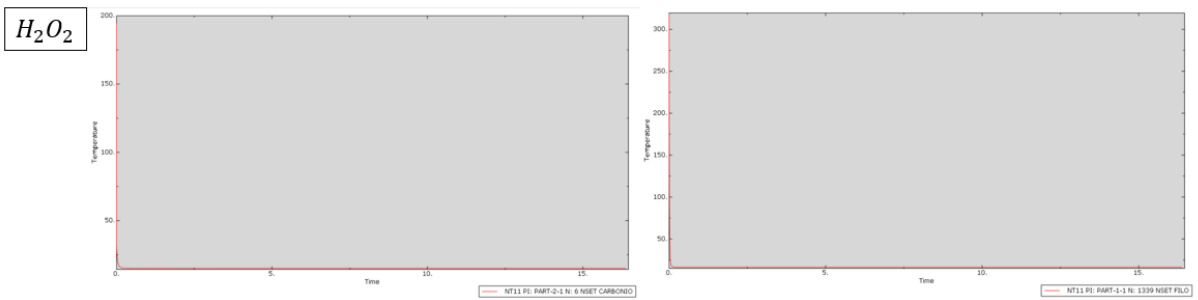
Figure 207: Hydrogen peroxide transient using Abaqus
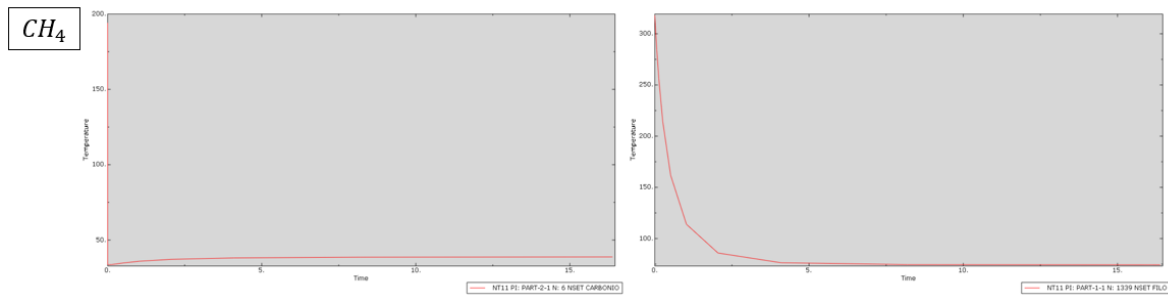
Figure 208: Methane transient using Abaqus
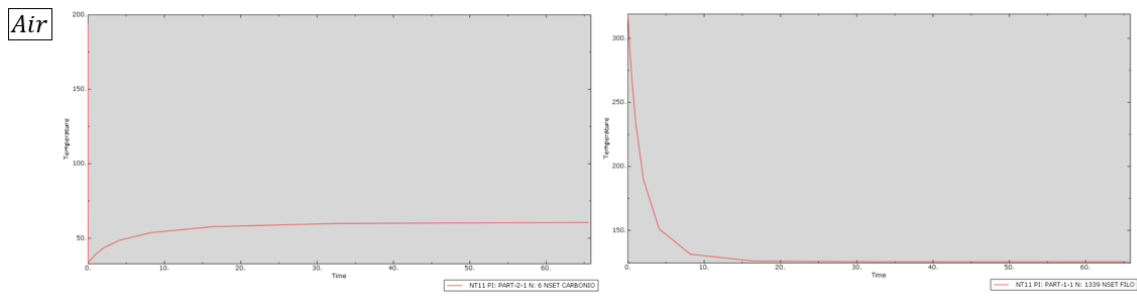
Figure 209: Air transient using Abaqus
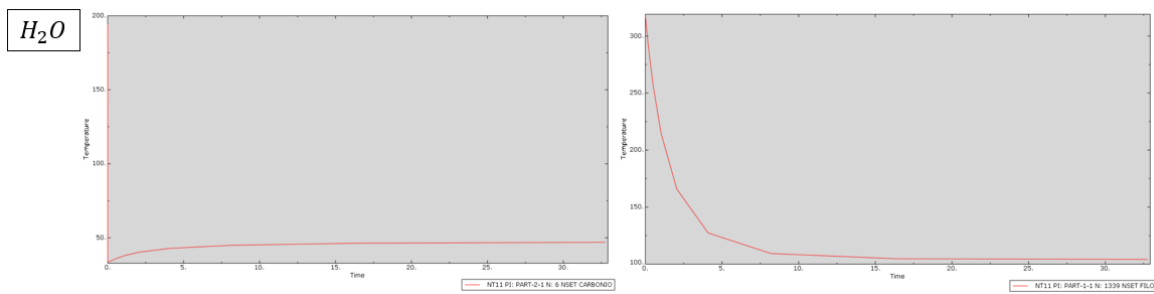
Figure 210: Water transient using Abaqus

D.3. 4 Glass layers 0.12 mm thick
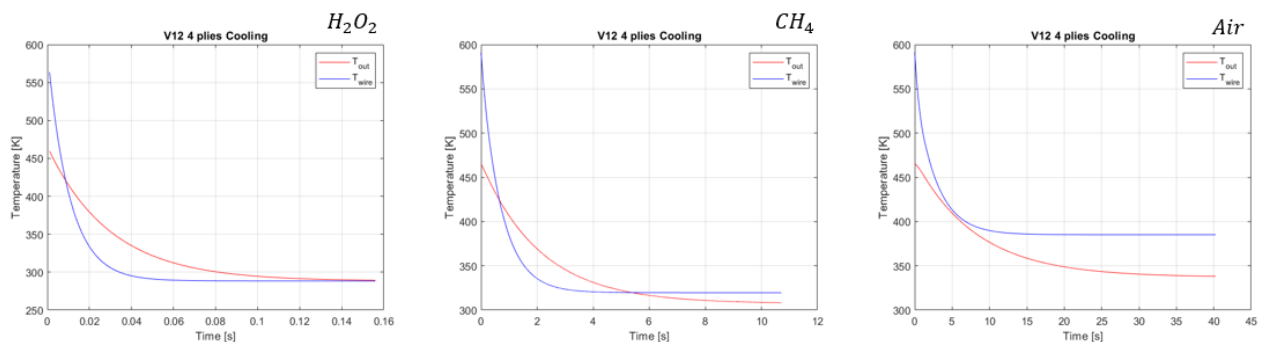
Figure 211: Transient of simulations with Matlab
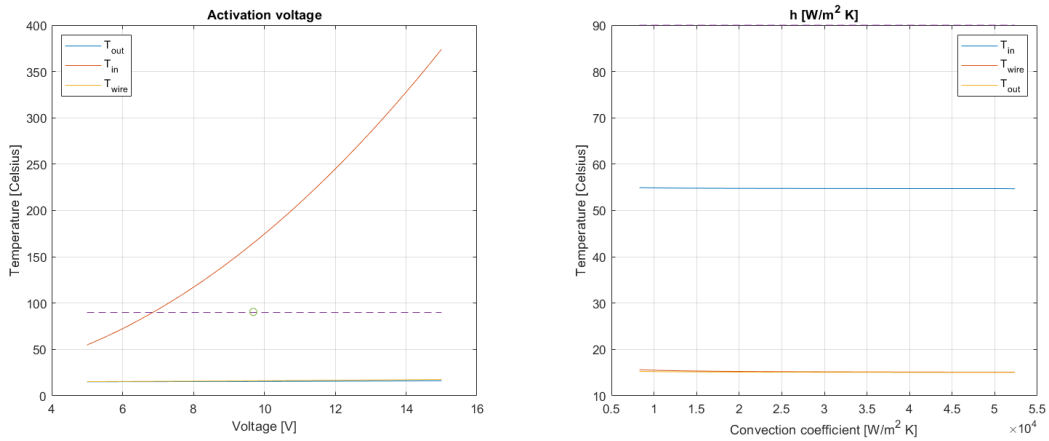
Figure 212: Temperature variation with voltage and convection coefficient using hydrogen peroxide
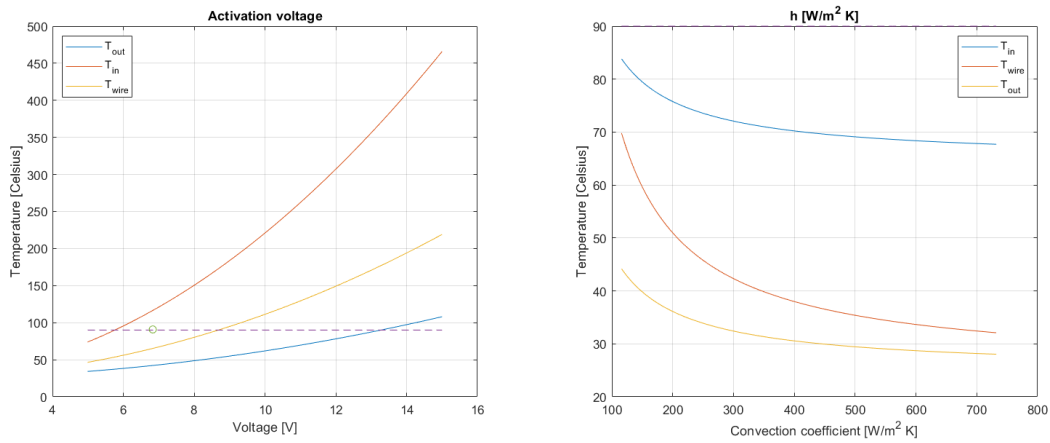
Figure 213: Temperature variation with voltage and convection coefficient using Methane
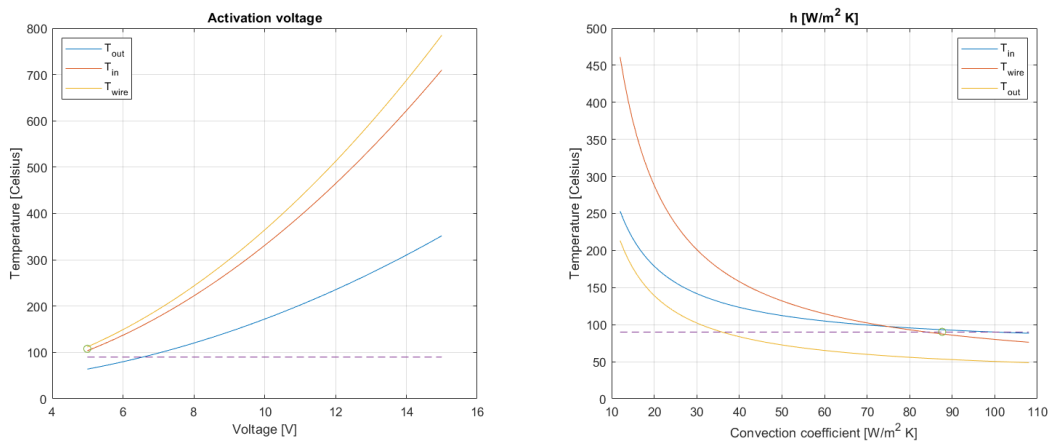
Figure 214: Temperature variation with voltage and convection coefficient using Air

In the case of free convection with water, the optimum convection coefficient is obtained from the graph:
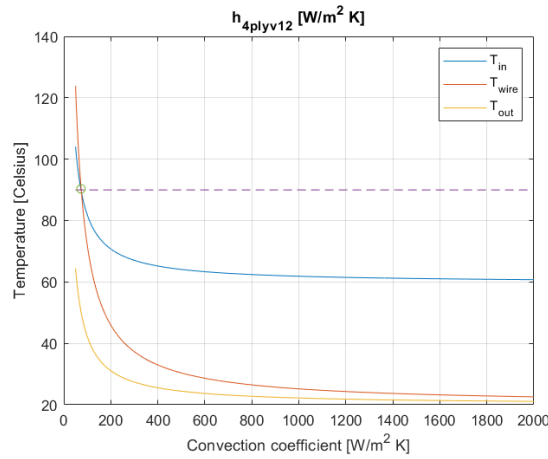
Figure 215: Cooling through free water convection

Transient charts with Matlab and Abaqus are shown below:
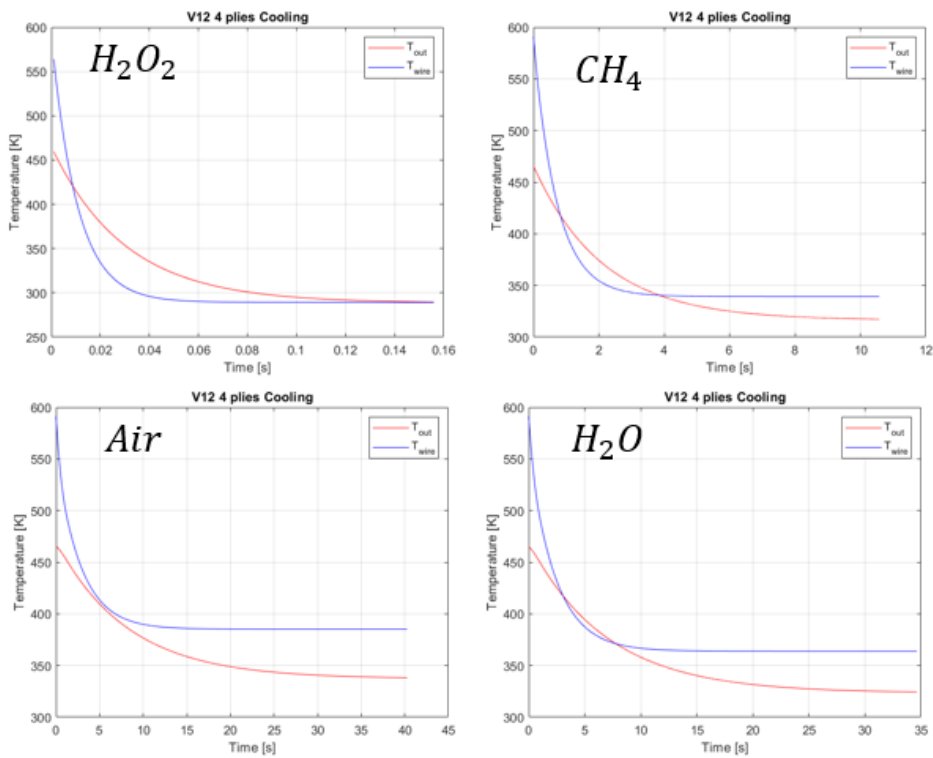
Figure 216: Results obtained with Matlab
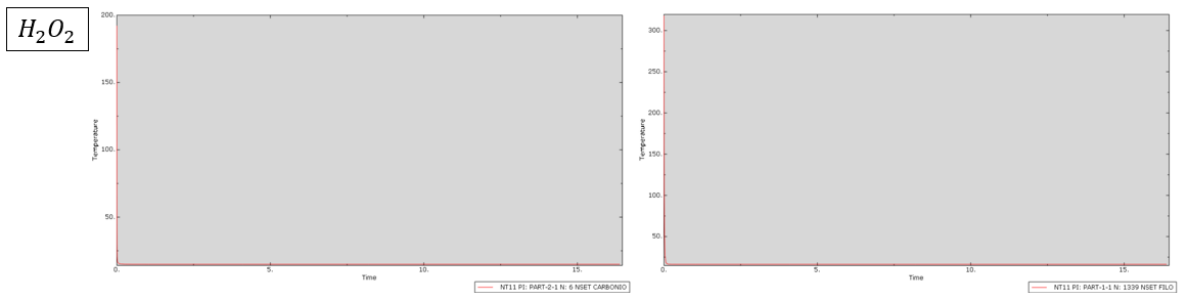
Figure 217: Hydrogen peroxide transient using Abaqus

CH_4
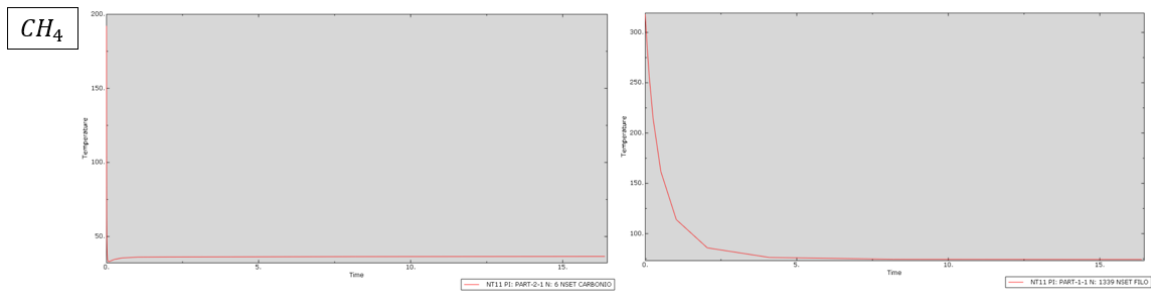
Figure 218: Methane transient using Abaqus

Air
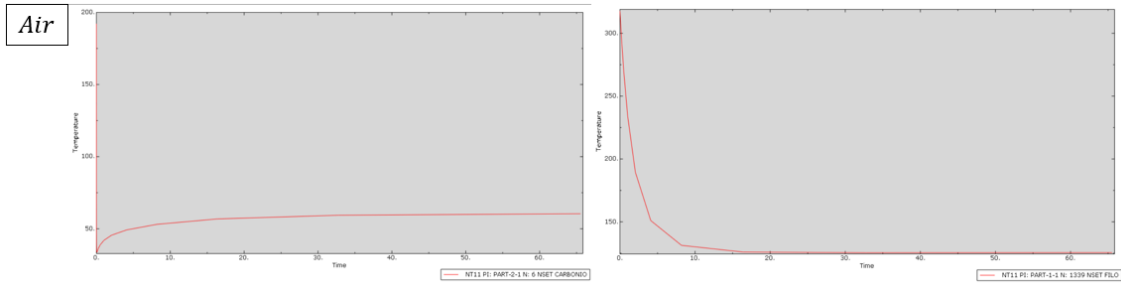
Figure 219: Air transient using Abaqus

H_2O
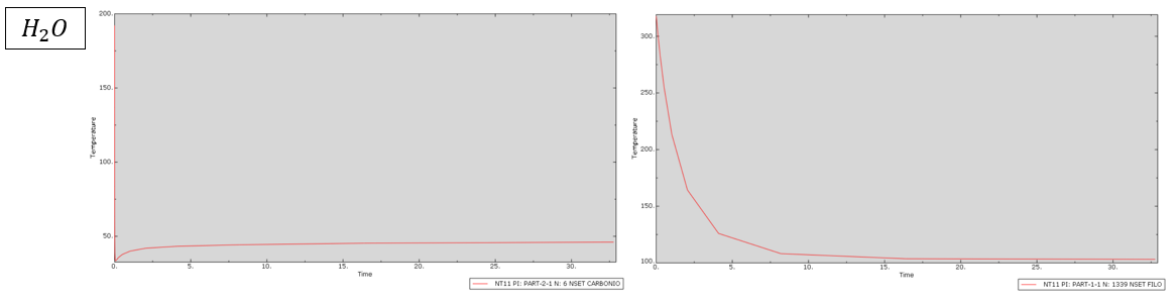
Figure 220: Water transient using Abaqus

D.4. 6 Glass layers 0.12 mm thick

H_2O_2 CH_4 Air
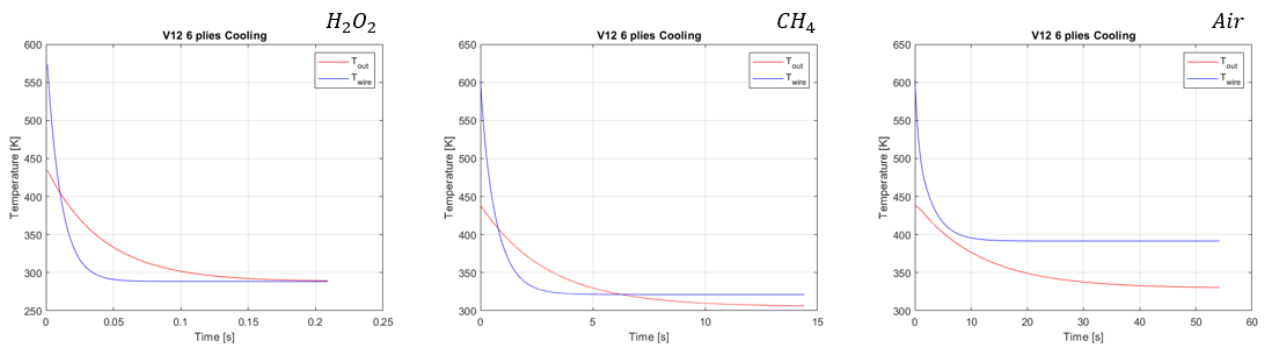
Figure 221: Transient of simulations with Matlab
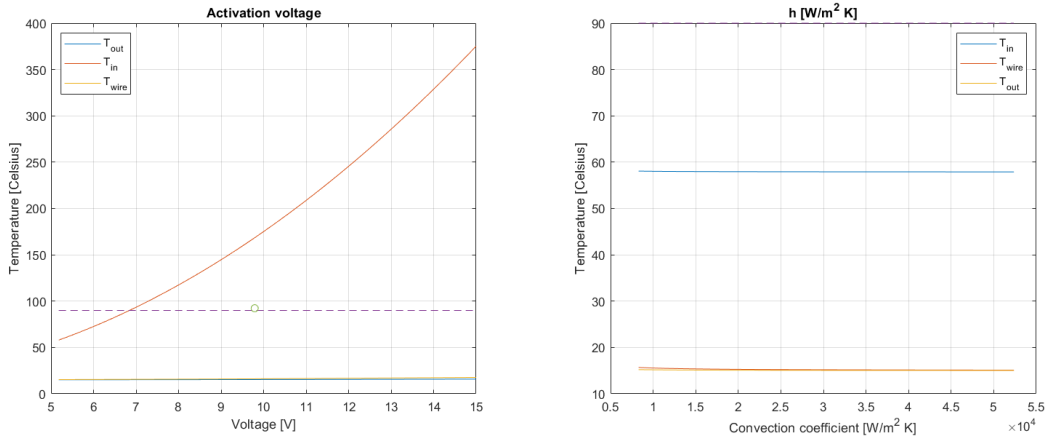
Figure 222: Temperature variation with voltage and convection coefficient using hydrogen peroxide
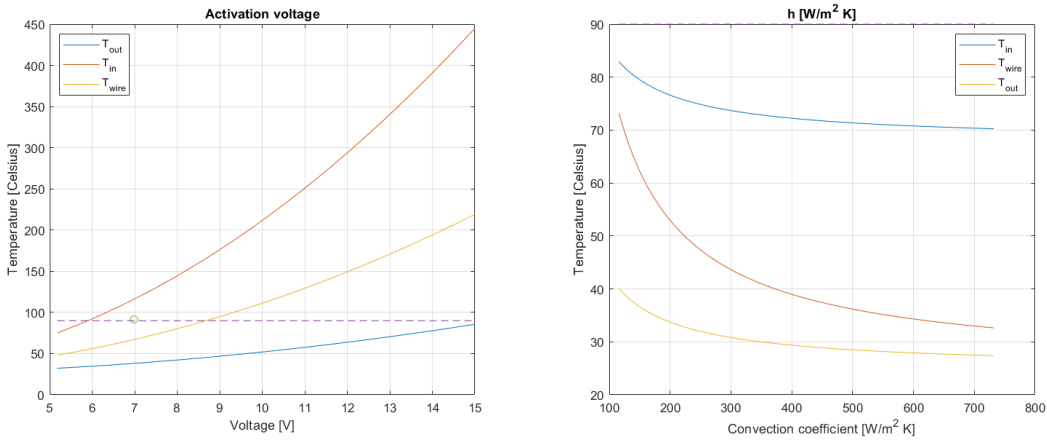
Figure 223: Temperature variation with voltage and convection coefficient using Methane
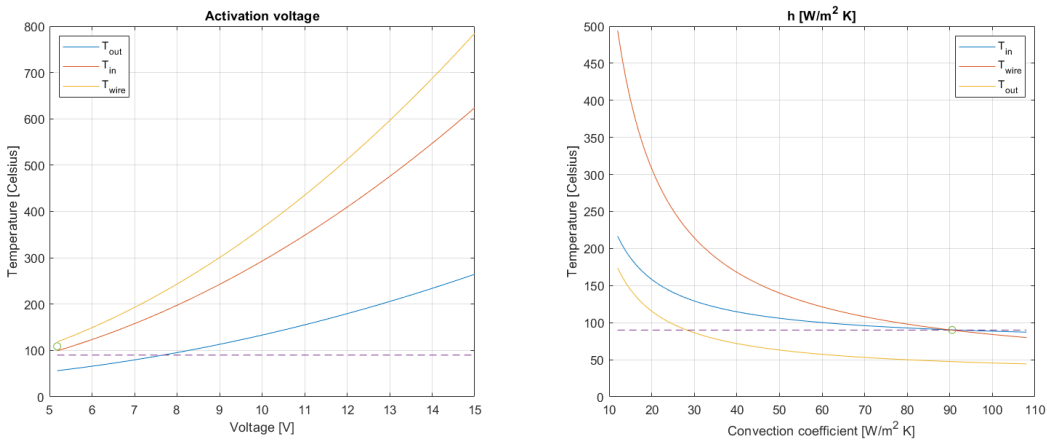
Figure 224: Temperature variation with voltage and convection coefficient using Air

In the case of free convection with water, the optimum convection coefficient is obtained from the graph:
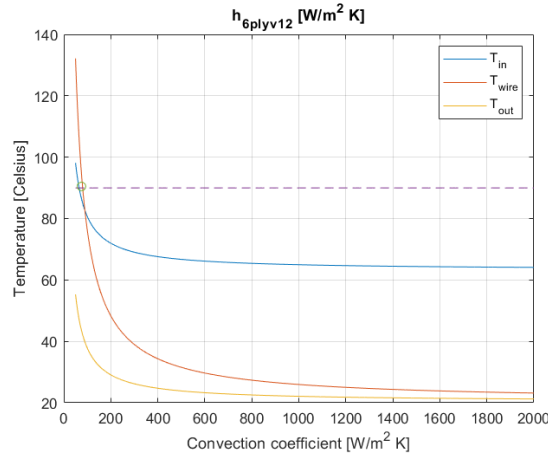
Figure 225: Cooling through free water convection

Transient charts with Matlab and Abaqus are shown below:
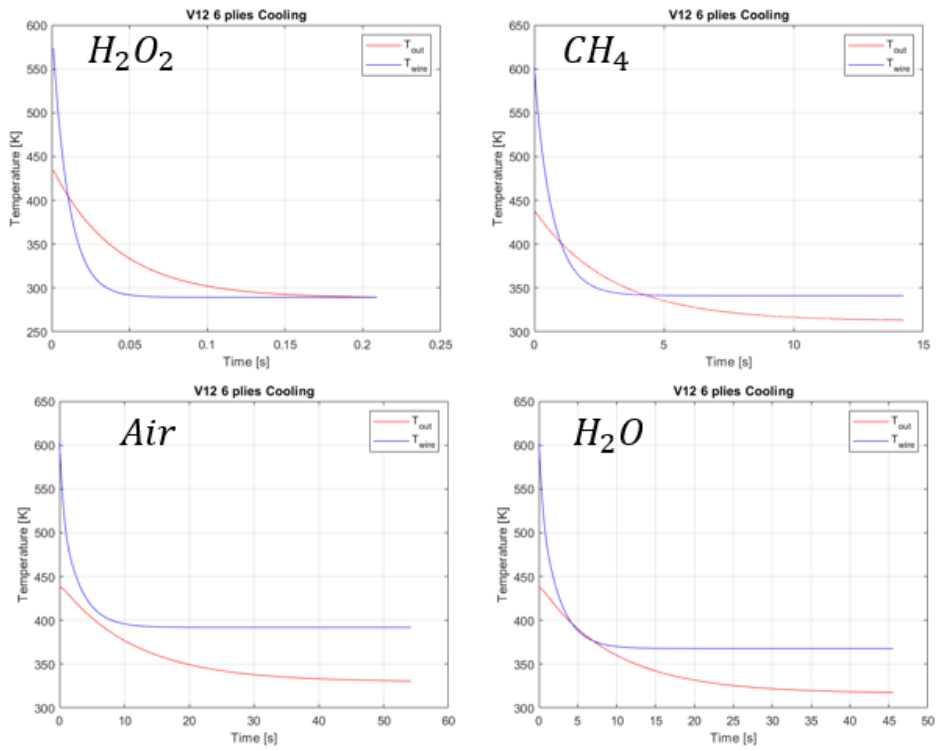
Figure 226: Results obtained with Matlab
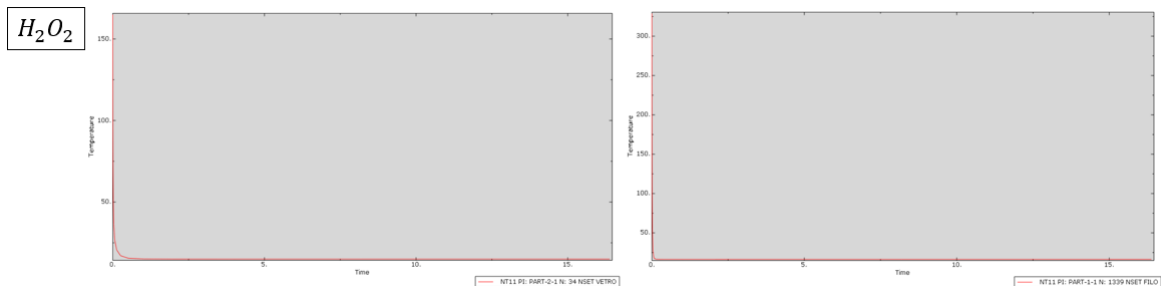
Figure 227: Hydrogen peroxide transient using Abaqus
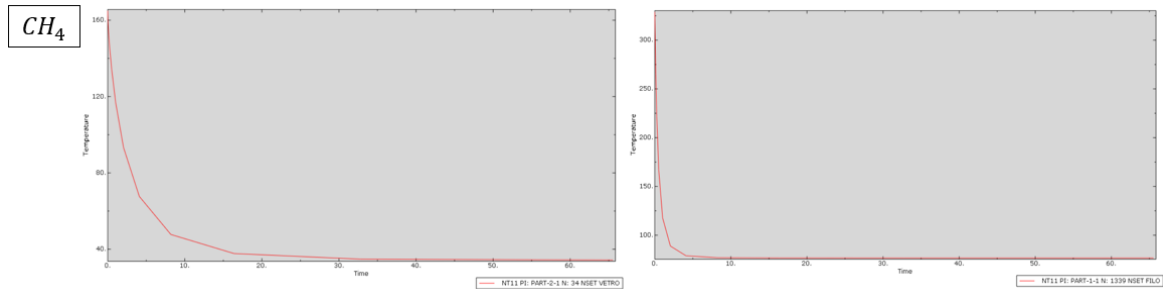
Figure 228: Methane transient using Abaqus
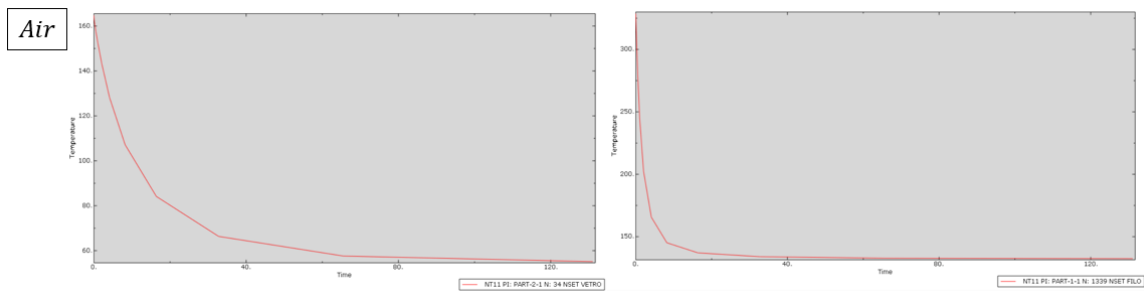
Figure 229: Air transient using Abaqus
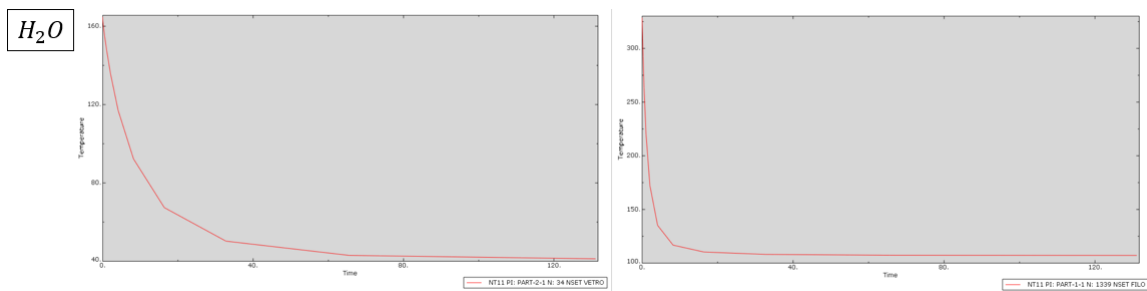
Figure 230: Water transient using Abaqus

E   Appendix E

E.1. Constant height of the spiral
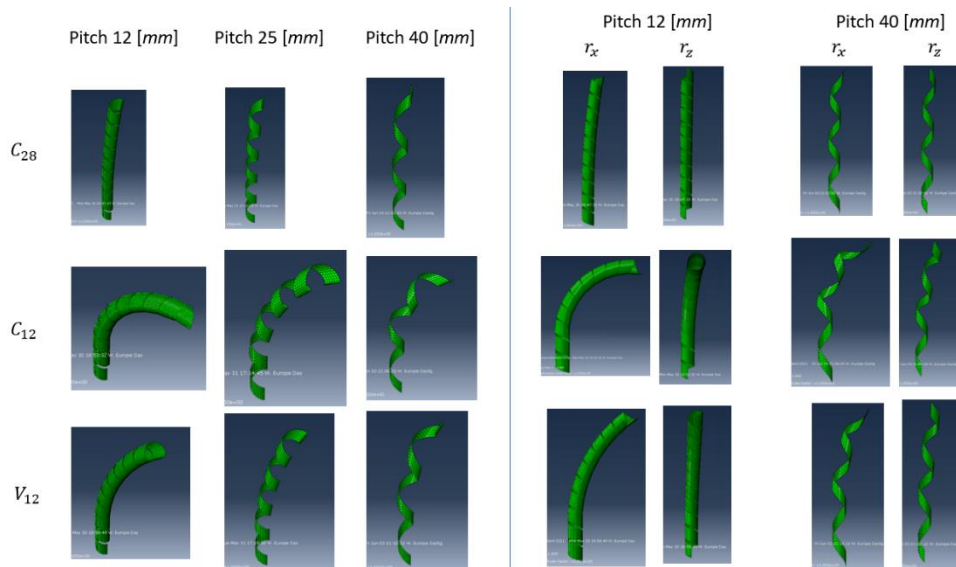
Figure 231: Example of pitch change and number of revolutions, keeping the height constant

E.2. Constant number of revolutions
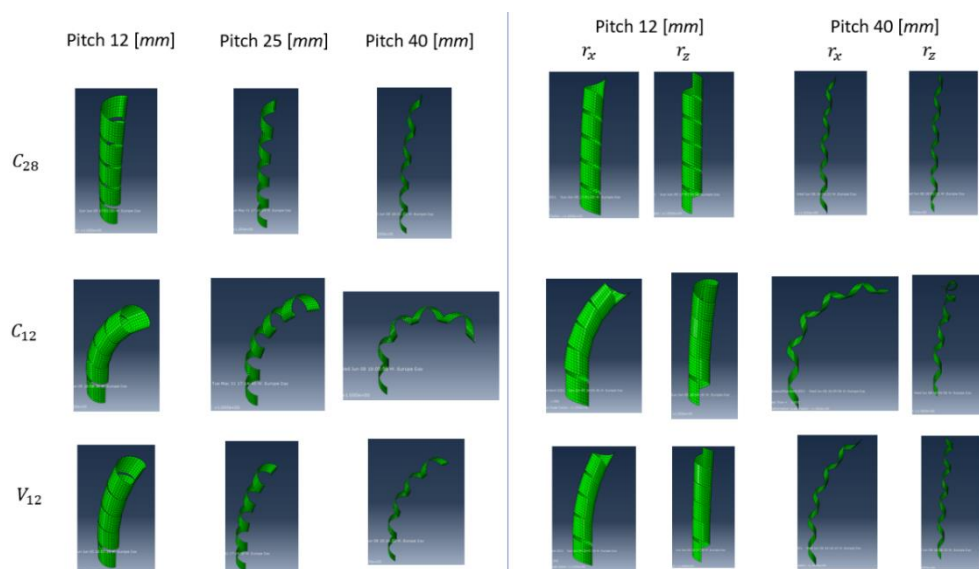
Figure 232: Example of changing pitch while keeping the number of revolutions constant

E.3.   Variation of diameter
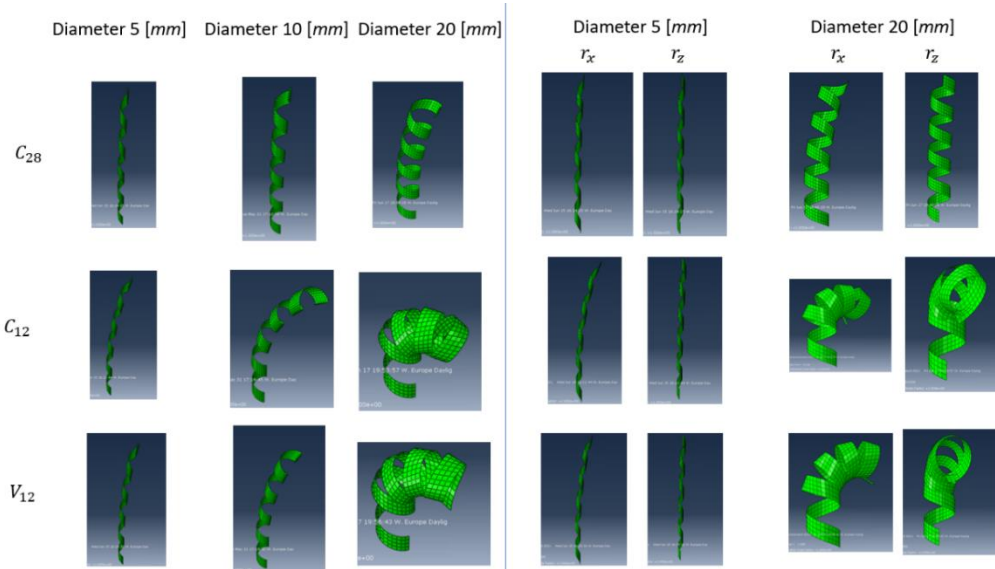
Figure 233: Example of variation of diameter with respect to nominal structure

E.4.   Variation of width of composite
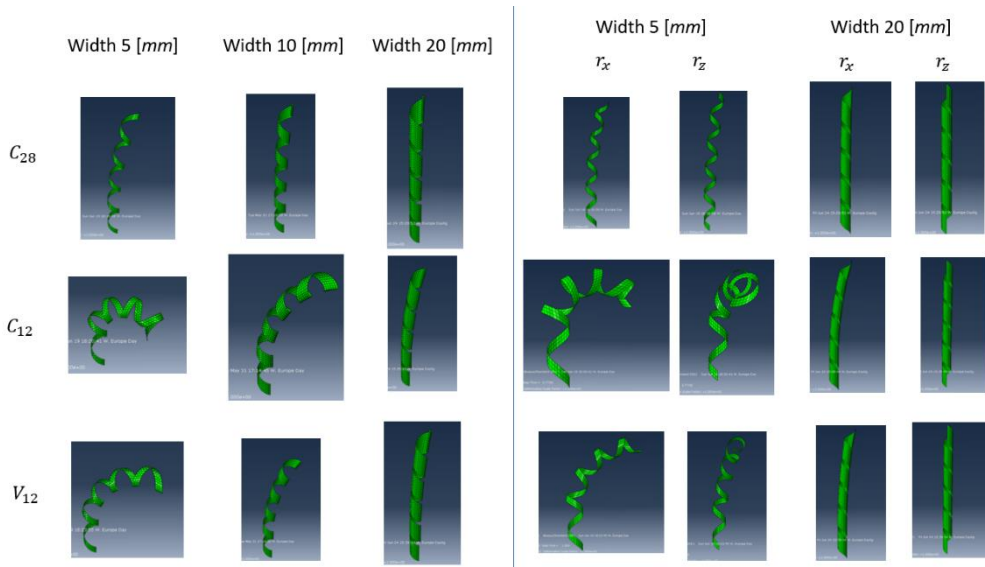
Figure 234: Example of variation of width with respect to nominal structure

F Appendix F

Only the calculated values for the 10 activations of each single wire are reported. Due to the large number, the graphs cannot be reported. The considered structure is composed of 4 layers of $0.12 - mm -$ thick carbon fiber fabric. Only one wire of NiTiNOL is embedded into the structure.

Table 105: Results obtained from wire activation

1st wire	Max displacement [cm]	Residual displacement [cm]	% Activation	% De-activation	N. elements
1	12.23920967	0.671517748	8.661417323	25.69792412	1398
2	12.15794644	0.715873999	12.07430341	25.90299278	970
3	12.21445974	0.748510773	14.19141914	28.60286029	910
4	12.13918849	0.677555095	9.282296651	30.81339713	1046
5	12.28274521	0.731655529	11.82458888	30.14878622	1278
6	11.93810284	0.452171518	12.45318352	26.49812734	1069
7	12.31037798	0.613765761	10.30351438	28.75399361	1253
8	12.36375729	0.781779179	6.68002672	27.18770875	1498
9	12.09940022	0.653956678	7.587253414	32.77693475	1319
10	12.09870169	0.756536462	12.04996326	31.66789126	1362

The considered structure is composed of 4 layers of $0.12 - mm -$ thick carbon fiber fabric. There are two wires of NiTiNOL inside sheaths that are embedded into the structure.

Table 106: Result of old wire displacements

1st old wire	Max displacement [cm]	Residual displacement [cm]	% Activation	% De-activation	N. elements
1	15.343636	1.10113188	3.183023873	53.10344828	1886
2	14.82637743	0.975956393	4.124408384	54.22582826	1480
3	14.6412799	0.522848642	3.629764065	46.58197217	1654
4	14.59572034	1.01260575	3.606748109	56.77719604	1720
5	14.48177659	0.785705512	3.511801957	46.7472654	1738
6	14.07022145	1.370444842	3.577611079	50.83669937	1734
7	14.22036981	1.536826471	4.953560372	60.91331269	1293
8	13.73794962	1.018020818	3.738317757	49.47040498	1606
9	13.94557692	1.340539023	3.64321608	50.43969849	1593
10	13.74082141	1.228168464	2.915451895	47.86200194	2059

Table 107: Result of new wire displacements

1st new wire	Max displacement [cm]	Residual displacement [cm]	% Activation	% De-activation	N. elements
1	36.19479634	1.645286603	6.641221374	41.52671756	1311
2	35.91884041	1.321310798	6.147859922	42.72373541	1286
3	35.13336761	1.145859311	5.28246515	46.51504035	1364
4	34.77554479	1.799423738	4.906703525	39.5300622	1448
5	33.82090504	0.958147592	5.243161094	46.2006079	1317
6	33.80700251	0.919766355	4.655870445	42.37516869	1483
7	33.77920008	0.937934813	4.846103471	45.77603143	1528
8	33.80967173	0.830792678	4.06504065	37.74680604	1723
9	33.45672349	0.777759515	3.98205272	40.32529445	1784
10	33.62050162	1.059378894	3.993055556	37.84722222	1729

Table 108: Result of second wire displacements

2nd wire	Max displacement [cm]	Residual displacement [cm]	% Activation	% De-activation	N. elements
1	31.83758784	0.351878286	14.94661922	31.31672598	1125
2	30.63356057	0.997964714	8.090185676	34.8806366	1509
3	30.16459889	1.046353804	8.26306914	34.56998314	1187
4	29.97251799	0.74496232	7.288629738	34.81049563	1716
5	29.72279613	1.321642402	7.099945385	33.91589295	1832
6	29.45049049	0.769822197	7.458143075	35.84474886	1315
7	29.51526806	0.473556299	4.896626768	28.07399347	1839
8	30.13637949	1.037448842	6.503198294	30.49040512	1877
9	29.51909176	1.031834504	5.936920223	29.87012987	1618
10	29.56397622	1.085556496	6.552901024	31.39931741	1466

The considered structure is composed of 4 layers of $0.12 - mm -$ thick carbon fiber fabric. There are two wires of NiTiNOL directly embedded into the structure.

Table 109: Result of first wire displacements

1st wire	Max displacement [cm]	Residual displacement [cm]	% Activation	% De-activation	N. elements
1	10.31728554	0.44032894	7.564102564	19.23076923	781
2	10.7906399	0.455402485	7.112375533	27.16927454	704
3	10.68247174	0.43117658	7.462686567	19.85074627	671
4	10.35967029	0.825528654	7.815275311	15.80817052	564
5	10.1515791	0.436957091	6.324972737	17.44820065	918
6	10.66759859	0.40051171	6.666666667	23.84615385	781
7	9.807757814	0.444454284	9.745762712	28.81355932	473
8	10.26029331	0.46586247	7.108239095	23.42487884	620
9	10.25329154	0.264943044	6.910039113	21.25162973	768

| 10 | 9.727523029 | 0.434573477 | 6.285714286 | 18.71428571 | 701 |

Table 110: Result of second wire displacements

2nd wire	Max displacement [cm]	Residual displacement [cm]	% Activation	% De-activation	N. elements
1	10.08351579	0.503202986	5.054151625	23.10469314	832
2	10.2924597	0.489795234	6.764705882	24.41176471	681
3	10.2668234	0.451168006	4.498977505	15.33742331	979
4	9.728343788	0.423065768	6.18705036	22.44604317	696
5	9.796703262	0.408383703	5.942622951	21.61885246	977
6	9.713653456	0.392101826	7.142857143	27	701
7	9.957248877	0.521743978	7.866868381	27.98789713	662
8	9.918302566	0.529475515	6.303030303	23.75757576	826
9	9.999013145	0.360407945	7.209302326	20.58139535	861
10	10.03661052	0.577752365	4.831460674	23.03370787	891

The considered structure is composed of 4 layers of $0.12 - mm -$ thick carbon fiber fabric. There are three wires of NiTiNOL inside sheaths that are embedded into the structure.

Table 111: Result of first wire displacements

1st wire	Max displacement [cm]	Residual displacement [cm]	% Activation	% De-activation	N. elements
1	28.24187883	1.067907324	7.332796132	27.39726027	1242
2	28.13105199	0.534445252	14.54783748	34.07601573	764
3	28.46869921	0.560922305	12.91560102	33.63171355	783
4	28.10781042	0.148988367	13.41890315	30.9218203	858
5	28.2528303	0.565456716	12.32876712	29.5143213	804
6	28.11354782	0.304764823	7.445956765	32.3458767	1250
7	29.93368519	0.636491043	9.515418502	28.72246696	1136
8	29.54805169	0.588757648	11.31270011	27.53468517	938
9	27.71084377	0.299384381	12.65356265	32.8009828	815
10	29.70574677	1.187933198	10.53719008	26.03305785	969

Table 112: Result of second wire displacements

2nd wire	Max displacement [cm]	Residual displacement [cm]	% Activation	% De-activation	N. elements
1	31.15107983	0.867181147	28.48920863	27.62589928	696
2	31.09632578	1.08381417	25.20868114	28.5475793	600
3	29.54807952	0.694559728	12.31155779	24.74874372	797
4	30.23412297	0.834910414	23.988006	27.43628186	668
5	30.22093326	0.697593429	26.81047766	28.81355932	650
6	31.1615678	0.658578545	24.78873239	26.1971831	711
7	30.90939155	0.697116879	24.11444142	24.93188011	735

8	31.55294476	1.195479654	22.79005525	28.03867403	725
9	31.03180676	1.2907604	27.84810127	29.90506329	633
10	31.7091156	0.648884365	22.62773723	27.00729927	686

Table 113: Result of third wire displacements

3rd wire	Max displacement [cm]	Residual displacement [cm]	% Activation	% De-activation	N. elements
1	26.44884056	0.905075846	21.49068323	27.20496894	806
2	27.30346189	1.366302317	28	29.51724138	726
3	27.5940189	0.643122082	18.38565022	26.27802691	1116
4	26.83147108	0.869043501	15.9847764	25.49952426	1052
5	27.01763631	0.841030573	21.98067633	37.92270531	829
6	26.55427476	0.761118147	19.76369495	30.18259936	932
7	26.3786163	0.885506845	18.69822485	25.91715976	846
8	26.77646354	0.740334956	17.39618406	27.27272727	892
9	26.08817812	0.343461919	13.33333333	27.95454545	1321
10	25.90661771	0.920068601	23.02052786	30.35190616	683

The considered structure is composed of 4 layers of $0.12 - mm -$ thick carbon fiber fabric. There are six wires of NiTiNOL directly embedded into the structure.

Table 114: Result of first wire displacements

1st wire	Max displacement [cm]	Residual displacement [cm]	% Activation	% De-activation	N. elements
1	7.450162008	0.296123501	21.19635891	27.56827048	770
2	7.560983551	0.353094433	22.75574113	29.95824635	959
3	7.640609619	0.428251089	16.10738255	33.44519016	895
4	7.673638424	0.307032189	20.43269231	22.47596154	833
5	7.422887228	0.364647895	14.28571429	21.2406015	1065
6	7.267667076	0.38733962	22.22222222	36.76470588	613
7	7.393095947	0.455327642	29.25457103	27.42616034	712
8	7.295158043	0.466982446	19.59183673	35.51020408	736
9	7.126196914	0.389540194	37.56019262	30.65810594	624
10	7.262994914	0.486639707	24.01685393	28.51123596	713

Table 115: Result of second wire displacements

2nd wire	Max displacement [cm]	Residual displacement [cm]	% Activation	% De-activation	N. elements
1	10.12241861	0.463271324	45.29331514	24.1473397	734
2	10.32841364	0.483717628	22.01622248	20.27809965	864
3	10.49323864	0.362679704	18.56540084	25.84388186	949
4	10.62105967	0.469795399	9.951690821	22.41545894	1036
5	10.86719011	0.387212717	24.82690406	23.83778437	1012
6	10.81438027	0.35076707	18.7962963	21.2962963	1081

7	10.67869581	0.483905704	32.06997085	24.63556851	687
8	10.53694398	0.506739304	27.37306843	24.39293598	907
9	10.64218584	0.576906836	20.13574661	21.71945701	885
10	11.07806907	0.460632271	21.09617373	20.47569804	968

Table 116: Result of third wire displacements

3rd wire	Max displacement [cm]	Residual displacement [cm]	% Activation	% De-activation	N. elements
1	12.68483569	0.559473933	30.04484305	24.43946188	893
2	12.44758084	0.646130445	27.81316348	15.39278132	943
3	12.50197296	0.471407663	20.67209776	24.33808554	983
4	12.87984826	0.638351917	21.875	22.12837838	1185
5	12.48678312	0.685122014	20.63037249	25.3104107	1048
6	11.96164341	0.520244729	20.45184304	25.32699168	842
7	12.04673163	0.413024494	24.75463468	19.41112323	918
8	11.75363108	0.472116797	25.09541985	20.99236641	1049
9	11.85393581	0.685112174	18.63488624	24.7020585	924
10	11.54150103	0.522246262	16.41490433	22.1550856	994

Table 117: Result of fourth wire displacements

4th wire	Max displacement [cm]	Residual displacement [cm]	% Activation	% De-activation	N. elements
1	7.794600374	0.275026946	17.13244228	21.9927096	824
2	7.891811276	0.516907897	29.41847206	19.61231471	878
3	7.703980458	0.467057247	27.81371281	19.1461837	774
4	8.093074613	0.357453542	31.37996219	15.59546314	1059
5	7.964551166	0.519196255	20	16.08465608	946
6	7.85491993	0.411260991	16.84284708	11.62790698	1420
7	7.904467768	0.340781764	11.49425287	11.49425287	1306
8	7.876128444	0.385151727	15.81291759	17.03786192	899
9	7.592673034	0.321500356	25.26315789	20.60150376	666
10	7.776547205	0.278719134	22.97008547	16.23931624	937

Table 118: Result of fifth wire displacements

5th wire	Max displacement [cm]	Residual displacement [cm]	% Activation	% De-activation	N. elements
1	6.915864506	0.647086844	14.27425822	22.45388933	1248
2	6.737860357	0.493284453	19.79695431	22.84263959	986
3	6.587850564	0.28431505	16.76445935	20.20117351	1194
4	6.670454617	0.424554593	11.50700935	16.58878505	1713
5	6.491131699	0.556687717	20.32032032	24.32432432	1000
6	6.456572632	0.546223349	18.04995971	27.07493956	1242
7	6.473011305	0.463889746	13.76868607	22.97403619	1272

8	6.402038298	0.491743744	16.05415861	22.05029014	1035
9	6.485488045	0.43841507	16.82242991	17.41716228	1178
10	6.470080403	0.304423241	15.13327601	18.57265692	1164

Table 119: Result of sixth wire displacements

6th wire	Max displacement [cm]	Residual displacement [cm]	% Activation	% De-activation	N. elements
1	6.600368299	0.432110415	16.41137856	21.66301969	915
2	6.722401538	0.452866717	25.40540541	25.40540541	926
3	6.759918825	0.454288195	18.59582543	27.79886148	1055
4	6.424474543	0.405494955	17.54385965	17.34892788	1027
5	6.369715301	0.519677849	21.25	24.58333333	961
6	6.606097894	0.485862089	19.5035461	24.94089835	847
7	6.641175153	0.687735414	19.62134251	20.99827883	1163
8	6.494378445	0.407754721	18.01140994	17.4409128	1228
9	6.707148261	0.607807722	15.7980456	15.06514658	1229
10	6.567608008	0.650657031	13.88235294	17.25490196	1276

The considered structure is composed of 6 layers of $0.12 - mm -$ thick glass fiber fabric. There are three wires of NiTiNOL inside sheaths that are embedded into the structure.

Table 120: Result of first wire displacements

1st wire	Max displacement [cm]	Residual displacement [cm]	% Activation	% De-activation	N. elements
1	24.22963225	1.218353855	10.54512958	26.54155496	1120
2	23.59535592	0.834929926	12.81533804	27.34611504	992
3	23.39835379	0.513858821	12.04139229	26.434619	1064
4	23.34836556	0.542066386	11.3865932	24.42607897	1090
5	23.14093029	0.690834968	11.77042802	27.72373541	1029
6	23.38091985	1.087798138	9.270516717	24.39209726	1317
7	22.96526984	0.657192666	10.2233677	21.82130584	1165
8	22.60441933	0.986752175	10.82089552	29.94402985	1073
9	23.43996033	0.721283091	12.57995736	34.43496802	939
10	23.55120895	0.672908851	8.737283064	30.34111311	1672

Table 121: Result of second wire displacements

2nd wire	Max displacement [cm]	Residual displacement [cm]	% Activation	% De-activation	N. elements
1	25.00432203	1.344248791	9.448275862	15.93103448	1451
2	25.15440291	1.33341222	7.324106113	14.41753172	1735
3	25.49616032	2.380569496	7.977026165	16.20931717	1568
4	25.90450634	1.278669276	6.839622642	13.11320755	2121
5	27.05600972	0.510044101	6.928746929	12.08845209	2036

	25.40707783	0.994971074	19.23601637	32.46930423	734
6					
7	26.43968015	1.912130424	10.54239878	18.86936593	1310
8	26.64225729	1.427659317	7.299703264	14.83679525	1686
9	24.8690117	1.914115843	10.6943336	19.07422187	1254
10	25.31520212	1.082118147	10.67961165	21.197411	1237

Table 122: Result of third wire displacements

3rd wire	Max displacement [cm]	Residual displacement [cm]	% Activation	% De-activation	N. elements
1	24.23298004	1.082112142	11.45092461	23.75533428	1407
2	23.30492979	0.616870014	9.661835749	22.29123533	1450
3	24.34102882	0.903423513	10.06202619	22.46726396	1452
4	25.78180652	2.559418492	9.694209499	20.10409889	1538
5	23.26717423	0.4314855	7.127192982	19.40789474	1825
6	23.27286061	1.181608752	7.643678161	17.81609195	1741
7	25.45291488	0.662113992	7.456588355	19.81613892	1959
8	24.22801253	1.155565776	11.52263374	22.22222222	1216
9	23.36955092	0.792795251	7.710144928	19.30434783	1726
10	24.45298164	1.583015284	9.066305819	23.27469553	1479

8 List of Figures

9 List of Tables

10 List of symbols

Variable	Description	SI unit
A_s, A_f	Austenitic start and finish temperatures	K
M_s, M_f	Martensitic start and finish temperatures	K
M_d	Pseudo-elastic limit temperature	K
E_x, E_y	Elastic modulus in x and y direction	MPa
ν_{12}	Poisson coefficient	
G_{12}, G_{23}, G_{13}	Shear modulus	MPa
σ	Stress state	Pa
c_A, c_M	Coefficients of the Clausius-Clapeyron equation	Pa
λ	Thermal conductivity	W/mK
ρ	Density	Kg/m^3
c	Specific heat	J/KgK
h	Convective coefficient	W/m^2K
Nu	Nusselt number	
Pr	Prandtl number	
Re	Reynolds number	
$\dot{Q}$	Thermal heat flux	W/m^2
ε	Emissivity	
α	Coefficient of thermal expansion	K^{-1}
T_{out}	External temperature of the composite	K
T_{in}	Internal temperature of the composite	K
T_{wire}	Temperature of the uncovered wire	K
Bi	Biot number	
P	Electric power	W
R	Resistance	Ω
F_{i-j}	View factor	
q	Flow of thermal power	W/m^2
Q_{sun}	Power generated by solar radiation	W
Q_{albedo}	Power generated by albedo radiation	W
Q_{IR}	Power generated by infrared radiation	W
μ	Dynamic viscosity	Pa s
γ	Adiabatic coefficient of expansion	
β	Compressibility module	GPa
$t_{activation}$	Time for activation	s

M	Mach number	
e	Roughness	*mm*
u	Velocity vector	*m/s*
n	Vector normal to surface	
ṁ	Mass flow rate	*Kg/s*
U1	Displacement in direction 1	*mm*
U2	Displacement in direction 2	*mm*
U3	Displacement in direction 3	*mm*
r	Radius of curvature	*m*
d	Distance of the extremis of the spiral	*m*
θ	Angle of curvature	*Degree*
L	Height of the reduced model of the structure	*m*
bc	Height of the constraint at the base of the reduced model of the structure	*m*
i	Electric current	*A*
V	Voltage	*V*

11 Acknowledgments

Senza di te niente sarebbe stato possibile.